

Submitted by  
**Dipl.-Ing.**  
**Victoria Hutterer,**  
**BSc.**

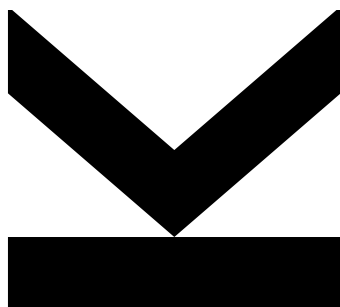
Submitted at  
**Industrial Mathematics**  
**Institute**

Supervisor and  
First Examiner  
**Univ.-Prof. Dr.**  
**Ronny Ramlau**

Second Examiner  
**Eric Todd Quinto,**  
**Ph.D., Robinson Profes-**  
**sor of Mathematics**

October 2018

# Model-based wavefront reconstruction approaches for pyramid wavefront sensors in Adaptive Optics



Doctoral Thesis  
to obtain the academic degree of  
Doktorin der Technischen Wissenschaften  
in the Doctoral Program  
Technische Wissenschaften



## Abstract

Atmospheric turbulence and diffraction of light result in the blurring of images of celestial objects when they are observed by ground based telescopes. To correct for the distortions caused by wind flow or small varying temperature regions in the atmosphere, the new generation of Extremely Large Telescopes (ELTs) uses Adaptive Optics (AO) techniques. An AO system consists of wavefront sensors, control algorithms and deformable mirrors. A wavefront sensor measures incoming distorted wavefronts, the control algorithm links the wavefront sensor measurements to the mirror actuator commands, and deformable mirrors mechanically correct for the atmospheric aberrations in real-time. Reconstruction of the unknown wavefront from given sensor measurements is an Inverse Problem.

Many instruments currently under development for ELT-sized telescopes have pyramid wavefront sensors included as the primary option. For this sensor type, the relation between the intensity of the incoming light and sensor data is non-linear. The high number of correcting elements to be controlled in real-time or the segmented primary mirrors of the ELTs lead to unprecedented challenges when designing the control algorithms. Therefore, a precise mathematical investigation of the pyramid sensor and its forward models is essential for accurate and fast wavefront reconstruction.

In this Thesis, we present new approaches for wavefront reconstruction from pyramid wavefront sensor data for which our detailed analytical study of the pyramid sensor lays the mathematical foundation. Therefore, we derive the pyramid sensor models in a distributional sense and provide a thorough analysis of the underlying operators, e.g., we linearize the models or calculate Fréchet derivatives and adjoint operators. Using further approximations that are suggested by the physical setting of the sensor itself, we can describe the sensor's forward models as roof sensor configurations or as a variant of the finite Hilbert transform of the incoming wavefront. The analysis is extended to these operators as well.

Based on various approximate models, several algorithms have been developed in recent years for a stable, high-quality, and high-speed wavefront correction. Among those, we emphasize interaction-matrix-based approaches, Fourier domain methods, iterative algorithms, and methods based on the inversion of the finite Hilbert transform. We briefly present the core ideas of already existing algorithms and explicitly provide the theoretical background of new approaches for wavefront reconstruction from pyramid and roof wavefront sensor data.

We divide the new algorithms into two groups: linear and non-linear wavefront reconstruction methods. With linear approaches, we use a singular value expansion for wavefront reconstruction or apply well-known iterative methods such as the conjugate gradient method, the steepest descent algorithm, Landweber iteration or Kaczmarz versions of the previously mentioned methods. With non-linear approaches, we employ non-linear Landweber iteration and Landweber-Kaczmarz iteration to the problem of wavefront reconstruction from pyramid sensor data.

An additional complication arises due to the structure of the ELTs. So called telescope spiders create areas where the information of the phase is isolated on the wavefront sensor detector, leading to pupil fragmentation and a break in the spatial continuity of the data, and further to extremely poor wavefront reconstruction. These unwanted errors make several existing control algorithms unfeasible for telescope systems with wide spiders. To overcome the effects induced by telescope spider obstruction we propose a hybrid scheme, the so called Split Approach, which combines model-based algorithms with methods that provide the lost information directly from isolated reconstructors resulting in accurate wavefront reconstruction for segmented pupils.

The effectiveness of the proposed algorithms is demonstrated in the context of the 39 m Extremely Large Telescope. Numerical evaluations using European Southern Observatory's end-to-end simulation tool Octopus include detailed comparisons of speed and reconstruction quality of the proposed new methods to previously developed algorithms.

## Zusammenfassung

Aufgrund von atmosphärischen Turbulenzen und Lichtbrechung sind Bilder von Himmelskörpern, die mit erdgebundenen Teleskopen aufgenommen werden, verschwommen. Um die Störungen, hervorgerufen von Windströmungen oder kleinen, veränderlichen Temperaturzonen in der Atmosphäre, auszugleichen, verwendet man für die neue Generation von Extremely Large Telescopes (ELTs) die Methode der Adaptiven Optik (AO). Ein AO System besteht aus Wellenfrontsensoren, Kontrollalgorithmen und verstellbaren Spiegeln. Ein Wellenfrontsensor misst einfallende, verzerrte Wellenfronten, der Kontrollalgorithmus verbindet die Wellenfrontsensormessungen mit den Kommandos für die Spiegelaktuatoren und die verstellbaren Spiegel korrigieren die atmosphärischen Bildfehler mechanisch in Echtzeit. Die Rekonstruktion der unbekanntenen Wellenfront aus den gegebenen Sensormessungen ist ein Inverses Problem.

In vielen der Instrumente, die derzeit für Teleskope der Größenordnung von ELTs entwickelt werden, ist der Pyramid Wellenfrontsensor als erste Option vorgesehen. Für diese Art von Sensor ist die Verbindung zwischen der Intensität des einfallenden Lichtes und der Sensordaten nichtlinear. Die hohe Anzahl der Korrektur Elemente, die in Echtzeit kontrolliert werden müssen, oder die segmentierten Hauptspiegel der ELTs führen zu noch nie dagewesenen Herausforderungen bei der Umsetzung von Kontrollalgorithmen. Deshalb ist für eine genaue und schnelle Wellenfrontrekonstruktion eine präzise mathematische Untersuchung des Pyramid Wellenfrontsensors und seiner Vorwärtsmodelle essentiell.

In dieser Dissertation präsentieren wir neue Ansätze zur Wellenfrontrekonstruktion aus Pyramid Wellenfrontsensordaten, für welche unsere detaillierte Untersuchung des Pyramid Sensors die mathematische Grundlage bildet. Für diesen Zweck leiten wir die Pyramid Sensormodelle im Distributionensinn her und geben eine ausführliche Analyse der zu Grunde liegenden Operatoren an; zum Beispiel linearisieren wir die Modelle oder berechnen Fréchet Ableitungen und adjungierte Operatoren. Unter Verwendung weiterer Approximationen, die vom physikalischen Aufbau des Sensors abgeleitet werden, können wir die Vorwärtsmodelle des Sensors als eine Roof Sensor-Konfigurationen oder als eine Variante der endlichen Hilbert Transformation der einfallenden Wellenfront beschreiben. Die Analyse wird auch auf diese Operatoren ausgedehnt.

Basierend auf verschiedenen Vorwärtsmodellen sind in den letzten Jahren zahlreiche Algorithmen für eine stabile und hochqualitative Hochgeschwindigkeits-Wellenfrontkorrektur entwickelt worden. Wir beschreiben unter diesen Ansätze solche, die auf

einer Interaktions-Matrix basieren, Methoden im Fourierraum, iterative Ansätze und Verfahren, die auf der Inversion der endlichen Hilbert Transformation beruhen. Wir präsentieren kurz die Kernideen von bereits existierenden Algorithmen and stellen den theoretischen Hintergrund von neuen Herangehensweisen zur Wellenfrontrekonstruktion aus Pyramid und Roof Wellenfrontsensordaten im Detail dar.

Die neuen Algorithmen teilen wir in zwei Gruppen auf: lineare und nichtlineare Wellenfrontrekonstruktionsmethoden. Als lineare Ansätze verwenden wir eine Singulärwert-Erweiterung für die Wellenfrontrekonstruktion oder bekannte iterative Methoden wie das CG-Verfahren, den Algorithmus des steilsten Abstiegs, Landweber Iteration oder Kaczmarz Versionen der zuvor genannten Methoden. Als nichtlineare Ansätze benutzen wir nichtlineare Landweber Iteration und Landweber-Kaczmarz Iteration für das Problem der Wellenfrontrekonstruktion aus Pyramid Sensordaten.

Eine zusätzliche Komplikation tritt aufgrund des Aufbaus der ELTs auf. Sogenannte Teleskop-Spiders erzeugen Bereiche, in welchen die Information über die Phase am Detektor des Wellenfrontsensors isoliert ist, was zu einer Fragmentierung der Teleskopapertur und einem Verlust der gebietlichen Verbundenheit der Daten und weiters zu äußerst schlechter Wellenfrontrekonstruktion führt. Diese unerwünschten Fehlerquellen machen existierende Kontrollalgorithmen unbrauchbar für Teleskopsysteme mit breiten Spider-Strukturen. Um die Effekte, die durch Teleskop-Spider-Beschattung entstehen, zu korrigieren, entwickeln wir ein zweiteiliges Schema, den sogenannten Split Ansatz, welcher Modell-basierende Algorithmen mit Methoden, die die verlorene Information direkt aus unabhängigen Rekonstruktoren gewinnen, kombiniert und so in genaue Wellenfrontrekonstruktion für segmentierte Teleskopöffnungen resultiert.

Die Effektivität der eingeführten Algorithmen wird im Kontext des 39 m großen Extremely Large Telescopes demonstriert. Numerische Evaluierungen aus der “end-to-end“ Simulationsumgebung Octopus von der Europäischen Südsternwarte beinhalten detaillierte Geschwindigkeits- und Qualitätsvergleiche der präsentierten neuen Methoden zu vorher entwickelten Algorithmen.

# Acknowledgments

I would like to express my deep gratitude to my supervisor Prof. Ronny Ramlau for his guidance, support, and the unique opportunity to be involved in the fascinating work on the technology for the ELT. During my time as a doctoral student, I have enjoyed the freedom and trust he offered me to accomplish my work, kindness, patience, and friendship which I really appreciate.

My heartfelt thanks go to the second referee Eric Todd Quinto, Robinson Prof. of Mathematics for the time he invested in reading this dissertation, his untiring support, and the inspiration he gave me.

I also would like to express my kindest thanks to my close collaborators Dr. Iuliia Shatokhina and Dr. Andreas Obereder especially for sharing the expertise they have already built up over the years before I began working in the field of Adaptive Optics. My gratitude also goes to all co-workers from the Austrian Adaptive Optics team (Dr. Roland Wagner, Dr. Günter Auzinger, DI Markus Pöttinger, Dr. Simon Hubmer, DI Stefan Raffetseder, Dr. Jenny Niebsch, Elisabeth Hager, Dr. Daniela Saxenhuber, DI Bernadett Stadler), Prof. Andreas Neubauer, Dr. Kirk Soodhalter, and Dr. Miska Le Louarn for frequent help and support, fruitful discussions, and cordial friendship.

Without the support of my family this journey would not have ever started. I am truly grateful to my parents Brigitte and Gerhard and my brothers Andreas and Gerhard for giving me the inspiration for my work. They have lovingly taught me every day that in-depth knowledge alone is not sufficient for success in life. They have always encouraged me to follow my dreams, which I sincerely appreciate. Their support is worth more than I can put into words.

I thank my relatives, friends, and former fellow students for supporting me through this entire process, for offering me advice, and for many happy hours we spent together. I greatly appreciate the cheerfulness and enthusiasm as well as the necessary distractions from research they offered me.

This research was partially supported by the Upper Austrian Government, strategic program “Innovatives OÖ 2010 plus“ and by the Austrian Science Fund (FWF): F6805-N36, project 5 and W1214-N15, project DK8.

Victoria Hutterer  
Linz, October 2018



*To my family  
Brigitte, Gerhard, Andreas, and Gerhard*



# Contents

<b>1</b>	<b>Introduction</b>	<b>1</b>
<b>2</b>	<b>Astronomical Adaptive Optics</b>	<b>5</b>
2.1	The new era of Extremely Large Telescopes . . . . .	5
2.1.1	ESO's Extremely Large Telescope . . . . .	7
2.2	Principles on image formation on telescope systems . . . . .	8
2.3	Atmospheric turbulence . . . . .	10
2.3.1	Kolmogorov turbulence model . . . . .	11
2.3.2	Von Karman turbulence model . . . . .	12
2.3.3	Atmospheric layer model . . . . .	12
2.3.4	Atmospheric parameters . . . . .	13
2.4	Basics on Adaptive Optics . . . . .	14
2.4.1	AO component: guide star . . . . .	15
2.4.2	AO component: wavefront sensor . . . . .	17
2.4.3	AO component: deformable mirror . . . . .	20
2.4.4	AO component: real-time control unit . . . . .	20
2.4.5	AO systems . . . . .	22
2.4.6	Open and closed loop configurations . . . . .	24
2.5	Numerical analysis . . . . .	24
2.5.1	Measures in AO . . . . .	25
2.5.2	Quality measure: Strehl ratio . . . . .	26
2.5.3	Simulation environment . . . . .	27
<b>3</b>	<b>The pyramid sensor model</b>	<b>29</b>
3.1	Pyramid sensor modeling: state of the art . . . . .	29
3.1.1	Physical design of a pyramid wavefront sensor . . . . .	30
3.2	Pyramid sensor modeling: new mathematical foundation . . . . .	33
3.2.1	Mathematical derivation of transmission mask model . . . . .	37
3.2.2	Mathematical derivation of phase mask model . . . . .	50
3.3	Pyramid and roof wavefront sensor forward operators (transmission mask model) . . . . .	51
3.4	Linearization of the roof sensor operators . . . . .	56
3.5	Adjoints of the linearized forward operators . . . . .	61
3.6	The discrete pyramid wavefront sensor . . . . .	65

3.7	Summary on forward models . . . . .	66
<b>4</b>	<b>Linear wavefront reconstruction using a singular value type expansion</b>	<b>67</b>
4.1	Underlying pyramid forward model . . . . .	68
4.2	The singular value type expansion of the underlying operator . . . . .	69
4.2.1	Finite Hilbert transform operator . . . . .	69
4.2.2	Decomposition with Chebychev polynomials . . . . .	71
4.3	Numerical validation . . . . .	76
4.3.1	Iterative reconstruction using a measurement extension . . . . .	79
4.4	Summary on the SVTR method . . . . .	83
<b>5</b>	<b>Linear wavefront reconstruction using iterative methods</b>	<b>85</b>
5.1	Underlying forward models . . . . .	85
5.2	Iterative wavefront reconstruction methods . . . . .	87
5.2.1	CGNE approach . . . . .	87
5.2.2	Steepest descent approach . . . . .	88
5.2.3	Landweber approach . . . . .	90
5.2.4	Kaczmarz methods for wavefront reconstruction from pyramid sensor data . . . . .	91
5.3	Numerical results . . . . .	97
5.3.1	Optimal step size choice for SD iteration in the context of WF reconstruction from pyramid data . . . . .	98
5.3.2	Simulated closed loop performance . . . . .	99
5.3.3	Comparison to interaction-matrix-based approaches . . . . .	102
5.4	Computational complexity . . . . .	103
5.4.1	Complexity of linear LIPS and KLIPS . . . . .	103
5.4.2	Complexity of SD and SD-Kaczmarz for pyramid sensors . . . . .	104
5.4.3	Complexity of CGNE for pyramid sensors . . . . .	104
5.4.4	Comparison to MVM . . . . .	105
5.5	Summary on linear iterative methods . . . . .	106
<b>6</b>	<b>Non-linear wavefront reconstruction using Landweber and Landweber-Kaczmarz iteration</b>	<b>109</b>
6.1	Non-linear problem of wavefront reconstruction using pyramid sensors . . . . .	110
6.2	Non-linear Landweber iteration for solving the wavefront reconstruction problem . . . . .	112
6.2.1	Non-linear Landweber algorithm applied to pyramid sensors . . . . .	115
6.2.2	Non-linear Landweber-Kaczmarz algorithm applied to pyramid sensors . . . . .	116
6.3	Fréchet derivatives and corresponding adjoint operators of the roof sensor model . . . . .	117
6.4	Numerical implementation and complexity . . . . .	120

6.4.1	Computational complexity . . . . .	123
6.5	End-to-end simulation results . . . . .	124
6.5.1	Comparison to the linear versions of the algorithms . . . . .	126
6.6	Summary on non-linear LIPS and KLIPS . . . . .	128
<b>7</b>	<b>Overview on wavefront reconstruction methods for pyramid sensors</b>	<b>131</b>
7.1	Wavefront reconstruction: current state of the art . . . . .	134
7.1.1	Interaction-matrix-based reconstructors . . . . .	134
7.1.2	Fourier domain methods: P-CuReD . . . . .	134
7.1.3	Fourier domain methods: FTR . . . . .	136
7.1.4	Fourier domain methods: CLIF & PFTR . . . . .	137
7.1.5	Hilbert transform methods: HTR . . . . .	139
7.1.6	Hilbert transform methods: TCR . . . . .	140
7.1.7	Hilbert transform methods: FHTR . . . . .	140
7.1.8	Non-linear iterative methods: phase retrieval algorithm . . . . .	142
7.1.9	Non-linear iterative methods: JR method . . . . .	142
7.1.10	Non-linear iterative methods: quasi-Newton method . . . . .	143
7.2	Model, speed, and quality performance comparisons . . . . .	144
<b>8</b>	<b>Accurate wavefront reconstruction in the presence of telescope spiders</b>	<b>149</b>
8.1	Differential piston effects induced by telescope spiders . . . . .	149
8.2	Interaction-matrix-based reconstructors . . . . .	153
8.2.1	Generating the interaction matrix . . . . .	153
8.2.2	Working with DM influence functions . . . . .	154
8.2.3	Deterministic setting . . . . .	155
8.2.4	Bayesian setting . . . . .	157
8.2.5	Performance of interaction-matrix-based MVM in presence of spiders . . . . .	159
8.3	Advanced model-based reconstructors . . . . .	160
8.3.1	Quality and speed performance of model-based reconstructors without spiders . . . . .	161
8.3.2	Adapting advanced reconstructors to segmented pupils . . . . .	162
8.4	Split Approach . . . . .	164
8.4.1	Piston-free wavefront reconstruction on segments . . . . .	165
8.4.2	Direct segment piston reconstruction . . . . .	166
8.4.3	Fast and robust wavefront reconstruction under pupil segmentation using the Split Approach . . . . .	169
8.5	Numerical validation . . . . .	171
8.5.1	Simulation environment and parameters . . . . .	171
8.5.2	Numerical results . . . . .	172
8.6	Details on the realization . . . . .	174
8.7	Summary on wavefront reconstruction in the presence of spiders . . . . .	177

<b>9</b>	<b>Conclusions and Outlook</b>	<b>179</b>
<b>A</b>	<b>Mathematical preliminaries</b>	<b>183</b>
	<b>List of Figures</b>	<b>185</b>
	<b>List of Algorithms</b>	<b>189</b>
	<b>List of Tables</b>	<b>191</b>
	<b>References</b>	<b>195</b>

# Chapter 1

## Introduction

Time-varying optical perturbations introduced by the atmosphere severely degrade the image quality of ground based telescopes. Adaptive Optics systems correct these aberrations in real-time: The facilities have devices incorporated that sense the incoming wavefronts and cancel the originated perturbations with a deformable mirror. Suitable mirror configurations are based on an accurate estimation of the shape of the incoming wavefront and can be calculated from wavefront sensor measurements. Reconstruction of the wavefront from sensor data is an Inverse Problem for which the underlying mathematical forward model depends on the type of the wavefront sensor. This Thesis is mainly concerned with solving the Inverse Problem of wavefront reconstruction using a pyramid wavefront sensor.

More than twenty years ago the pyramid wavefront sensor was proposed for the first time as a promising alternative to other types of wavefront measuring devices [164]. Nowadays, wavefront reconstruction algorithms for the pyramid sensor are in high demand since the devices are planned to be part of many instruments currently under development for ground based telescopes. For the next generation of Extremely Large Telescopes having mirror sizes up to 40 m, the pyramid sensor has been gaining attention from the astronomical community by setting new standards for AO correction quality.

Aside from astronomical applications, the pyramid wavefront sensor is considered in adaptive loops in ophthalmology and microscopy where the underlying concepts are comparable to atmosphere induced perturbations sensing for adaptive optics in astronomy.

The focus of the Thesis lies in the development of wavefront reconstruction algorithms for the pyramid sensor on non-segmented and segmented pupils based on detailed investigations of the mathematical forward models. The theoretical part is accompanied by numerical simulations using an end-to-end simulation environment in which the algorithms have been implemented.

The derivation of mathematically well-defined pyramid wavefront sensor forward models in a distributional sense as well as an extensive theoretical analysis of the underlying operators are the basis of our research. As a result of these investigations, we have developed several reconstruction algorithms which are either based on a linearization of the generally non-linear problem or consist of the application of non-linear iterative algorithms. The reconstruction methods are precisely analyzed in numerical test cases. Detailed comparisons of the new methods to already existing reconstructors are presented. Additionally, we describe two approaches for direct segment piston reconstruction needed in combination with model-based reconstructors for high-quality and high-speed wavefront estimation on segmented telescope pupils.

The Thesis, which uses parts of our work in [106, 107, 108, 109, 110, 111, 149], is organized as follows:

In Chapter 2 we give an introduction to earthbound telescope systems and the principles of astronomical Adaptive Optics. We review the basic concepts on light formation and atmospheric turbulence. Moreover, several components, different operating modes, and quality measures of an AO system are established.

Chapter 3 addresses the pyramid wavefront sensor modeling. We start with specifications on the physical configuration of a pyramid sensor. The mathematical model of the sensor, which is the foundation of the developed model-based reconstruction algorithms, is derived by the usage of distribution theory. We consider different variants, approximations and linearizations of the full non-linear Fourier optics based model and evaluate the corresponding Fourier transforms, Fréchet derivatives, and adjoint operators.

In Chapter 4 a new linear wavefront reconstructor for the non-modulated pyramid wavefront sensor is introduced. The idea is based on a singular value expansion of the underlying operator. Additionally, we consider an iterative method for measurement continuation which was used in combination with the presented wavefront reconstruction approach.

In Chapter 5 we adapt several well-known mathematical algorithms from the field of Inverse Problems to the problem of wavefront reconstruction using pyramid sensor data. The considered approaches are the conjugate gradient algorithm, the steepest descent method, linear Landweber iteration as well as Kaczmarz strategies of the above mentioned approaches.

In Chapter 6 we present one of the first model-based non-linear algorithms for wavefront estimation on telescope instruments using pyramid sensors based on the application of the non-linear Landweber and Landweber-Kaczmarz method.

Chapter 7 contains an overview on wavefront reconstruction methods for the pyramid wavefront sensor. We briefly present the core ideas of previously developed algorithms

---

and make thorough comparisons of underlying pyramid sensor models, computational complexities, and the quality performance between already existing approaches and those introduced in this Thesis.

In Chapter 8 we investigate the effects of large secondary mirror support structures on wavefront reconstruction. We review several variants of interaction-matrix-based algorithms for reconstruction and introduce a new method for accurate and fast wavefront reconstruction on segmented pupils. This approach is a hybrid scheme in which the application of piston reconstructors is necessary. Two such methods for direct segment piston reconstruction on segmented pupils are established.

Finally, Chapter 9 contains conclusions on the results obtained in the previous Chapters and an outlook to future work.



## Chapter 2

# Astronomical Adaptive Optics

Ground based telescope facilities suffer from degraded image quality caused by atmospheric turbulence. When light from a distant star passes the Earth's atmosphere, initially planar wavefronts get distorted due to turbulent air motion related to fluctuations of the index of refraction. Therefore, advanced Adaptive Optics (AO) systems [99, 174] are incorporated in innovative telescope systems to mechanically correct in real-time for the distortions with deformable mirrors. The shape of the deformable mirrors is determined by measuring wavefronts coming from either bright astronomical stars or artificially produced laser beacons. The basic idea is to reflect the distorted wavefronts on a mirror that is shaped appropriately such that the corrected wavefronts allow for high image quality when observed by the science camera (see Figure 2.1). The according positioning of the mirror actuators implies the knowledge of the incoming wavefronts. Thus, in Adaptive Optics one is interested in the reconstruction of the unknown incoming wavefront  $\Phi$  from available data in order to calculate the optimal shape of the deformable mirror. Unfortunately, there exists no optical device which is able to measure the wavefront directly. Instead, a wavefront sensor measures the time-averaged characteristic of the captured light that is related to the incoming phase.

This Chapter contains an introduction to the new generation of Extremely Large Telescopes and provides a review on basic principles for image formation on such telescope systems. We mention the concept of atmospheric turbulence affecting the observations on earthbound telescope facilities and describe the main components and quality measures of an AO system.

## 2.1 The new era of Extremely Large Telescopes

Since the invention of the first telescopes in the 1600s, our view from Earth is continuously enhancing and pushing towards a new breakthrough for the new generation of Extremely Large Telescopes (ELTs). Currently, there are several ground based telescope systems in development having larger mirrors than ever (cf Figure 2.2). Today's

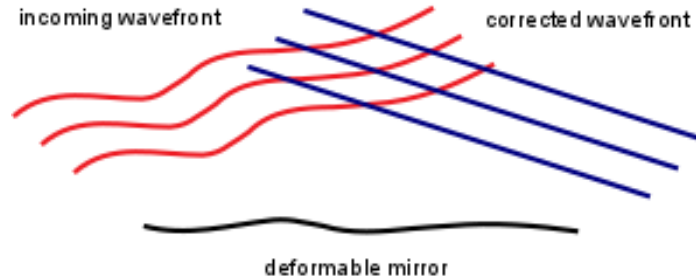


Figure 2.1: Fundamental idea of astronomical AO, source: [43]. Reflection of the light of a distorted wavefront on a mirror results in a corrected wavefront propagating to the science camera.

largest telescope, the Gran Telescopio Canarias located in La Palma, has a primary mirror diameter of 10.4 m. However, the very much smaller 2.4 m Hubble space telescope is surpassing with respect to image quality. For space telescopes, the light does not pass the atmosphere during observations, and therefore is not affected by atmospheric turbulence. This is different on earthbound observing sites. Nevertheless, by the usage of specific image improving techniques, known as Adaptive Optics, observers on Earth’s surface expect outstanding results with the new ELTs. With the help of deformable, computer-controlled mirrors that adjust for atmospheric aberrations in real-time, we will see light from farther and fainter objects than before.

The scientific programs of the new astronomical technologies consist of, e.g., studies of the formation of the first galaxies, investigations of dark matter and dark energy, black holes and exoplanets, as well as searches for life in space or predictions on the Universe in a few trillion years from now on.

The largest telescope planned, the *Extremely Large Telescope* (ELT)[150], with a primary mirror diameter of 39 m will gather more light than all existing ground based telescopes combined. This telescope system is considered in the numerical simulations contained in the Thesis. It is explained in more detail in the subsequent Section 2.1.1.

Another ELT-sized telescope, the *Giant Magellan Telescope* (GMT) [152], is expected to offer 10 times sharper images than the Hubble space telescope. As the ELT, it will be situated in the Atacama desert in Chile, and it will consist of 7 primary mirrors each having 8.4 m in diameter. First light is planned in 2024.

As a complement to the James Webb Space Telescope, the project on the *Thirty Meter Telescope* (TMT) [151] started in the 1990s. The main mirror will constitute of 492 segments each having a diameter of 1.4 m. The telescope is planned to be build on Mauna Kea in Hawaii and shall see first light in 2027.

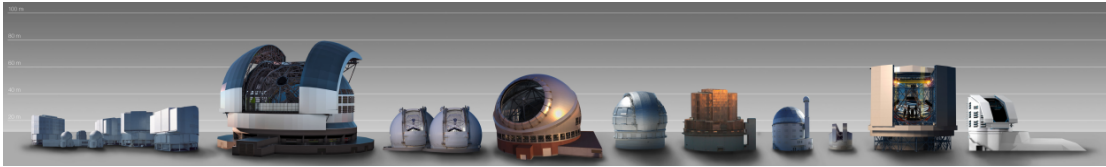


Figure 2.2: Size comparison of existing and planned telescope systems, source: [150]. The Very Large Telescope, Extremely Large Telescope (largest telescope planned), Keck Telescopes, Thirty Meter Telescope, Gran Telescopio Canarias (largest state of the art telescope), Subaru Telescope, South African Large Telescope, New Technology Telescope, Giant Magellan Telescope, and Large Synoptic Survey Telescope (from left to right).

### 2.1.1 ESO's Extremely Large Telescope

The Extremely Large Telescope formerly known as European Extremely Large Telescope (E-ELT) is currently constructed by the European Southern Observatory (ESO). ESO is an intergovernmental astronomy organisation supported by 17 member states. Austria joined ESO in 2008. The Headquarters are situated in Garching close to Munich, Germany, and ESO employs about 700 staff members. The organisation builds and operates ground based telescope systems on the Southern Hemisphere. It provides powerful research facilities to enable astrophysicists and astronomers scientific discoveries. Many of ESO's observing sites are in Chile, e.g., La Silla or Paranal where the Very Large Telescope (VLT) is located. At a distance not too far from Cerro Paranal, more precisely on Cerro Armazones at an altitude of more than 3000 m, ESO is now constructing the ELT.

With a 39.3 m primary mirror resulting in a light collecting area of 978 m<sup>2</sup>, the ELT will become “the world's biggest eye on the sky“. The largest telescope will collect 15 times more light than any of the present day state of the art observing facilities. The primary mirror will compose of altogether 798 hexagonal mirror segments being approximately 1.4 m wide and 50 cm thick.

The concept is based on a 5-mirror-scheme including a deformable mirror (M4) with around 5300 actuators that adapt the mirror's shape more than a thousand times per second. The secondary mirror will have about 4 m in diameter and shades the primary mirror which is known as central obstruction. The support structures of the secondary mirror, also named spiders, shade the primary mirror too. These shadows pose new challenges to wavefront reconstruction for the generation of Extremely Large Telescopes as precisely explained in Chapter 8.

In 2005, ESO started first studies on the development of an ELT. The official beginning of construction was in June 2014 and first light is currently scheduled around 2026. After Austria had entered into the European Southern Observatory, the government had to provide financial and scientific contribution for this membership. That time

was the birth of the *Austrian Adaptive Optics* (AAO) team – a group of researchers at the Industrial Mathematics Institute of the Johannes Kepler University and the Johann Radon Institute for Computational and Applied Mathematics (RICAM) Linz. Its first project aimed at the development of algorithms and software for the E-ELT [148]. Today, the AAO group participates in the consortia of two first light instruments of the ELT, namely METIS [24] and MICADO [49].

### Instruments of the ELT

The first light ELT instruments are the *High Angular Resolution Monolithic Optical and Near-infrared Integral field spectograph* (HARMONI), the *Mid-infrared ELT Imager and Spectograph* (METIS), and the *Multi-AO Imaging CAmera for Deep Observations* (MICADO) combined with the Adaptive Optics module *Multi conjugate Adaptive Optics RelaY* (MAORY). It will be possible to change the position of the whole telescope dome and to switch from one instrument to another within minutes. Having the variety of instruments, the ELT offers the ability to perform observations in a wide range of wavelengths from the optical to the mid-infrared.

Let us now explain those instruments we use in numerical simulations more precisely. As one of three first light instruments of the ELT, the Mid-infrared ELT Imager and Spectograph [24] will allow investigations of exoplanets with respect to physical and chemical properties like weather, temperature, seasons or the composition of their atmospheres. It will amongst others focus on proto-planetary disks, the formation of planets and the Solar System as well as the growth of super massive black holes. The instrument will enable medium-resolution spectroscopy, coronagraphy, imaging and high-resolution integral field spectroscopy. For the METIS instrument, an annular mask is currently considered with an outer diameter of 37 m and an inner diameter of 11.1 m, i.e., all edges of the real ELT primary mirror having a diameter of 39 m are cropped such that there remains a circular area. The currently scheduled sensing device is a pyramid wavefront sensor (see Chapter 3). Within the METIS consortium the AAO team is involved in the development of AO control algorithms.

Another instrument is the *ExoPlanet Imaging Camera and Spectograph* (EPICS) [120] which is planned for the direct imaging and characterization of extra-solar planets. The 2<sup>nd</sup>-generation-instrument of the ELT will be optimized for an application in the visible and the near-infrared and equipped with photometric, spectroscopic, and polarimetric capabilities. In the EPICS simulations contained in this Thesis we consider the originally planned 42 m ELT having a pyramid wavefront sensor.

## 2.2 Principles on image formation on telescope systems

For the description of the imaging process on a telescope, we mainly follow the lines of [91, 139, 174, 178]. If we neglect amplitude variations, the telescope pupil  $\Omega$  is

represented by a characteristic function  $\mathcal{X}_\Omega$ . This means that the function describing the telescope aperture is equal to one within the pupil and zero outside. The telescope aperture usually has a circular shape. Due to the central obstruction induced by the secondary mirror, light is often only usable on an annular domain. In case of large support structures of the secondary mirrors we additionally have to take obstruction effects of the spiders into account. Those divide the light capturing area of the telescope pupil into disconnected segments (cf Chapter 8).

The image  $I_o$  observed on a telescope is related to the astronomical object  $I_a$  by a convolution with the *point spread function*  $PSF$  of the telescope, i.e.,

$$I_o(r) = \int_{\mathbb{R}^2} I_a(r') \cdot PSF(r - r') dr', \quad (2.1)$$

where  $r \in \mathbb{R}^2$  indicates the spatial coordinates. Utilizing the *optical transfer function*  $OTF$  given by

$$OTF(r) = \mathcal{X}_\Omega(r) e^{i\Phi(r)},$$

the point spread function  $PSF : \mathbb{R}^2 \rightarrow \mathbb{R}$  is connected to the Fourier transform of the OTF by

$$PSF(\xi, \eta) = \left| \mathcal{F} \left\{ \mathcal{X}_\Omega e^{i\Phi} \right\} (\xi, \eta) \right|^2.$$

The wavefront aberration  $\varphi$  in optical path distance (meters) is said to be related to the incoming phase  $\Phi$  given in radians by

$$\Phi = \frac{2\pi}{\lambda} \varphi$$

for the wavelength  $\lambda$ . In this Thesis, we omit the multiplicative constant and do not distinguish between phase and wavefront, i.e., we use the notation  $\Phi$  for both since we are mainly interested in the shape of the incoming wavefront aberrations. However, we keep in mind that they differ in their units and that the phase strongly depends on the wavelength  $\lambda$ .

If we do not take atmospheric aberrations into account and assume  $\Phi = 0$ , we receive the diffraction limited PSF. When considering a circular telescope pupil the intensity distribution of an ideal point source formed by a telescope is [91]

$$PSF(r) = \left( \frac{|\Omega|}{\lambda z} \right)^2 \left[ 2 \frac{J_1(kDr/(2z))}{kDr/(2z)} \right]^2$$

for the first order Bessel function  $J_1$  of the first kind, the wave number  $k = (2\pi)/\lambda$ , the telescope diameter  $D$ , the aperture surface  $|\Omega| = \pi (D/2)^2$ , and the normal distance  $z$ . The above term is referred to as the *Airy pattern*. Note that  $J_1$  can be represented by the series expansion around zero as

$$J_1(x) = \sum_{j=0}^{\infty} \frac{(-1)^j}{j! \Gamma(j+2)} \left( \frac{x}{2} \right)^{2j+1}$$

with  $\Gamma(n) = (n-1)!$  for  $n \in \mathbb{N}$  denoting the Gamma function.

Having a look onto equation (2.1), the best choice of a PSF is a delta distribution, i.e., the observed image corresponds to the real image. The larger a telescope aperture becomes the better the corresponding PSF fits a delta distribution as illustrated in Figure 2.3 for the VLT and the ELT. This is due to the dependence of the PSF on the telescope diameter  $D$ .

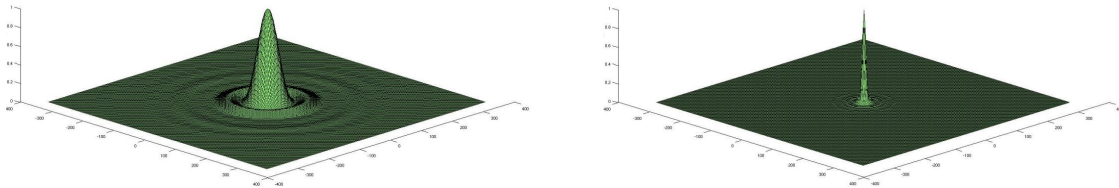


Figure 2.3: Diffraction limited PSF of an 8 m and a 42 m telescope, source [191]. The PSF of the ELT better approximates a delta distribution.

For ground based observations, the diffraction limited PSF is affected by atmospheric aberrations which results in a lower maximum intensity and oscillation patterns towards the outer rings. The goal is to correct these perturbations and come as close as possible to the diffraction limited PSF resulting in sharp images.

Point spread reconstruction algorithms and blind deconvolution methods for Extremely Large Telescopes can be found, e.g., in [104, 210, 220, 221].

## 2.3 Atmospheric turbulence

Turbulent mixing in the Earth's atmosphere causes blurring of astronomical objects. For observations with earthbound telescope systems, the light has to pass the atmosphere, and therefore suffers from distortions [99, 174, 178]. Atmospheric turbulence itself can be described by changes in the index of refraction  $r$  defined as

$$r = \frac{c}{v}$$

for  $c$  the speed of light in vacuum and  $v$  the phase velocity of light in the considered medium. Turbulent air motion, whose energy source is the differential heating and cooling of the Earth's surface caused by the sun and the diurnal cycle, is experienced as wind. The resulting temperature inhomogeneity leads to random variations of the refractive index in the Earth's atmosphere. As a consequence, initially planar wavefronts get distorted when they travel through the atmosphere. In order to compensate these aberrations, the knowledge of the statistics of the spatial structure of turbulence is crucial.

Atmospheric models are mainly based on two parameters, the inner and the outer scale. The outer scale  $L_0$  gives the size limit of the energy added to the fluid medium

and initiating turbulence. The inner scale  $l_0$  characterizes the threshold where the so called Reynolds number (determining the properties of fluid flows) reaches its critical value induced by an energy cascade of the kinetic energy continually transferred to smaller scale motions. In simple terms,  $L_0$  describes the size of the largest and  $l_0$  the size of the smallest turbulent eddies. The inner scale varies from about 1 mm near the ground and 1 cm close to the tropopause. The outer scale usually ranges from tens to hundreds of meters but its value still is the subject of debate [163].

### 2.3.1 Kolmogorov turbulence model

One approach describing optical effects caused by atmospheric turbulence is the *Kolmogorov turbulence model* [121]. Kolmogorov investigated the mechanical structure of turbulence and proposed a scheme for the velocity of motion in a fluid medium. In the inertial regime between the inner and outer scale, the model of Kolmogorov assumes homogeneity and isotropy of turbulence and describes the turbulence statistics by a stationary, isotropic Gaussian random field.

We are interested in the difference in the refractive index between a point  $r$  and another nearby point  $r'$ . For this reason, we consider the *structure function*

$$D_x(r, r') = \mathbb{E}(|x(r) - x(r')|^2)$$

of a random variable  $x$  in order to describe the spatial structure of a random process. The homogeneity causes the independence of the turbulence statistics on the specific position and the isotropy induces that higher-order statistical moments are dependent on the radial distance  $|r - r'|$  of the points only. The local strength of the variation of the index of refraction is measured by the *index structure coefficient*  $c_n^2$ . These considerations result in

$$D_n(r, r') = c_n^2 |r - r'|^{2/3}. \quad (2.2)$$

Thus, the turbulence spectrum is described only by the turbulence strength  $c_n^2$  which is given in units of  $\text{m}^{-2/3}$ . If we consider the integral over  $c_n^2$  along the light propagation path, we obtain a measure for the total amount of wavefront degradation, i.e., the *seeing*. Equation (2.2) is valid as long as the distance between the two considered points is less than  $L_0$ , and energy is dissipated at the inner scale  $l_0$ .

The  $c_n^2$ -profile varies with altitude, location and time of day. Methods for measuring its values empirically and several analytical models of the  $c_n^2$ -profile based on experimental measurements, for instance made by balloons, can be found, e.g., in [178].

For the analysis of propagation through turbulence, a criterion that describes the statistical distribution of the number and the size of the turbulent eddies in the atmosphere was derived from the structure function  $D_n$ . This 3d power spectrum is called *power spectral density* (PSD)  $\Phi_n$ . In the Kolmogorov model,  $\Phi_n^{Kol}$  is given by [178]

$$\Phi_n^{Kol}(\kappa) = 0.033 \cdot c_n^2 |\kappa|^{-11/3} \quad \text{for} \quad \frac{2\pi}{L_0} < |\kappa| < \frac{2\pi}{l_0}, \quad (2.3)$$

where  $\kappa = (\kappa_1, \kappa_2, \kappa_3)$  denotes the spatial frequency of turbulence with the Euclidian norm  $|\kappa| = \sqrt{\kappa_1^2 + \kappa_2^2 + \kappa_3^2}$ . For  $|\kappa| \rightarrow 0$ , the above model suffers from effects induced by the singularity. For this reason, the model of von Karman was introduced.

Note that based on the considerations of the turbulence statistics in the Kolmogorov model, the incoming wavefront  $\Phi$  is an element of the Sobolev space  $\mathcal{H}^{11/6}(\mathbb{R}^2)$  with a high probability as derived from [55] in [60, 147].

### 2.3.2 Von Karman turbulence model

An alternative form of the power spectral density referred to as the *von Karman spectrum* [119, 178] has been introduced in order to avoid the difficulties arising from the pole at  $\kappa = 0$  in (2.3). The PSD  $\Phi_n^{Kar}$  in the von Karman model is written as

$$\Phi_n^{Kar}(\kappa) = \frac{0.033 \cdot c_n^2}{(\kappa^2 + \kappa_0^2)^{11/6}} e^{-\kappa^2/\kappa_m^2}$$

with  $\kappa_0 = 2\pi/L_0$ ,  $\kappa_m = 5.92/L_0$ . The von Karman PSD has a finite value for  $|\kappa| \rightarrow 0$  and rapidly decreases for growing frequencies.

### 2.3.3 Atmospheric layer model

The Earth's atmosphere extends to an height of about 300 km [99]. Its pressure decreases smoothly with increasing height following an exponential law. This is different for the profile of atmospheric turbulence. Most of the turbulence is concentrated in distinguishable layers as derived from Taylor's hypothesis of frozen flow [203]. These layers travel parallel to the Earth's surface at a certain velocity. It was observed that the time frame of changes in the turbulence pattern of an atmospheric layer is slower than the wind speed. Hence, over short time frames constant  $c_n^2$ -profiles, which are blown as "frozen" structures over the telescope pupil at a typical speed of approximately 20 m/s, are assumed [163].

Due to solar heating and the development of thermal currents, turbulence is usually stronger near the Earth's surface at daytime. At night, turbulence occurrence is less significant near the ground and most perturbations are present at higher altitudes, especially at the tropopause, as a result of wind shear [99].

Following the descriptions, e.g., in [176], the atmosphere can be modeled by a finite number  $L$  of infinitely thin layers under the assumptions of statistical independence of each layer and a homogeneous statistics of turbulence in subregions. Let us denote the amount of atmospheric turbulence in layer  $l$  at height  $h_l$  by  $\gamma_l := c_n^2(h_l)$  for  $1 \leq l \leq L$ . Then, the relative turbulence strength is normalized in numerical simulations such that it holds  $\sum_{l=1}^L \gamma_l = 1$ . As analyzed in [6, 7, 186], the usage of only a certain amount of atmospheric layers is sufficient.

Layer	1	2	3	4	5	6	7	8	9
Height (m)	47	140	281	562	1125	2250	4500	9000	18000
$c_n^2$ -profile	0.522	0.026	0.044	0.116	0.098	0.030	0.060	0.043	0.060

Table 2.1: Parameters of the 9-layer atmosphere used in the EPICS simulations. The layer heights (in m) and approximate  $c_n^2$ -profiles (in  $\text{m}^{-2/3}$ ) of the ESO standard 9-layer atmosphere are listed. The corresponding Fried parameter is  $r_0 = 12.9$  cm.

In the numerical analysis in Chapter 4 - 8, we consider the *ESO standard 9-layer atmosphere* for the EPICS instrument and the *ESO 35-layer atmosphere* for simulations of the METIS instrument.

The ESO standard 9-layer atmosphere [129] was derived from measurements at ESO's site Paranal in the Atacama desert in Northern Chile. The values for a median seeing with a Fried parameter of  $r_0 = 12.9$  cm are shown in Table 2.1. The values used in our numerical simulations for the ESO 35-layer atmosphere [183] were as well provided by the European Southern Observatory.

### 2.3.4 Atmospheric parameters

Atmospheric seeing conditions can be derived from the turbulence  $c_n^2$ -profiles, the atmospheric layer altitudes, and the wind speeds. They are described, e.g., by the Fried parameter  $r_0$  and the isoplanatic angle  $\theta_0$ .

#### Fried parameter

The Fried parameter or coherence radius  $r_0$  characterizes atmospheric seeing with respect to the wavelength  $\lambda$  [82]. As a measure of the strength of turbulence, it represents the integrated effect induced by refractive index fluctuations for the entire atmosphere [99]. According to [178],  $r_0$  is described by

$$r_0 = 0.185 \cdot \left( \frac{\lambda^2}{\int_0^\infty c_n^2(h) dh} \right)^{3/5},$$

and hence  $r_0 \propto \lambda^{6/5}$ . The ratio

$$\beta = \frac{\lambda}{r_0}$$

between the optical wavelength  $\lambda$  and the Fried parameter  $r_0$  is known as the *atmospheric seeing*.

The Fried parameter is typically specified in the visible, more precisely at a wavelength of  $0.5 \mu\text{m}$ . Large values of  $r_0$  correspond to good seeing and weak turbulence effects

while small numbers indicate bad seeing and strong atmospheric turbulence. Usually, the Fried parameter covers a range of less than 5 cm when strong daytime turbulence is present to more than 20 cm for good seeing at nighttime. Over periods of seconds to minutes, the Fried parameter is continually changing [99].

The Fried parameter is decisive on proper choices of the number and the size of correcting elements (subapertures/mirror actuators described in Section 2.4.2 and Section 2.4.3) for an efficient compensation of the wavefront aberrations.

### Anisoplanatism and isoplanatic angle

In Adaptive Optics we use measurements of a reference source to correct for the wavefront aberrations of another (nearby) celestial object of interest (see Section 2.4). However, the measurements are strictly valid only for an object situated in exactly the same direction as the reference star. If the field angle increases, the wavefront error becomes decorrelated because turbulence is distributed along the light propagation path through the atmosphere. The effect that arises when two objects are separated by an angle bigger than  $\theta_0$  is known as *angular anisoplanatism*. The corresponding isoplanatic angle  $\theta_0$  describes the angle at which two speckle images start to look differently [99, 139]. For observations at an angle  $\theta$  of the guide star direction, the phase variance is calculated as

$$\mathbb{E}(\sigma_{\Phi}^2) = \left(\frac{\theta}{\theta_0}\right)^{5/3}.$$

In case of a single layer at height  $h$ , the isoplanatic angle is written as [99]

$$\theta_0 = 0.31 \cdot \frac{r_0}{h},$$

i.e., dependent on the layer altitude and the Fried parameter. For more precise considerations of  $\theta_0$  we refer the reader to [80, 163].

## 2.4 Basics on Adaptive Optics

Adaptive Optics (cf, e.g., [99, 174, 209]) is a technology that compensates for the rapidly changing optical perturbations arising during the imaging process on earth-bound telescopes and physically corrects for atmospheric blurring that is caused by turbulence via deformable mirrors in real-time. The correction is usually split into two steps: First, the distorted wavefronts of a guide star, which is situated in the vicinity of the astronomical object one wants to observe, are measured by wavefront sensors (WFS). The obtained information is then used to calculate the actuator commands of the deformable mirror in order to optimally balance the aberrations by shaping the mirror appropriately. Finally, the light from both guide star and celestial object is reflected at the mirror and distortions are removed. Thus, the optimal mirror shape is determined from wavefront sensor measurements of the emitted light of natural guide

stars as well as laser guide stars which are produced artificially. Figure 2.4 shows an Adaptive Optics system running in a closed loop setting. The incoming distorted wavefronts reach the deformable mirror where they are corrected. Afterwards, the light – now stemming from corrected waves – is split into two parts by a beam splitter (BS) and propagates to the high resolution camera and to the WFS. The corresponding wavefront sensor data of the already corrected wavefronts are used to evaluate the right mirror actuator commands for the next incoming wavefront. Restoration of the unknown wavefront and further calculation of the optimal mirror deformations from given sensor measurements is an Inverse Problem which has to be solved within milliseconds. For the new generation of Extremely Large Telescopes, there is a strong increase in the computational load due to steadily growing mirror sizes up to 40 m. As a result, existing control algorithms become challenging and fast reconstruction methods are more important in order to obtain good corrections in accessible time.

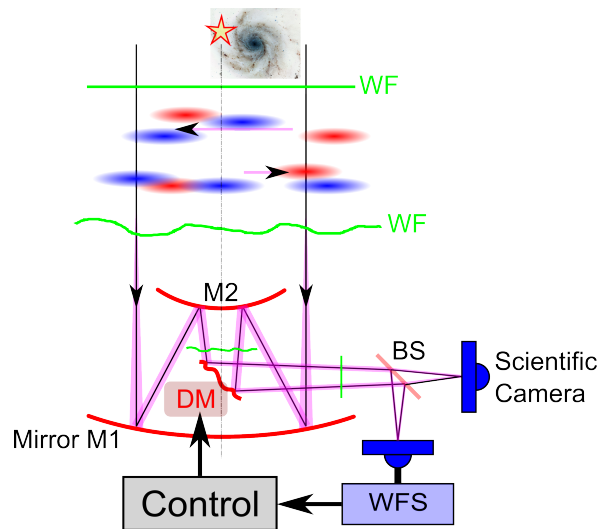


Figure 2.4: Design of an AO system, source [107]. Adaptive Optics improves the performance of optical systems by deforming a mirror in order to reduce the effect of wavefront aberrations.

The three main AO-components of a ground based telescope are wavefront sensors, control algorithms and deformable mirrors. A wavefront sensor provides information on the incoming phase by measuring light intensity changes caused by wavefront aberrations, the control algorithm links the measurements to the mirror actuator commands, and deformable mirrors physically correct for the distortions.

### 2.4.1 AO component: guide star

A bright object which serves as a reference source for AO is named a guide star (GS). We distinguish between natural guide stars (NGS) and laser guide stars (LGS). In case of limited sky-coverage, i.e., if there is no bright celestial object in the near vicinity,

laser beacons are released from the telescope facility into the night sky. They stimulate the sodium layer at a height of approximately 90 km and serve as artificial guide stars known as LGS (cf, e.g., [99]). However, three major effects appear for laser guide stars, namely spot elongation, cone effect, and tip-tilt indetermination [99, 174] and an AO system does not work without the use of at least one NGS.

In contrast to natural guide stars, for laser guide stars the light source is finitely high. As a consequence, the light travels down to the Earth's surface in a cone as shown in Figure 2.5. This phenomenon is known as *cone effect*. It needs to be compensated in atmospheric tomography (cf Section 2.4.5), e.g., by the introduction of layer specific scaling factors (cf, e.g., [85, 181, 182]).

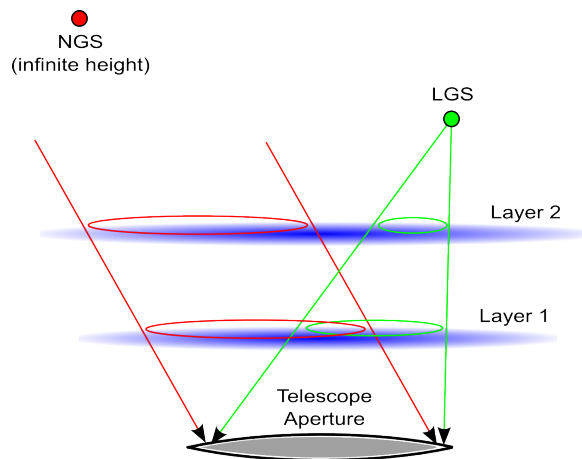


Figure 2.5: Sketch of cone effect introduced by an LGS, source [6].

The *spot elongation* is caused by the thickness of the sodium layer. While turbulent layers are assumed to be infinitely thin, the vertical width of the sodium layer is not approaching zero. Thus, the scattering of the laser beacon is a small stripe on the sky rather than a single point source as valid for natural guide stars. As indicated in Figure 2.6, the source detected on the telescope is elongated and degrades the quality of the measurements. The originated error increases linearly with the size of the spot elongation in the direction of the centroid [40] and possibly introduces unwanted correlation effects between measurements [202].

The laser beam passes the atmosphere when traveling up to the sodium layer and a second time when being scattered from the sodium layer. As a consequence, the real position of the LGS remains unknown since tip or tilt modes of the incoming wavefront cannot be determined. In order to overcome this *tip-tilt indetermination*, at least one NGS has to be used in every AO operating system which are later discussed in Section 2.4.5. Figure 2.7 gives an example illustrating an undetectable tip & tilt mode induced, e.g., by a layer having different temperature distributions. For more precise explanations of this effect and solution statements we refer to [184, 208, 225].

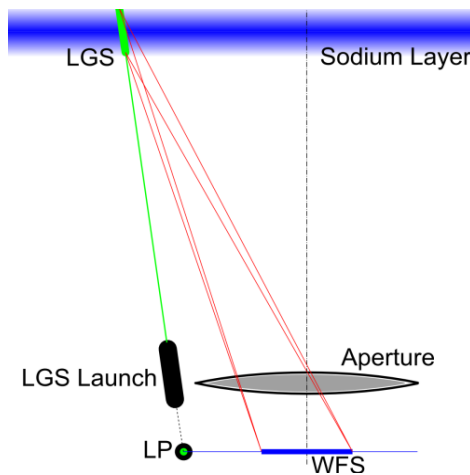


Figure 2.6: Spot elongation caused by an LGS, source [6].

### 2.4.2 AO component: wavefront sensor

Wavefront sensors (WFSs) provide information on the perturbations of a planar wave originating from a guide star. Unfortunately, the wavefronts cannot be measured directly and sophisticated wavefront reconstruction methods need to be applied. Those heavily depend on the incorporated wavefront sensor type. For an arbitrary WFS model  $\mathbf{W}$ , sensor measurements  $s$ , and an incoming wavefront  $\Phi$ , the general relation is given by

$$s = \mathbf{W}\Phi. \quad (2.4)$$

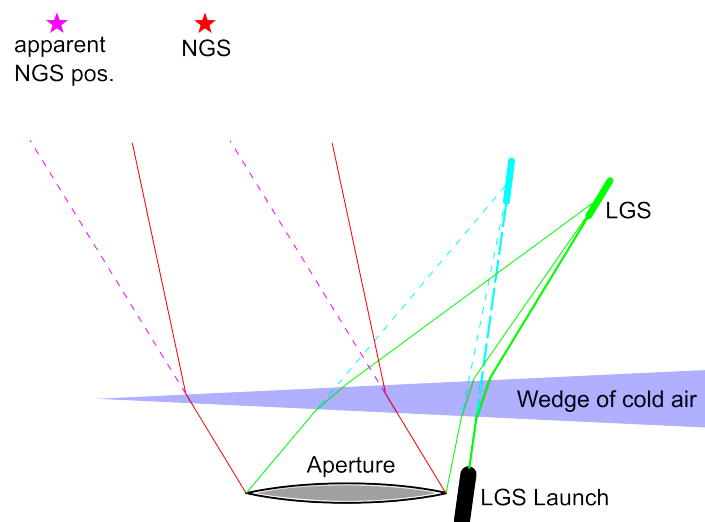


Figure 2.7: LGS tip-tilt indetermination, source [6]. Light emitted by a GS is refracted by a wedge of cold air. On the detectors of the telescope, the GS appears dislocated. However, the true location of the natural guide star is known, and therefore the tip-tilt indetermination is overcome.

Several possible choices for the wavefront sensor model  $\mathbf{W}$ , e.g., Shack-Hartmann or pyramid wavefront sensors, are discussed below.

### Shack-Hartmann sensor

For a Shack-Hartmann (SH) sensor [56, 159, 190], an image of the telescope entrance pupil is built on a lenslet array. Each of those lenslets forms an image of the reference source on a CCD detector which is situated behind the lenslet array. The quadratic area on the CCD detector that is covered by one lenslet is called *subaperture*. For undistorted wavefronts, the detected images consist of sharp point sources regularly arranged in the subapertures. In the presence of atmospheric turbulence, however, the spots detected behind the lenslet array are blurred and dislocated from the center of the subapertures as shown in Figure 2.8. The shifts give a measure of the local wavefront slope averaged over the lenslet area. The dependence between the incoming wavefront  $\Phi$  and SH sensor data  $s_{SH}$  is linear and represented by

$$s_{SH}(i, j) = \left( \frac{1}{|\Omega_{ij}|} \int_{\Omega_{ij}} \frac{\partial}{\partial x} \Phi(x, y) d(x, y), \frac{1}{|\Omega_{ij}|} \int_{\Omega_{ij}} \frac{\partial}{\partial y} \Phi(x, y) d(x, y) \right)$$

for  $i, j = 1, \dots, n$  and  $\Omega_{ij}$  denoting the  $(i, j)$ -th subaperture of altogether  $n \times n$  subapertures.

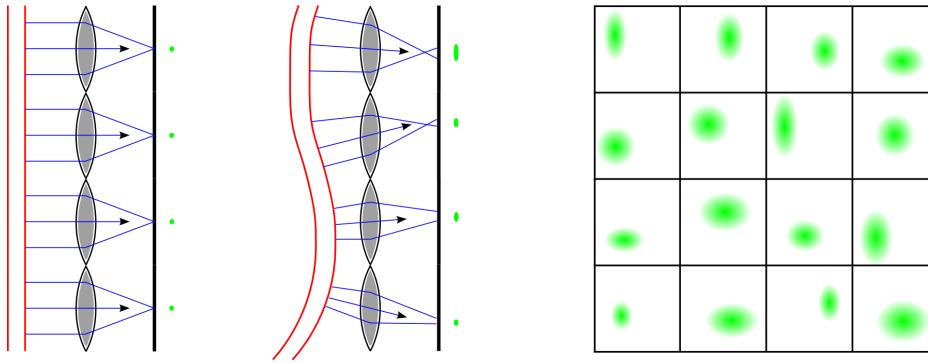


Figure 2.8: Scheme of a Shack-Hartmann sensor, source [6]. Signals detected from undistorted and distorted wavefronts are shown as well as a signal captured on the sensor array which corresponds to a blurred image (from left to right).

### Pyramid wavefront sensor

Several of the instruments planned for future ELTs have pyramid wavefront sensors (PWFS) [164] included as baseline. As illustrated in Figure 2.9, the incoming light is focused on top of a pyramidal prism. Due to the splitting by the prism, the light propagates into 4 slightly different directions and every intensity pattern is later captured on a CCD detector. The detector is divided into quadrants and counts the number

of incident photons over a short exposure time. PWFS measurements are calculated as specific sums of the intensities (see Chapter 3). The pyramid sensor relates the incoming wavefront with the measurements in a non-linear way.

In principle, the concept is comparable to a SH sensor with quad-cells, i.e., 4 pixels per subaperture. For the SH sensor, the lenslets produce multiple images of the light source through the aperture. In the PWFS, the subdivision is performed in the focal plane which produces multiple images of the aperture. Based on the close connection between both sensor types, one of the first wavefront reconstruction ideas for the PWFS were carried out as applications of SH wavefront reconstruction methods (cf, e.g., [162]).

### Roof wavefront sensor and other sensor types similar to the PWFS

The roof wavefront sensor (see Figure 2.9) can either be seen as a standalone wavefront sensor or utilized as a simplification of the pyramid sensor. For this sensor type, the four-sided pyramidal prism is substituted with two orthogonally placed two-sided roof prisms. As a consequence,  $x$ - and  $y$ - direction are decoupled [28, 155, 212]. Nowadays there are several other concepts of pyramid wavefront sensors under investigation: a generalized PWFS with an arbitrary number (from three to infinity) of facets [3, 41, 51, 59, 219], a digital PWFS which imposes a pyramid-like phase profile on a spatial light modulator [2, 3], a flattened pyramid or roof WFS [74], a lenslet based PWFS [38, 39, 115], and a sequential PWFS realized with a reflective micromirror array [35, 224].

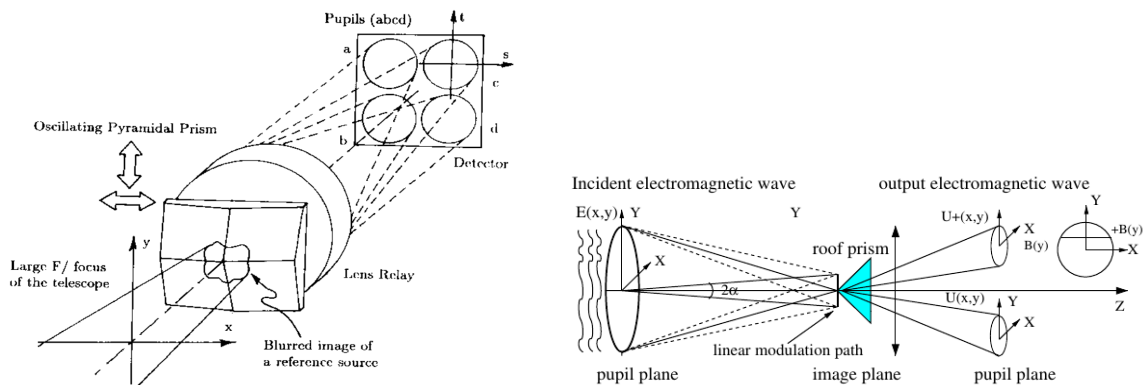


Figure 2.9: Concept of a pyramid and roof wavefront sensor, source [164, 212].

This Thesis is focused on the four-sided pyramid wavefront sensor. A detailed description of the physical principles and a mathematical derivation of the pyramid sensor forward models are given in Chapter 3. Wavefront reconstruction methods using pyramid sensor data are later presented in Chapter 4 - 7 on non-segmented pupils and in Chapter 8 on segmented pupils.

### Further wavefront sensor types

The *Zernike wavefront sensor* [145] is known for its excellence in terms of noise propagation, i.e., the device has an extremely high sensitivity to photon noise at all spatial frequencies [92].

The *curvature sensor* [53, 175] detects the Laplacian  $\nabla^2\Phi$  of the wavefront  $\Phi$ .

For the *Mach-Zehnder interferometer* [136], the light is split into 2 paths by a semi-transparent beam splitter. Subsequent superposition of the two paths causes interference patterns which are detected and contain information on the wavefront.

In another wavefront sensor type, the *Lateral Shear Interferometer* [53], light is reflected twice on a transparent shear plate. An interference pattern in the outgoing path caused by the lateral shift is registered by appropriate detectors and gives information on the WF.

### 2.4.3 AO component: deformable mirror

Deformable mirrors (DMs) (cf, e.g., [99, 174]) are under development since the early 1970s with the initiation of defense-oriented research as it was the case for AO itself. Under their flexible mirror surfaces, there are hundreds of actuators located that will be adjusted in real-time to counteract the atmospheric distortions by applying voltages.

Figure 2.10 illustrates several DM types. *Segmented DMs* only have up to three degrees of freedom (piston and two axes of tilt), but a good frequency response and a large dynamic range since each element is unconstrained. These mirror types are considered as a simple and low risk concept. Drawbacks of the segmented control are diffraction effects induced by the gaps between the segments and the high fitting error compared to another mirror type, the *continuous face-sheet DM*, when having the same number of actuators. Face-sheet DMs have good stability over time and temperature changes due to the use of the continuous faceplate that produces local smooth distortions when applying considerable force. However, the stroke with this mirror type is limited by the stress that actuator motion possibly induces in the faceplate.

For the ELT, the 2.5 m deformable fourth mirror will consist of a flat segmented thin shell composed of 6 identical patterns. Deformation of the DM will be achieved by the motion of about 5300 actuators within a time of less than 1 millisecond. As mirror geometries, we consider in this Thesis either the currently planned actuator positions of the ELT M4 as shown in Figure 2.11 or the Fried geometry with equidistant actuator positions [32].

### 2.4.4 AO component: real-time control unit

The real-time control unit computes the commands of the mirror actuators from wavefront sensor measurements. Based on the knowledge of the incoming wavefront  $\Phi$ , voltages are applied on the actuators in order to change the shape of the DM, and thus

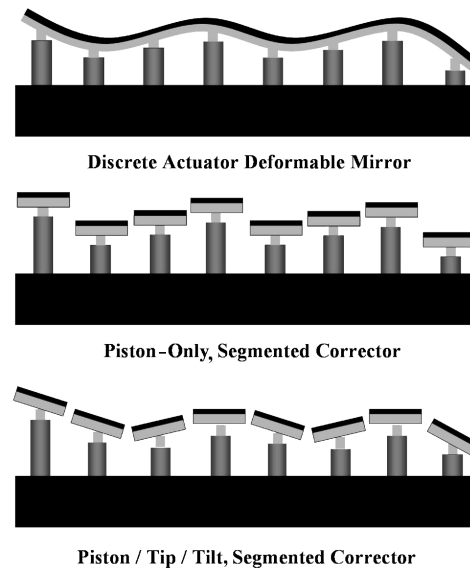


Figure 2.10: Different DM types, source [52].

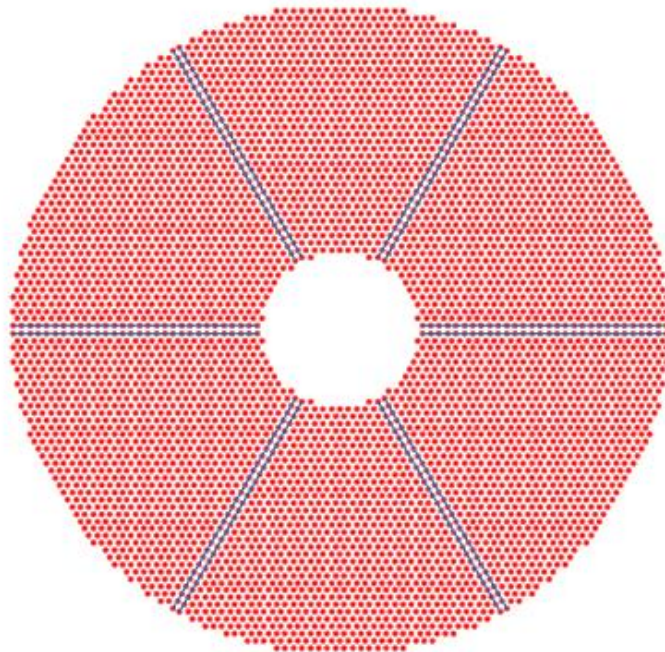


Figure 2.11: Actuator positions of the ELT M4 geometry implemented in the end-to-end simulation tool Octopus (cf Section 2.5.3), source [110, 149]. Additionally, the telescope spider positions, which are considered in Chapter 8, are shown.

compensate atmospheric aberrations by repeating a damped version of the wavefront shape with a negative sign.

Nowadays, successfully running control algorithms on telescopes use matrix-vector multiplication (MVM) [174]. The main idea is based on an interaction matrix that maps mirror actuator commands to wavefront sensor measurements. Therefore, the required mirror commands are computed by applying the pseudo-inverse of the interaction matrix, called control matrix, to the measurement vector. While results of MVM methods are very good in quality, the computational load is immense for large-scale AO. Future telescopes will have a high number of actuators ( $10^4 - 10^5$ ) to be controlled at a frequency of around 500–3000 Hz. Due to the computational complexity of  $\mathcal{O}(n_a^2)$ , where  $n_a$  is the total number of active mirror actuators, the application of interaction-matrix based methods on existing real-time computer systems is extremely demanding since further, the interaction matrix does not fulfill the sparsity assumption. Hence, the development of fast control algorithms which provide high reconstruction qualities becomes indispensable for future ELT-sized telescopes. Besides MVM, very efficient reconstruction algorithms having a lower computational complexity have been developed in the last years, e.g., [179, 204] for Shack-Hartmann wavefront sensors or several methods for pyramid sensors reviewed in Chapter 7. Interaction-matrix-based methods are often the benchmark against which our new model-based wavefront reconstruction approaches are compared in this Thesis (cf, e.g., Section 5.3.3).

### Decoupling of wavefront estimation and wavefront control

The impact on the mirror of pushing the  $i$ -th actuator is described mathematically by the actuator's influence function  $IF_i$ . The relation between the reconstructed wavefront  $\Phi$  and the overall  $n_a$  DM influence functions  $(IF_i)_{i=1}^{n_a}$  can be represented by

$$\Phi(x, y) = \sum_{i=1}^{n_a} a_i IF_i(x, y). \quad (2.5)$$

For interaction-matrix-based wavefront reconstruction approaches (as described in Section 8.2), the steps of wavefront reconstruction and projection onto the DM are often coupled. In this case, the interaction matrix is generated by only using the DM specific influence functions or modes as basis functions. The matrix-free, model-based methods (as, e.g., introduced in Chapter 4 - 6) are more general in the sense that WF reconstruction is completely decoupled from the DM and can be used in combination with an arbitrary DM geometry. After a successful wavefront estimation, an additional projection onto the DM is applied. Decoupling of WF estimation and WF correction is repeated in more depth in Section 8.2.2.

#### 2.4.5 AO systems

*Single Conjugate Adaptive Optics* (SCAO) (cf Figure 2.12) is the most simple AO system. It uses only one natural guide star, that has to be situated sufficiently near the

astronomical object one wants to observe, one wavefront sensor, and one deformable mirror conjugated to the ground layer. Since for SCAO we are interested in an optimal image quality in the center of the field of view we assume the light from the guide star (and the celestial object we want to observe) traveling approximately parallel to the optical axis. This causes atmospheric perturbations to simply add up.

Because of high contrast in brightness between small planets and giant stars they orbit, direct imaging and characterization of extra-solar planets is a big challenge in modern astronomy. Telescope instruments such as EPICS for the ELT are under development to allow high contrast imaging (HCI) at small angular separations. HCI-instruments will include an *eXtreme Adaptive Optics* (XAO) system which is a SCAO system using a huge number of subapertures and mirror actuators.

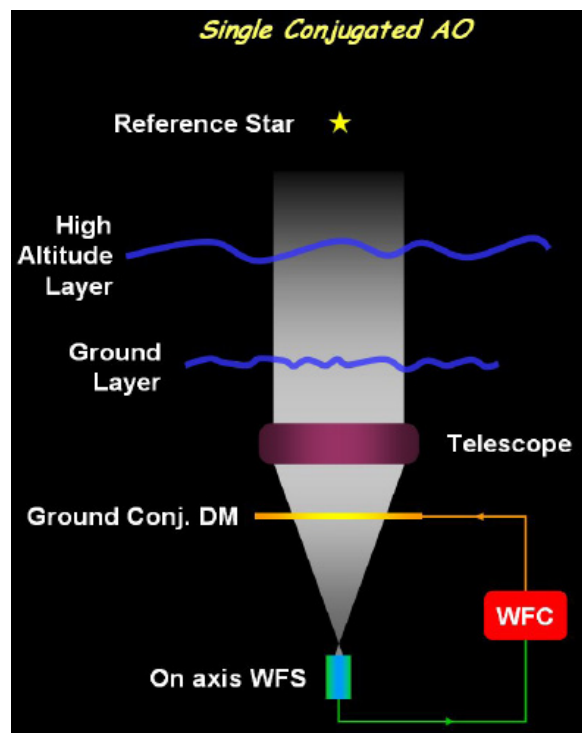


Figure 2.12: Principle of SCAO, source [150].

Besides SCAO and XAO systems, there exist more advanced AO operating modes such as *Ground Layer Adaptive Optics* (GLAO), *Multi Conjugate Adaptive Optics* (MCAO)[5], *Multi Object Adaptive Optics* (MOAO)[61], and *Laser Tomography Adaptive Optics* (LTAO), e.g., for applications over a wide field of view in combination with the usage of laser guide stars. In Figure 2.13 the concepts of several AO operating modes are illustrated.

The more complex AO systems rely on atmospheric tomography which is a limited angle tomography problem and thus is severely ill-posed. The aim is to reconstruct a discrete layered atmosphere from input data of multiple guide star directions.

In this Thesis, only SCAO and XAO systems are simulated for which no atmospheric tomography is needed.

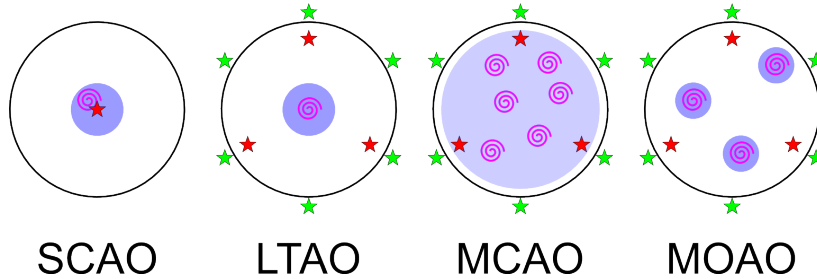


Figure 2.13: Schemes of fundamental AO operating modes, source [6]. The red/green stars indicate natural/laser guide stars, the magenta spirals stand for the astronomical object one wants to observe and the blue areas will be corrected by the AO system.

## 2.4.6 Open and closed loop configurations

There are two possibilities of aligning the DM and the corresponding WFS in the optical path of an AO system: If the WFS is arranged before the DM, measurements of the uncorrected wavefront are sensed. This configuration, which is installed in systems such as MOAO, is called *open loop* (OL) control.

Figure 2.4 shows a *closed loop* (CL) system. The DM is situated before the WFS in the optical path, i.e., the WFS measures already corrected residual wavefronts. SCAO, MCAO, and LTAO systems run in closed loop.

For deriving the current DM shape  $\Phi_t^{DM}$  in a CL system, only an update  $\Phi_t^{DMupdate}$  is computed and a damped version of it (with a properly chosen loop gain  $\gamma_{CL}$ ) is added to the previous DM shape  $\Phi_{t-1}^{DM}$ , i.e.,

$$\Phi_t^{DM} = \Phi_{t-1}^{DM} + \gamma_{CL} \Phi_t^{DMupdate}.$$

Another control system called *pseudo open loop control* (POLC) [54] offers an alternative to integrator control in closed loop systems but has to be considered carefully for non-linear wavefront sensors such as the pyramid sensor.

## 2.5 Numerical analysis

Finally, we give a short overview on several measures which are crucial in AO systems, define quality metrics used to specify the AO correction and briefly describe the simulation environment utilized for the numerical analysis of the developed wavefront reconstruction algorithms.

## 2.5.1 Measures in AO

### Wavelength

Wavefront sensing can be performed in different wavelengths. In the METIS simulations, we consider a PWFS sensing in the near infrared at a sensing wavelength of  $\lambda = 2.2 \mu\text{m}$  (K-band) and in the EPICS instrument a PWFS sensing in the visible at  $\lambda = 0.7 \mu\text{m}$ . Several parameters are wavelength-dependent such as, e.g., the modulation parameter (cf (3.7)) of the modulated pyramid sensor. The AO performance can significantly change with variations of  $\lambda$ . Generally, Adaptive Optics correction is easier at longer wavelengths – a fact that was experienced to be crucial in the presence of wide telescope spiders as analyzed in Chapter 8.

The quality performance of an AO system can be evaluated in different wavelengths. Mostly, we use the K-band as evaluation wavelength  $\lambda_{science}$  in the numerical simulations contained in this Thesis.

### Photon flux

The intensity of the light reaching the telescope pupil and being captured by the wavefront sensor is measured by the number of photons  $n_{ph}$  falling on one subaperture of the WFS per frame. We distinguish low photon flux from high photon flux where the threshold is not a fixed number but heavily depending on the signal-to-noise-ratio. One possibility to increase the number of photons per subaperture is to enlarge the subaperture size. However, an enlargement brings several drawbacks caused by diminished sensor resolution. Additionally, we experienced improved reconstruction quality for smaller subaperture sizes because the grid on which WFS measurements are available becomes finer. Therefore, it is inevitable to find a good balance between both parameters.

### Sensor noise

The two most dominant error sources are the photon noise described by the *signal-to-noise-ratio* (SNR) and the *read-out noise*. The SNR identifies the noise in the sensor output caused by quantum effects on the CCD detector and depends on the sensor size, the number of subapertures, the number of pixels, and the photon flux. The read-out noise is caused by unavoidable uncertainties and latency during the read-out process of the CCD detector. If we combine the two main error sources with additional ones such as those stemming from dead CCD-pixels and describe them by one probabilistic quantity  $\eta$ , the more realistic model for WFS operation compared to (2.4) is

$$s = \mathbf{W}\Phi + \eta.$$

Keeping the error propagation from  $s$  to  $\Phi$  low needs the usage of regularization methods during the wavefront reconstruction process.

### Minimum subaperture illumination

Due to, e.g., obstructions caused by the secondary mirror or its support structures, not all subapertures are illuminated by the same amount of light and it may happen that several of them are not sufficiently illuminated to produce reliable measurements. Therefore, one has to decide which subapertures are active and utilized for wavefront reconstruction. Only if a subaperture is illuminated more than a certain percentage given by the minimum subaperture illumination threshold, it is considered as active.

### Frame rate

The time frame during which the CCD detector senses the incident photons is given by the frame rate in Hertz. Approximately half of this time frame is available for wavefront reconstruction. The frame rate in our simulations ranges from 500 Hz to more than 3 kHz and directly determines the duration of one time step in the used end-to-end simulation specified in Section 2.5.3.

## 2.5.2 Quality measure: Strehl ratio

The reconstruction quality is quantified in terms of the short-exposure (SE) and the long-exposure (LE) Strehl ratio. This quality metric commonly used in astronomical communities is defined as the ratio of the peak aberrated image intensity from a point source compared to the maximum attainable intensity for an ideal optical system limited only by diffraction over the telescope aperture. This means that the Strehl ratio [139, 174, 178] relates the point spread function  $PSF_{\Phi}$  obtained within the AO correction to the diffraction limited point spread function  $PSF_{tel}$  of the telescope as presented in Section 2.2 by

$$SR = \frac{PSF_{\Phi}(0)}{PSF_{tel}(0)}.$$

It is evaluated at the origin which gives a relation between its respective peaks in case they are perfectly centered. If the peak of  $PSF_{\Phi}$  is slightly off-centered due to atmospheric aberrations, the resulting Strehl ratio is reduced. Generally, the Strehl ratio has values  $0 \leq SR \leq 1$  with 1 being the maximum Strehl ratio induced by a perfect atmospheric correction.

The SE Strehl ratio  $SR$  can be estimated by Maréchal's approximation (cf, e.g., [173]) as

$$SR(\Phi) \approx \exp\left(-\left(2\pi \cdot \sigma(\Phi) / \lambda_{science}\right)^2\right).$$

The term  $\lambda_{science}$  denotes the observing wavelength and  $\sigma(\Phi)$  the root-mean-square deviation of the wavefront  $\Phi$ , i.e.,

$$\sigma^2(\Phi) = \frac{1}{|\Omega|} \left\| \bar{\Phi} - \Phi \right\|_{\mathcal{L}_2(\Omega)}^2 \quad \text{with} \quad \bar{\Phi} = \frac{1}{|\Omega|} \int_{\Omega} \Phi(x, y) \, d(x, y),$$

where  $\Omega$  denotes the telescope aperture. The average on-axis SE Strehl ratio over the whole observing time is related by the LE Strehl ratio.

### 2.5.3 Simulation environment

Testing developed AO configurations and control algorithms requires accurate simulation environments. In this Thesis, we use ESO's official end-to-end simulation tool Octopus [129, 130]. The phase screens generated therein follow the von Karman turbulence model. The simulation tool is written in C-code, but we chiefly run our algorithms via an interface in Matlab. After reconstruction of the incoming wavefront and identification of the corresponding DM commands, the SE and LE Strehl ratios are derived from the resulting PSF. Although Octopus is implemented in a massive parallel manner, simulating a few seconds of real-time may take several hours due to the large scale of the AO systems for ELTs having thousands of actuators to control.



## Chapter 3

# The pyramid sensor model

Having a look at the detailed representation of the forward models of the pyramid wavefront sensor lays the mathematical foundation for wavefront reconstruction in which the aim is to calculate the undistorted wavefront from given sensor measurements. In Section 3.1 we start with an introduction to the physical principles of a pyramid sensor and a review on state of the art pyramid sensor configurations. We derive and analyze new mathematical models based on distribution theory for both the non- and modulated pyramid sensor in Section 3.2. First, we focus on the transmission mask modeling approach in Section 3.2.1, which ignores the phase shifts introduced by the pyramidal prism and models the prism facets as transmitting only. Later on, in Section 3.2.2, we consider the more complicated phase mask model taking interference effects between the four pupils into account. In Section 3.3 we analyze the non-linear forward operators describing the pyramid sensor and additionally investigate the basic principles of the roof wavefront sensor either serving as an approximation of the pyramid sensor or being seen as a standalone WFS. In order to simplify the problem of solving the WFS equation, we calculate linearizations for roof wavefront sensors in Section 3.4. Furthermore, in Section 3.5, we consider the underlying operators in the Fourier domain and evaluate adjoint operators which will be necessary for the application of iterative methods, e.g., gradient based algorithms or Landweber iteration, for wavefront reconstruction addressed in Chapter 5. Finally, Section 3.6 contains details on the discretization of the continuous pyramid sensor model.

This Chapter contains parts of the work presented in [108] as a collaboration with Iuliia Shatokhina and Ronny Ramlau.

### 3.1 Pyramid sensor modeling: state of the art

Wavefront reconstruction methods heavily depend on the incorporated wavefront sensor. As such, the pyramid wavefront sensor is gradually gaining more and more attention from the Adaptive Optics community due to its improved signal-to-noise ratio, robustness to spatial aliasing and adjustable spatial sampling compared to the other

popular wavefront sensor choice — the Shack-Hartmann sensor. Several theoretical studies [28, 64, 65, 125, 165, 166, 191, 211, 212, 213, 216] including numerical simulations and laboratory investigations with optical test benches [17, 18, 93, 135, 157, 207, 215] have confirmed the advantages of pyramid wavefront sensors while additionally promising surveys were operated on sky [69, 76, 89, 154, 158]. The first single star AO loop was closed on AdOpt@TNG at the Telescopio Nazionale Galileo [167] with a PWFS. In recent years, remarkable operational results have been reported at the 8 m Large Binocular Telescope (LBT) [67, 68, 153]. In addition to the LBT, the pyramid sensor is integrated in the AO systems of the Subaru Telescope (SCexAO), the Magellan Telescope (MagAO), the Mont Megantic Telescope (INO Demonstrator), and the Calar Alto Telescope (PYRAMIR).

The current development of a new era of Extremely Large Telescopes with primary mirrors of 25 – 40 m in diameter brings new challenges to the field of Adaptive Optics. For ELTs, pyramid sensors show enhanced performance in real life settings, e.g., they provide the ability to sense differential piston modes induced by diffraction effects of realistic telescope spiders that support secondary mirrors and perform even under significant levels of non-common path aberrations [48, 71]. Thus, pyramid wavefront sensors are going to be included in many ELT instruments [23, 42, 48, 71, 83, 84, 122, 134, 141, 146, 211].

Besides astronomical applications, the pyramid sensor is considered as device in adaptive loops in ophthalmology [34, 47, 51, 114] and microscopy [112, 113]. The underlying concepts are comparable to atmosphere induced perturbations sensing for adaptive optics in astronomy. In microscopy, the pyramid sensor is introduced for direct phase detection. Unstained cellular media sometimes appear transparent. Hence, measuring the imprinted phase changes induced by variations in the index of refraction is necessary for the observation of biological structures. For adaptive optics systems in the eye, the pyramid sensor is used to perform high efficient and flexible wavefront sensing to compensate ocular aberrations.

### 3.1.1 Physical design of a pyramid wavefront sensor

The inventor of the PWFS for astronomical investigations was R. Ragazzoni [164, 165] in the 1990s. As seen in Figure 3.1, the wavefront sensor is based on a static or oscillating pyramidal optical component that splits the light into four beams providing information on the intensity of the aberrated wavefront. The glass prism is situated in the focal plane of the telescope pupil. The incoming light of a star is focused by the telescope onto the pyramidal prism apex. The prism divides the field into quadrants by propagating the light in slightly different directions. A relay lens after the prism acts as a re-imager and creates four different images of the pupil on the detector. A decisive physical property of the pyramid sensor is the beam divergence of the incorporated pyramidal prism [4]. The divergence angle of the prism describes the splitting of the

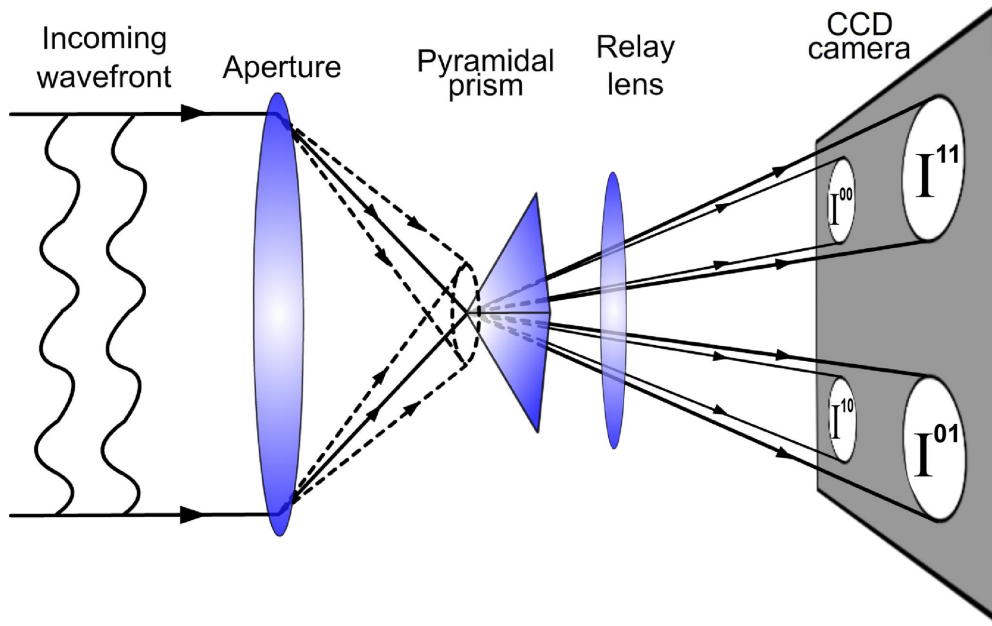


Figure 3.1: Optical setting of a PWFS, source [108].

starlight and affects the relative distance between the four intensity patterns falling on the CCD-detector.

The most common pyramidal glass prism models are the so called *phase mask* and *transmission mask model*. While the phase mask model takes interference effects between the beams falling onto the detector into account, the transmission mask model does not. The latter ignores the phase shifts introduced by the pyramidal prism and models the prism facets as transmitting only.

Under unfavorable conditions it might occur that the incoming beam is not exactly focused on the spot of the pyramidal prism and light doesn't fall on every side of the pyramid. Hence, the spot of the pyramid is modulated (usually circularly). At the cost of sensitivity, the modulation of the beam strengthens the linearity and increases the dynamic range of the PWFS [38, 72, 73, 166, 212]. There exist several possibilities to accomplish a dynamic modulation of the beam. In [164] they describe an approach in which the prism itself is physically rotated. Alternatively, one can use a steering mirror [28, 131] or a static diffuse optical element [131]. A drawback of the pyramid sensor operated with modulation is the generation of heat, which makes the application in cryogenic environments difficult.

Pyramid wavefront sensor measurements are provided on an equally spaced grid divided into subapertures, where the maximum number of available subapertures in a row or column is given by  $n = D/d$  with  $D$  the primary mirror diameter of the telescope and  $d$  the subaperture size. The latter is fixed according to the physical setup

of the telescope instrument (availability of corresponding devices such as the CCD detector) in advance. The number of active subapertures  $N \leq n^2$  depends on the telescope and mirror geometry and a suitable illumination factor that rejects subapertures receiving too little incident photons in order to produce usable measurements. In contrast,  $n_a$  corresponds to the number of active mirror actuators that will be poked in order to give the deformable mirror the appropriate shape and therefore depends on the incorporated deformable mirror geometry. Often,  $n_a$  is comparable to  $N$  and therefore we do not strictly distinguish between  $n_a$  and  $N$  when considering numerical complexities in the Thesis.

On the CCD detector, each image of the aperture is split into subapertures. For each subaperture, the signal in  $x$ - and  $y$ -direction is given by the formula [212]

$$\begin{aligned} s_x(x, y) &= \frac{[I^{01}(x, y) + I^{00}(x, y)] - [I^{11}(x, y) + I^{10}(x, y)]}{I_0}, \\ s_y(x, y) &= \frac{[I^{01}(x, y) + I^{11}(x, y)] - [I^{00}(x, y) + I^{10}(x, y)]}{I_0}, \end{aligned} \quad (3.1)$$

where  $I_i(x, y)$ ,  $i \in \{1, 2, 3, 4\}$  denotes the intensity located at  $(x, y)$  in quadrant  $i$  (cf Figure 3.1) and  $I_0$  represents the average intensity over the whole detector plane.

As derived in [212] and shown in Figure 3.2, the pyramid sensor acts either similar to a slope or a direct phase sensor depending on the spatial frequencies of the incoming wavefront. The sensor's response to low frequencies is linear and stagnates for higher spatial frequencies, i.e., the signal-to-noise ratio is the same at all those frequencies. The transition between both regimes depends on the modulation amplitude  $\alpha$  and the wavefront sensing wavelength  $\lambda$ . In particular, the modulation amplitude controls to some extent the linearity of the sensor's response. In the absence of oscillation, the sensor is fully comparable to a Foucault knife-edge test [87] and one mostly benefits from the characteristics of the PWFS acting as a phase sensor.

Within geometric optics the modulated pyramid sensor was first seen similar to the linear SH sensor, i.e., as a slope sensor with higher sensitivity [63, 164, 166, 213]. When the non-modulated sensor was investigated in more depth, e.g., in [123, 124, 165, 222], a connection to the Hilbert transform was found. As analytically derived in [125], the sensor without modulation can be represented as non-linear combinations of 1d and 2d Hilbert transforms of the sine and cosine of the incoming phase in the Fourier optics framework. The direct inversion of this mathematical model seems to be impossible. Considering modulation, which is described by a zero-order Bessel function of the first kind and an additional integral of a cosine, further complicates the model as later seen in Definition 3.2.

Approximating the pyramid sensor model by a roof wavefront sensor (see Figure 2.9 right) seems to be a promising possibility to make the development of model-based methods easier. For this type of sensor, two orthogonally placed two-sided roof prisms

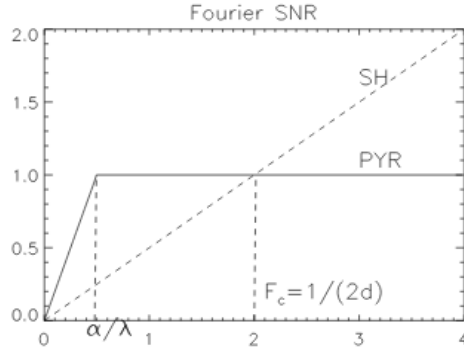


Figure 3.2: Fourier signal-to-noise ratio curves, source [212]. The dotted line represents the response to varying spatial frequencies (plotted on the x-axis) for a Shack-Hartmann sensor and the solid line for a pyramid sensor. One can clearly identify both regimes of the pyramid sensor with the threshold  $\alpha/\lambda$ . The system's cut-off frequency is denoted by  $F_c$  and the subaperture size by  $d$ .

instead of the pyramidal one are used. The orthogonality of the roof leads to a decoupling of the dependence on the incoming phase in  $x$ - and  $y$ -direction. For roof wavefront sensors, a linear modulation path is additionally considered in the literature as an approximation to the circular one.

The simplification of using the roof sensor often comes together with a linearization of the highly non-linear Fourier optics based pyramid sensor model examined more closely in Section 3.4. However, after several years of using the linearized roof sensor [28] as a simplification, especially for those algorithms developed by the AAO team, the trend nowadays is to consistently come closer to the full pyramid sensor model in order to improve the existing reconstruction algorithms and reach even more accurate wavefront estimates.

## 3.2 Pyramid sensor modeling: new mathematical foundation

Control of a deformable mirror requires the knowledge of the wavefront shape. Unfortunately, wavefronts are not measured directly. The generally non-linear relation between pyramid wavefront sensor measurements  $s$  and the wavefront  $\Phi$  of the incoming light can be described via the equation

$$s = \mathbf{P}\Phi + \eta, \quad (3.2)$$

where the operator  $\mathbf{P}$  represents a mathematical model of the pyramid wavefront sensor and  $\eta$  denotes the unpredictable measurement noise. Restoration of the unknown

incoming wavefront  $\Phi$  from noisy measurements  $s$  and further calculation of the optimal mirror deformation is an Inverse Problem. In order to develop model-based high-quality wavefront reconstruction algorithms, the derivation of a mathematical model accurately describing the pyramid sensor is necessary.

Different pyramid wavefront sensor forward models have already been considered multiply in the literature, for instance the phase mask model in [30, 86, 214] and the transmission mask model in [30, 64, 86, 125, 166, 214]. The models of the pyramid and roof wavefront sensors, which build the foundation of the development of model-based reconstruction algorithms by the AAO team, have been presented in [191] in a Fourier optics setting. In the following, we will focus on a correct mathematical derivation of these models using distribution theory, but finally ending up with the same pyramid and roof sensor measurements as, e.g., in [191]. Note that we have already introduced the transmission mask scheme in a distributional sense in [108].

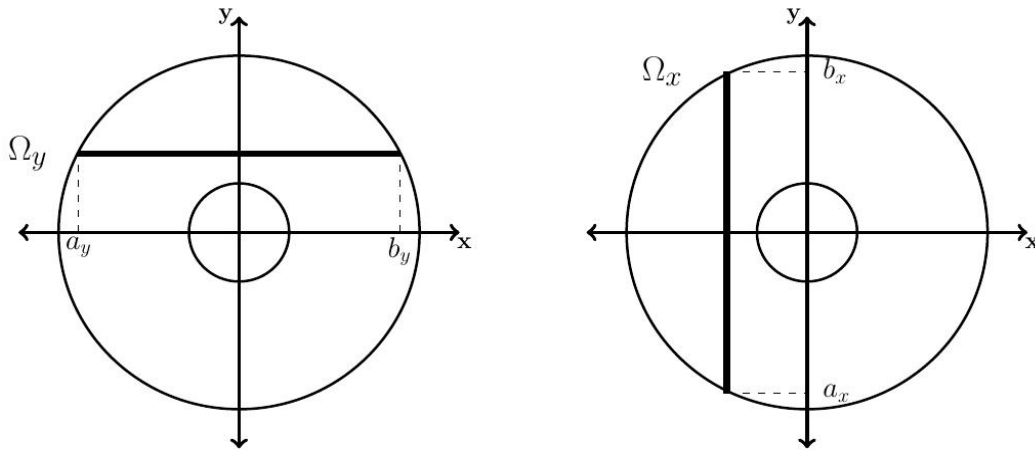


Figure 3.3: Borders of the annular aperture mask for fixed  $x$  and  $y$ , source [108]. The domain  $\Omega_x$  changes with  $x$  and  $\Omega_y$  with  $y$  respectively. In some cases the intervals are split due to the central obstruction of the telescope.

We start with restricting the availability of measurements to the size of the region captured by the sensor. For several telescope systems the pupil is annular instead of circular since a secondary mirror shades the primary mirror, making the area of central obstruction hardly attainable for photons. Thus, the remaining light in the area of the central obstruction does not produce reliable measurements. Moreover, the incoming phases are defined on  $\mathbb{R}^2$  but for the control of the deformable mirror we consider the reconstructed wavefront shape only on a restricted domain (bounded by the size of the telescope pupil).

For the following considerations, we describe the annular telescope aperture mask by  $\Omega = \Omega_y \times \Omega_x \subseteq [-D/2, D/2]^2$  as shown in Figure 3.3. Single lines of the annular

aperture are represented by  $\Omega_x = [a_x, b_x]$  and  $\Omega_y = [a_y, b_y]$ , with  $a_x < b_x$ ,  $a_y < b_y$  being the borders of the pupil for fixed  $x$  and  $y$  correspondingly. The sensor provides measurement on the region of the CCD-detector  $D$ . Throughout the Thesis, we do not distinguish between pupil and CCD-detector and assume  $D = \Omega$ . Further, the limitation onto the CCD detector (indicated as multiplication with a characteristic function of  $D$ ) is not marked explicitly for the underlying operators for simplicity of notation. However, please keep in mind the compact support of the considered functions because of the restricted size of the aperture and the CCD-detector. For instance, we consider the norms in  $\mathcal{L}_2(\mathbb{R}^2)$  but since the operators map from and to functions with compact support on  $\Omega$  it is equivalent to considering the norms in  $\mathcal{L}_2(\Omega)$ .

Let  $\Phi \in \mathcal{H}^{11/6}(\mathbb{R}^2)$  denote the phase screen in radians coming into the telescope. Using wave optics based models and assuming constant amplitude over the full telescope pupil  $\Omega = \Omega_y \times \Omega_x$  the complex amplitude (wave)  $\psi_{aper}$  corresponding to this incoming phase reads as

$$\psi_{aper}(x, y) = \mathcal{X}_\Omega(x, y) \cdot \exp(-i\Phi(x, y)).$$

Note that  $\psi_{aper} \in \mathcal{L}_p(\mathbb{R}^2)$  for all  $1 \leq p \leq \infty$  due to the compact support of  $\psi_{aper}$ , the continuity of  $\Phi$ , and further the continuity of  $\psi_{aper}$  on  $\Omega$ . In order to assume the continuity of  $\psi_{aper}$  on  $\mathbb{R}^2$ , we slightly modify the telescope aperture mask  $\mathcal{X}_\Omega$  and approximate it by  $\mathcal{X}_\Omega^\epsilon \in \mathcal{C}_0^\infty(\mathbb{R}^2)$  fulfilling  $\mathcal{X}_\Omega = \mathcal{X}_\Omega^\epsilon$  on  $\Omega$ .

The idea of the extended mask is to smoothen the sharp edges of the telescope pupil in order to guarantee  $\psi_{aper}^\epsilon \in \mathcal{H}^{11/6}(\mathbb{R}^2)$  using

$$\psi_{aper}^\epsilon(x, y) := \mathcal{X}_\Omega^\epsilon(x, y) \cdot \exp(-i\Phi(x, y)).$$

The above assertion is fulfilled for an approximation of the aperture mask denoted by  $\mathcal{X}_\Omega^\epsilon \in \mathcal{C}_0^\infty(\mathbb{R}^2)$ . One possible representation of  $\mathcal{X}_\Omega^\epsilon$  can be constructed utilizing the following Lemma in which we consider the sets  $\Omega = \Omega_y \times \Omega_x = [a_y, b_y] \times [a_x, b_x]$  and  $\Omega^\epsilon = (a_y - \epsilon, b_y + \epsilon) \times (a_x - \epsilon, b_x + \epsilon)$  for a small  $\epsilon > 0$ , i.e.,  $\Omega \subset \Omega^\epsilon$ .

**Lemma 3.1** (Lemma 4.2, [206]). *Let  $\Omega \subset \mathbb{R}^n$  and  $\Omega^\epsilon \subset \mathbb{R}^n$  be bounded sets with  $\overline{\Omega} \subset \Omega^\epsilon$  and  $\Omega^\epsilon$  open. Then, there exists a real-valued function  $\mathcal{X}_\Omega^\epsilon \in \mathcal{C}_0^\infty(\Omega^\epsilon)$  with  $0 \leq \mathcal{X}_{\Omega_y \times \Omega_x}^\epsilon(z) \leq 1$  for  $z \in \Omega^\epsilon$  and  $\mathcal{X}_\Omega^\epsilon(z) = 1$  for  $z \in \Omega$ .*

Outside of  $\Omega^\epsilon$  we extend  $\mathcal{X}_\Omega^\epsilon$  with zeros and obtain  $\mathcal{X}_\Omega^\epsilon \in \mathcal{C}_0^\infty(\mathbb{R}^2)$ .

We investigate the construction of the new smooth aperture mask  $\mathcal{X}_\Omega^\epsilon$  in more detail. As in [206], we consider the smooth function  $f \in \mathcal{C}_0^\infty(\mathbb{R}^2)$ ,

$$f(z) := \begin{cases} c \exp\left(-\frac{1}{1-|z|^2}\right), & \text{for } |z| < 1, \\ 0, & \text{for } |z| \geq 1, \end{cases}$$

having compact support on  $[-1, 1]^2$ . The constant  $c \in \mathbb{R}$  is chosen such that

$$\int_{\mathbb{R}^2} f(z) dz = \int_{|z| \leq 1} f(z) dz = 1.$$

Additionally, we introduce

$$f^\epsilon(z) := \frac{1}{\epsilon^2} f\left(\frac{z}{\epsilon}\right)$$

for  $\epsilon > 0$ . Using this function, S. L. Sobolev established a method [199] which is utilized for the smoothing of the characteristic function describing the telescope pupil. With the coordinate transformation

$$z - \epsilon z' = z'', \quad (3.3)$$

for  $\mathcal{X}_\Omega \in \mathcal{L}_p(\mathbb{R}^2)$ ,  $1 \leq p \leq \infty$  we build the average function  $\mathcal{X}_\Omega^\epsilon \in \mathcal{C}_0^\infty(\mathbb{R}^2)$  by

$$\begin{aligned} \mathcal{X}_\Omega^\epsilon(z) &= \int_{\mathbb{R}^2} \mathcal{X}_\Omega(z - \epsilon z') f(z') dz' \\ &\stackrel{(3.3)}{=} \int_{\mathbb{R}^2} \frac{1}{\epsilon^2} \mathcal{X}_\Omega(z'') f\left(\frac{z - z''}{\epsilon}\right) dz'' \\ &= \int_{|z - z''| \leq \epsilon} f^\epsilon(z - z'') \mathcal{X}_\Omega(z'') dz''. \end{aligned}$$

Altogether,  $\psi_{aper}^\epsilon$  is an element of  $\mathcal{H}^{11/6}(\mathbb{R}^2)$  using that from  $\Phi \in \mathcal{H}^{11/6}$  it follows  $e^{-i\Phi} \in \mathcal{H}^{11/6}$  as stated in [25, 26].

The adaption of the aperture mask is necessary to guarantee a well-defined mathematical derivation of the pyramid wavefront sensor model. Please note that

$$\left\| \mathcal{X}_\Omega - \mathcal{X}_{\Omega_y \times \Omega_x}^\epsilon \right\|_{\mathcal{L}_2(\mathbb{R}^2)} = \mathcal{O}(\epsilon^2),$$

and therefore  $\mathcal{X}_\Omega^\epsilon$  is an arbitrarily good approximation of the aperture mask  $\mathcal{X}_\Omega$ . The following physical argument supports the usage of a smoothed aperture mask  $\Omega^\epsilon$  instead of the one with the sharp edges. Both masks have a compact support. Therefore, on the Fourier domain they are both represented with infinite spectra. Since  $\epsilon < d$  (with  $d$  denoting the telescope subaperture size) is small, the difference between the two masks, when looking in the Fourier domain, appears only in the very high frequency components. Because the pyramidal prism is a physical device of finite size, it anyway cuts off high frequency components of the input. Additionally, the sensor brings spatial discretization in the model due to subaperture averaging. As a result, the spectra of the resulting sensor data contain frequencies only up to a given cut-off frequency defined via the subaperture size  $d$  as  $\xi_{cut} = 1/(2d)$ . Therefore, in practice there is no difference between the smoothed and the sharp aperture mask. In the following and throughout the Thesis, we write  $\mathcal{X}_\Omega$  but keep in mind that we always

mean  $\mathcal{X}_\Omega^\epsilon$  for a small  $\epsilon > 0$  for the pyramid wavefront sensor model to be well-defined.

As a next step, we consider the point spread function (PSF) of the glass pyramid. The PSF is the inverse Fourier transform of the optical transfer function (OTF) of the pyramidal prism

$$PSF_{pyr} = \mathcal{F}_{2d}^{-1}\{OTF_{pyr}\}. \quad (3.4)$$

We distinguish between two models of the pyramidal mask, namely the transmission mask model and the phase mask model.

### 3.2.1 Mathematical derivation of transmission mask model

We start with a mathematical derivation of the pyramid wavefront sensor model which is based on the transmission mask. For the pyramid wavefront sensor, we only consider the non-modulated and the sensor with circular modulation since they make sense from the physical point of view.

**Definition 3.2.** We introduce the operators  $\mathbf{P}_x^{\{n,c\}}$  in  $x$ -direction given by

$$\begin{aligned} \left(\mathbf{P}_x^{\{n,c\}}\Phi\right)(x, y) &:= \frac{1}{\pi} \mathcal{X}_\Omega(x, y) \text{ p.v.} \int_{\Omega_y} \frac{\sin[\Phi(x', y) - \Phi(x, y)] \cdot k^{\{n,c\}}(x' - x)}{x' - x} dx' \\ &+ \frac{1}{\pi^3} \mathcal{X}_{\Omega_y}(x) \text{ p.v.} \int_{\Omega_y} \int_{\Omega_x} \int_{\Omega_x} \frac{\sin[\Phi(x', y') - \Phi(x, y'')] \cdot l^{\{n,c\}}(x' - x, y' - y)}{(x' - x)(y' - y)(y'' - y)} dy'' dy' dx' \end{aligned} \quad (3.5)$$

and  $\mathbf{P}_y^{\{n,c\}}$  in  $y$ -direction given by

$$\begin{aligned} \left(\mathbf{P}_y^{\{n,c\}}\Phi\right)(x, y) &:= \frac{1}{\pi} \mathcal{X}_\Omega(x, y) \text{ p.v.} \int_{\Omega_x} \frac{\sin[\Phi(x, y') - \Phi(x, y)] \cdot k^{\{n,c\}}(y' - y)}{y' - y} dy' \\ &+ \frac{1}{\pi^3} \mathcal{X}_{\Omega_x}(y) \text{ p.v.} \int_{\Omega_y} \int_{\Omega_x} \int_{\Omega_y} \frac{\sin[\Phi(x', y') - \Phi(x'', y)] \cdot l^{\{n,c\}}(x'' - x', y' - y)}{(x' - x)(y' - y)(x'' - x)} dx'' dy' dx'. \end{aligned} \quad (3.6)$$

The functions  $k^{\{n,c\}}$  are defined by  $k^n(x) := 1$ ,  $k^c(x) := J_0(\alpha_\lambda x)$ , and the functions  $l^{\{n,c\}}$  by  $l^n(x, y) := 1$  and

$$l^c(x, y) := \frac{1}{T} \int_{-T/2}^{T/2} \cos[\alpha_\lambda x \sin(2\pi t/T)] \cos[\alpha_\lambda y \cos(2\pi t/T)] dt.$$

The function  $J_0$  denotes the zero-order Bessel function of the first kind given by

$$J_0(x) = \frac{1}{\pi} \int_0^\pi \cos(x \sin t) dt = \frac{1}{\pi} \int_0^\pi \cos(x \cos t) dt$$

and  $\alpha_\lambda$  the modulation parameter defined by

$$\alpha_\lambda = \frac{2\pi\alpha}{\lambda} \quad (3.7)$$

with  $\alpha = r\lambda/D$  for a positive integer  $r$  representing the modulation radius,  $\lambda$  the sensing wavelength, and  $D$  the telescope diameter.

**Theorem 3.3.** *The relation between the pyramid wavefront sensor data and the incoming wavefront following the transmission mask model is given by*

$$\begin{aligned} s_x^{\{n,c\}}(x,y) &= -\frac{1}{2} \left( \mathbf{P}_x^{\{n,c\}} \Phi \right) (x,y), \\ s_y^{\{n,c\}}(x,y) &= \frac{1}{2} \left( \mathbf{P}_y^{\{n,c\}} \Phi \right) (x,y), \end{aligned} \quad (3.8)$$

where  $\mathbf{P}^{\{n,c\}}$  denote the pyramid sensor operators defined in (3.5)-(3.6).

*Proof.* Within the transmission mask approach [125], the OTF only takes splitting of the light into account and ignores the phase shifts introduced by the pyramid facets. It is represented as a sum of 2d Heaviside functions

$$OTF_{pyr}(\xi, \eta) = \sum_{m=0}^1 \sum_{n=0}^1 T^{mn}(\xi, \eta) \quad (3.9)$$

with

$$T^{mn}(\xi, \eta) = H_{2d} [(-1)^m \xi, (-1)^n \eta] := \begin{cases} 1, & \text{if } (-1)^m \xi \geq 0, \quad (-1)^n \eta \geq 0, \\ 0, & \text{otherwise.} \end{cases}$$

The 2d Heaviside function is the product of two 1d Heaviside functions

$$H_{2d}(\xi, \eta) = H_{1d}(\xi) \cdot H_{1d}(\eta)$$

and the 1d Heaviside function can be represented as

$$H_{1d}(\xi) = \frac{1}{2} + \frac{1}{2} \cdot \mathbf{sgn}(\xi).$$

Therefore,

$$H_{2d}(\xi, \eta) = \frac{1}{4} [1 + \mathbf{sgn}(\xi) + \mathbf{sgn}(\eta) + \mathbf{sgn}(\xi) \cdot \mathbf{sgn}(\eta)],$$

which for  $g_m(\xi) := \mathbf{sgn}((-1)^m \xi)$  results in

$$\begin{aligned} T^{mn}(\xi, \eta) &= \frac{1}{4} [1 + \mathbf{sgn}((-1)^m \xi) + \mathbf{sgn}((-1)^n \eta) + \mathbf{sgn}((-1)^m \xi) \cdot \mathbf{sgn}((-1)^n \eta)] \\ &= \frac{1}{4} [1 + g_m(\xi) + g_n(\eta) + g_m(\xi) \cdot g_n(\eta)]. \end{aligned}$$

Please note that in the above notation,  $g_m$  is always meant as function of the first variable  $\xi$  and  $g_n$  as function of the second variable  $\eta$  for 2d considerations. Furthermore,  $\mathcal{F}_x$  will denote the 1d Fourier transform in the first variable and  $\mathcal{F}_y$  the 1d Fourier transform in the second variable. With (3.4) and due to the linearity of the Fourier transform, the PSF of the pyramid is represented as a sum of four PSFs

$$\begin{aligned} PSF_{pyr} &= \mathcal{F}_{2d}^{-1} \left\{ \sum_{m=0}^1 \sum_{n=0}^1 T^{mn} \right\} = \sum_{m=0}^1 \sum_{n=0}^1 \mathcal{F}_{2d}^{-1} \{T^{mn}\} \\ &= \sum_{m=0}^1 \sum_{n=0}^1 \underbrace{\mathcal{F}_{2d}^{-1} \left\{ \frac{1}{4} [1 + g_m + g_n + g_m \cdot g_n] \right\}}_{=: PSF_{pyr}^{mn}}. \end{aligned} \quad (3.10)$$

The OTF is a sum of products of functions depending either on  $\xi$  or  $\eta$ . Hence, the inverse 2d Fourier transform reduces to products of 1d inverse Fourier transforms. For  $PSF_{pyr}^{mn}$ , we obtain

$$\begin{aligned} PSF_{pyr}^{mn}(x, y) &= \frac{1}{4} \left[ \mathcal{F}_x^{-1} \{1\}(x) \cdot \mathcal{F}_y^{-1} \{1\}(y) \right. \\ &\quad + \mathcal{F}_x^{-1} \{g_m\}(x) \cdot \mathcal{F}_y^{-1} \{1\}(y) \\ &\quad + \mathcal{F}_x^{-1} \{1\}(x) \cdot \mathcal{F}_y^{-1} \{g_n\}(y) \\ &\quad \left. + \mathcal{F}_x^{-1} \{g_m\}(x) \cdot \mathcal{F}_y^{-1} \{g_n\}(y) \right]. \end{aligned}$$

The Fourier transforms of the involved constant and signum functions do only exist in a distributional sense.

For test functions  $\varphi$ , we introduce the delta distribution  $\delta$  defined as  $\langle \delta, \varphi \rangle = \varphi(0)$ . This application is well-defined for continuous functions, e.g.,  $\varphi \in \mathcal{H}^{1/2+\epsilon}(\mathbb{R})$ , and on account of this  $\delta \in \mathcal{H}^{-1/2-\epsilon}(\mathbb{R})$  for  $\epsilon > 0$ . The distribution  $(p.v. \frac{1}{x})$  is defined via the Cauchy principal value by

$$\left\langle \left( p.v. \frac{1}{x} \right), \varphi \right\rangle = \lim_{\epsilon \rightarrow 0^+} \int_{|x'| > \epsilon} \frac{\varphi(x')}{x'} dx' = \pi (\mathbf{H}\varphi)(0)$$

for the 1d Hilbert transform operator

$$(\mathbf{H}\varphi)(x) := \frac{1}{\pi} p.v. \int_{\mathbb{R}} \frac{\varphi(x')}{x' - x} dx'. \quad (3.11)$$

Since the 1d Hilbert transform  $\mathbf{H} : \mathcal{L}_2(\mathbb{R}) \rightarrow \mathcal{L}_2(\mathbb{R})$  is a well-defined operator (see, e.g., [29, Theorem 8.1.12]), the evaluation of  $\langle (p.v. \frac{1}{x}), \varphi \rangle$  is well-defined in a distributional sense for  $\varphi \in \mathcal{H}^{1/2+\epsilon}(\mathbb{R}) \subset \mathcal{L}_2(\mathbb{R})$ , which results in  $(p.v. \frac{1}{x}) \in \mathcal{H}^{-1/2-\epsilon}(\mathbb{R})$ .

Specifically,

$$\mathcal{F}_x^{-1} \{1\}(x) = \sqrt{2\pi} \cdot \delta(x) \in \mathcal{H}^{-1/2-\epsilon}(\mathbb{R}),$$

$$\mathcal{F}_x^{-1}\{\text{sgn}(\cdot)\}(x) = i \cdot \sqrt{\frac{2}{\pi}} \cdot p.v. \frac{1}{x} \in \mathcal{H}^{-1/2-\epsilon}(\mathbb{R}),$$

and in the same way

$$\mathcal{F}_x^{-1}\{g_m\}(x) = i \cdot \sqrt{\frac{2}{\pi}} \cdot p.v. \frac{1}{(-1)^m x} = i \cdot (-1)^m \cdot \sqrt{\frac{2}{\pi}} \cdot p.v. \frac{1}{x} \in \mathcal{H}^{-1/2-\epsilon}(\mathbb{R}).$$

Using the notations  $\delta_x$  in case the delta distribution is only applied in  $x$ -direction and  $\delta_y$  accordingly,

$$v_x := \left(p.v. \frac{1}{x}\right) \quad \text{and} \quad v_y := \left(p.v. \frac{1}{y}\right) \quad \text{as well as} \quad v_{xy} := \left(p.v. \frac{1}{xy}\right),$$

the 2d  $PSF_{pyr}^{mn} \in \mathcal{H}^{-1-\epsilon}(\mathbb{R}^2)$  is given by

$$PSF_{pyr}^{mn} = \frac{\pi}{2} \cdot \delta_x \delta_y + \frac{1}{2} \cdot i \cdot (-1)^m \cdot v_x \delta_y + \frac{1}{2} \cdot i \cdot (-1)^n \cdot \delta_x v_y + \frac{1}{2\pi} \cdot (-1)^{m+n+1} \cdot v_{xy}.$$

According to the standard description of optical systems, the wave  $\psi_{det}$  coming to the detector plane is the inverse 2d Fourier transform of the complex amplitude after the pyramid ( $\psi_{aper}^\epsilon \cdot OTF_{pyr}$ ) which results (by application of the convolution theorem (A.1)) in a convolution of the incoming complex amplitude  $\psi_{aper}^\epsilon$  with the point spread function of the glass pyramid as described, e.g., in [125]. This step can mathematically be written in the sense of distributions as a shifted PSF distribution applied to the complex amplitude of the incoming phase

$$\psi_{det}(x, y) = \frac{1}{2\pi} \left\langle PSF_{pyr}((x, y) - (\cdot, \cdot)), \psi_{aper}^\epsilon \right\rangle. \quad (3.12)$$

Then, by linearity, the 4 independent beams  $\psi_{det}^{mn}$ ,  $m, n \in \{0, 1\}$ , falling onto the detector are given by

$$\begin{aligned} \psi_{det}^{mn}(x, y) &= \frac{1}{2\pi} \left\langle PSF_{pyr}^{mn}((x, y) - (\cdot, \cdot)), \psi_{aper}^\epsilon \right\rangle \\ &= \frac{1}{4} \left\langle (\delta_x \delta_y)((x, y) - (\cdot, \cdot)), \psi_{aper}^\epsilon \right\rangle + \frac{(-1)^m i}{4\pi} \left\langle (v_x \delta_y)((x, y) - (\cdot, \cdot)), \psi_{aper}^\epsilon \right\rangle \\ &\quad + \frac{(-1)^n i}{4\pi} \left\langle (\delta_x v_y)((x, y) - (\cdot, \cdot)), \psi_{aper}^\epsilon \right\rangle + \frac{(-1)^{m+n+1}}{4\pi^2} \left\langle v_{xy}((x, y) - (\cdot, \cdot)), \psi_{aper}^\epsilon \right\rangle \\ &= \frac{1}{4} \psi_{aper}^\epsilon(x, y) + \frac{(-1)^m i}{4\pi} \left\langle v_x(x - \cdot), \psi_{aper}^\epsilon(\cdot, y) \right\rangle \\ &\quad + \frac{(-1)^n i}{4\pi} \left\langle v_y(y - \cdot), \psi_{aper}^\epsilon(x, \cdot) \right\rangle + \frac{(-1)^{m+n+1}}{4\pi^2} \left\langle v_{xy}((x, y) - (\cdot, \cdot)), \psi_{aper}^\epsilon \right\rangle. \end{aligned}$$

The four complex amplitudes are explicitly formulated as

$$\begin{aligned} \psi_{det}^{00}(x, y) &= \frac{1}{4} \psi_{aper}^\epsilon(x, y) + \frac{i}{4\pi} \left\langle v_x(x - \cdot), \psi_{aper}^\epsilon(\cdot, y) \right\rangle \\ &\quad + \frac{i}{4\pi} \left\langle v_y(y - \cdot), \psi_{aper}^\epsilon(x, \cdot) \right\rangle - \frac{1}{4\pi^2} \left\langle v_{xy}((x, y) - (\cdot, \cdot)), \psi_{aper}^\epsilon \right\rangle, \end{aligned}$$

$$\begin{aligned}\psi_{det}^{01}(x, y) &= \frac{1}{4}\psi_{aper}^{\epsilon}(x, y) + \frac{i}{4\pi}\left\langle v_x(x - \cdot), \psi_{aper}^{\epsilon}(\cdot, y) \right\rangle \\ &\quad - \frac{i}{4\pi}\left\langle v_y(y - \cdot), \psi_{aper}^{\epsilon}(x, \cdot) \right\rangle + \frac{1}{4\pi^2}\left\langle v_{xy}((x, y) - (\cdot, \cdot)), \psi_{aper}^{\epsilon} \right\rangle,\end{aligned}$$

$$\begin{aligned}\psi_{det}^{10}(x, y) &= \frac{1}{4}\psi_{aper}^{\epsilon}(x, y) - \frac{i}{4\pi}\left\langle v_x(x - \cdot), \psi_{aper}^{\epsilon}(\cdot, y) \right\rangle \\ &\quad + \frac{i}{4\pi}\left\langle v_y(y - \cdot), \psi_{aper}^{\epsilon}(x, \cdot) \right\rangle + \frac{1}{4\pi^2}\left\langle v_{xy}((x, y) - (\cdot, \cdot)), \psi_{aper}^{\epsilon} \right\rangle,\end{aligned}$$

$$\begin{aligned}\psi_{det}^{11}(x, y) &= \frac{1}{4}\psi_{aper}^{\epsilon}(x, y) - \frac{i}{4\pi}\left\langle v_x(x - \cdot), \psi_{aper}^{\epsilon}(\cdot, y) \right\rangle \\ &\quad - \frac{i}{4\pi}\left\langle v_y(y - \cdot), \psi_{aper}^{\epsilon}(x, \cdot) \right\rangle - \frac{1}{4\pi^2}\left\langle v_{xy}((x, y) - (\cdot, \cdot)), \psi_{aper}^{\epsilon} \right\rangle.\end{aligned}$$

Now, the intensities on the detector are computed as

$$I^{mn}(x, y) = \psi_{det}^{mn}(x, y) \overline{\psi_{det}^{mn}(x, y)}, \quad m, n \in \{0, 1\}. \quad (3.13)$$

If we abbreviate  $\psi_{aper}^{\epsilon}$  by  $\psi$  and omit the arguments for simplicity of notation, the four intensities are evaluated as

$$\begin{aligned}I^{00}(x, y) &= \psi_{det}^{00}(x, y) \overline{\psi_{det}^{00}(x, y)} \\ &= \left[ \frac{1}{4}\psi + \frac{i}{4\pi}\langle v_x, \psi \rangle + \frac{i}{4\pi}\langle v_y, \psi \rangle - \frac{1}{4\pi^2}\langle v_{xy}, \psi \rangle \right] \\ &\quad \cdot \left[ \frac{1}{4}\bar{\psi} - \frac{i}{4\pi}\langle v_x, \bar{\psi} \rangle - \frac{i}{4\pi}\langle v_y, \bar{\psi} \rangle - \frac{1}{4\pi^2}\langle v_{xy}, \bar{\psi} \rangle \right] \\ &= \frac{1}{16}\psi\bar{\psi} - \frac{i}{16\pi}\psi\langle v_x, \bar{\psi} \rangle - \frac{i}{16\pi}\psi\langle v_y, \bar{\psi} \rangle - \frac{1}{16\pi^2}\psi\langle v_{xy}, \bar{\psi} \rangle \\ &\quad + \frac{i}{16\pi}\langle v_x, \psi \rangle\bar{\psi} + \frac{1}{16\pi^2}\langle v_x, \psi \rangle\langle v_x, \bar{\psi} \rangle + \frac{1}{16\pi^2}\langle v_x, \psi \rangle\langle v_y, \bar{\psi} \rangle - \frac{i}{16\pi^3}\langle v_x, \psi \rangle\langle v_{xy}, \bar{\psi} \rangle \\ &\quad + \frac{i}{16\pi}\langle v_y, \psi \rangle\bar{\psi} + \frac{1}{16\pi^2}\langle v_y, \psi \rangle\langle v_x, \bar{\psi} \rangle + \frac{1}{16\pi^2}\langle v_y, \psi \rangle\langle v_y, \bar{\psi} \rangle - \frac{i}{16\pi^3}\langle v_y, \psi \rangle\langle v_{xy}, \bar{\psi} \rangle \\ &\quad - \frac{1}{16\pi^2}\langle v_{xy}, \psi \rangle\bar{\psi} + \frac{i}{16\pi^3}\langle v_{xy}, \psi \rangle\langle v_x, \bar{\psi} \rangle + \frac{i}{16\pi^3}\langle v_{xy}, \psi \rangle\langle v_y, \bar{\psi} \rangle + \frac{1}{16\pi^4}\langle v_{xy}, \psi \rangle\langle v_{xy}, \bar{\psi} \rangle,\end{aligned}$$

$$\begin{aligned}I^{01}(x, y) &= \psi_{det}^{01}(x, y) \overline{\psi_{det}^{01}(x, y)} \\ &= \left[ \frac{1}{4}\psi + \frac{i}{4\pi}\langle v_x, \psi \rangle - \frac{i}{4\pi}\langle v_y, \psi \rangle + \frac{1}{4\pi^2}\langle v_{xy}, \psi \rangle \right] \\ &\quad \cdot \left[ \frac{1}{4}\bar{\psi} - \frac{i}{4\pi}\langle v_x, \bar{\psi} \rangle + \frac{i}{4\pi}\langle v_y, \bar{\psi} \rangle + \frac{1}{4\pi^2}\langle v_{xy}, \bar{\psi} \rangle \right] \\ &= \frac{1}{16}\psi\bar{\psi} - \frac{i}{16\pi}\psi\langle v_x, \bar{\psi} \rangle + \frac{i}{16\pi}\psi\langle v_y, \bar{\psi} \rangle + \frac{1}{16\pi^2}\psi\langle v_{xy}, \bar{\psi} \rangle \\ &\quad + \frac{i}{16\pi}\langle v_x, \psi \rangle\bar{\psi} + \frac{1}{16\pi^2}\langle v_x, \psi \rangle\langle v_x, \bar{\psi} \rangle - \frac{1}{16\pi^2}\langle v_x, \psi \rangle\langle v_y, \bar{\psi} \rangle + \frac{i}{16\pi^3}\langle v_x, \psi \rangle\langle v_{xy}, \bar{\psi} \rangle \\ &\quad - \frac{i}{16\pi}\langle v_y, \psi \rangle\bar{\psi} - \frac{1}{16\pi^2}\langle v_y, \psi \rangle\langle v_x, \bar{\psi} \rangle + \frac{1}{16\pi^2}\langle v_y, \psi \rangle\langle v_y, \bar{\psi} \rangle - \frac{i}{16\pi^3}\langle v_y, \psi \rangle\langle v_{xy}, \bar{\psi} \rangle\end{aligned}$$

$$+ \frac{1}{16\pi^2} \langle v_{xy}, \psi \rangle \bar{\psi} - \frac{i}{16\pi^3} \langle v_{xy}, \psi \rangle \langle v_x, \bar{\psi} \rangle + \frac{i}{16\pi^3} \langle v_{xy}, \psi \rangle \langle v_y, \bar{\psi} \rangle + \frac{1}{16\pi^4} \langle v_{xy}, \psi \rangle \langle v_{xy}, \bar{\psi} \rangle,$$

$$\begin{aligned} I^{10}(x, y) &= \psi_{det}^{10}(x, y) \overline{\psi_{det}^{10}(x, y)} \\ &= \left[ \frac{1}{4} \psi - \frac{i}{4\pi} \langle v_x, \psi \rangle + \frac{i}{4\pi} \langle v_y, \psi \rangle + \frac{1}{4\pi^2} \langle v_{xy}, \psi \rangle \right] \\ &\quad \cdot \left[ \frac{1}{4} \bar{\psi} + \frac{i}{4\pi} \langle v_x, \bar{\psi} \rangle - \frac{i}{4\pi} \langle v_y, \bar{\psi} \rangle + \frac{1}{4\pi^2} \langle v_{xy}, \bar{\psi} \rangle \right] \\ &= \frac{1}{16} \psi \bar{\psi} + \frac{i}{16\pi} \psi \langle v_x, \bar{\psi} \rangle - \frac{i}{16\pi} \psi \langle v_y, \bar{\psi} \rangle + \frac{1}{16\pi^2} \psi \langle v_{xy}, \bar{\psi} \rangle \\ &\quad - \frac{i}{16\pi} \langle v_x, \psi \rangle \bar{\psi} + \frac{1}{16\pi^2} \langle v_x, \psi \rangle \langle v_x, \bar{\psi} \rangle - \frac{1}{16\pi^2} \langle v_x, \psi \rangle \langle v_y, \bar{\psi} \rangle - \frac{i}{16\pi^3} \langle v_x, \psi \rangle \langle v_{xy}, \bar{\psi} \rangle \\ &\quad + \frac{i}{16\pi} \langle v_y, \psi \rangle \bar{\psi} - \frac{1}{16\pi^2} \langle v_y, \psi \rangle \langle v_x, \bar{\psi} \rangle + \frac{1}{16\pi^2} \langle v_y, \psi \rangle \langle v_y, \bar{\psi} \rangle + \frac{i}{16\pi^3} \langle v_y, \psi \rangle \langle v_{xy}, \bar{\psi} \rangle \\ &\quad + \frac{1}{16\pi^2} \langle v_{xy}, \psi \rangle \bar{\psi} + \frac{i}{16\pi^3} \langle v_{xy}, \psi \rangle \langle v_x, \bar{\psi} \rangle - \frac{i}{16\pi^3} \langle v_{xy}, \psi \rangle \langle v_y, \bar{\psi} \rangle + \frac{1}{16\pi^4} \langle v_{xy}, \psi \rangle \langle v_{xy}, \bar{\psi} \rangle, \end{aligned}$$

$$\begin{aligned} I^{11}(x, y) &= \psi_{det}^{11}(x, y) \overline{\psi_{det}^{11}(x, y)} \\ &= \left[ \frac{1}{4} \psi - \frac{i}{4\pi} \langle v_x, \psi \rangle - \frac{i}{4\pi} \langle v_y, \psi \rangle - \frac{1}{4\pi^2} \langle v_{xy}, \psi \rangle \right] \\ &\quad \cdot \left[ \frac{1}{4} \bar{\psi} + \frac{i}{4\pi} \langle v_x, \bar{\psi} \rangle + \frac{i}{4\pi} \langle v_y, \bar{\psi} \rangle - \frac{1}{4\pi^2} \langle v_{xy}, \bar{\psi} \rangle \right] \\ &= \frac{1}{16} \psi \bar{\psi} + \frac{i}{16\pi} \psi \langle v_x, \bar{\psi} \rangle + \frac{i}{16\pi} \psi \langle v_y, \bar{\psi} \rangle - \frac{1}{16\pi^2} \psi \langle v_{xy}, \bar{\psi} \rangle \\ &\quad - \frac{i}{16\pi} \langle v_x, \psi \rangle \bar{\psi} + \frac{1}{16\pi^2} \langle v_x, \psi \rangle \langle v_x, \bar{\psi} \rangle + \frac{1}{16\pi^2} \langle v_x, \psi \rangle \langle v_y, \bar{\psi} \rangle + \frac{i}{16\pi^3} \langle v_x, \psi \rangle \langle v_{xy}, \bar{\psi} \rangle \\ &\quad - \frac{i}{16\pi} \langle v_y, \psi \rangle \bar{\psi} + \frac{1}{16\pi^2} \langle v_y, \psi \rangle \langle v_x, \bar{\psi} \rangle + \frac{1}{16\pi^2} \langle v_y, \psi \rangle \langle v_y, \bar{\psi} \rangle + \frac{i}{16\pi^3} \langle v_y, \psi \rangle \langle v_{xy}, \bar{\psi} \rangle \\ &\quad - \frac{1}{16\pi^2} \langle v_{xy}, \psi \rangle \bar{\psi} - \frac{i}{16\pi^3} \langle v_{xy}, \psi \rangle \langle v_x, \bar{\psi} \rangle - \frac{i}{16\pi^3} \langle v_{xy}, \psi \rangle \langle v_y, \bar{\psi} \rangle + \frac{1}{16\pi^4} \langle v_{xy}, \psi \rangle \langle v_{xy}, \bar{\psi} \rangle. \end{aligned}$$

Taking the sums according to (3.1), we obtain the non-modulated (indicated by the superscript  $n$ ) pyramid sensor data  $s_x^n$  in  $x$ -direction as

$$\begin{aligned} I_0 \cdot s_x^n(x, y) &= [I^{01}(x, y) + I^{00}(x, y)] - [I^{11}(x, y) + I^{10}(x, y)] \\ &= \frac{1}{16} \psi \bar{\psi} - \frac{i}{16\pi} \psi \langle v_x, \bar{\psi} \rangle + \frac{i}{16\pi} \psi \langle v_y, \bar{\psi} \rangle + \frac{1}{16\pi^2} \psi \langle v_{xy}, \bar{\psi} \rangle \\ &\quad + \frac{i}{16\pi} \langle v_x, \psi \rangle \bar{\psi} + \frac{1}{16\pi^2} \langle v_x, \psi \rangle \langle v_x, \bar{\psi} \rangle - \frac{1}{16\pi^2} \langle v_x, \psi \rangle \langle v_y, \bar{\psi} \rangle + \frac{i}{16\pi^3} \langle v_x, \psi \rangle \langle v_{xy}, \bar{\psi} \rangle \\ &\quad - \frac{i}{16\pi} \langle v_y, \psi \rangle \bar{\psi} - \frac{1}{16\pi^2} \langle v_y, \psi \rangle \langle v_x, \bar{\psi} \rangle + \frac{1}{16\pi^2} \langle v_y, \psi \rangle \langle v_y, \bar{\psi} \rangle - \frac{i}{16\pi^3} \langle v_y, \psi \rangle \langle v_{xy}, \bar{\psi} \rangle \\ &\quad + \frac{1}{16\pi^2} \langle v_{xy}, \psi \rangle \bar{\psi} - \frac{i}{16\pi^3} \langle v_{xy}, \psi \rangle \langle v_x, \bar{\psi} \rangle + \frac{i}{16\pi^3} \langle v_{xy}, \psi \rangle \langle v_y, \bar{\psi} \rangle + \frac{1}{16\pi^4} \langle v_{xy}, \psi \rangle \langle v_{xy}, \bar{\psi} \rangle \\ &\quad + \frac{1}{16} \psi \bar{\psi} - \frac{i}{16\pi} \psi \langle v_x, \bar{\psi} \rangle - \frac{i}{16\pi} \psi \langle v_y, \bar{\psi} \rangle - \frac{1}{16\pi^2} \psi \langle v_{xy}, \bar{\psi} \rangle \\ &\quad + \frac{i}{16\pi} \langle v_x, \psi \rangle \bar{\psi} + \frac{1}{16\pi^2} \langle v_x, \psi \rangle \langle v_x, \bar{\psi} \rangle + \frac{1}{16\pi^2} \langle v_x, \psi \rangle \langle v_y, \bar{\psi} \rangle - \frac{i}{16\pi^3} \langle v_x, \psi \rangle \langle v_{xy}, \bar{\psi} \rangle \\ &\quad + \frac{i}{16\pi} \langle v_y, \psi \rangle \bar{\psi} + \frac{1}{16\pi^2} \langle v_y, \psi \rangle \langle v_x, \bar{\psi} \rangle + \frac{1}{16\pi^2} \langle v_y, \psi \rangle \langle v_y, \bar{\psi} \rangle - \frac{i}{16\pi^3} \langle v_y, \psi \rangle \langle v_{xy}, \bar{\psi} \rangle \end{aligned}$$

$$\begin{aligned}
& -\frac{1}{16\pi^2}\langle v_{xy}, \psi \rangle \bar{\psi} + \frac{i}{16\pi^3}\langle v_{xy}, \psi \rangle \langle v_x, \bar{\psi} \rangle + \frac{i}{16\pi^3}\langle v_{xy}, \psi \rangle \langle v_y, \bar{\psi} \rangle + \frac{1}{16\pi^4}\langle v_{xy}, \psi \rangle \langle v_{xy}, \bar{\psi} \rangle \\
& -\frac{1}{16}\psi \bar{\psi} - \frac{i}{16\pi}\psi \langle v_x, \bar{\psi} \rangle - \frac{i}{16\pi}\psi \langle v_y, \bar{\psi} \rangle + \frac{1}{16\pi^2}\psi \langle v_{xy}, \bar{\psi} \rangle \\
& + \frac{i}{16\pi}\langle v_x, \psi \rangle \bar{\psi} - \frac{1}{16\pi^2}\langle v_x, \psi \rangle \langle v_x, \bar{\psi} \rangle - \frac{1}{16\pi^2}\langle v_x, \psi \rangle \langle v_y, \bar{\psi} \rangle - \frac{i}{16\pi^3}\langle v_x, \psi \rangle \langle v_{xy}, \bar{\psi} \rangle \\
& + \frac{i}{16\pi}\langle v_y, \psi \rangle \bar{\psi} - \frac{1}{16\pi^2}\langle v_y, \psi \rangle \langle v_x, \bar{\psi} \rangle - \frac{1}{16\pi^2}\langle v_y, \psi \rangle \langle v_y, \bar{\psi} \rangle - \frac{i}{16\pi^3}\langle v_y, \psi \rangle \langle v_{xy}, \bar{\psi} \rangle \\
& + \frac{1}{16\pi^2}\langle v_{xy}, \psi \rangle \bar{\psi} + \frac{i}{16\pi^3}\langle v_{xy}, \psi \rangle \langle v_x, \bar{\psi} \rangle + \frac{i}{16\pi^3}\langle v_{xy}, \psi \rangle \langle v_y, \bar{\psi} \rangle - \frac{1}{16\pi^4}\langle v_{xy}, \psi \rangle \langle v_{xy}, \bar{\psi} \rangle \\
& -\frac{1}{16}\psi \bar{\psi} - \frac{i}{16\pi}\psi \langle v_x, \bar{\psi} \rangle + \frac{i}{16\pi}\psi \langle v_y, \bar{\psi} \rangle - \frac{1}{16\pi^2}\psi \langle v_{xy}, \bar{\psi} \rangle \\
& + \frac{i}{16\pi}\langle v_x, \psi \rangle \bar{\psi} - \frac{1}{16\pi^2}\langle v_x, \psi \rangle \langle v_x, \bar{\psi} \rangle + \frac{1}{16\pi^2}\langle v_x, \psi \rangle \langle v_y, \bar{\psi} \rangle + \frac{i}{16\pi^3}\langle v_x, \psi \rangle \langle v_{xy}, \bar{\psi} \rangle \\
& -\frac{i}{16\pi}\langle v_y, \psi \rangle \bar{\psi} + \frac{1}{16\pi^2}\langle v_y, \psi \rangle \langle v_x, \bar{\psi} \rangle - \frac{1}{16\pi^2}\langle v_y, \psi \rangle \langle v_y, \bar{\psi} \rangle - \frac{i}{16\pi^3}\langle v_y, \psi \rangle \langle v_{xy}, \bar{\psi} \rangle \\
& -\frac{1}{16\pi^2}\langle v_{xy}, \psi \rangle \bar{\psi} - \frac{i}{16\pi^3}\langle v_{xy}, \psi \rangle \langle v_x, \bar{\psi} \rangle + \frac{i}{16\pi^3}\langle v_{xy}, \psi \rangle \langle v_y, \bar{\psi} \rangle - \frac{1}{16\pi^4}\langle v_{xy}, \psi \rangle \langle v_{xy}, \bar{\psi} \rangle,
\end{aligned}$$

which simplifies to

$$\begin{aligned}
I_0 \cdot s_x^n(x, y) &= -\frac{i}{4\pi}\psi \langle v_x, \bar{\psi} \rangle + \frac{i}{4\pi}\langle v_x, \psi \rangle \bar{\psi} - \frac{i}{4\pi^3}\langle v_y, \psi \rangle \langle v_{xy}, \bar{\psi} \rangle + \frac{i}{4\pi^3}\langle v_{xy}, \psi \rangle \langle v_y, \bar{\psi} \rangle \\
&= -\frac{i}{4\pi}[\psi \langle v_x, \bar{\psi} \rangle - \langle v_x, \psi \rangle \bar{\psi}] - \frac{i}{4\pi^3}[\langle v_y, \psi \rangle \langle v_{xy}, \bar{\psi} \rangle - \langle v_{xy}, \psi \rangle \langle v_y, \bar{\psi} \rangle] \\
&= -\frac{i}{4\pi}[\psi(x, y) \langle v_x(x - \cdot), \bar{\psi}(\cdot, y) \rangle - \langle v_x(x - \cdot), \psi(\cdot, y) \rangle \bar{\psi}(x, y)] \\
&\quad - \frac{i}{4\pi^3}[\langle v_y(y - \cdot), \psi(x, \cdot) \rangle \langle v_{xy}(x - \cdot, y - \cdot), \bar{\psi} \rangle \\
&\quad - \langle v_{xy}(x - \cdot, y - \cdot), \psi \rangle \langle v_y(y - \cdot), \bar{\psi}(x, \cdot) \rangle].
\end{aligned}$$

This can further be formulated as

$$\begin{aligned}
I_0 \cdot s_x^n(x, y) &= -\frac{i}{4\pi} \cdot \left[ \mathcal{X}_\Omega(x, y) \cdot \exp(-i\Phi(x, y)) \text{ p.v.} \int_{\mathbb{R}} \mathcal{X}_\Omega(x', y) \cdot \exp(i\Phi(x', y)) \frac{1}{x-x'} dx' \right. \\
&\quad \left. - \mathcal{X}_\Omega(x, y) \cdot \exp(i\Phi(x, y)) \text{ p.v.} \int_{\mathbb{R}} \mathcal{X}_\Omega(x', y) \cdot \exp(-i\Phi(x', y)) \frac{1}{x-x'} dx' \right] \\
&\quad - \frac{i}{4\pi^3} \left[ \text{p.v.} \int_{\mathbb{R}} \mathcal{X}_\Omega(x, y'') \cdot \exp(-i\Phi(x, y'')) \frac{1}{y-y''} dy'' \right. \\
&\quad \cdot \text{p.v.} \int_{\mathbb{R}} \text{p.v.} \int_{\mathbb{R}} \mathcal{X}_\Omega(x', y') \cdot \exp(i\Phi(x', y')) \frac{1}{(x-x')(y-y')} dy' dx' \\
&\quad \left. - \text{p.v.} \int_{\mathbb{R}} \mathcal{X}_\Omega(x, y'') \cdot \exp(i\Phi(x, y'')) \frac{1}{y-y''} dy'' \right. \\
&\quad \left. \cdot \text{p.v.} \int_{\mathbb{R}} \text{p.v.} \int_{\mathbb{R}} \mathcal{X}_\Omega(x', y') \cdot \exp(-i\Phi(x', y')) \frac{1}{(x-x')(y-y')} dy' dx' \right]
\end{aligned}$$

$$\begin{aligned}
&= -\frac{i}{4\pi} \left[ \mathcal{X}_\Omega(x, y) \cdot \exp(-i\Phi(x, y)) \text{ p.v.} \int_{\Omega_y} \exp(i\Phi(x', y)) \frac{1}{x-x'} dx' \right. \\
&\quad \left. - \mathcal{X}_\Omega(x, y) \cdot \exp(i\Phi(x, y)) \text{ p.v.} \int_{\Omega_y} \exp(-i\Phi(x', y)) \frac{1}{x-x'} dx' \right] \\
&\quad - \frac{i}{4\pi^3} \left[ \mathcal{X}_{\Omega_y}(x) \text{ p.v.} \int_{\Omega_x} \exp(-i\Phi(x, y'')) \frac{1}{y-y''} dy'' \right. \\
&\quad \cdot \text{ p.v.} \int_{\Omega_y} \text{ p.v.} \int_{\Omega_x} \exp(i\Phi(x', y')) \frac{1}{(x-x')(y-y')} dy' dx' \\
&\quad - \mathcal{X}_{\Omega_y}(x) \text{ p.v.} \int_{\Omega_x} \exp(i\Phi(x, y'')) \frac{1}{y-y''} dy'' \\
&\quad \left. \cdot \text{ p.v.} \int_{\Omega_y} \text{ p.v.} \int_{\Omega_x} \exp(-i\Phi(x', y')) \frac{1}{(x-x')(y-y')} dy' dx' \right].
\end{aligned}$$

With Euler's and trigonometric formulas we obtain

$$\begin{aligned}
I_0 \cdot s_x^n(x, y) &= -\frac{i}{4\pi} \mathcal{X}_\Omega(x, y) \left[ 2i \text{ p.v.} \int_{\Omega_y} \frac{\sin[\Phi(x', y) - \Phi(x, y)]}{x-x'} dx' \right] \\
&\quad - \frac{i}{4\pi^3} \mathcal{X}_{\Omega_y}(x) \left[ 2i \text{ p.v.} \int_{\Omega_x} \text{ p.v.} \int_{\Omega_y} \text{ p.v.} \int_{\Omega_x} \frac{\sin[\Phi(x', y') - \Phi(x, y'')]}{(x-x')(y-y')(y-y'')} dy' dx' dy'' \right] \\
&= \mathcal{X}_\Omega(x, y) \frac{1}{2\pi} \text{ p.v.} \int_{\Omega_y} \frac{\sin[\Phi(x', y) - \Phi(x, y)]}{x-x'} dx' \\
&\quad + \mathcal{X}_{\Omega_y}(x) \frac{1}{2\pi^3} \text{ p.v.} \int_{\Omega_y} \text{ p.v.} \int_{\Omega_x} \text{ p.v.} \int_{\Omega_x} \frac{\sin[\Phi(x', y') - \Phi(x, y'')]}{(x-x')(y-y')(y-y'')} dy'' dy' dx'.
\end{aligned}$$

Taking the sums according to (3.1), the non-modulated pyramid sensor data  $s_y^n$  in  $y$ -direction are written as

$$\begin{aligned}
I_0 \cdot s_y^n(x, y) &= [I^{01}(x, y) + I^{11}(x, y)] - [I^{00}(x, y) + I^{10}(x, y)] \\
&= \frac{1}{16} \psi \bar{\psi} - \frac{i}{16\pi} \psi \langle v_x, \bar{\psi} \rangle + \frac{i}{16\pi} \psi \langle v_y, \bar{\psi} \rangle + \frac{1}{16\pi^2} \psi \langle v_{xy}, \bar{\psi} \rangle \\
&\quad + \frac{i}{16\pi} \langle v_x, \psi \rangle \bar{\psi} + \frac{1}{16\pi^2} \langle v_x, \psi \rangle \langle v_x, \bar{\psi} \rangle - \frac{1}{16\pi^2} \langle v_x, \psi \rangle \langle v_y, \bar{\psi} \rangle + \frac{i}{16\pi^3} \langle v_x, \psi \rangle \langle v_{xy}, \bar{\psi} \rangle \\
&\quad - \frac{i}{16\pi} \langle v_y, \psi \rangle \bar{\psi} - \frac{1}{16\pi^2} \langle v_y, \psi \rangle \langle v_x, \bar{\psi} \rangle + \frac{1}{16\pi^2} \langle v_y, \psi \rangle \langle v_y, \bar{\psi} \rangle - \frac{i}{16\pi^3} \langle v_y, \psi \rangle \langle v_{xy}, \bar{\psi} \rangle \\
&\quad + \frac{1}{16\pi^2} \langle v_{xy}, \psi \rangle \bar{\psi} - \frac{i}{16\pi^3} \langle v_{xy}, \psi \rangle \langle v_x, \bar{\psi} \rangle + \frac{i}{16\pi^3} \langle v_{xy}, \psi \rangle \langle v_y, \bar{\psi} \rangle + \frac{1}{16\pi^4} \langle v_{xy}, \psi \rangle \langle v_{xy}, \bar{\psi} \rangle \\
&\quad + \frac{1}{16} \psi \bar{\psi} + \frac{i}{16\pi} \psi \langle v_x, \bar{\psi} \rangle + \frac{i}{16\pi} \psi \langle v_y, \bar{\psi} \rangle - \frac{1}{16\pi^2} \psi \langle v_{xy}, \bar{\psi} \rangle \\
&\quad - \frac{i}{16\pi} \langle v_x, \psi \rangle \bar{\psi} + \frac{1}{16\pi^2} \langle v_x, \psi \rangle \langle v_x, \bar{\psi} \rangle + \frac{1}{16\pi^2} \langle v_x, \psi \rangle \langle v_y, \bar{\psi} \rangle + \frac{i}{16\pi^3} \langle v_x, \psi \rangle \langle v_{xy}, \bar{\psi} \rangle
\end{aligned}$$

$$\begin{aligned}
& -\frac{i}{16\pi}\langle v_y, \psi \rangle \bar{\psi} + \frac{1}{16\pi^2}\langle v_y, \psi \rangle \langle v_x, \bar{\psi} \rangle + \frac{1}{16\pi^2}\langle v_y, \psi \rangle \langle v_y, \bar{\psi} \rangle + \frac{i}{16\pi^3}\langle v_y, \psi \rangle \langle v_{xy}, \bar{\psi} \rangle \\
& -\frac{1}{16\pi^2}\langle v_{xy}, \psi \rangle \bar{\psi} - \frac{i}{16\pi^3}\langle v_{xy}, \psi \rangle \langle v_x, \bar{\psi} \rangle - \frac{i}{16\pi^3}\langle v_{xy}, \psi \rangle \langle v_y, \bar{\psi} \rangle + \frac{1}{16\pi^4}\langle v_{xy}, \psi \rangle \langle v_{xy}, \bar{\psi} \rangle \\
& -\frac{1}{16}\psi \bar{\psi} + \frac{i}{16\pi}\psi \langle v_x, \bar{\psi} \rangle + \frac{i}{16\pi}\psi \langle v_y, \bar{\psi} \rangle + \frac{1}{16\pi^2}\psi \langle v_{xy}, \bar{\psi} \rangle \\
& -\frac{i}{16\pi}\langle v_x, \psi \rangle \bar{\psi} - \frac{1}{16\pi^2}\langle v_x, \psi \rangle \langle v_x, \bar{\psi} \rangle - \frac{1}{16\pi^2}\langle v_x, \psi \rangle \langle v_y, \bar{\psi} \rangle + \frac{i}{16\pi^3}\langle v_x, \psi \rangle \langle v_{xy}, \bar{\psi} \rangle \\
& -\frac{i}{16\pi}\langle v_y, \psi \rangle \bar{\psi} - \frac{1}{16\pi^2}\langle v_y, \psi \rangle \langle v_x, \bar{\psi} \rangle - \frac{1}{16\pi^2}\langle v_y, \psi \rangle \langle v_y, \bar{\psi} \rangle + \frac{i}{16\pi^3}\langle v_y, \psi \rangle \langle v_{xy}, \bar{\psi} \rangle \\
& + \frac{1}{16\pi^2}\langle v_{xy}, \psi \rangle \bar{\psi} - \frac{i}{16\pi^3}\langle v_{xy}, \psi \rangle \langle v_x, \bar{\psi} \rangle - \frac{i}{16\pi^3}\langle v_{xy}, \psi \rangle \langle v_y, \bar{\psi} \rangle - \frac{1}{16\pi^4}\langle v_{xy}, \psi \rangle \langle v_{xy}, \bar{\psi} \rangle \\
& -\frac{1}{16}\psi \bar{\psi} - \frac{i}{16\pi}\psi \langle v_x, \bar{\psi} \rangle + \frac{i}{16\pi}\psi \langle v_y, \bar{\psi} \rangle - \frac{1}{16\pi^2}\psi \langle v_{xy}, \bar{\psi} \rangle \\
& + \frac{i}{16\pi}\langle v_x, \psi \rangle \bar{\psi} - \frac{1}{16\pi^2}\langle v_x, \psi \rangle \langle v_x, \bar{\psi} \rangle + \frac{1}{16\pi^2}\langle v_x, \psi \rangle \langle v_y, \bar{\psi} \rangle + \frac{i}{16\pi^3}\langle v_x, \psi \rangle \langle v_{xy}, \bar{\psi} \rangle \\
& -\frac{i}{16\pi}\langle v_y, \psi \rangle \bar{\psi} + \frac{1}{16\pi^2}\langle v_y, \psi \rangle \langle v_x, \bar{\psi} \rangle - \frac{1}{16\pi^2}\langle v_y, \psi \rangle \langle v_y, \bar{\psi} \rangle - \frac{i}{16\pi^3}\langle v_y, \psi \rangle \langle v_{xy}, \bar{\psi} \rangle \\
& -\frac{1}{16\pi^2}\langle v_{xy}, \psi \rangle \bar{\psi} - \frac{i}{16\pi^3}\langle v_{xy}, \psi \rangle \langle v_x, \bar{\psi} \rangle + \frac{i}{16\pi^3}\langle v_{xy}, \psi \rangle \langle v_y, \bar{\psi} \rangle - \frac{1}{16\pi^4}\langle v_{xy}, \psi \rangle \langle v_{xy}, \bar{\psi} \rangle,
\end{aligned}$$

which is equivalent to

$$\begin{aligned}
I_0 \cdot s_y^n(x, y) &= \frac{i}{4\pi}\psi \langle v_y, \bar{\psi} \rangle + \frac{i}{4\pi^3}\langle v_x, \psi \rangle \langle v_{xy}, \bar{\psi} \rangle - \frac{i}{4\pi}\langle v_y, \psi \rangle \bar{\psi} - \frac{i}{4\pi^3}\langle v_{xy}, \psi \rangle \langle v_x, \bar{\psi} \rangle \\
&= \frac{i}{4\pi} [\psi \langle v_y, \bar{\psi} \rangle - \langle v_y, \psi \rangle \bar{\psi}] + \frac{i}{4\pi^3} [\langle v_x, \psi \rangle \langle v_{xy}, \bar{\psi} \rangle - \langle v_{xy}, \psi \rangle \langle v_x, \bar{\psi} \rangle] \\
&= \frac{i}{4\pi} \left[ \psi(x, y) \langle v_y(y - \cdot), \bar{\psi}(x, \cdot) \rangle - \langle v_y(y - \cdot), \psi(x, \cdot) \rangle \bar{\psi}(x, y) \right] \\
&\quad + \frac{i}{4\pi^3} \left[ \langle v_x(x - \cdot), \psi(\cdot, y) \rangle \langle v_{xy}(x - \cdot, y - \cdot), \bar{\psi} \rangle \right. \\
&\quad \left. - \langle v_{xy}(x - \cdot, y - \cdot), \psi \rangle \langle v_x(x - \cdot), \bar{\psi}(\cdot, y) \rangle \right]
\end{aligned}$$

and results in

$$\begin{aligned}
I_0 \cdot s_y^n(x, y) &= \frac{i}{4\pi} \left[ \mathcal{X}_\Omega(x, y) \cdot \exp(-i\Phi(x, y)) \text{ p.v.} \int_{\mathbb{R}} \mathcal{X}_\Omega(x, y') \cdot \exp(i\Phi(x, y')) \frac{1}{y - y'} dy' \right. \\
&\quad \left. - \mathcal{X}_\Omega(x, y) \cdot \exp(i\Phi(x, y)) \text{ p.v.} \int_{\mathbb{R}} \mathcal{X}_\Omega(x, y') \cdot \exp(-i\Phi(x, y')) \frac{1}{y - y'} dy' \right] \\
&\quad + \frac{i}{4\pi^3} \left[ \text{p.v.} \int_{\mathbb{R}} \mathcal{X}_\Omega(x'', y) \cdot \exp(-i\Phi(x'', y)) \frac{1}{x - x''} dx'' \right. \\
&\quad \cdot \text{p.v.} \int_{\mathbb{R}} \text{p.v.} \int_{\mathbb{R}} \mathcal{X}_\Omega(x', y') \cdot \exp(i\Phi(x', y')) \frac{1}{(x - x')(y - y')} dy' dx' \\
&\quad \left. - \text{p.v.} \int_{\mathbb{R}} \mathcal{X}_\Omega(x'', y) \cdot \exp(i\Phi(x'', y)) \frac{1}{x - x''} dx'' \right. \\
&\quad \left. \cdot \text{p.v.} \int_{\mathbb{R}} \text{p.v.} \int_{\mathbb{R}} \mathcal{X}_\Omega(x', y') \cdot \exp(-i\Phi(x', y')) \frac{1}{(x - x')(y - y')} dy' dx' \right]
\end{aligned}$$

$$\begin{aligned}
&= \frac{i}{4\pi} \left[ \mathcal{X}_\Omega(x, y) \cdot \exp(-i\Phi(x, y)) \text{ p.v.} \int_{\Omega_x} \exp(i\Phi(x, y')) \frac{1}{y - y'} dy' \right. \\
&\quad \left. - \mathcal{X}_\Omega(x, y) \cdot \exp(i\Phi(x, y)) \text{ p.v.} \int_{\Omega_x} \exp(-i\Phi(x, y')) \frac{1}{y - y'} dy' \right] \\
&\quad + \frac{i}{4\pi^3} \left[ \mathcal{X}_{\Omega_x}(y) \text{ p.v.} \int_{\Omega_y} \exp(-i\Phi(x'', y)) \frac{1}{x - x''} dx'' \right. \\
&\quad \cdot \text{ p.v.} \int_{\Omega_y} \text{ p.v.} \int_{\Omega_x} \exp(i\Phi(x', y')) \frac{1}{(x - x')(y - y')} dy' dx' \\
&\quad - \mathcal{X}_{\Omega_x}(y) \text{ p.v.} \int_{\Omega_y} \exp(i\Phi(x'', y)) \frac{1}{x - x''} dx'' \\
&\quad \left. \cdot \text{ p.v.} \int_{\Omega_y} \text{ p.v.} \int_{\Omega_x} \exp(-i\Phi(x', y')) \frac{1}{(x - x')(y - y')} dy' dx' \right].
\end{aligned}$$

Using Euler's and trigonometric formulas we get

$$\begin{aligned}
I_0 \cdot s_y^n(x, y) &= \frac{i}{4\pi} \mathcal{X}_\Omega(x, y) \left[ 2i \text{ p.v.} \int_{\Omega_x} \frac{\sin[\Phi(x, y') - \Phi(x, y)]}{y - y'} dy' \right] \\
&\quad + \frac{i}{4\pi^3} \mathcal{X}_{\Omega_x}(y) \left[ 2i \text{ p.v.} \int_{\Omega_y} \text{ p.v.} \int_{\Omega_y} \text{ p.v.} \int_{\Omega_x} \frac{\sin[\Phi(x', y') - \Phi(x'', y)]}{(x - x')(y - y')(x - x'')} dy' dx' dx'' \right] \\
&= -\mathcal{X}_\Omega(x, y) \frac{1}{2\pi} \text{ p.v.} \int_{\Omega_x} \frac{\sin[\Phi(x, y') - \Phi(x, y)]}{y - y'} dy' \\
&\quad - \mathcal{X}_{\Omega_x}(y) \frac{1}{2\pi^3} \text{ p.v.} \int_{\Omega_y} \text{ p.v.} \int_{\Omega_x} \text{ p.v.} \int_{\Omega_y} \frac{\sin[\Phi(x', y') - \Phi(x'', y)]}{(x - x')(y - y')(x - x'')} dx'' dy' dx'.
\end{aligned}$$

This completes the derivation of the model for the sensor without modulation.

The kernels of the involved integral operators are strongly singular. They are defined in the p.v. (principal value) meaning. Throughout the Thesis,  $p.v. \int \int \int$  is always meant as abbreviation of  $p.v. \int p.v. \int p.v. \int$  in the context of the pyramid sensor operator.

Let us derive the pyramid sensor model with circular modulation. For the modulated sensor, we use the modulation parameter  $\alpha_\lambda$  defined in (3.7).

The theoretical scheme of the non-modulated PWFS described above serves as a basis for the modulated PWFS model. The only modification to be done is to include the physical modulation of the beam into the model:

First, physical rotation of the beam of light with a steering mirror is represented in the theoretical model by adding a time-dependent periodic tilt [28]

$$\Phi^{mod}(x, y, t) = \alpha_\lambda (x \sin(2\pi t/T) + y \cos(2\pi t/T)) \quad (3.14)$$

introducing the circular modulation path to the incoming screen  $\Phi$ .

Clearly, by using the non-modulated model from above, one obtains for each time step  $t$  the non-modulated measurements  $s_x^n(x, y, t), s_y^n(x, y, t)$  corresponding to the tilted phase  $\Phi(x, y) + \Phi^{mod}(x, y, t)$ .

As the second step, one has to integrate these time-dependent non-modulated pyramid measurements  $s_x^n(x, y, t), s_y^n(x, y, t)$  over one full time period  $T$ , which gives the measurements  $[s_x^c, s_y^c]$  of the circularly modulated pyramid wavefront sensor as

$$\begin{aligned} s_x^c(x, y) &= \frac{1}{T} \int_{-T/2}^{T/2} s_x^n(x, y, t) dt, \\ s_y^c(x, y) &= \frac{1}{T} \int_{-T/2}^{T/2} s_y^n(x, y, t) dt. \end{aligned} \tag{3.15}$$

Thus, the modulated sensor measurements are described by

$$\begin{aligned} s_x^c(x, y) &= \frac{1}{T} \int_{-T/2}^{T/2} \frac{1}{2\pi} \mathcal{X}_\Omega(x, y) \\ &\quad p.v. \int_{\Omega_y} \frac{\sin[\Phi(x', y) + \Phi^{mod}(x', y, t) - \Phi(x, y) - \Phi^{mod}(x, y, t)]}{x - x'} dx' dt \\ &\quad + \frac{1}{T} \int_{-T/2}^{T/2} \frac{1}{2\pi^3} \mathcal{X}_{\Omega_y}(x) \\ &\quad p.v. \int_{\Omega_y} \int_{\Omega_x} \int_{\Omega_x} \frac{\sin[\Phi(x', y') + \Phi^{mod}(x', y', t) - \Phi(x, y'') - \Phi^{mod}(x, y'', t)]}{(x - x')(y - y')(y - y'')} dy'' dy' dx' dt. \end{aligned}$$

First, we want to separate the parts which depend on time to be able to integrate them,

$$\begin{aligned} s_x^c(x, y) &= \frac{1}{T} \int_{-T/2}^{T/2} \frac{1}{2\pi} \mathcal{X}_\Omega(x, y) \\ &\quad p.v. \int_{\Omega_y} \frac{\sin[(\Phi(x', y) - \Phi(x, y)) + (\Phi^{mod}(x', y, t) - \Phi^{mod}(x, y, t))]}{x - x'} dx' dt \\ &\quad + \frac{1}{T} \int_{-T/2}^{T/2} \frac{1}{2\pi^3} \mathcal{X}_{\Omega_y}(x) \\ &\quad p.v. \int_{\Omega_y} \int_{\Omega_x} \int_{\Omega_x} \frac{\sin[(\Phi(x', y') - \Phi(x, y'')) + (\Phi^{mod}(x', y', t) - \Phi^{mod}(x, y'', t))]}{(x - x')(y - y')(y - y'')} dy'' dy' dx' dt. \end{aligned}$$

Note that the modulation function  $\Phi^{mod}$  is linear in the first two arguments, i.e.,

$$\begin{aligned}
\Phi^{mod}(x', y, t) - \Phi^{mod}(x, y, t) &= \alpha_\lambda x' \sin(2\pi t/T) + \alpha_\lambda y \cos(2\pi t/T) \\
&\quad - \alpha_\lambda x \sin(2\pi t/T) - \alpha_\lambda y \cos(2\pi t/T) \\
&= \alpha_\lambda (x' - x) \sin(2\pi t/T) \\
&= \Phi^{mod}(x' - x, 0, t), \\
\Phi^{mod}(x', y', t) - \Phi^{mod}(x, y'', t) &= \alpha_\lambda x' \sin(2\pi t/T) + \alpha_\lambda y' \cos(2\pi t/T) \\
&\quad - \alpha_\lambda x \sin(2\pi t/T) - \alpha_\lambda y'' \cos(2\pi t/T) \\
&= \alpha_\lambda (x' - x) \sin(2\pi t/T) + \alpha_\lambda (y' - y'') \cos(2\pi t/T) \\
&= \Phi^{mod}(x' - x, y' - y'', t).
\end{aligned} \tag{3.16}$$

Hence, we have

$$\begin{aligned}
s_x^c(x, y) &= \frac{1}{T} \int_{-T/2}^{T/2} \frac{1}{2\pi} \mathcal{X}_\Omega(x, y) \\
&\quad p.v. \int_{\Omega_y} \frac{\sin[(\Phi(x', y) - \Phi(x, y)) + \Phi^{mod}(x' - x, 0, t)]}{x - x'} dx' dt \\
&\quad + \frac{1}{T} \int_{-T/2}^{T/2} \frac{1}{2\pi^3} \mathcal{X}_{\Omega_y}(x) \\
&\quad p.v. \int \int \int_{\Omega_y \Omega_x \Omega_x} \frac{\sin[(\Phi(x', y') - \Phi(x, y'')) + \Phi^{mod}(x' - x, y' - y'', t)]}{(x - x')(y - y')(y - y'')} dy'' dy' dx' dt.
\end{aligned}$$

Using trigonometric formulas, we separate the time-dependent parts

$$\begin{aligned}
s_x^c(x, y) &= \mathcal{X}_\Omega(x, y) \left[ \frac{1}{2\pi} p.v. \int_{\Omega_y} \frac{\sin[\Phi(x', y) - \Phi(x, y)]}{x - x'} \left( \frac{1}{T} \int_{-T/2}^{T/2} \cos[\Phi^{mod}(x' - x, 0, t)] dt \right) dx' \right. \\
&\quad \left. + \frac{1}{2\pi} p.v. \int_{\Omega_y} \frac{\cos[\Phi(x', y) - \Phi(x, y)]}{x - x'} \left( \frac{1}{T} \int_{-T/2}^{T/2} \sin[\Phi^{mod}(x' - x, 0, t)] dt \right) dx' \right] \\
&\quad + \mathcal{X}_{\Omega_y}(x) \frac{1}{2\pi^3} p.v. \int \int \int_{\Omega_y \Omega_x \Omega_x} \left[ \frac{\sin[\Phi(x', y') - \Phi(x, y'')]}{(x - x')(y - y')(y - y'')} \right. \\
&\quad \cdot \left. \left( \frac{1}{T} \int_{-T/2}^{T/2} \cos[\Phi^{mod}(x' - x, y' - y'', t)] dt \right) \right] dy'' dy' dx' \\
&\quad + \mathcal{X}_{\Omega_y}(x) \frac{1}{2\pi^3} p.v. \int \int \int_{\Omega_y \Omega_x \Omega_x} \left[ \frac{\cos[\Phi(x', y') - \Phi(x, y'')]}{(x - x')(y - y')(y - y'')} \right. \\
&\quad \cdot \left. \left( \frac{1}{T} \int_{-T/2}^{T/2} \sin[\Phi^{mod}(x' - x, y' - y'', t)] dt \right) \right] dy'' dy' dx'.
\end{aligned}$$

The second and the fourth terms equal zero, since the integrands are odd functions. After substitution of the explicit expressions (3.16) for  $\Phi^{mod}$ , the remaining time integrals simplify to

$$\begin{aligned}
& \frac{1}{T} \int_{-T/2}^{T/2} \cos [\Phi^{mod}(x' - x, y' - y'', t)] dt \\
&= \frac{1}{T} \int_{-T/2}^{T/2} \cos [\alpha_\lambda(x' - x) \sin(2\pi t/T) + \alpha_\lambda(y' - y'') \cos(2\pi t/T)] dt \\
&= \frac{1}{T} \int_{-T/2}^{T/2} \cos [\alpha_\lambda(x' - x) \sin(2\pi t/T)] \cos [\alpha_\lambda(y' - y'') \cos(2\pi t/T)] dt \\
&\quad - \frac{1}{T} \int_{-T/2}^{T/2} \sin [\alpha_\lambda(x' - x) \sin(2\pi t/T)] \sin [\alpha_\lambda(y' - y'') \cos(2\pi t/T)] dt \\
&= \frac{1}{T} \int_{-T/2}^{T/2} \cos [\alpha_\lambda(x' - x) \sin(2\pi t/T)] \cos [\alpha_\lambda(y' - y'') \cos(2\pi t/T)] dt - 0.
\end{aligned}$$

and

$$\begin{aligned}
\frac{1}{T} \int_{-T/2}^{T/2} \cos [\Phi^{mod}(x' - x, 0, t)] dt &= \frac{1}{T} \int_{-T/2}^{T/2} \cos [\alpha_\lambda(x' - x) \sin(2\pi t/T)] dt \\
&= \frac{1}{2\pi} \int_{-\pi}^{\pi} \cos [\alpha_\lambda(x' - x) \sin(t')] dt' \\
&= J_0[\alpha_\lambda(x' - x)],
\end{aligned}$$

where we used the substitution  $t' = 2\pi t/T$  and the definition of the zero-order Bessel function

$$\begin{aligned}
J_0(x) &= \frac{1}{\pi} \int_0^\pi \cos(x \sin t) dt \\
&= \frac{1}{2\pi} \int_{-\pi}^\pi \cos(x \sin t) dt.
\end{aligned}$$

Altogether, it results in

$$\begin{aligned}
s_x^c(x, y) &= \mathcal{X}_\Omega(x, y) \frac{1}{2\pi} p.v. \int_{\Omega_y} \frac{\sin [\Phi(x', y) - \Phi(x, y)] J_0[\alpha_\lambda(x' - x)]}{x - x'} dx' \\
&\quad + \mathcal{X}_{\Omega_y}(x) \frac{1}{2\pi^3} p.v. \int_{\Omega_y} \int_{\Omega_x} \int_{\Omega_x} \frac{\sin [\Phi(x', y') - \Phi(x, y'')] l^c(x' - x, y' - y'')}{(x - x')(y - y')(y - y'')} dy'' dy' dx'.
\end{aligned}$$

with

$$l^c(x, y) := \frac{1}{T} \int_{-T/2}^{T/2} \cos[\alpha_\lambda x \sin(2\pi t/T)] \cos[\alpha_\lambda y \cos(2\pi t/T)] dt.$$

All steps can be performed for the data  $s_y^{\{c\}}$  analogously.  $\square$

### 3.2.2 Mathematical derivation of phase mask model

Taking interference effects of the four subbeams falling on the detector into account by utilizing the pyramidal phase mask  $\Pi$  instead of the transmission mask  $T^{mn}$  in (3.9) gives the optical transfer function [30, 86, 214]

$$OTF_{pyr}(\xi, \eta) = \exp(-i\Pi(\xi, \eta)).$$

The phase mask is represented by

$$\Pi(\xi, \eta) := \frac{\pi q}{p} (|\xi| + |\eta|),$$

where  $p$  is the so called PSF sampling number and  $q$  the distance between the subbeam centers on the detector given in units of the aperture diameter, i.e., the distance between the four intensity patterns on the detector is related to the factor  $p/q$ .

In contrast to (3.10), we cannot write the PSF as a sum of four independent inverse Fourier transforms of four separated parts of the pyramidal phase mask. This fact makes the phase mask approach more complicated. The derivations result in a long expression of the pyramid signal and it is difficult to use the analytical formula of the full phase mask measurements as foundation for the development of model-based approaches similar to some of the in Chapter 7 summarized ones. Therefore, the pyramid sensor measurements corresponding to the phase mask model are in the following written in a more general sense compared to those associated with the transmission mask representation.

As before, the PSF is the 2d Fourier transform of the OTF

$$PSF_{pyr} = \mathcal{F}_{2d}^{-1}\{OTF_{pyr}\},$$

the complex amplitude falling onto the detector plane is given by

$$\psi_{det}(x, y) = \frac{1}{2\pi} \left\langle PSF_{pyr}((x, y) - (\cdot, \cdot)), \psi_{aper}^\epsilon \right\rangle,$$

and the intensity  $I(x, y)$  on the detector plane is calculated as

$$I(x, y) = \psi_{det}(x, y) \overline{\psi_{det}(x, y)}.$$

according to (3.4), (3.12), and (3.13).

The pyramid measurements are then calculated as in (3.1). In order to obtain the intensity patterns  $I^{00}, I^{01}, I^{10}$  and  $I^{11}$ , we have to cut out the corresponding single quadrants of the coordinate plane  $I$ .

Most simulation environments having the pyramid sensor incorporated use the phase mask forward model such as Octopus [129, 130] or OOMAO [44].

### 3.3 Pyramid and roof wavefront sensor forward operators (transmission mask model)

Based on the mathematical derivations in Section 3.2.1, we analyze the operators describing the pyramid and roof wavefront sensor models. In the following Chapter,  $\mathbf{P}^{\{n,c\}} = [\mathbf{P}_x^{\{n,c\}}, \mathbf{P}_y^{\{n,c\}}]$  denote the operators representing the pyramid sensor,  $\mathbf{R}^{\{n,c,l\}} = [\mathbf{R}_x^{\{n,c,l\}}, \mathbf{R}_y^{\{n,c,l\}}]$  the operators representing the roof wavefront sensor, and  $\mathbf{R}^{\{n,c,l\},lin} = [\mathbf{R}_x^{\{n,c,l\},lin}, \mathbf{R}_y^{\{n,c,l\},lin}]$  indicate the linearized roof sensor operators. The superscripts  $\{n, c, l\}$  represent the regime in which the sensor is operated – no modulation, circular or linear modulation applied.

Let us first consider the mathematical model of the roof wavefront sensor in more detail.

The roof WFS (shown in Figure 2.9 right) constitutes a part of the pyramid WFS. In the roof sensor, the pyramidal prism is replaced by two orthogonally placed two-sided roof prisms, resulting in a decoupling of  $x$ - and  $y$ -direction. Therefore, the roof WFS operators  $\mathbf{R}^{\{n,c\}}$  are much simpler, as it contains only (variations of) 1d Hilbert transforms in one particular direction [125, 192, 212].

Due to the physical setup of the roof WFS, linear modulation induces characteristics which are of interest especially for roof wavefront sensors. Hence, we additionally investigate the linear modulated roof wavefront sensor model. In case of circular modulation the amplitude of modulation is assumed to be  $\alpha_\lambda$ , already introduced in (3.7). For linear modulation,  $2\alpha$  denotes the angle of ray displacement along the desired direction, which is equivalent to the assumed circular modulation. We substitute the zero-order Bessel function by a sinc-term in order to describe a linear modulation instead of a circular one.

For further investigations, we again do not take interference between the four beams into account and consider the roof WFS operator  $\mathbf{R}^{\{n,c,l\}}$  on the one hand as a standalone wavefront sensor and on the other hand as an approximation to the pyramid WFS, i.e.,  $\mathbf{P}^{\{n,c\}} \approx \mathbf{R}^{\{n,c\}}$ .

**Definition 3.4.** We introduce the operators  $\mathbf{R}_x^{\{n,c,l\}}$  and  $\mathbf{R}_y^{\{n,c,l\}}$  by

$$\left(\mathbf{R}_x^{\{n,c,l\}}\Phi\right)(x,y) := \mathcal{X}_\Omega(x,y) \frac{1}{\pi} \text{p.v.} \int_{\Omega_y} \frac{\sin[\Phi(x',y) - \Phi(x,y)] \cdot k^{\{n,c,l\}}(x'-x)}{x'-x} dx', \quad (3.17)$$

$$\left(\mathbf{R}_y^{\{n,c,l\}}\Phi\right)(x,y) := \mathcal{X}_\Omega(x,y) \frac{1}{\pi} \text{p.v.} \int_{\Omega_x} \frac{\sin[\Phi(x,y') - \Phi(x,y)] \cdot k^{\{n,c,l\}}(y'-y)}{y'-y} dy', \quad (3.18)$$

where the functions  $k^{\{n,c,l\}}$  of modulation are given by  $k^n(x) := 1$ ,  $k^c(x) := J_0(\alpha_\lambda x)$ , and  $k^l(x) := \text{sinc}(\alpha_\lambda x)$ .

**Theorem 3.5.** Using the operators defined in (3.17)-(3.18) the measurements of the roof WFS in the transmission mask model are written as

$$s_x^{\{n,c,l\}}(x,y) = -\frac{1}{2} \left(\mathbf{R}_x^{\{n,c,l\}}\Phi\right)(x,y),$$

$$s_y^{\{n,c,l\}}(x,y) = \frac{1}{2} \left(\mathbf{R}_y^{\{n,c,l\}}\Phi\right)(x,y).$$

*Proof.* See [28, 191, 212]. □

The operators  $\mathbf{P}_x^{\{n,c\}}$  and  $\mathbf{P}_y^{\{n,c\}}$  as well as  $\mathbf{R}_x^{\{n,c,l\}}$  and  $\mathbf{R}_y^{\{n,c,l\}}$  are constructed in the same way, one only has to interchange the roles of  $x$  and  $y$  in the model. In the following, we will concentrate on the operators  $\mathbf{P}_x^{\{n,c\}}$  and  $\mathbf{R}_x^{\{n,c,l\}}$  since the obtained results can easily be transferred to the operators  $\mathbf{P}_y^{\{n,c\}}$  and  $\mathbf{R}_y^{\{n,c,l\}}$  as well. Let us now analyze the pyramid and roof sensor operators in more detail.

**Proposition 3.6.** The non-linear operators  $\mathbf{R}^{\{n,c,l\}} : \mathcal{H}^{11/6}(\mathbb{R}^2) \rightarrow \mathcal{L}_2(\mathbb{R}^2)$ , representing roof wavefront sensors, are well-defined operators between the above given spaces.

*Proof.* From the proof of Theorem 3.3 it follows that the pyramid and further the roof operators are well-defined for any wavefront  $\Phi \in \mathcal{H}^{11/6}(\mathbb{R}^2)$ . It remains to show  $(\mathbf{R}^{\{n,c,l\}}\Phi) \in \mathcal{L}_2(\mathbb{R}^2)$ . The proof uses the boundedness<sup>(1)</sup>  $|\sin(\Phi)| \leq |\Phi|$  and the Hölder continuity<sup>(2)</sup> with  $\alpha = 5/6$  and Hölder constant  $C > 0$  in one direction of any function  $\Phi \in \mathcal{H}^{11/6}(\mathbb{R}^2)$  (cf Sobolev embedding theorem, e.g., [1, Theorem 5.4]). We start with showing that for  $\mathcal{D}(\mathbf{R}^{\{n,c,l\}}) \subseteq \mathcal{H}^{11/6}(\mathbb{R}^2)$  the integrand of (3.17) in fact is integrable. Together with  $|k^{\{n,c,l\}}| \leq 1$ , this infers from

$$\begin{aligned} \int_{\Omega_y} \left| \frac{\sin[\Phi(x',y) - \Phi(x,y)] \cdot k^{\{n,c,l\}}(x'-x)}{x'-x} \right| dx' &\stackrel{(1)}{\leq} \int_{\Omega_y} \frac{|\Phi(x',y) - \Phi(x,y)|}{|x'-x|} dx' \\ &\stackrel{(2)}{\leq} C \int_{\Omega_y} \frac{|x'-x|^{5/6}}{|x'-x|} dx' = C \int_{\Omega_y} \frac{1}{|x'-x|^{1/6}} dx' \\ &= \frac{6C}{5} \left( (b_y - x)^{5/6} + (x + a_y)^{5/6} \right) < \infty \end{aligned}$$

for  $x \in \Omega_y$ ,  $\Omega_y = [a_y, b_y] \subseteq [-D/2, D/2]$ . As the proper integral exists, the Cauchy principal value exists as well. For  $\mathcal{D}(\mathbf{R}^{\{n,c,l\}}) \subseteq \mathcal{H}^{11/6}(\mathbb{R}^2)$ , it follows that the *p.v.* meaning is negligible in (3.17)-(3.18). By usage of the Cauchy-Schwarz inequality<sup>(3)</sup>, we obtain that the  $\mathcal{L}_2$ -norm

$$\begin{aligned}
\left\| \mathbf{R}_x^{\{n,c,l\}} \Phi \right\|_{\mathcal{L}_2(\mathbb{R}^2)}^2 &= \int_{\mathbb{R}^2} \left| \mathbf{R}_x^{\{n,c,l\}} \Phi(x, y) \right|^2 d(x, y) \\
&= \int_{\mathbb{R}^2} \left| \mathcal{X}_\Omega(x, y) \frac{1}{\pi} \int_{\Omega_y} \frac{\sin[\Phi(x', y) - \Phi(x, y)] \cdot k^{\{n,c,l\}}(x' - x)}{x' - x} dx' \right|^2 d(x, y) \\
&\stackrel{(3)}{\leq} \frac{1}{\pi^2} \int_{\Omega} \left( \int_{\Omega_y} \left| \frac{\sin[\Phi(x', y) - \Phi(x, y)] \cdot k^{\{n,c,l\}}(x' - x)}{x' - x} \right|^2 dx' \cdot \int_{\Omega_y} 1 dx' \right) d(x, y) \\
&\leq \frac{|\Omega_y|}{\pi^2} \int_{\Omega} \int_{\Omega_y} \left( \frac{|\sin[\Phi(x', y) - \Phi(x, y)]|}{|x' - x|} \right)^2 dx' d(x, y) \\
&\stackrel{(1)}{\leq} \frac{|\Omega_y|}{\pi^2} \int_{\Omega} \int_{\Omega_y} \left( \frac{|\Phi(x', y) - \Phi(x, y)|}{|x' - x|} \right)^2 dx' d(x, y) \\
&\stackrel{(2)}{\leq} \frac{C^2 |\Omega_y|}{\pi^2} \int_{\Omega} \int_{\Omega_y} \left( \frac{|x' - x|^{5/6}}{|x' - x|} \right)^2 dx' d(x, y) \\
&= \frac{C^2 |\Omega_y|}{\pi^2} \int_{\Omega} \int_{\Omega_y} \frac{1}{|x' - x|^{1/3}} dx' d(x, y) \\
&\leq \sup_{x \in \Omega_y} |M(x)| \frac{C^2 |\Omega| |\Omega_y|}{\pi^2} < \infty
\end{aligned}$$

is finite as for  $\Omega_y \subseteq [-D/2, D/2]$  holds

$$\begin{aligned}
M(x, y) &:= \int_{\Omega_y} \frac{1}{|x' - x|^{1/3}} dx' \leq \int_{-D/2}^{D/2} \frac{1}{|x' - x|^{1/3}} dx' \\
&= \frac{3}{2} \left[ \left( \frac{D}{2} - x \right)^{2/3} + \left( x + \frac{D}{2} \right)^{2/3} \right] =: M(x)
\end{aligned} \tag{3.19}$$

and further

$$\sup_{x \in \Omega_y} |M(x)| < \infty. \tag{3.20}$$

□

From the considerations in the above proof it follows the following statement:

**Remark 3.7.** *If  $\Phi \in \mathcal{H}^{11/6}(\mathbb{R}^2)$ , the principal value integrals of the operators (3.17)-(3.18) describing the roof wavefront sensor model coincide with the standard definition of Lebesgue integrals.*

**Proposition 3.8.** *The non-linear operators  $\mathbf{P}^{\{n,c\}} : \mathcal{H}^{11/6}(\mathbb{R}^2) \rightarrow \mathcal{L}_2(\mathbb{R}^2)$ , representing pyramid wavefront sensors, are well-defined operators between the above given spaces.*

*Proof.* As already shown in the proof of Theorem 3.3, the pyramid sensor operators are non-linear, well-defined operators for any wavefront  $\Phi \in \mathcal{H}^{11/6}(\mathbb{R}^2)$ .

In order to verify that  $(\mathbf{P}^{\{n,c\}}\Phi) \in \mathcal{L}_2$  we split the corresponding operators into two parts:

$$(\mathbf{P}_x^{\{n,c\}}\Phi)(x, y) = (\mathbf{R}_x^{\{n,c\}}\Phi)(x, y) + (\mathbf{S}_x^{\{n,c\}}\Phi)(x, y)$$

with the roof sensor operators  $\mathbf{R}_x^{\{n,c\}}$  defined in (3.17) and the second term

$$(\mathbf{S}_x^{\{n,c\}}\Phi)(x, y) := \frac{1}{\pi^3} \mathcal{X}_{\Omega_y}(x) \text{ p.v.} \int_{\Omega_y} \int_{\Omega_x} \int_{\Omega_x} \frac{\sin[\Phi(x', y') - \Phi(x, y'')] \cdot l^{\{n,c\}}(x' - x, y'' - y')}{(x' - x)(y' - y)(y'' - y)} dy'' dy' dx'.$$

With Proposition 3.6 and

$$\left\| \mathbf{P}_x^{\{n,c\}}\Phi \right\|_{\mathcal{L}_2(\mathbb{R}^2)} \leq \left\| \mathbf{R}_x^{\{n,c\}}\Phi \right\|_{\mathcal{L}_2(\mathbb{R}^2)} + \left\| \mathbf{S}_x^{\{n,c\}}\Phi \right\|_{\mathcal{L}_2(\mathbb{R}^2)},$$

it remains to show  $\left\| \mathbf{S}_x^{\{n,c\}}\Phi \right\|_{\mathcal{L}_2(\mathbb{R}^2)} < \infty$ .

First, we focus on the non-modulated sensor and consider the operator  $\mathbf{S}_x^n$ .

The proof uses the  $\mathcal{L}_p$ -boundedness of the classical Hilbert transform for  $1 < p < \infty$  as found in, e.g., [29]. For our purposes, we define the Hilbert transforms  $\mathbf{H}_x$  in  $x$ -direction and  $\mathbf{H}_y$  in  $y$ -direction according to (3.11) by

$$\begin{aligned} \mathbf{H}_x\Phi(x, y) &:= \frac{1}{\pi} \text{ p.v.} \int_{-\infty}^{\infty} \frac{\Phi(x', y)}{x' - x} dx', \\ \mathbf{H}_y\Phi(x, y) &:= \frac{1}{\pi} \text{ p.v.} \int_{-\infty}^{\infty} \frac{\Phi(x, y')}{y' - y} dy'. \end{aligned} \tag{3.21}$$

**Theorem 3.9** (Theorem 8.1.12, [29]). *For  $\Phi \in \mathcal{L}_p(\mathbb{R}^2)$ ,  $1 < p < \infty$ , the Hilbert transform defined in (3.21) exists almost everywhere, belongs to  $\mathcal{L}_p(\mathbb{R}^2)$  and satisfies*

$$\left\| \mathbf{H}_x\Phi \right\|_{\mathcal{L}_p} \leq c_p \left\| \Phi \right\|_{\mathcal{L}_p} \quad \text{and} \quad \left\| \mathbf{H}_y\Phi \right\|_{\mathcal{L}_p} \leq d_p \left\| \Phi \right\|_{\mathcal{L}_p} \tag{3.22}$$

with constants  $c_p, d_p > 0$ . (3.22) is often referred to as the Marcel Riesz inequality for Hilbert transforms.

The 2d Hilbert transform  $\mathbf{H}_{xy} : \mathcal{L}_p(\mathbb{R}^2) \rightarrow \mathcal{L}_p(\mathbb{R}^2)$  for  $1 < p < \infty$  is considered as the composition  $\mathbf{H}_{xy} = \mathbf{H}_x \circ \mathbf{H}_y$ .

Using trigonometric formulas, we rewrite  $\mathbf{S}_x^n$  into

$$\begin{aligned}
(\mathbf{S}_x^n \Phi)(x, y) &= \frac{1}{\pi^3} \mathcal{X}_{\Omega_y}(x) \text{ p.v.} \int_{\Omega_y} \int_{\Omega_x} \int_{\Omega_x} \frac{\sin [\Phi(x', y') - \Phi(x, y'')]}{(x' - x)(y' - y)(y'' - y)} dy'' dy' dx' \\
&= \frac{1}{\pi^3} \mathcal{X}_{\Omega_y}(x) \text{ p.v.} \int_{\Omega_y} \int_{\Omega_x} \int_{\Omega_x} \frac{\sin [\Phi(x', y')] \cos [\Phi(x, y'')] - \cos [\Phi(x', y')] \sin [\Phi(x, y'')]}{(x' - x)(y' - y)(y'' - y)} dy'' dy' dx' \\
&= \frac{1}{\pi^3} \mathcal{X}_{\Omega_y}(x) \left[ (\mathbf{H}_{xy}(\mathcal{X}_{\Omega} \cdot \sin \Phi))(x, y) \cdot (\mathbf{H}_y(\mathcal{X}_{\Omega_x} \cdot \cos \Phi))(x, y) \right. \\
&\quad \left. - (\mathbf{H}_{xy}(\mathcal{X}_{\Omega} \cdot \cos \Phi))(x, y) \cdot (\mathbf{H}_y(\mathcal{X}_{\Omega_x} \cdot \sin \Phi))(x, y) \right]
\end{aligned}$$

and obtain for  $2 \leq p < \infty$

$$\begin{aligned}
\pi^3 \|\mathbf{S}_x^n \Phi\|_{\mathcal{L}_{p/2}} &= \|(\mathbf{H}_{xy}(\sin \Phi)) \cdot (\mathbf{H}_y(\cos \Phi)) - (\mathbf{H}_{xy}(\cos \Phi)) \cdot (\mathbf{H}_y(\sin \Phi))\|_{\mathcal{L}_{p/2}} \\
&\leq \|(\mathbf{H}_{xy}(\sin \Phi)) \cdot (\mathbf{H}_y(\cos \Phi))\|_{\mathcal{L}_{p/2}} + \|(\mathbf{H}_{xy}(\cos \Phi)) \cdot (\mathbf{H}_y(\sin \Phi))\|_{\mathcal{L}_{p/2}} \\
&\leq \|(\mathbf{H}_{xy}(\sin \Phi))\|_{\mathcal{L}_p} \|(\mathbf{H}_y(\cos \Phi))\|_{\mathcal{L}_p} + \|(\mathbf{H}_{xy}(\cos \Phi))\|_{\mathcal{L}_p} \|(\mathbf{H}_y(\sin \Phi))\|_{\mathcal{L}_p} \\
&< \infty
\end{aligned}$$

by using the generalized Hölder inequality. Note that we omitted the multiplication with the characteristic functions due to simplicity of notation.

It follows that

$$(\mathbf{P}^n \Phi) \in \mathcal{L}_p(\mathbb{R}^2)$$

for  $1 \leq p < \infty$  and  $\Phi \in \mathcal{H}^{11/6}(\mathbb{R}^2)$ .

In order to prove  $(\mathbf{P}^c \Phi) \in \mathcal{L}_2$  we use relation (3.15) between non-modulated and modulated pyramid data, i.e.,

$$s_x^c(x, y) = \frac{1}{T} \int_{-T/2}^{T/2} s_x^n(x, y, t) dt. \quad (3.23)$$

Let  $T$  denote one full time period and  $t \in [-T/2, T/2]$ . For deriving the time-dependent non-modulated pyramid sensor data, we introduce an operator  $\mathbf{M}_t^{mod}$  given by

$$(\mathbf{M}_t^{mod} \Phi)(x, y) := \Phi(x, y) + \Phi^{mod}(x, y, t)$$

for the periodic tilt  $\Phi^{mod}$  inducing modulation. As in (3.14), this tilt is represented by

$$\Phi^{mod}(x, y, t) = \alpha_\lambda(x \sin(2\pi t/T) + y \cos(2\pi t/T)).$$

Due to the structure of  $\Phi^{mod}$  and its compact support on the telescope pupil, it holds that

$$\Phi^{mod}(\cdot, \cdot, t) \in \mathcal{H}^{11/6}(\mathbb{R}^2) \quad \forall t \in [-T/2, T/2].$$

This gives a continuous map  $\mathbf{M}_t^{mod} : \mathcal{H}^{11/6}(\mathbb{R}^2) \rightarrow \mathcal{H}^{11/6}(\mathbb{R}^2)$  and further

$$(\mathbf{P}^n \mathbf{M}_t^{mod} \Phi) \in \mathcal{L}_p(\mathbb{R}^2) \quad \forall t \in [-T/2, T/2], 1 \leq p < \infty. \quad (3.24)$$

Using the generalized Minkowski's integral inequality<sup>(1)</sup> (cf, e.g., [98, Theorem 202], [200], Appendix A.2), the equality  $s_x^n(\cdot, \cdot, t) = (\mathbf{P}^n \mathbf{M}_t^{mod} \Phi)$ , and (3.23) we obtain

$$\begin{aligned} \|\mathbf{s}_x^c\|_{\mathcal{L}_p} &= \left( \int_{\mathbb{R}^2} |s_x^c(x, y)|^p d(x, y) \right)^{1/p} \\ &= \left( \int_{\mathbb{R}^2} \left| \frac{1}{T} \int_{-T/2}^{T/2} (\mathbf{P}^n \mathbf{M}_t^{mod} \Phi)(x, y) dt \right|^p d(x, y) \right)^{1/p} \\ &\stackrel{(1)}{\leq} \frac{1}{T} \int_{-T/2}^{T/2} \left( \int_{\mathbb{R}^2} |(\mathbf{P}^n \mathbf{M}_t^{mod} \Phi)(x, y)|^p d(x, y) \right)^{1/p} dt \\ &= \frac{1}{T} \int_{-T/2}^{T/2} \|\mathbf{P}^n \mathbf{M}_t^{mod} \Phi\|_{\mathcal{L}_p} dt \stackrel{(3.24)}{<} \infty, \end{aligned}$$

which shows  $(\mathbf{P}^c \Phi) \in \mathcal{L}_p(\mathbb{R}^2)$ ,  $1 \leq p < \infty$  for the modulated pyramid sensor operators. Note that we omitted the factor  $(-\frac{1}{2})$  in (3.8) for the above considerations.  $\square$

Merely the light which is captured on the telescope pupil  $\Omega$  influences the pyramid sensor response. We consider only the light falling on the aperture  $(\mathcal{X}_\Omega \cdot \Phi)$  but use the notation  $\Phi \in \mathcal{H}^{11/6}(\mathbb{R}^2)$  for both considered variants of wavefronts with and without compact support on the telescope pupil.

Alternatively, one can also define the pyramid sensor operators only on the telescope aperture as  $\mathbf{P}_x^{\{n,c\}} : \mathcal{H}^{11/6}(\Omega) \rightarrow \mathcal{L}_2(\Omega)$  and  $\mathbf{P}_y^{\{n,c\}}$ ,  $\mathbf{R}_x^{\{n,c,l\}}$ ,  $\mathbf{R}_y^{\{n,c,l\}}$  respectively. However, since we apply, e.g., Plancherel's theorem, we define the operators on the whole  $\mathbb{R}^2$  but keep in mind that one can always restrict to the region of the telescope aperture and CCD-detector. More precisely, the pyramid sensor operators are applied to functions with compact support on the pupil  $\Omega$  and map to functions with compact support on the detector  $\Omega$  (cf Section 3.2).

### 3.4 Linearization of the roof sensor operators

Linear approximations of WFS operators around the zero phase are sufficient in closed loop AO in which the wavefront sensor measures already corrected and very small incoming wavefronts. The linearization of the operators can be obtained by different ways, e.g., by replacing

$$\sin[\Phi(x', y) - \Phi(x, y)] \approx \Phi(x', y) - \Phi(x, y)$$

which is valid for

$$|\Phi(x', y) - \Phi(x, y)| \ll 1.$$

Linearizations  $\mathbf{R}^{\{n,c,l\},lin}$  based on these approximations were already considered in [28, 125, 198, 212]. We concentrate on linear approximations for the roof wavefront sensor operators by means of the Fréchet derivative. For this purpose, we calculate the Gâteaux derivatives. Then, we show that the Gâteaux derivatives coincide with the Fréchet derivatives and finally, we evaluate the corresponding linearizations.

**Theorem 3.10.** *The Gâteaux derivatives  $\left(\mathbf{R}_x^{\{n,c,l\}}\right)'(\Phi) \in \mathcal{L}\left(\mathcal{H}^{11/6}, \mathcal{L}_2\right)$  of the non-linear roof sensor operators  $\mathbf{R}_x^{\{n,c,l\}} : \mathcal{D}\left(\mathbf{R}_x^{\{n,c,l\}}\right) \subseteq \mathcal{H}^{11/6}(\mathbb{R}^2) \rightarrow \mathcal{L}_2(\mathbb{R}^2)$  defined in (3.17) at  $\Phi \in \mathcal{D}\left(\mathbf{R}_x^{\{n,c,l\}}\right)$  are given by*

$$\left(\left(\mathbf{R}_x^{\{n,c,l\}}\right)'(\Phi) \psi\right)(x, y) = \chi_{\Omega}(x, y) \frac{1}{\pi} \int_{\Omega_y} \frac{\cos[\Phi(x', y) - \Phi(x, y)] [\psi(x', y) - \psi(x, y)] \cdot k^{\{n,c,l\}}(x' - x)}{(x' - x)} dx' \quad (3.25)$$

and  $\left(\mathbf{R}_y^{\{n,c,l\}}\right)'(\Phi) \in \mathcal{L}\left(\mathcal{H}^{11/6}, \mathcal{L}_2\right)$  respectively.

*Proof.* We utilize the representation (cf Taylor's theorem with Lagrange form of the remainder)

$$\sin(\Phi + \psi) = \sin(\Phi) + \sin'(\Phi) \psi + \frac{1}{2} \sin''(\Phi + \theta\psi) \psi^2 \quad (3.26)$$

for a  $\theta = \theta(\Phi, \psi) \in (0, 1)$ . For simplicity of notation, we omit the multiplication with the characteristic function of the aperture in front of every integral and the multiplication with the modulation kernels  $k^{\{n,c,l\}}$  as these functions are independent of the phase  $\Phi$  anyway.

The Gâteaux derivatives  $\left(\mathbf{R}_x^{\{n,c,l\}}\right)'(\Phi)$  are computed as

$$\begin{aligned} \left(\left(\mathbf{R}_x^{\{n,c,l\}}\right)'(\Phi) \psi\right)(x, y) &= \lim_{t \rightarrow 0} \frac{\left(\mathbf{R}_x^{\{n,c,l\}}(\Phi + t\psi)\right)(x, y) - \left(\mathbf{R}_x^{\{n,c,l\}}\Phi\right)(x, y)}{t} \\ &= \lim_{t \rightarrow 0} \frac{1}{\pi} \int_{\Omega_y} \left( \frac{\sin[\Phi(x', y) + t\psi(x', y) - \Phi(x, y) - t\psi(x, y)]}{t(x' - x)} \right. \\ &\quad \left. - \frac{\sin[\Phi(x', y) - \Phi(x, y)]}{t(x' - x)} \right) dx' \\ &\stackrel{(3.26)}{=} \lim_{t \rightarrow 0} \frac{1}{\pi} \int_{\Omega_y} \left( \frac{\sin'[\Phi(x', y) - \Phi(x, y)] [t\psi(x', y) - t\psi(x, y)]}{t(x' - x)} \right. \\ &\quad \left. + \frac{\frac{1}{2} \sin''[\Phi(x', y) - \Phi(x, y) + \theta t [\psi(x', y) - \psi(x, y)]]}{t(x' - x)} \right. \\ &\quad \left. \cdot t^2 [\psi(x', y) - \psi(x, y)]^2 \right) dx' \\ &= \frac{1}{\pi} \int_{\Omega_y} \frac{\cos[\Phi(x', y) - \Phi(x, y)] [\psi(x', y) - \psi(x, y)]}{(x' - x)} dx'. \end{aligned}$$

Obviously, the Gâteaux derivatives are linear in  $\psi$ .

For any  $\Phi \in \mathcal{H}^{11/6}(\mathbb{R}^2)$  we deduce that the Gâteaux derivatives are bounded and further continuous in the direction  $\psi$ , i.e.,  $(\mathbf{R}_x^{\{n,c,l\}})'(\Phi) \in \mathcal{L}(\mathcal{H}^{11/6}, \mathcal{L}_2)$ , by showing

$$\left\| \left( \mathbf{R}_x^{\{n,c,l\}} \right)'(\Phi) \right\|_{\mathcal{L}(\mathcal{H}^{11/6}, \mathcal{L}_2)} = \sup_{\|\psi\|_{\mathcal{H}^{11/6}}=1} \left\| \underbrace{\left( \left( \mathbf{R}_x^{\{n,c,l\}} \right)'(\Phi) \psi \right)}_{=:U_1} \right\|_{\mathcal{L}_2(\mathbb{R}^2)} < \infty.$$

By application of the Cauchy-Schwarz inequality<sup>(1)</sup>,  $|k^{\{n,c,l\}}| \leq 1$ , as well as the Hölder continuity<sup>(2)</sup> with  $\alpha = 5/6$  and Hölder constant  $C > 0$  of any function in  $\mathcal{H}^{11/6}(\mathbb{R}^2)$ , the statement results from

$$\begin{aligned} \|U_1\|_{\mathcal{L}_2(\mathbb{R}^2)}^2 &= \int_{\mathbb{R}^2} \left| \left( \left( \mathbf{R}_x^{\{n,c,l\}} \right)'(\Phi) \psi \right)(x, y) \right|^2 d(x, y) \\ &= \int_{\Omega} \left| \frac{1}{\pi} \int_{\Omega_y} \frac{\cos[\Phi(x', y) - \Phi(x, y)] [\psi(x', y) - \psi(x, y)] \cdot k^{\{n,c,l\}}(x' - x)}{x' - x} dx' \right|^2 d(x, y) \\ &\stackrel{(1)}{\leq} \frac{1}{\pi^2} \int_{\Omega} \left( \int_{\Omega_y} \left| \cos[\Phi(x', y) - \Phi(x, y)] \cdot k^{\{n,c,l\}}(x' - x) \right|^2 dx' \right) \\ &\quad \cdot \left( \int_{\Omega_y} \left| \frac{\psi(x', y) - \psi(x, y)}{x' - x} \right|^2 dx' \right) d(x, y) \\ &\stackrel{(2)}{\leq} \frac{1}{\pi^2} \int_{\Omega} \left( \int_{\Omega_y} 1 dx' \right) \cdot \left( C^2 \int_{\Omega_y} \left( \frac{|x' - x|^{5/6}}{|x' - x|} \right)^2 dx' \right) d(x, y) \\ &= \frac{C^2 |\Omega_y|}{\pi^2} \int_{\Omega} \int_{\Omega_y} \frac{1}{|x' - x|^{1/3}} dx' d(x, y) \stackrel{(3.19)-(3.20)}{<} \infty. \end{aligned}$$

□

**Theorem 3.11.** *The Gâteaux derivatives (3.25) coincide with the Fréchet derivatives.*

*Proof.* For the proof we use the following assertion found in, e.g., [9, 223].

**Proposition 3.12** (Theorem III.5.4, [223]; p.10, [9]). *If the Gâteaux derivatives  $(\mathbf{R}_x^{\{n,c,l\}})'(\Phi)$  exist for all  $\Phi$  from a neighborhood of  $\Phi_0 \in \mathcal{D}(\mathbf{R}_x^{\{n,c,l\}})$  and the mappings  $\Phi \rightarrow (\mathbf{R}_x^{\{n,c,l\}})'(\Phi)$  are continuous from  $\mathcal{H}^{11/6}(\mathbb{R}^2)$  into  $\mathcal{L}(\mathcal{H}^{11/6}, \mathcal{L}_2)$  at  $\Phi = \Phi_0$ , then the operators  $\mathbf{R}_x^{\{n,c,l\}}$  are Fréchet differentiable at  $\Phi_0$ .*

Hence, it suffices to show that for any  $\Phi_1, \Phi_2 \in \mathcal{H}^{11/6}(\mathbb{R}^2)$  holds

$$\left\| \left( \mathbf{R}_x^{\{n,c,l\}} \right)'(\Phi_1) - \left( \mathbf{R}_x^{\{n,c,l\}} \right)'(\Phi_2) \right\|_{\mathcal{L}(\mathcal{H}^{11/6}, \mathcal{L}_2)}^2 \leq \tilde{C} \|\Phi_1 - \Phi_2\|_{\mathcal{H}^{11/6}}^2,$$

i.e.,

$$\sup_{\|\psi\|_{\mathcal{H}^{11/6}}=1} \left\| \underbrace{\left( \left( \mathbf{R}_x^{\{n,c,l\}} \right)' (\Phi_1) \psi \right) - \left( \left( \mathbf{R}_x^{\{n,c,l\}} \right)' (\Phi_2) \psi \right)}_{:=U_2} \right\|_{\mathcal{L}_2}^2 \leq \tilde{C} \|\Phi_1 - \Phi_2\|_{\mathcal{H}^{11/6}}^2$$

with  $\tilde{C} < \infty$ .

Under the Lipschitz continuity<sup>(3)</sup> of the cosine function with the Lipschitz constant  $L > 0$  we obtain

$$\begin{aligned} \|U_2\|_{\mathcal{L}_2}^2 &= \int_{\mathbb{R}^2} \left| \left( \left( \mathbf{R}_x^{\{n,c,l\}} \right)' (\Phi_1) \psi \right) (x, y) - \left( \left( \mathbf{R}_x^{\{n,c,l\}} \right)' (\Phi_2) \psi \right) (x, y) \right|^2 d(x, y) \\ &= \int_{\Omega} \left| \frac{1}{\pi} \int_{\Omega_y} \left[ \cos [\Phi_1(x', y) - \Phi_1(x, y)] - \cos [\Phi_2(x', y) - \Phi_2(x, y)] \right] \right. \\ &\quad \left. \cdot \frac{[\psi(x', y) - \psi(x, y)] \cdot k^{\{n,c,l\}}(x' - x)}{x' - x} dx' \right|^2 d(x, y) \\ &\stackrel{(1)}{\leq} \frac{1}{\pi^2} \int_{\Omega} \left( \int_{\Omega_y} \left| \cos [\Phi_1(x', y) - \Phi_1(x, y)] - \cos [\Phi_2(x', y) - \Phi_2(x, y)] \right|^2 dx' \right) \\ &\quad \cdot \left( \int_{\Omega_y} \left| \frac{[\psi(x', y) - \psi(x, y)] \cdot k^{\{n,c,l\}}(x' - x)}{x' - x} \right|^2 dx' \right) d(x, y) \\ &\stackrel{(2),(3)}{\leq} \frac{L^2 C^2}{\pi^2} \int_{\Omega} \left( \int_{\Omega_y} |\Phi_1(x', y) - \Phi_1(x, y) - \Phi_2(x', y) + \Phi_2(x, y)|^2 dx' \right) \\ &\quad \cdot \left( \int_{\Omega_y} \left( \frac{|x' - x|^{5/6}}{|x' - x|} \right)^2 dx' \right) d(x, y) \\ &= \frac{L^2 C^2}{\pi^2} \int_{\Omega} \left( \int_{\Omega_y} \left| [\Phi_1(x', y) - \Phi_2(x', y)] - [\Phi_1(x, y) - \Phi_2(x, y)] \right|^2 dx' \right) \\ &\quad \cdot \left( \int_{\Omega_y} \frac{1}{|x' - x|^{1/3}} dx' \right) d(x, y) \\ &\stackrel{(3,19)}{\leq} \frac{2L^2 C^2}{\pi^2} \int_{\Omega} \left( \int_{\Omega_y} |\Phi_1(x', y) - \Phi_2(x', y)|^2 + |\Phi_1(x, y) - \Phi_2(x, y)|^2 dx' \right) \\ &\quad \cdot M(x, y) d(x, y) \end{aligned}$$

$$\begin{aligned}
&\leq \sup_{x \in \Omega_y} |M(x)| \frac{2L^2 C^2}{\pi^2} \left( \int_{\Omega_y} \int_{\Omega_x} \int_{\Omega_y} |\Phi_1(x', y) - \Phi_2(x', y)|^2 dx' dy dx \right. \\
&\quad \left. + \int_{\Omega_y} \int_{\Omega_x} \int_{\Omega_y} |\Phi_1(x, y) - \Phi_2(x, y)|^2 dx dy dx' \right) \\
&= \sup_{x \in \Omega_y} |M(x)| \frac{2L^2 C^2 |\Omega_y|}{\pi^2} \left( \|\Phi_1 - \Phi_2\|_{\mathcal{L}_2}^2 + \|\Phi_1 - \Phi_2\|_{\mathcal{L}_2}^2 \right) \\
&= \sup_{x \in \Omega_y} |M(x)| \frac{4L^2 C^2 |\Omega_y|}{\pi^2} \|\Phi_1 - \Phi_2\|_{\mathcal{L}_2}^2 \\
&\leq \sup_{x \in \Omega_y} |M(x)| \frac{4L^2 C^2 |\Omega_y|}{\pi^2} \|\Phi_1 - \Phi_2\|_{\mathcal{H}^{11/6}}^2 \stackrel{(3.20)}{\leq} \tilde{C} \|\Phi_1 - \Phi_2\|_{\mathcal{H}^{11/6}}^2,
\end{aligned}$$

i.e., the mapping  $\Phi \rightarrow \left( \mathbf{R}_x^{\{n,c,l\}} \right)'(\Phi)$  is continuous. Thus, the operators  $\mathbf{R}_x^{\{n,c,l\}}$  representing the roof sensor are Fréchet differentiable.  $\square$

**Theorem 3.13.** *The linearizations  $\mathbf{R}^{\{n,c,l\},lin} : \mathcal{H}^{11/6}(\mathbb{R}^2) \rightarrow \mathcal{L}_2(\mathbb{R}^2)$  by means of the Fréchet derivative of the operators  $\mathbf{R}^{\{n,c,l\}}$  introduced in (3.17)-(3.18) are given by*

$$\begin{aligned}
\left( \mathbf{R}_x^{\{n,c,l\},lin} \Phi \right)(x, y) &:= \left( \left( \mathbf{R}_x^{\{n,c,l\}} \right)'(0) \Phi \right)(x, y) \\
&= \mathcal{X}_\Omega(x, y) \frac{1}{\pi} \int_{\Omega_y} \frac{[\Phi(x', y) - \Phi(x, y)] \cdot k^{\{n,c,l\}}(x' - x)}{x' - x} dx' \quad (3.27)
\end{aligned}$$

for  $x$ -direction and  $\mathbf{R}_y^{\{n,c,l\},lin}$  accordingly.

*Proof.* The claim immediately follows from  $\left( \mathbf{R}_x^{\{n,c,l\},lin} \Phi \right) := \left( \left( \mathbf{R}_x^{\{n,c,l\}} \right)'(0) \Phi \right)$ , i.e., considering the Fréchet derivatives (3.25) at  $\Phi = 0$  and in direction  $\Phi$ .  $\square$

### Simplified linearized operators $\mathbf{L}_x^{\{n,c,l\}}$

Variations of the finite Hilbert transform operator allow to simplify the linear approximations of the roof sensor model. Let us, thus, consider the following operators.

**Definition 3.14.** *We define the integral operators  $\mathbf{L}^{\{n,c,l\}} = [\mathbf{L}_x^{\{n,c,l\}}, \mathbf{L}_y^{\{n,c,l\}}]$  by*

$$\left( \mathbf{L}_x^{\{n,c,l\}} \Phi \right)(x, y) := \frac{1}{\pi} p.v. \int_{\Omega_y} \frac{\Phi(x', y) k^{\{n,c,l\}}(x' - x)}{x' - x} dx' \quad (3.28)$$

and  $\mathbf{L}_y^{\{n,c,l\}}$  accordingly.

As derived in [75, 200],  $\mathbf{L}^{\{n,c,l\}}$  are bounded operators on  $\mathcal{L}_p(\mathbb{R}^2)$  for  $1 < p < \infty$  due to the structure of the functions  $k^{\{n,c,l\}}$  introducing modulation. According to the

pyramid and roof sensor model, we consider the operators  $\mathbf{L}^{\{n,c,l\}}$  from  $\mathcal{H}^{11/6}(\mathbb{R}^2)$  into  $\mathcal{L}_2(\mathbb{R}^2)$ . In case of no modulation the operator  $\mathbf{L}_x^n$  coincides with the finite Hilbert transform – a singular Cauchy integral operator.

Using the above defined operators, the linearized roof sensor measurements read as

$$\begin{aligned} s_x^{\{n,c,l\},lin}(x,y) &= -\frac{1}{2} \left( \mathbf{R}_x^{\{n,c,l\},lin} \Phi \right) (x,y) \\ &= -\frac{1}{2} \mathcal{X}_\Omega(x,y) \left[ \left( \mathbf{L}_x^{\{n,c,l\}} \Phi \right) (x,y) - \Phi(x,y) \cdot \left( \mathbf{L}_x^{\{n,c,l\}} 1 \right) (x,y) \right]. \end{aligned} \quad (3.29)$$

Equation (3.29) provides two possibilities for wavefront reconstruction. As it is shown in [192, 193], when an AO system enters the closed loop, the first term in the forward model gains in importance and an assumption of neglecting the second term in the reconstruction procedure is justifiable. Therefore, one could either use the full linearized roof sensor model or ignore the second term  $\left( \mathbf{L}_x^{\{n,c,l\}} 1 \right)$  as it is done in several existing algorithms for pyramid wavefront sensor, e.g., the Preprocessed Cumulative Reconstructor with Domain decomposition (P-CuReD) [111, 195, 198], the Pyramid Fourier Transform Reconstructor [111, 194, 196], the Finite Hilbert Transform Reconstructor [111, 191], or the Singular Value Type Reconstructor [107, 111].

### 3.5 Adjoint of the linearized forward operators

Several iterative algorithms for solving Inverse Problems (e.g., the conjugate gradient method for the normal equation, Landweber iteration or steepest descent method) include the application of adjoint operators. In order to make these approaches suitable for wavefront reconstruction, we derive the adjoints of the underlying operators.

First, we will evaluate the Fourier transforms of the one-term assumptions  $\mathbf{L}^{\{n,c,l\}}$  defined in (3.28) and afterwards use Plancherel's theorem to calculate the corresponding adjoints.

The underlying operators  $\mathbf{L}^{\{n,c,l\}}$  are defined from  $\mathcal{H}^{11/6}(\mathbb{R}^2)$  into  $\mathcal{L}_2(\mathbb{R}^2)$ . In order to calculate the corresponding adjoint operators from  $\mathcal{L}_2(\mathbb{R}^2)$  into  $\mathcal{H}^{11/6}(\mathbb{R}^2)$ , we introduce the embedding operator

$$i_s : \mathcal{H}^{11/6} \rightarrow \mathcal{L}_2 \quad (3.30)$$

and derive the adjoints according to [169] as, e.g.,

$$\left( \mathbf{L}_x^{\{n,c,l\},lin} \right)^* : \mathcal{L}_2 \rightarrow \mathcal{H}^{11/6} \quad \text{with} \quad \left( \mathbf{L}_x^{\{n,c,l\},lin} \right)^* = i_s^* \left( \tilde{\mathbf{L}}_x^{\{n,c,l\},lin} \right)^*$$

for  $\left( \tilde{\mathbf{L}}_x^{\{n,c,l\},lin} \right)^* : \mathcal{L}_2 \rightarrow \mathcal{L}_2$ . For simplicity, we use the notation  $\left( \mathbf{L}_x^{\{n,c,l\},lin} \right)^*$  instead of  $\left( \tilde{\mathbf{L}}_x^{\{n,c,l\},lin} \right)^*$  and omit the multiplication with the aperture mask in the following. The adjoints of the roof sensor operators are considered accordingly.

**Proposition 3.15.** *The 1d Fourier transforms in  $x$ -direction of the operators  $\mathbf{L}_x^{\{n,c,l\}}$  defined in (3.28) are given by*

$$\left(\mathbf{L}_x^{\{n,c,l\}}\Phi\right)^\wedge(\xi, y) = c^{\{n,c,l\}}(\xi) \cdot \widehat{\Phi}(\xi, y) \quad (3.31)$$

with

$$c^n(\xi) = i \operatorname{sgn}(\xi) \quad (3.32)$$

for the non-modulated sensor,

$$c^c(\xi) = i \begin{cases} \operatorname{sgn}(\xi), & \text{for } |\xi| > \frac{\alpha}{\lambda}, \\ \frac{2}{\pi} \arcsin\left(\xi \frac{\lambda}{\alpha}\right), & \text{for } |\xi| \leq \frac{\alpha}{\lambda} \end{cases} \quad (3.33)$$

for the circularly modulated sensor, and

$$c^l(\xi) = i \begin{cases} \operatorname{sgn}(\xi), & \text{for } |\xi| > \frac{\alpha}{\lambda}, \\ \xi \frac{\lambda}{\alpha}, & \text{for } |\xi| \leq \frac{\alpha}{\lambda} \end{cases} \quad (3.34)$$

for the linearly modulated sensor. The Fourier transforms of  $\mathbf{L}_y^{\{n,c,l\}}$  are represented accordingly.

*Proof.* Note that similar considerations are contained in [198, 212]. Since we examine the 1d Hilbert transform  $\mathcal{L}_2(\mathbb{R}) \rightarrow \mathcal{L}_2(\mathbb{R})$  we fix  $y \in \Omega_x$  and investigate the operators  $\mathbf{L}_x^{\{n,c,l\}} : \mathcal{H}^{11/6}(\mathbb{R}) \subseteq \mathcal{L}_2(\mathbb{R}) \rightarrow \mathcal{L}_2(\mathbb{R})$  defined according to (3.28) without indicating the fixed  $y$  specifically. The operators  $\mathbf{L}_y^{\{n,c,l\}} : \mathcal{H}^{11/6}(\mathbb{R}) \subseteq \mathcal{L}_2(\mathbb{R}) \rightarrow \mathcal{L}_2(\mathbb{R})$  are analyzed for fixed  $x \in \Omega_y$  respectively. We introduce the even kernel functions  $v^{\{n,c,l\}}$  by

$$v^{\{n,c,l\}}(x) := p.v. \frac{k^{\{n,c,l\}}(x)}{x}$$

and obtain

$$\begin{aligned} \left(\mathbf{L}_x^{\{n,c,l\}}\Phi\right)(x, y) &= -\frac{1}{\pi} \left(\Phi(\cdot, y) * v^{\{n,c,l\}}\right)(x) \\ &= -\frac{1}{\pi} \int_{-\infty}^{\infty} \Phi(x', y) v^{\{n,c,l\}}(x - x') dx' \\ &= \lim_{\delta \rightarrow 0^+} \frac{1}{\pi} \left[ \int_{-\infty}^{x-\delta} \frac{\Phi(x', y) k^{\{n,c,l\}}(x' - x)}{x' - x} dx' \right. \\ &\quad \left. + \int_{x+\delta}^{\infty} \frac{\Phi(x', y) k^{\{n,c,l\}}(x' - x)}{x' - x} dx' \right]. \end{aligned} \quad (3.35)$$

By the convolution theorem (A.1), the 1d convolution in (3.35) is a multiplication in the Fourier domain, i.e.,

$$\left(\mathbf{L}_x^{\{n,c,l\}}\Phi\right)^\wedge(\xi, y) = -\sqrt{\frac{2}{\pi}} \widehat{\Phi}(\xi, y) \cdot \widehat{v^{\{n,c,l\}}}(\xi). \quad (3.36)$$

As already used in [198, 212], the Fourier transforms of the kernel functions are calculated as

$$\widehat{v^n}(\xi) = -i\sqrt{\frac{\pi}{2}} \operatorname{sgn}(\xi)$$

for the non-modulated sensor,

$$\widehat{v^c}(\xi) = -i \begin{cases} \sqrt{\frac{\pi}{2}} \operatorname{sgn}(\xi), & \text{for } |\xi| > \frac{\alpha}{\lambda}, \\ \sqrt{\frac{2}{\pi}} \arcsin\left(\frac{\xi\lambda}{\alpha}\right), & \text{for } |\xi| \leq \frac{\alpha}{\lambda} \end{cases}$$

for the circularly modulated sensor, and

$$\widehat{v^l}(\xi) = -i \begin{cases} \sqrt{\frac{\pi}{2}} \operatorname{sgn}(\xi), & \text{for } |\xi| > \frac{\alpha}{\lambda}, \\ \sqrt{\frac{\pi}{2}} \xi \frac{\lambda}{\alpha}, & \text{for } |\xi| \leq \frac{\alpha}{\lambda} \end{cases}$$

for the linearly modulated sensor.

The claim of the Proposition follows by (3.36) and  $c^{\{n,c,l\}} = -\sqrt{\frac{2}{\pi}} \widehat{v^{\{n,c,l\}}}$ .  $\square$

Note that by the isometry of the Fourier transform we obtain

$$\left\| \mathbf{L}_x^{\{n,c,l\}}\Phi(\cdot, y) \right\|_{\mathcal{L}_2} = \left\| \left(\mathbf{L}_x^{\{n,c,l\}}\Phi\right)^\wedge(\cdot, y) \right\|_{\mathcal{L}_2} = \left\| c^{\{n,c,l\}} \cdot \widehat{\Phi}(\cdot, y) \right\|_{\mathcal{L}_2} = \tilde{c} \left\| \widehat{\Phi}(\cdot, y) \right\|_{\mathcal{L}_2},$$

i.e.,

$$\left\| \mathbf{L}_x^{\{n,c,l\}}\Phi(\cdot, y) \right\|_{\mathcal{L}_2} = \tilde{c} \left\| \Phi(\cdot, y) \right\|_{\mathcal{L}_2}$$

for a constant  $0 < \tilde{c} < \infty$ .

### Adjoint operators $\left(\mathbf{L}_x^{\{n,c,l\}}\right)^*$ in $\mathcal{L}_2(\mathbb{R}^2)$

As previously mentioned, it is sufficient to derive the adjoints as operators from  $\mathcal{L}_2$  into itself and use the embedding operator (3.30) in order to obtain adjoint operators from  $\mathcal{L}_2$  into  $\mathcal{H}^{11/6}$  [169].

**Proposition 3.16.** *The adjoints  $\left(\mathbf{L}_x^{\{n,c,l\}}\right)^* : \mathcal{L}_2(\mathbb{R}^2) \rightarrow \mathcal{L}_2(\mathbb{R}^2)$  of the operators  $\mathbf{L}_x^{\{n,c,l\}}$  defined in (3.28) are given by*

$$\left(\left(\mathbf{L}_x^{\{n,c,l\}}\right)^* \Psi\right)(x, y) = -\frac{1}{\pi} \text{p.v.} \int_{\Omega_y} \frac{\Psi(x', y) \cdot k^{\{n,c,l\}}(x' - x)}{x' - x} dx',$$

and  $\left(\mathbf{L}_y^{\{n,c,l\}}\right)^*$  accordingly, i.e.,  $\mathbf{L}^{\{n,c,l\}}$  are skew-adjoint in  $\mathcal{L}_2(\mathbb{R}^2)$ .

*Proof.* The proof is performed in the Fourier domain in which we have to consider the  $\mathcal{L}_2(\mathbb{C})$ -inner product due to  $c^{\{n,c,l\}} \in \mathbb{C}$  defined in (3.32)-(3.34). We use Plancherel's theorem and the equality  $c^{\{n,c,l\}} = -\overline{c^{\{n,c,l\}}}$  for the complex conjugate<sup>(1)</sup>.

For any  $\Phi, \Psi \in \mathcal{L}_2(\mathbb{R}^2)$  with support on  $\Omega$  and  $y \in \Omega_x$  holds

$$\begin{aligned}
\left\langle \left( \mathbf{L}_x^{\{n,c,l\}} \Phi \right) (\cdot, y), \Psi (\cdot, y) \right\rangle_{\mathcal{L}_2(\mathbb{C})} &= \left\langle \left( \mathbf{L}_x^{\{n,c,l\}} \Phi \right)^\wedge (\cdot, y), \widehat{\Psi} (\cdot, y) \right\rangle_{\mathcal{L}_2(\mathbb{C})} \\
&= \int_{\mathbb{R}} \left( \mathbf{L}_x^{\{n,c,l\}} \Phi \right)^\wedge (\xi, y) \overline{\widehat{\Psi}(\xi, y)} d\xi \\
&\stackrel{(3.31)}{=} \int_{\mathbb{R}} \left( c^{\{n,c,l\}} (\xi) \cdot \widehat{\Phi}(\xi, y) \right) \overline{\widehat{\Psi}(\xi, y)} d\xi \\
&\stackrel{(1)}{=} - \int_{\mathbb{R}} \widehat{\Phi}(\xi, y) \overline{\left( c^{\{n,c,l\}} (\xi) \cdot \widehat{\Psi}(\xi, y) \right)} d\xi \\
&= \left\langle \widehat{\Phi} (\cdot, y), \left( \left( \mathbf{L}_x^{\{n,c,l\}} \right)^* \Psi \right)^\wedge (\cdot, y) \right\rangle_{\mathcal{L}_2(\mathbb{C})} \\
&= \left\langle \Phi (\cdot, y), \left( \left( \mathbf{L}_x^{\{n,c,l\}} \right)^* \Psi \right) (\cdot, y) \right\rangle_{\mathcal{L}_2(\mathbb{C})}
\end{aligned}$$

with  $\left( \left( \mathbf{L}_x^{\{n,c,l\}} \right)^* \Psi \right)^\wedge (\xi, y) = -c^{\{n,c,l\}} (\xi) \widehat{\Psi} (\xi, y)$ , i.e.,  $\left( \mathbf{L}_x^{\{n,c,l\}} \right)^* = -\mathbf{L}_x^{\{n,c,l\}}$ .  $\square$

### Adjoint operators $\left( \mathbf{R}_x^{\{n,c,l\},lin} \right)^*$ in $\mathcal{L}_2(\mathbb{R}^2)$

Let us now derive the adjoints of the operators representing the linearized roof wave-front sensor.

**Proposition 3.17.** *The adjoints  $\left( \mathbf{R}_x^{\{n,c,l\},lin} \right)^* : \mathcal{L}_2(\mathbb{R}^2) \rightarrow \mathcal{L}_2(\mathbb{R}^2)$  of the linearized roof sensor operators  $\mathbf{R}_x^{\{n,c,l\},lin}$  defined in (3.27) are given by*

$$\begin{aligned}
\left( \left( \mathbf{R}_x^{\{n,c,l\},lin} \right)^* \Psi \right) (x, y) &= \left( \left( \mathbf{L}_x^{\{n,c,l\}} \right)^* \Psi \right) (x, y) - \Psi(x, y) \left( \mathbf{L}_x^{\{n,c,l\}} \mathbf{1} \right) (x, y) \\
&= -\frac{1}{\pi} p.v. \int_{\Omega_y} \frac{[\Psi(x', y) + \Psi(x, y)] \cdot k^{\{n,c,l\}}(x' - x)}{x' - x} dx'
\end{aligned}$$

and  $\left( \mathbf{R}_y^{\{n,c,l\},lin} \right)^*$  respectively.

*Proof.* We choose any  $\Phi, \Psi \in \mathcal{L}_2(\mathbb{R}^2)$  with support on the telescope pupil  $\Omega$ . Due to

the linearity of the inner product and with representation (3.29), it holds that

$$\begin{aligned}
\left\langle \left( \mathbf{R}_x^{\{n,c,l\},lin} \Phi \right), \Psi \right\rangle &= \left\langle \mathcal{X}_\Omega \left( \mathbf{L}_x^{\{n,c,l\}} \Phi - \Phi \mathbf{L}_x^{\{n,c,l\}} \mathbf{1} \right), \Psi \right\rangle \\
&= \left\langle \mathbf{L}_x^{\{n,c,l\}} \Phi, \Psi \right\rangle - \left\langle \Phi \mathbf{L}_x^{\{n,c,l\}} \mathbf{1}, \Psi \right\rangle \\
&= \left\langle \Phi, \left( \mathbf{L}_x^{\{n,c,l\}} \right)^* \Psi \right\rangle - \left\langle \Phi, \Psi \mathbf{L}_x^{\{n,c,l\}} \mathbf{1} \right\rangle \\
&= \left\langle \Phi, \left( \mathbf{L}_x^{\{n,c,l\}} \right)^* \Psi - \Psi \mathbf{L}_x^{\{n,c,l\}} \mathbf{1} \right\rangle \\
&= \left\langle \Phi, \left( \mathbf{R}_x^{\{n,c,l\},lin} \right)^* \Psi \right\rangle,
\end{aligned}$$

where we consider the inner product with respect to  $\mathcal{L}_2(\mathbb{R}^2)$  or  $\mathcal{L}_2(\Omega)$  respectively.  $\square$

### 3.6 The discrete pyramid wavefront sensor

The full continuous measurements  $s_x(x, y)$  and  $s_y(x, y)$  of the pyramid wavefront sensor are not available in practice. For the description of the discrete pyramid sensor we perform a division of the continuous two dimensional process into finitely many equispaced regions called subapertures. The data are then assumed to be averaged over every subaperture which corresponds to the finite sampling of the pyramid sensor. Note that in reality, the subaperture grid is predefined by the sensor's physics. Following the approach in [212], we examine the sensor data as functions evaluated in the (discrete) middle points of the WFS subapertures. In the two dimensional case we consider quadratic subapertures of size  $d \times d$  with  $d = \frac{D}{n}$ , where  $D$  represents the telescope diameter, i.e., the primary mirror size, and  $n$  the number of subapertures in one direction.

Note that all considerations are valid for measurements both in  $x$ -direction  $s_x(x, y)$  and  $y$ -direction  $s_y(x, y)$ , as well as for non-modulated, circularly, and linearly modulated data. Thus, we consider general measurements identified by  $s(x, y)$ . Discretizing  $s(x, y)$  delivers  $n^2$  data values  $s_{jk}$  with  $j, k = 1, \dots, n$ .

For the following, we use the delta distribution  $\delta$  (already introduced in the proof of Theorem 3.3) and the Dirac comb  $\text{III}_d$  defined as

$$\text{III}_d(x, y) := \sum_{\ell=-\infty}^{\infty} \sum_{m=-\infty}^{\infty} \delta(x - \ell d, y - m d).$$

The continuous signal is captured by the wavefront sensor as follows:

First, the average of the measurements over one subaperture is calculated. This is represented as a convolution of the continuous data  $s(x, y)$  with a characteristic function

$\mathcal{X}_{[-d/2, d/2]^2}(x, y)$ , i.e.,

$$\begin{aligned}\tilde{s}(x, y) &= \frac{1}{d^2} \int_{x-d/2}^{x+d/2} \int_{y-d/2}^{y+d/2} s(x', y') dy' dx' \\ &= \frac{1}{d^2} \int_{-\infty}^{\infty} \int_{-\infty}^{\infty} s(x', y') \cdot \mathcal{X}_{[-d/2, d/2]}(x - x') \cdot \mathcal{X}_{[-d/2, d/2]}(y - y') dy' dx' \\ &= \frac{1}{d^2} \int_{-\infty}^{\infty} \int_{-\infty}^{\infty} s(x', y') \cdot \mathcal{X}_{[-d/2, d/2]^2}(x - x', y - y') dy' dx' \\ &= \frac{1}{d^2} (s * \mathcal{X}_{[-d/2, d/2]^2})(x, y).\end{aligned}$$

The discretization is carried out as an application of the Dirac comb  $\text{III}_d$  assuming that the measurements  $s$  fulfill the necessary conditions on applying the distribution  $\delta$ . Herewith, we assign a discrete set of measurements  $\bar{s}$  centered on the subapertures

$$\bar{s} = \left\langle \text{III}_d, \tilde{s} \right\rangle = \left\langle \sum_{\ell=-\infty}^{\infty} \sum_{m=-\infty}^{\infty} \delta(\cdot - \ell d, \cdot - m d), \tilde{s} \right\rangle$$

from the floating average values  $\tilde{s}(x, y)$  to the discrete set of subaperture middle points  $\{(jd, kd) : j, k \in \mathbb{Z}\}$ .

Finally, we restrict the number of measurements to the size of the region captured by the sensor. We describe this mask by  $\Omega$  as in Section 3.2.

Hence, the last step is realized as a multiplication with a second characteristic function

$$s_{j,k} = \left( \left\langle \text{III}_d, \tilde{s} \right\rangle \cdot \mathcal{X}_{\Omega} \right)_{j,k}$$

for  $j, k = 1, \dots, n$ . To be precise, we usually consider less than  $n^2$  measurements due to, e.g., the annular shape of the aperture and ignore subapertures which are too less illuminated in order to produce reliable data.

### 3.7 Summary on forward models

In this Chapter we have considered the mathematical background for pyramid and roof wavefront sensors. The theoretical analysis of the forward operators was aimed at the subsequent development of fast and stable algorithms for wavefront reconstruction from pyramid sensor data presented in Chapter 4 - 6. We introduced the transmission and the phase mask model in a distributional sense. The analysis allows any kind of modulation (no, circular, linear) to be applied to the sensors. We linearized the initially non-linear forward operators based on the closed loop operation assumption and further simplified the linearized operators to approximate the measurements by only one term comparable to the finite Hilbert transform in case of the non-modulated sensor. Further, we investigated the Fourier transforms of the “one-term“ operators and derived the corresponding adjoint operators. Finally, we reviewed the concept of the discrete pyramid wavefront sensor. Extensive studies of the full pyramid sensor operator (i.e., calculations of Fréchet derivatives or linear approximations) are dedicated to future work.

## Chapter 4

# Linear wavefront reconstruction using a singular value type expansion

In this Chapter we present a new approach for wavefront reconstruction from non-modulated pyramid sensor data using a singular value decomposition of the corresponding operator introduced in [107] as a joint work with Ronny Ramlau. The method is based on the simplified linearization of the sensor model represented as the finite Hilbert transform of the incoming phase (cf one-term assumption  $\mathbf{L}^n$  in 3.28). Due to the non-compactness of the finite Hilbert transform operator, the classical theory for singular systems is not applicable. Nevertheless, we can express the Moore-Penrose inverse as a singular value type expansion with weighted Chebychev polynomials. The method is named *Singular Value Type Reconstructor* (SVTR).

Section 4.1 gives a brief review on the underlying pyramid sensor model. The theoretical background of the finite Hilbert transform operator and the main ideas of its singular value type expansion are contained in Section 4.2. A numerical validation of the presented theory including details of the practical implementation of the method itself is given in Section 4.3. In this Section, we as well introduce the idea of an iterative measurement extension method which is based on the forward model of the pyramid wavefront sensor.

Having a look at the detailed representation of the forward models of the PWFS lays the mathematical foundation for this wavefront reconstruction method. Starting with the non-modulated pyramid sensor we simplify the non-linear model and consider the basic principles of the roof wavefront sensor serving as an approximation of the pyramid sensor. The assumption of small wavefront distortions, as expected in closed loop systems, allows to consider the non-modulated roof wavefront sensor measurements related in a linear way to the incoming phase.

Numerical results show the effectiveness of the proposed method. With a computational complexity of  $\mathcal{O}(N^{3/2})$ , where  $N = n^2$  indicates approximately the number of

unknowns to be found for an  $n \times n$  PWFS, our algorithm has a computational complexity which makes wavefront reconstruction using a singular value type expansion attractive, especially for XAO telescope settings. As we focus on wavefront estimation only, the evaluation of the mirror actuator commands is not considered (cf Section 8.2.1 - 8.2.2). In general, the computation of the actuator commands depends on the underlying influence functions of the used mirror. However, for non-overlapping bilinear influence functions which are frequently used, the mirror commands are obtained by a point evaluation of the mirror shape at the positions of the actuators, and thus the computation has no significant contribution to the computational load.

## 4.1 Underlying pyramid forward model

An extensive mathematical analysis of the pyramid and roof wavefront sensor models have already been given in Chapter 3. This Section is aimed at repeating the necessary considerations of the model on which the new wavefront reconstruction method is based. Instead of the full pyramid sensor performance described by non-linear singular integral equations we consider linearized roof sensor models as a basis for the reconstruction algorithm.

We simplify the pyramid sensor model by a substitution of the four-sided pyramidal prism with two two-sided roof prisms [155, 212]. As a result, each roof provides two different images of the aperture on the detector plane. Interference between the two beams is neglected in the model. With respect to their orthogonal placement, the measurements  $s_x$  influence the phase  $\Phi$  only in  $x$ -direction and  $s_y$  only in  $y$ -direction correspondingly. Taking the roof simplifications into account, the non-modulated PWFS measurements are approximated by (cf Theorem 3.5)

$$s_x(x, y) = -\frac{1}{2\pi} \int_{\Omega_y} \frac{\sin[\Phi(x', y) - \Phi(x, y)]}{x' - x} dx'.$$

Due to the symmetry of the problem, measurements  $s_y$  can be computed accordingly. Note that we omit the multiplication with the characteristic function  $\mathcal{X}_\Omega$  of the aperture (as, e.g., in (3.17)) throughout this Chapter for simplicity of notation.

Another simplification follows from the assumption of a closed loop telescope system. The incoming phases are measured after the deformable mirror, i.e., we measure already corrected wavefronts  $\Phi \ll 1$ . Hence, the non-modulated roof wavefront sensor measurements are approximately represented by (cf linearization of the operators in Section 3.4 and Theorem 3.13)

$$s_x(x, y) = -\frac{1}{2\pi} \int_{\Omega_y} \frac{\Phi(x', y) - \Phi(x, y)}{x' - x} dx'. \quad (4.1)$$

## 4.2 The singular value type expansion of the underlying operator

We define the operator that is used for the description of the underlying simplified PWFS model (4.1) and investigate some properties of the operator in detail. We would expect a compact and ill-posed operator. But according to [57], the spectrum is continuous and the operator non-compact.

### 4.2.1 Finite Hilbert transform operator

The finite Hilbert transform operator  $\mathbf{T} : \mathcal{L}_2([a, b]) \rightarrow \mathcal{L}_2([a, b])$  is defined by

$$\mathbf{T}f(x) := \frac{1}{\pi} p.v. \int_a^b \frac{f(y)}{y-x} dy \quad \text{for } a \leq x \leq b,$$

with  $a, b \in \mathbb{R}$ ,  $a < b$  and a function  $f : [a, b] \rightarrow \mathbb{R}$ . The integral has to be understood in the principal value sense and the kernel of the integral operator is given by  $k(x, y) = (y-x)^{-1}$ , and thus is not weakly singular. Integral operators with kernels of the previous form being on the border to weakly singular are called *singular Cauchy integral operators* as mentioned in [57].

A substitution of the intervals  $\Omega_x$  and  $\Omega_y$  to  $[-1, 1]$  enables us to express the non-modulated wavefront sensor operator in (4.1) as the finite Hilbert transform on  $[-1, 1]$ . Due to the annular shape of the telescope aperture  $\Omega = \Omega_y \times \Omega_x$ ,  $\Omega_x$  and  $\Omega_y$  consist of either one or two parts. In the second case, we look at each part of  $\Omega_x = \Omega_x^1 \cup \Omega_x^2$  or  $\Omega_y = \Omega_y^1 \cup \Omega_y^2$  separately. The transformation from  $\bar{\Omega} = [\omega_a, \omega_b]$  to  $[-1, 1]$  is given by

$$t(z) := -1 + (z - \omega_a) \frac{2}{\omega_b - \omega_a},$$

where  $\bar{\Omega}$  represents one (part of the) line of the telescope pupil as shown in Figure 4.1. Using the above substitution we obtain

$$\frac{1}{\pi} p.v. \int_{\omega_a}^{\omega_b} \frac{f(y)}{y-x} dy = \frac{\omega_b - \omega_a}{2} \frac{1}{\pi} p.v. \int_{-1}^1 \frac{f(t^{-1}(z))}{t^{-1}(z) - x} dz.$$

For simplicity, we only examine

$$\frac{1}{\pi} p.v. \int_{-1}^1 \frac{f(y)}{y-x} dy$$

in the following. Additionally, we consider the finite Hilbert transform operator in a weighted Lebesgue space  $\mathcal{L}_2^\omega([-1, 1])$  with weighted norm

$$\|f\|_\omega^2 := \int_{-1}^1 |f(y)|^2 \omega(y) dy, \quad \text{where} \quad \omega(y) := \frac{1}{\sqrt{1-y^2}} \quad (4.2)$$

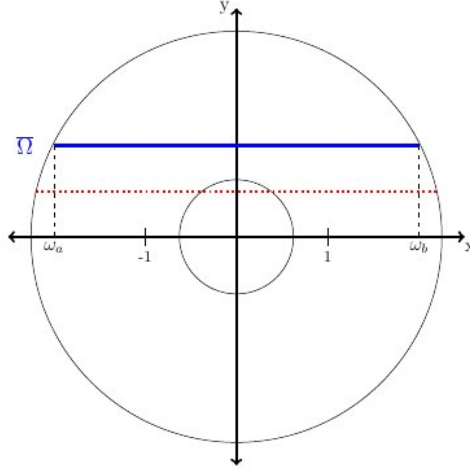


Figure 4.1: Transformation of telescope aperture, source [107]. We transform the annular telescope aperture  $\Omega$  onto the region  $[-1, 1]^2$ . The blue line represents a chord  $\bar{\Omega} = \Omega_y$  of the pupil for fixed  $y$ . If the chord consists of two parts (dotted red line), we consider each part separately.

and define  $\mathbf{T}_{\{x,y\}} : \mathcal{L}_2^\omega([-1, 1]) \rightarrow \mathcal{L}_2^\omega([-1, 1])$  by

$$\begin{aligned} (\mathbf{T}_x \Phi)(x, y) &:= \frac{1}{\pi} \text{p.v.} \int_{-1}^1 \frac{\Phi(x', y)}{x' - x} dx' \\ (\mathbf{T}_y \Phi)(x, y) &:= \frac{1}{\pi} \text{p.v.} \int_{-1}^1 \frac{\Phi(x, y')}{y' - y} dy'. \end{aligned} \quad (4.3)$$

Note that  $\mathbf{T}_x$  describes the 1d finite Hilbert transform operator integrating in  $x$ -direction for fixed  $y$ , i.e., independent for all  $y$ , and similarly,  $\mathbf{T}_y$  in  $y$ -direction for fixed  $x$ . The operators  $\mathbf{T}_x$  and  $\mathbf{T}_y$  represent the simplified model of the pyramid sensor including the assumptions of a roof wavefront sensor and a closed loop system similar to  $\mathbf{L}^n$  in 3.28.

**Proposition 4.1.** *The operators  $\mathbf{T}_{\{x,y\}} : \mathcal{L}_2^\omega([-1, 1]) \rightarrow \mathcal{L}_2^\omega([-1, 1])$  which describe the simplified roof wavefront sensor model are linear, non-compact, but continuous and injective operators with spectrum  $[-i, i]$ .*

*Proof.* See [57] for the finite Hilbert transform operator.  $\square$

In the following, we only consider measurements  $s_x$  in  $x$ -direction. Due to the symmetry of the roof sensor, all considerations are also valid for  $s_y$ . Using the finite Hilbert transform operator  $\mathbf{T}_x$  defined in (4.3) the sensor data in (4.1) can be rewritten as a sum

$$s_x(x, y) = -\frac{1}{2} [(\mathbf{T}_x \Phi)(x, y) - \Phi(x, y) (\mathbf{T}_x 1)(x, y)]. \quad (4.4)$$

Equation (4.4) provides two possibilities of wavefront reconstruction. Either we use the full expression and reconstruct with an iterative algorithm or we ignore the second term because of its little impact in closed loop systems as investigations in [191] show. In the following, we analyze the second approach.

An idea for the inversion of the measurement equations

$$s_x(x, y) = -\frac{1}{2} (\mathbf{T}_x \Phi)(x, y) \quad \text{and} \quad s_y(x, y) = \frac{1}{2} (\mathbf{T}_y \Phi)(x, y) \quad (4.5)$$

consists in the application of the inverse operator to the sensor data.

**Proposition 4.2.** *Consider the operator  $\mathbf{T}_x : \mathcal{L}_2^\omega([-1, 1]) \rightarrow \mathcal{L}_2^\omega([-1, 1])$ . For all  $y \in [-1, 1]$  a solution of*

$$-\frac{1}{2} (\mathbf{T}_x \Phi)(x, y) = s_x(x, y)$$

is given by

$$\Phi(x, y) = 2 \left[ \frac{1}{\pi} \int_{-1}^1 \frac{s_x(x', y)}{x' - x} \sqrt{\frac{1 - x'^2}{1 - x^2}} dx' + \frac{C(y)}{\sqrt{1 - x^2}} \right] \quad (4.6)$$

with

$$C(y) = \frac{1}{\pi} \int_{-1}^1 \Phi(x', y) dx'.$$

*Proof.* See [103, 160, 205]. □

A reconstruction method that is based on formula (4.6) is described in Section 7.1.7 as the Finite Hilbert Transform Reconstructor (FHTR). Here, we propose a different method for restoration using a singular value type expansion of the operator. According to the weighted norm we have introduced in (4.2), the singular functions we consider for wavefront reconstruction are weighted Chebychev polynomials.

## 4.2.2 Decomposition with Chebychev polynomials

We define  $(f_k, g_k)_{k \geq 0}$  by

$$f_k(x) := -\sqrt{\frac{2}{\pi}} T_{k+1}(x), \quad g_k(x) := \sqrt{\frac{2}{\pi}} \sqrt{1 - x^2} U_k(x), \quad (4.7)$$

where  $T_k(x)$  and  $U_k(x)$  are Chebychev polynomials of the first and second kind given by

$$T_k(x) := \cos(k\theta) \quad \text{and} \quad U_k(x) := \frac{\sin[(k+1)\theta]}{\sin(\theta)}$$

with  $x = \cos(\theta)$ . Furthermore, we set  $f_{-1}(x) := \sqrt{\frac{1}{\pi}}$ .

**Proposition 4.3.** *The functions  $\{f_k\}_{k \geq -1}$  and  $\{g_k\}_{k \geq 0}$  defined in (4.7) are orthonormal in  $\mathcal{L}_2^\omega([-1, 1])$  and the functions  $\{f_k\}_{k \geq -1}$  are a complete orthonormal system in  $\mathcal{L}_2^\omega([-1, 1])$ .*

*Proof.* First, we prove the normalization of  $f_k$  and  $g_k$ . It follows immediately with the substitution  $x = \cos(\xi)$

$$\|f_{-1}\|_{\omega}^2 = \frac{1}{\pi} \int_{-1}^1 \frac{1}{\sqrt{1-x^2}} dx = \frac{1}{\pi} \int_0^{\pi} \frac{1}{\sqrt{1-\cos^2(\xi)}} \sin(\xi) d\xi = \frac{1}{\pi} \int_0^{\pi} 1 dx = 1$$

and

$$\begin{aligned} \|f_{k-1}\|_{\omega}^2 &= \frac{2}{\pi} \int_{-1}^1 |T_k(x)|^2 \frac{1}{\sqrt{1-x^2}} dx = \frac{2}{\pi} \int_{-1}^1 \cos^2(k \arccos(x)) \frac{1}{\sqrt{1-x^2}} dx \\ &= \frac{2}{\pi} \int_0^{\pi} \frac{\cos^2(k\xi)}{\sqrt{1-\cos^2(\xi)}} \sin(\xi) d\xi = \frac{2}{\pi} \int_0^{\pi} \cos^2(k\xi) d\xi \\ &= \frac{2}{\pi} \left[ \frac{\xi}{2} + \frac{\sin(k\xi) \cos(k\xi)}{2k} \right]_0^{\pi} = 1 \end{aligned}$$

as well as

$$\begin{aligned} \|g_{k-1}\|_{\omega}^2 &= \frac{2}{\pi} \int_{-1}^1 (1-x^2) |U_{k-1}(x)|^2 \frac{1}{\sqrt{1-x^2}} dx \\ &= \frac{2}{\pi} \int_{-1}^1 (1-x^2) \frac{\sin^2(k \arccos(x))}{\sin^2(\arccos(x))} \frac{1}{\sqrt{1-x^2}} dx \\ &= \frac{2}{\pi} \int_0^{\pi} (1-\cos^2(\xi)) \frac{\sin^2(k\xi)}{\sin^2(\xi)} \frac{1}{\sqrt{1-\cos^2(\xi)}} \sin(\xi) d\xi \\ &= \frac{2}{\pi} \int_0^{\pi} \sin^2(k\xi) d\xi = \frac{2}{\pi} \left[ \frac{\xi}{2} + \frac{\cos(k\xi) \sin(k\xi)}{2k} \right]_0^{\pi} = 1 \end{aligned}$$

for all  $k \geq 1$ .

In order to prove the orthogonality we choose  $m, n \geq 1$  and  $m \neq n$ . With substitution (as described above) we obtain

$$\begin{aligned} \langle f_{m-1}, f_{n-1} \rangle_{\omega} &= \int_{-1}^1 f_{m-1}(x) f_{n-1}(x) \frac{1}{\sqrt{1-x^2}} dx \\ &= \frac{2}{\pi} \int_{-1}^1 T_m(x) T_n(x) \frac{1}{\sqrt{1-x^2}} dx \\ &= \frac{2}{\pi} \int_{-1}^1 \cos(m \arccos(x)) \cos(n \arccos(x)) \frac{1}{\sqrt{1-x^2}} dx \end{aligned}$$

$$\begin{aligned}
 &= \frac{2}{\pi} \int_0^{\pi} \cos(m\xi) \cos(n\xi) \frac{1}{\sqrt{1 - \cos^2(\xi)}} \sin(\xi) d\xi \\
 &= \frac{2}{\pi} \int_0^{\pi} \cos(m\xi) \cos(n\xi) d\xi = 0
 \end{aligned}$$

and

$$\begin{aligned}
 \langle g_{m-1}, g_{n-1} \rangle_{\omega} &= \int_{-1}^1 g_{m-1}(x) g_{n-1}(x) \frac{1}{\sqrt{1-x^2}} dx \\
 &= \frac{2}{\pi} \int_{-1}^1 (1-x^2) U_{m-1}(x) U_{n-1}(x) \frac{1}{\sqrt{1-x^2}} dx \\
 &= \frac{2}{\pi} \int_{-1}^1 \sqrt{1-x^2} \frac{\sin(m \arccos(x)) \sin(n \arccos(x))}{\sin^2(\arccos(x))} dx \\
 &= \frac{2}{\pi} \int_0^{\pi} \sqrt{1-\cos(\xi)^2} \frac{\sin(m\xi) \sin(n\xi)}{\sin^2(\xi)} \sin(\xi) d\xi \\
 &= \frac{2}{\pi} \int_0^{\pi} \sin(m\xi) \sin(n\xi) d\xi = 0.
 \end{aligned}$$

Note that  $\langle \cdot, \cdot \rangle_{\omega}$  denotes the inner product in  $\mathcal{L}_2^{\omega}([-1, 1])$ . Furthermore, it holds for all  $k \geq 1$

$$\begin{aligned}
 \langle f_{-1}, f_{k-1} \rangle_{\omega} &= \int_{-1}^1 \sqrt{\frac{1}{\pi}} f_{k-1}(x) \frac{1}{\sqrt{1-x^2}} dx = -\frac{\sqrt{2}}{\pi} \int_{-1}^1 T_k(x) \frac{1}{\sqrt{1-x^2}} dx \\
 &= -\frac{\sqrt{2}}{\pi} \int_{-1}^1 \cos(k \arccos(x)) \frac{1}{\sqrt{1-x^2}} dx \\
 &= -\frac{\sqrt{2}}{\pi} \int_0^{\pi} \cos(k\xi) \frac{1}{\sqrt{1-\cos^2(\xi)}} \sin(\xi) d\xi \\
 &= -\frac{\sqrt{2}}{\pi} \int_0^{\pi} \cos(k\xi) d\xi = 0.
 \end{aligned}$$

The completeness of  $\{f_k\}_{k \geq -1}$  follows from the completeness of Chebychev polynomials.  $\square$

Now, we present a result that lays the foundations for the singular value type expansion. A similar one has already been proven in [205].

**Proposition 4.4.** For  $\{f_k\}_{k \geq -1}$  and  $\{g_k\}_{k \geq 0}$  defined in (4.7) hold the equations

$$\mathbf{T}_x f_k = g_k, \quad \forall k \in \mathbb{N}_0 \quad \text{and} \quad \mathbf{T}_x f_{-1} = 0,$$

where  $\mathbf{T}_x$  represents the finite Hilbert transform operator defined in (4.3).

*Proof.* The proof is centered around the equality

$$-\frac{1}{\pi} \int_0^\pi \frac{\cos(k\eta)}{\cos \eta - \cos \xi} \sin \eta \, d\eta = \sin(k\xi), \quad (4.8)$$

which is shown by the application of the residue theorem in [95, 103].

We verify  $\sqrt{\frac{\pi}{2}} \mathbf{T}_x f_{k-1} = \sqrt{\frac{\pi}{2}} g_{k-1}$  for all  $k \geq 1$  and  $\mathbf{T}_x f_{-1} = 0$ .

$$\begin{aligned} \sqrt{\frac{\pi}{2}} \mathbf{T}_x f_{k-1}(x) &= \sqrt{\frac{\pi}{2}} \frac{1}{\pi} \, p.v. \int_{-1}^1 \frac{f_{k-1}(x')}{x' - x} \, dx' = -\frac{1}{\pi} \, p.v. \int_{-1}^1 \frac{T_k(x')}{x' - x} \, dx' \\ &= -\frac{1}{\pi} \, p.v. \int_{-1}^1 \frac{\cos(k \arccos(x'))}{x' - x} \, dx'. \end{aligned}$$

The substitutions  $x = \cos(\xi)$ ,  $x' = \cos(\eta)$ , and formula (4.8) lead to

$$\begin{aligned} \sqrt{\frac{\pi}{2}} \mathbf{T}_x f_{k-1}(x) &= -\frac{1}{\pi} \int_0^\pi \frac{\cos(k\eta)}{\cos \eta - \cos \xi} \sin \eta \, d\eta \\ &\stackrel{(4.8)}{=} \sin(k\xi) = \sin(k \arccos(x)) = \sin(\arccos(x)) \frac{\sin(k \arccos(x))}{\sin(\arccos(x))} \\ &= \begin{cases} \sqrt{1-x^2} U_{k-1}(x) = \sqrt{\frac{\pi}{2}} g_{k-1}(x), & \text{for } k \geq 1, \\ 0, & \text{for } k = 0. \end{cases} \end{aligned}$$

□

With the complete orthonormal system  $(f_k)_{k \geq -1}$  we can express the solution of the wavefront reconstruction problem in (4.5) as a linear combination of basis functions

$$\Phi(x, y) = \sum_{k=-1}^{\infty} \Phi_{k,y} f_k(x) \quad (4.9)$$

with real coefficients  $\Phi_{k,y} = \langle \Phi(\cdot, y), f_k \rangle_\omega$  for  $k \geq -1$ . Note that we only consider measurements in x-direction and fix  $y$  to obtain a one dimensional reconstruction problem. Further explanations of the reduction from the two dimensional problem to a one dimensional problem will be given in the next Section.

Obviously, for  $\mathbf{T}_x$  defined in (4.3), the application of Proposition 4.4 and (4.9) results in

$$\begin{aligned} (\mathbf{T}_x \Phi)(\cdot, y) &= \mathbf{T}_x \left( \sum_{k=-1}^{\infty} \Phi_{k,y} f_k \right) \\ &= \Phi_{-1,y} \mathbf{T}_x f_{-1} + \sum_{k=0}^{\infty} \Phi_{k,y} g_k = \sum_{k=0}^{\infty} \Phi_{k,y} g_k = \sum_{k=0}^{\infty} \langle \Phi(\cdot, y), f_k \rangle_{\omega} g_k. \end{aligned} \quad (4.10)$$

This representation is similar to a singular value expansion of the operator  $\mathbf{T}_x$ . Although the non-compactness of  $\mathbf{T}_x$  does not allow a singular system  $(\sigma_k, f_k, g_k)_{k \geq 0}$  in the usual sense, equality (4.10) describes a *singular value type expansion* (with all “singular” values equal to one) of the operator  $\mathbf{T}_x$ . In contrast to compact operators, zero is not an accumulation point of the singular type values  $(\sigma_k)$ . The fact that all singular values are equal to one follows from the proper choice of the weighted Lebesgue space. Since the singular values do not decrease to zero, and therefore all contributions to the solution have the same weight, the application of regularization methods for the problem of wavefront reconstruction from pyramid sensor data based on a singular value type expansion of the finite Hilbert transform in  $\mathcal{L}_2^{\omega}([-1, 1])$  is not necessary.

Equation (4.10) and the injectivity of  $\mathbf{T}_x$  characterize

$$\begin{aligned} \mathcal{N}(\mathbf{T}_x) &= \{0\}, \\ \mathcal{N}(\mathbf{T}_x)^{\perp} &= \overline{\text{lin}\{f_k : k \geq -1\}}^{\mathcal{L}_2^{\omega}([-1, 1])} = \mathcal{L}_2^{\omega}([-1, 1]), \\ \mathcal{R}(\mathbf{T}_x) &= \text{lin}\{g_k : k \geq 0\}. \end{aligned}$$

Note that  $\mathcal{R}(\mathbf{T}_x)$  does not contain constant functions. However, a global piston mode, which is described by a constant function over the whole aperture, cannot be detected by the pyramid wavefront sensor anyway (cf Proposition 5.1).

Using the singular type system  $(f_k, g_k)_{k \geq 0}$  the Moore-Penrose inverse of the operator  $\mathbf{T}_x$  is represented as a sum.

**Theorem 4.5.** *Let  $\mathbf{T}_x$  be defined in (4.3) with corresponding singular type system  $(f_k, g_k)_{k \geq 0}$  given in (4.7). Then, the following assertions hold:*

- i)  $s_x(\cdot, y) \in \mathcal{D}(\mathbf{T}_x^{\dagger}) \iff \sum_{k=0}^{\infty} |\langle s_x(\cdot, y), g_k \rangle_{\omega}|^2 < \infty. \quad (\text{Picard criterion})$
- ii) *If  $s_x(\cdot, y) \in \mathcal{D}(\mathbf{T}_x^{\dagger})$ , then  $\mathbf{T}_x^{\dagger} s_x(\cdot, y) = \sum_{k=0}^{\infty} \langle s_x(\cdot, y), g_k \rangle_{\omega} f_k$ .*

*Proof.* The proof of the Theorem is analogous to that one of [58, Theorem 2.8] for compact operators.  $\square$

Theorem 4.5 characterizes the best approximate solution of equation (4.5). We describe the reconstructed wavefront  $\Phi(\cdot, y) \in \mathcal{L}_2^\omega([-1, 1])$  by

$$\Phi(x, y) = \sum_{k=0}^{\infty} \langle -2s_x(\cdot, y), g_k \rangle_\omega f_k(x). \quad (4.11)$$

Using the above formula we are able to reconstruct all modes of the incoming phase except constant terms, called global piston modes. Investigations of the pyramid and roof sensor operators show that these modes are in the null space of the operators, i.e., cannot be seen by the sensor (cf Proposition 5.1). Hence, equation (4.11) provides a unique reconstruction up to a constant additive term which, due to the null space of the operator, suffices for wavefront reconstruction from pyramid sensor data.

### 4.3 Numerical validation

For testing the effectiveness of the proposed method, we use the end-to-end simulation tool Octopus provided by the European Southern Observatory. We consider the closed loop performance of a large-scale XAO system on a telescope with a primary mirror diameter of  $D = 42$  m as it was originally planned for the ELT. The measurements of the incoming phase are received from a pyramid wavefront sensor. Furthermore, we assume a 9-layer atmospheric model where each layer is a random realization of the von Karman power spectrum. The system runs at a frequency of 3 kHz and we consider higher-order DM influence functions. The simulation parameters are summarized in Table 4.1. A simple integrator is used for the temporal control and the gain is optimized manually (on 500 time steps) with a resolution of 0.1.

For the numerical implementation, we choose the number of singular type functions in (4.11) such that we only use those with spatial frequencies which can be detected by the sensor. Thus, the Chebychev expansion is truncated at a value  $k_{max}$  corresponding to the highest frequency seen by the sensor.

Due to the fact that the sensor provides measurements which are averaged over subapertures, the sampling points are suggested by the model itself as the middle points of subapertures in  $x$ - and  $y$ -direction  $\{x_j^m\}$  and  $\{y_j^m\}_{1 \leq j \leq n}$  for  $j = 1, \dots, n$ , where  $n$  is the number of subapertures. The operator  $\mathbf{T}_x$  acts row-wise and therefore independently for  $y$  onto the wavefront. Hence, we reduce the two dimensional problem of wavefront reconstruction (4.5) to a one dimensional problem by fixing  $\bar{y} \in \{y_j^m\}$  and considering

$$s_x(x, \bar{y}) = -\frac{1}{2} (\mathbf{T}_x \Phi)(x, \bar{y}).$$

As already mentioned, we substitute the annular telescope aperture  $\Omega$  onto the squared region  $[-1, 1]^2$ , i.e.,  $\Omega_y \times \Omega_x \subset [-1, 1] \times [-1, 1]$ , and split  $\Omega$  into  $n \times n$  subapertures of size  $d = \frac{D}{n}$ . We assume the sensor data  $s_j = s(x_j^m)$  to be given in the middle points of subapertures  $\Omega_j^{\bar{y}} = [x_{j-1}^{\bar{y}}, x_j^{\bar{y}}]$ , where  $\{x_j^{\bar{y}}\}_{1 \leq j \leq n+1}$  represent the corner points of subapertures. There exist several possibilities for the representation of the measurements,

---

**Main parameters**

---

telescope diameter 42 m  
 central obstruction 28%  
 science target on-axis (SCAO)  
 pyramid WFS  
 science band K (2200 nm)  
 sensing band R (700 nm)  
 PWFS FoV 2.3 arcsec  
 frame rate 3 kHz  
 DM delay 1  
 higher-order DM influence functions  
 von Karman atmospheric model with  $L_0 = 25$  m  
 9 simulated atmospheric layers with heights from 47 m to 18 km  
 Fried radius  $r_0 = 0.129$  m for median atmosphere

---

Table 4.1: Parameters of ELT simulations for testing the SVTR.

e.g., spline functions. In our approach, we assume that the pyramid data are a linear combination of characteristic functions of the subapertures, i.e.,

$$s_x(x, \bar{y}) = \sum_{i=1}^n s_i \mathcal{X}_{\Omega_i^{\bar{y}}}(x).$$

Under these assumptions the Picard criterion of Theorem 4.5 is fulfilled and equation (4.11) reads as

$$\begin{aligned} \Phi_x(x, \bar{y}) &= \sum_{k=0}^{k_{max}} \langle -2s_x(\cdot, \bar{y}), g_k \rangle_{\omega} f_k(x) = -2 \sum_{k=0}^{k_{max}} \int_{-1}^1 \frac{s_x(x', \bar{y}) g_k(x')}{\sqrt{1-x'^2}} dx' f_k(x) \\ &= -2 \sum_{k=0}^{k_{max}} \int_{-1}^1 \frac{\sum_{i=1}^n s_i \mathcal{X}_{\Omega_i^{\bar{y}}}(x') g_k(x')}{\sqrt{1-x'^2}} dx' f_k(x) \\ &= -2 \sum_{i=1}^n s_i \sum_{k=0}^{k_{max}} \int_{x_{i-1}^{\bar{y}}}^{x_i^{\bar{y}}} \frac{g_k(x')}{\sqrt{1-x'^2}} dx' f_k(x) = -2 \sum_{i=1}^n s_i \alpha_i(x, \bar{y}) \end{aligned}$$

if we define

$$\alpha_i(x, \bar{y}) := \sum_{k=0}^{k_{max}} \int_{x_{i-1}^{\bar{y}}}^{x_i^{\bar{y}}} \frac{g_k(x')}{\sqrt{1-x'^2}} dx' f_k(x).$$

Note that the functions  $\alpha_i(x, \bar{y})$  are independent of the actual measurements and can be pre-computed. Therefore, the truncation mode  $k_{max}$  do not influence the speed of the algorithm.

In principle, the wavefront can be reconstructed from either the measurements in  $x$ - or  $y$ -direction. However, due to strong horizontal and vertical artifacts in the single reconstructions, we use both measurement sets (see Section 5.2.4 for more precise investigations). One way of combining the restored phases is the following: For every fixed  $\bar{y} \in \{y_j^m\}_{1 \leq j \leq n}$  we compute  $\Phi_x(x, \bar{y})$  and for every fixed  $\bar{x} \in \{x_j^m\}_{1 \leq j \leq n}$  we calculate  $\Phi_y(\bar{x}, y)$  accordingly. In total, we obtain two reconstructions and describe the final reconstructed wavefront  $\tilde{\Phi}(x, y)$  by the arithmetic mean of the two reconstructions  $\Phi_x$  and  $\Phi_y$  as proposed in [191].

Altogether, the proposed method consists in a multiplication of the measurements with the pre-computed functions  $\alpha_i(x, \bar{y})$  containing all the information about the singular system and a final averaging of the two reconstructions. We multiply the data  $s_x$  and  $s_y$  of size  $\sqrt{N} \times \sqrt{N}$  with the functions  $\alpha_i$  of size  $\sqrt{N} \times \sqrt{N}$  where  $N$  denotes the total number of subapertures. Hence, the computational complexity of the method is composed of  $\mathcal{O}(N\sqrt{N})$  for the multiplication and  $\mathcal{O}(\sqrt{N})$  for the summation and scales as  $\mathcal{O}(N^{3/2})$  in total.

We test the performance of the method for an XAO system having a  $200 \times 200$  pyramid wavefront sensor without modulation. The quality is evaluated for median atmospheric conditions (Fried radius  $r_0 = 0.129$  m) and a photon flux of 10000 photons per subaperture per frame as summarized in Table 4.2. In order to get a fast convergence to high Strehl ratios and to reduce the computational effort of the method, for the first 14 time steps we use the *Cumulative Reconstructor with Domain Decomposition* developed for Shack-Hartmann sensors [179].

First, we analyze the behavior of the errors of the presented reconstruction method in a self-created simulation environment. We use a pyramid sensor model given by the finite Hilbert transform without any additional influences in the forward model, i.e., we use data generated by the application of the finite Hilbert transform instead of pyramid sensor measurements. The problem is also known as airfoil equation. One can immediately see in Figure 4.2 that the reconstruction results are good in the interior of the telescope pupil and the main error sources are at the boundary of the annular aperture.

Test parameters	
modulation radius in $\lambda/D$	0
number of subapertures	$200 \times 200$
number of active subapertures	28796 out of 40000
atmosphere	median
photons per subaperture	10000
iterations	1000

Table 4.2: Test case setting for Octopus simulations using the SVTR.

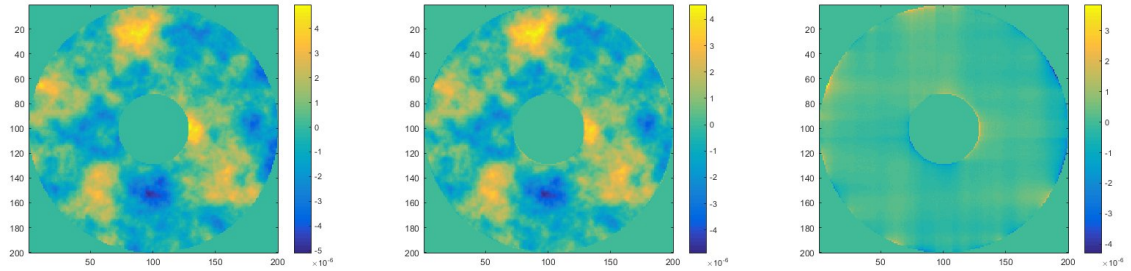


Figure 4.2: Wavefront reconstruction with the SVTR, source [107]. The incoming wavefront averaged over subapertures, the reconstructed wavefront as well as the residual wavefront are plotted for the reconstruction without measurement extension. The highest errors occur at the boundary of the telescope pupil mask. The RMSE is around  $3.1527 \times 10^{-7}$ .



Figure 4.3: Scheme of the measurement continuation, [107]. For the iterative method with measurement extension we reconstruct on the whole square  $[-1, 1] \times [-1, 1]$ . In the darkgray region the real measurements are known. Outside the annular shape (lightgray region) we calculate extended measurements using the finite Hilbert transform operator.

### 4.3.1 Iterative reconstruction using a measurement extension

In order to reduce the reconstruction errors at the boundary of the pupil, we establish a measurement extension for our method. The idea is to create data at a bigger domain than provided by the wavefront sensor. Similar data extrapolation approaches using for example Gerchberg-type iterations or extensions by copying the boundary slope have already been investigated in [20, 161, 177, 231, 232] for different kinds of wavefront sensors. In contrast to these methods, we concentrate on measurement continuation especially for pyramid sensors. Due to the fact that the forward model of

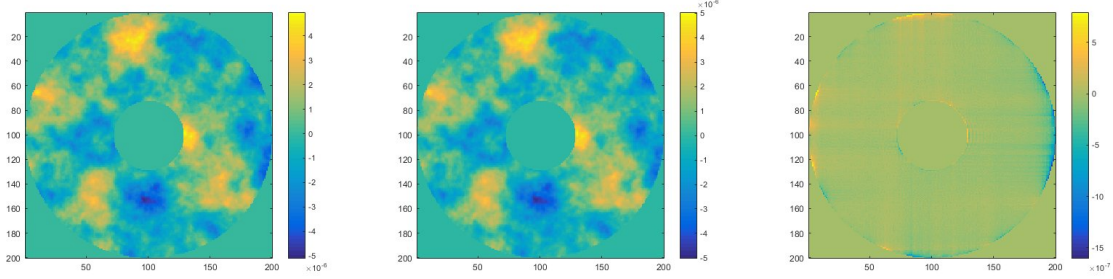


Figure 4.4: SVTR with iterative measurement extension, source [107]. The incoming wavefront averaged over subapertures, the reconstructed wavefront as well as the residual wavefront are plotted for the iterative reconstruction with measurement extension. Compared to Figure 4.2, we could improve the errors on the boundary. After 20 iteration steps, the RMSE is around  $8.8045 \times 10^{-8}$ .

the non-modulated PWFS is approximated by the finite Hilbert transform, we compute additional data outside the aperture by the application of the Hilbert transform:

Let  $s_x^{real}$  and  $s_y^{real}$  be real PWFS data given in the middle points of subapertures of the annular telescope pupil and  $\mathbf{T}_M$  with  $M(x, y) := (x, y) \cdot \mathcal{X}_{([-1,1] \times [-1,1]) \setminus \Omega}(x, y)$  a multiplication operator that sets measurements inside the annular aperture  $\Omega$  to zero. The operator  $\tilde{\mathbf{E}} : \Phi \rightarrow \tilde{s}$  describes the forward simulation necessary for the extension, e.g., the application of the finite Hilbert transform

$$\tilde{s}(x, y) = \tilde{\mathbf{E}}\Phi(x, y) = -\frac{1}{2\pi} p.v. \int_{-1}^1 \frac{\Phi(x', y)}{x' - x} dx',$$

and  $\mathbf{E}^{-1} : s \rightarrow \tilde{\Phi}$  the Singular Value Type Reconstructor as proposed above but now on the square region  $[-1, 1] \times [-1, 1]$ , i.e., we skip the transition to the borders of the telescope aperture. For the first iteration step we do not have any information on the incoming phase outside the telescope pupil. Therefore, we fill the square  $[-1, 1] \times [-1, 1]$  outside the annular aperture with zeros. Unlike previously, after the reconstruction  $\mathbf{E}^{-1}$  we obtain data of the incoming phase on the whole region  $[-1, 1] \times [-1, 1]$ . Consequently, the application of the forward operator  $\tilde{\mathbf{E}}$  delivers suitable measurements on the whole square. From now on, we use measurements provided by the pyramid wavefront sensor in the area of the telescope aperture (depicted as darkgray region in Figure 4.3) and self-created data in the region of the square left over (indicated as lightgray region in Figure 4.3). In order to get extended measurements

$s_{x,i}^{square}$  and  $s_{y,i}^{square}$ ,  $1 \leq i \leq i_{max}$  on the whole square  $[-1, 1] \times [-1, 1]$ , we apply

$$s_{x,1}^{square} = s_x^{real} + \text{zero-padding}$$

for the first iteration step and

$$s_{x,i+1}^{square} = \beta \mathbf{T}_M \tilde{\mathbf{E}} \mathbf{E}^{-1} s_{x,i}^{square} + s_x^{real}$$

with an attenuation coefficient  $\beta$  for  $2 \leq i \leq i_{max}$ . The data  $\{s_{y,i}^{square}\}_{1 \leq i \leq i_{max}}$  are computed accordingly. This type of fixpoint iteration is performed until we reach satisfying reconstruction quality. Due to the uniqueness up to modes of order zero (piston mode) of the reconstruction using a singular value type expansion in (4.11) represented by the operator  $\mathbf{E}^{-1}$ , for every extension technique  $\tilde{\mathbf{E}}$  (which in this setting is the finite Hilbert transform) we obtain a unique solution in  $\mathcal{N}(\mathbf{E})^\perp$ . Let us again assume that our extended measurements are given by

$$s^{square} = s^{real} + s^{ext}$$

for the real pyramid sensor measurements  $s^{real}$  and the artificially extended measurements  $s^{ext} = \mathbf{T}_M \tilde{\mathbf{E}} \mathbf{E}^{-1} s^{square}$  with  $s^{ext}|_\Omega = 0$ . Since  $\mathbf{E}^{-1} s^{real}$  and  $\mathbf{E}^{-1} s^{ext}$  deliver unique solutions in  $\mathcal{N}(\mathbf{E})^\perp$ , we obtain, due to linearity of the finite Hilbert transform operator, a unique reconstruction

$$\tilde{\Phi} = \mathbf{E}^{-1} s^{square} = \mathbf{E}^{-1} s^{real} + \mathbf{E}^{-1} s^{ext}$$

for each extension  $s^{ext}$  as well.

Numerical results show that the singular value type reconstruction method including measurement extension delivers smaller errors at the boundary of the annular aperture shape as shown in Figure 4.4. After 20 iterations we could improve the RMSE (root-mean-square error) from  $3.1527 \times 10^{-7}$  to  $8.8045 \times 10^{-8}$ . The biggest reconstruction errors appear at the domain where the boundary of the telescope pupil reaches the limits of the interval  $[-1, 1]$ . From the theoretical point of view this errors are confirmed. The distortions result from the singularities of the weight function near  $x = \pm 1$ . One only gets a stable inversion of the finite Hilbert transform in the interval  $[a, b]$  if one has information on a slightly bigger interval  $[a - \epsilon, b + \epsilon]$  for  $\epsilon > 0$ . For even larger extensions and further reduction of the errors near  $x = \pm 1$  we only attained slight improvements with a gain of less than 0.01 in terms of the LE Strehl ratio.

Let us now test the reconstruction quality of the proposed algorithms using the simulation tool Octopus. The convergence rates of both singular value type reconstruction methods with and without measurement extension are illustrated in Figure 4.5. It indicates the resulting long-exposure Strehl ratio in the K-band. For the second method, we use CuReD for the first 14 time steps of the simulation and afterwards measurement continuation with 3 iterations until time step 40. After 1000 iterations the LE Strehl ratio is around 0.89 for both reconstruction approaches.

Finally, we compare the Hilbert transform methods SVTR and FHTR (cf Section 7.1.7 and [191]) with Octopus results summarized in Table 4.3. The simulation parameters

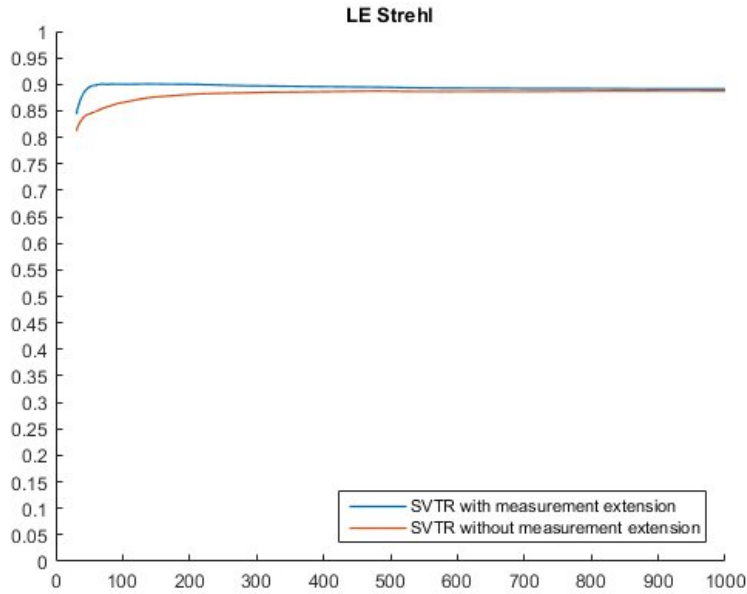


Figure 4.5: LE Strehl ratio in the K-band obtained with the singular value type reconstructor using the parameters from Table 4.2, source [107]. At the beginning, the continuation of measurements guarantees a faster convergence to higher Strehl ratios. After 1000 iterations the LE Strehl ratio is about 0.89 for both SVTR methods.

for the METIS and EPICS instruments of the ELT correspond to those later specified in Table 7.3 for the non-modulated sensor without taking telescope spiders into account. A direct comparison of both Hilbert transform methods shows that the FHTR outperforms the SVTR for simulations of the METIS instrument while for the EPICS instrument it is the other way round. The better performance of the SVTR on EPICS may come from a smaller subaperture size on the XAO system compared to the SCAO system of METIS to which the SVTR method is quite sensitive.

photon flux	EPICS		METIS	
	FHTR	SVTR	FHTR	SVTR
5		0.7826		
10		0.8331		0.5143
50	0.853	0.8840		0.7372
100		0.8867		0.7379
1000		0.8876		0.7386
10000		0.8876	0.779	0.7404

Table 4.3: LE Strehl ratios obtained with the Finite Hilbert Transform Reconstructor and the Singular Value Type Reconstructor on an XAO system and a SCAO system.

## 4.4 Summary on the SVTR method

We have presented a new method of wavefront reconstruction for the non-modulated pyramid sensor by accurately inverting the finite Hilbert transform. The method is based on a singular value type expansion developed for the finite Hilbert transform operator. The singular functions correspond to weighted Chebychev polynomials, the singular values are all equal to one. The new pyramid reconstructor provides good quality and speed results for small subaperture sizes but a huge number of active subapertures or DM actuators. With a computational complexity of  $\mathcal{O}(N^{3/2})$  the proposed method is very efficient which makes the approach attractive for wavefront reconstruction, especially in extreme AO.

Until now, the method has only been applied to data from pyramid sensors without modulation. The underlying theory can be adapted to the modulated sensor as well but the singular value decomposition of the considered pyramid sensor operator will change. Hence, one needs to find the singular values and singular functions of the linearized operators including modulation, e.g., of  $\mathbf{L}^c$  defined in (3.28). Additionally, further improvements may be attainable for the usage of a singular value decomposition of more appropriate pyramid sensor models. For instance, we expect higher reconstruction quality if we linearize the full pyramid sensor operator and derive its singular value expansion. However, this derivation is extremely difficult or may even be impossible. Moreover, we want to remark that we considered the SVD in the weighted Lebesgue space  $\mathcal{L}_2^\omega([-1, 1]^2)$ . If we examine the pyramid sensor operator from  $\mathcal{H}^{11/6}(\mathbb{R}^2)$  into  $\mathcal{L}_2(\mathbb{R}^2)$ , the corresponding SVD changes, since it is related to the inner product. The choice of the underlying space can affect the accuracy of wavefront estimates as well.

In principle, the above presented iterative measurement extension method can be combined with any algorithm for wavefront estimation. The idea was as well investigated in the presence of large telescope spiders. Unfortunately, the iterative measurement continuation applied under the obstructed spider areas could not avoid differential piston effects that severely degrade the image quality as precisely described in Section 8.3.2.

A detailed comparison of the quality performance between the SVTR algorithm and other wavefront reconstruction methods for the PWFS is given in Section 7.2. Briefly summarized, with respect to computational time, the SVTR takes an intermediate position. The same is valid for the obtainable reconstruction quality. However, we strongly believe in big improvements of the approach for future investigations of more appropriate pyramid sensor models.



## Chapter 5

# Linear wavefront reconstruction using iterative methods

This Chapter addresses the problem of stable and highly accurate wavefront correction for large-scale real-time closed loop Adaptive Optics systems on ELTs using iterative methods. We study and compare the performance (in terms of correction quality and speed) of well-known mathematical algorithms for solving Inverse Problems, namely the conjugate gradient method, steepest descent, Landweber, Landweber-Kaczmarz, and steepest descent-Kaczmarz iteration. The suggested approaches make real-time wavefront reconstruction easily feasible even for XAO systems. Parts of this Chapter rely on [109] and are a joint work with Iuliia Shatkhina and Ronny Ramlau.

We start with recalling the theoretical principles of wavefront sensing using the pyramid sensor in Section 5.1. Afterwards, we describe several iterative algorithms, namely the conjugate gradient method for the normal equation and the steepest descent method, Landweber iteration as well as Kaczmarz type algorithms in Section 5.2. This Section contains details on the numerical implementation of the involved operators as well. Section 5.3 presents the performance of the proposed algorithms and a comparison with respect to the achieved reconstruction quality. Finally, in Section 5.4 we evaluate and compare the computational complexities of the analyzed approaches. Both the reconstruction quality and the speed of the algorithms are additionally compared versus those of an interaction-matrix-based approach (cf Section 8.2).

### 5.1 Underlying forward models

All algorithms presented in this Chapter are based on a linearization of the wavefront sensor operators derived in Section 3.4. The corresponding adjoint operators were investigated in Section 3.5. The underlying theory needed for the application of the iterative methods is briefly recalled now. For a precise analysis of the full pyramid sensor model, details about the linearization procedure and proofs we refer the reader to Chapter 3 of the Thesis.

Generally, the two signal sets  $s = [s_x, s_y]$  provided by the pyramid sensor are given by

$$\begin{aligned} s_x &= -\frac{1}{2} \mathbf{P}_x \Phi \\ s_y &= \frac{1}{2} \mathbf{P}_y \Phi. \end{aligned} \quad (5.1)$$

Due to the symmetry of the problem, we only consider measurements in  $x$ -direction in the following. Data in  $y$ -direction are investigated analogously. Under the roof sensor assumption, the PWFS signal corresponding to no, circular and linear modulation is approximated by

$$s_x^{\{n,c,l\},lin} = -\frac{1}{2} \left( \mathbf{R}_x^{\{n,c,l\},lin} \Phi \right) (x, y)$$

with

$$\left( \mathbf{R}_x^{\{n,c,l\},lin} \Phi \right) (x, y) := \mathcal{X}_\Omega(x, y) \frac{1}{\pi} \int_{\Omega_y} \frac{[\Phi(x', y) - \Phi(x, y)] \cdot k^{\{n,c,l\}}(x' - x)}{x' - x} dx' \quad (5.2)$$

indicating the linearized roof sensor operators (cf Theorem 3.13).

The linearized roof sensor operators  $\mathbf{R}_x^{\{n,c,l\},lin}$  offer a further possibility for simplification of the model due to the splitting

$$\left( \mathbf{R}_x^{\{n,c,l\},lin} \Phi \right) (x, y) = \mathcal{X}_\Omega(x, y) \left[ \left( \mathbf{L}_x^{\{n,c,l\}} \Phi \right) (x, y) - \Phi(x, y) \cdot \left( \mathbf{L}_x^{\{n,c,l\}} 1 \right) (x, y) \right] \quad (5.3)$$

for the integral operators  $\mathbf{L}_x^{\{n,c,l\}} : \mathcal{H}^{11/6}(\mathbb{R}^2) \rightarrow \mathcal{L}_2(\mathbb{R}^2)$  defined by

$$\left( \mathbf{L}_x^{\{n,c,l\}} \Phi \right) (x, y) := \frac{1}{\pi} p.v. \int_{\Omega_y} \frac{\Phi(x', y) k^{\{n,c,l\}}(x' - x)}{x' - x} dx' \quad (5.4)$$

as introduced in Definition 3.14 and (3.29). Dropping the second term in (5.3) leads to the Inverse Problem

$$s_x = -\frac{1}{2} \mathbf{L}_x^{\{n,c,l\}} \Phi \quad (5.5)$$

for pyramid sensor data  $s_x$ .

The adjoint operators of the roof sensor approximations in  $\mathcal{L}_2(\mathbb{R}^2)$  are represented by

$$\begin{aligned} \left( \left( \mathbf{L}_x^{\{n,c,l\}} \right)^* \Psi \right) (x, y) &= -\frac{1}{\pi} p.v. \int_{\Omega_y} \frac{\Psi(x', y) \cdot k^{\{n,c,l\}}(x' - x)}{x' - x} dx', \\ \left( \left( \mathbf{R}_x^{\{n,c,l\},lin} \right)^* \Psi \right) (x, y) &= -\frac{1}{\pi} p.v. \int_{\Omega_y} \frac{[\Psi(x', y) + \Psi(x, y)] \cdot k^{\{n,c,l\}}(x' - x)}{x' - x} dx'. \end{aligned}$$

as given in Proposition 3.16 and Proposition 3.17. Additionally, we can consider the adjoints from  $\mathcal{L}_2(\mathbb{R}^2)$  into  $\mathcal{H}^{11/6}(\mathbb{R}^2)$  by utilizing the embedding described in Section 3.5.

## 5.2 Iterative wavefront reconstruction methods

In this Section, we adapt well-known iterative algorithms to the problem of wavefront reconstruction from pyramid sensor data.

For wavefront reconstruction we solve the two integral equations

$$-\frac{1}{2} \mathbf{R}_x^{\{n,c,l\},lin} \Phi = s_x \quad (5.6)$$

$$\frac{1}{2} \mathbf{R}_y^{\{n,c,l\},lin} \Phi = s_y, \quad (5.7)$$

where  $\mathbf{R}_x^{\{n,c,l\},lin}$  are the linearized operators of the roof WFS and  $s$  real pyramid sensor measurements. For simplicity of notation, we use  $\mathbf{Q} := \frac{1}{2} \cdot [-\mathbf{R}_x^{\{n,c,l\},lin}, \mathbf{R}_y^{\{n,c,l\},lin}]$  in the following since the basic idea is the same for all types of modulation. Moreover, we only concentrate on solving the Inverse Problem (5.6)-(5.7), but mention that solutions of (5.1) and (5.5) can be calculated accordingly.

Let us focus on concrete wavefront reconstruction algorithms for pyramid sensor data using iterative methods. In particular, we consider the conjugate gradient algorithm for the normal equation (CGNE), the steepest descent (SD), and Landweber iteration. Since the pyramid sensor provides two measurements  $s_x$  and  $s_y$ , the above named approaches are applied twice, i.e., separately in both directions, and deliver two solutions  $\Phi = [\Phi_x, \Phi_y]$ , one in  $x$ - and one in  $y$ - direction. The final reconstruction  $\Phi^{rec}$  is then computed as the average of the two temporary solutions. An alternative combination of the two measurements  $s_x$  and  $s_y$  using Kaczmarz loops is investigated in Section 5.2.4. Note that the theory of the presented algorithms is mainly based on [58, 133]. The considered norms are the  $\mathcal{L}_2$ -norms.

### 5.2.1 CGNE approach

The conjugate gradient (CG) method is one of the most powerful algorithms for solving self-adjoint, positive (semi-)definite linear equations [22, 58, 90, 96, 101, 118]. For solving the wavefront reconstruction problem we apply the conjugate gradient method to the normal equation

$$\mathbf{Q}^* \mathbf{Q} \Phi = \mathbf{Q}^* s. \quad (5.8)$$

Let  $\mathbf{Q}^\dagger$  denote the Moore-Penrose generalized inverse. The CG-iterates  $(\Phi_i)$  converge to  $\mathbf{Q}^\dagger s$  for all  $s \in \mathcal{D}(\mathbf{Q}^\dagger)$  [58] by requiring the fewest iterations among all semiiterative methods.

Algorithm 5.1 describes the CGNE method applied to the Inverse Problem of wavefront reconstruction from pyramid wavefront sensor data. Note that for the following algorithms we fix the number of iterations by  $K$ . Further considerations on stopping rules and optimal choices of  $K$  follow in Section 5.3.2.

---

**Algorithm 5.1** CGNE for pyramid sensors
 

---

 choose  $\Phi_0$ , initialize  $d_0 = s - \mathbf{Q}\Phi_0$ ,  $p_1 = s_0 = \mathbf{Q}^*d_0$ 
**for**  $i = 1, \dots, K$  **do**

$$q_i = \mathbf{Q}p_i$$

$$\alpha_i = \|s_{i-1}\|^2 / \|q_i\|^2$$

$$\Phi_i = \Phi_{i-1} + \alpha_i p_i$$

$$d_i = d_{i-1} - \alpha_i q_i$$

$$s_i = \mathbf{Q}^*d_i$$

$$\beta_i = \|s_i\|^2 / \|s_{i-1}\|^2$$

$$p_{i+1} = s_i + \beta_i p_i$$

**endfor**

$$\Phi^{rec} = (\Phi_{x,K} + \Phi_{y,K}) / 2$$


---

### 5.2.2 Steepest descent approach

For solving the system (5.6)-(5.7) we are additionally interested in the method of steepest descent for which we consider different choices of the step sizes in the iterative process. For pyramid sensors, we use the SD method to minimize the least-squares functional

$$J(\Phi) = \|\mathbf{Q}\Phi - s\|_{\mathcal{L}_2}^2 \rightarrow \min. \quad (5.9)$$

The method of steepest descent was originally introduced by Cauchy [31] as one of the most basic procedures to minimize a differentiable functional. A popular step size is determined by an exact line search in the direction of the negative gradient. Alternative choices of the step size have already been considered, e.g., in [184, 185] and will be discussed below for the problem of wavefront reconstruction from pyramid data using the SD method. The gradient of the classical least-squares functional is given by

$$J'(\Phi) = \mathbf{Q}^*(\mathbf{Q}\Phi - s) \quad (5.10)$$

and the resulting algorithm reads as Algorithm 5.2.

---

**Algorithm 5.2** Steepest Descent for pyramid sensors
 

---

 choose  $\Phi_0$ 
**for**  $i = 1, \dots, K$  **do**

$$d_{i-1} = -J'(\Phi_{i-1})$$

$$\tau_{i-1} = \min_{t \in [0, \infty)} J(\Phi_{i-1} + td_{i-1})$$

$$\Phi_i = \Phi_{i-1} + \tau_{i-1} d_{i-1}$$

**endfor**

$$\Phi^{rec} = (\Phi_{x,K} + \Phi_{y,K}) / 2$$


---

### Step size choices and convergence

The speed of convergence of the gradient iteration

$$\begin{aligned}\Phi_i &= \Phi_{i-1} + \tau_{i-1}d_{i-1} \\ d_{i-1} &= -J'(\Phi_{i-1})\end{aligned}$$

depends highly on the choice of the step size  $\tau_i$ . We consider the classical steepest descent (line search) step size that is defined by

$$\tau_i^{SD} = \min_{t \in [0, \infty)} J(\Phi_i + td_i).$$

This means that an exact line search is performed in the direction of steepest descent which corresponds to the direction of the negative gradient. For the least-squares functional (5.9) and corresponding derivative (5.10), the steepest descent step size with  $d_i = -\mathbf{Q}^*(\mathbf{Q}\Phi_i - s)$  reads as

$$\tau_i^{SD} = \frac{\|d_i\|^2}{\|\mathbf{Q}d_i\|^2} \quad (5.11)$$

and results in the so called *Cauchy method*.

If we minimize the gradient norm along the search direction, we obtain another line search method for finite dimensions, namely the method of *minimal gradient* (MG) [46] given by

$$\tau_i^{MG} = \frac{\|\mathbf{Q}d_i\|^2}{\|\mathbf{Q}^*\mathbf{Q}d_i\|^2}. \quad (5.12)$$

From Cauchy-Schwarz inequality it follows  $\tau_i^{MG} \leq \tau_i^{SD}$ .

Because of zigzagging between consecutive steps the SD method suffers from slow convergence in some cases. To overcome these effects, a fast and efficient alternative step size choice was introduced by *Barzilai and Borwein* (BB) in [13]. The BB technique is motivated by quasi-Newton methods and derived from a two-point approximation to the secant equation. There exist two versions of the BB method which are defined by

$$\tau_i^{BB1} = \frac{\langle \Delta\Phi_i, \Delta d_i \rangle}{\langle \Delta d_i, \Delta d_i \rangle} \quad \text{and} \quad \tau_i^{BB2} = \frac{\langle \Delta\Phi_i, \Delta\Phi_i \rangle}{\langle \Delta\Phi_i, \Delta d_i \rangle}$$

with  $\Delta\Phi_i = \Phi_i - \Phi_{i-1}$  and  $\Delta d_i = d_i - d_{i-1}$ . Plugging in the calculations corresponding to Algorithm 5.2 we obtain

$$\begin{aligned}\Delta\Phi_i &= \Phi_i - \Phi_{i-1} = \tau_{i-1}d_{i-1}, \\ \Delta d_i &= d_i - d_{i-1} = -\mathbf{Q}^*\mathbf{Q}(\Phi_i - \Phi_{i-1}) = -\tau_{i-1}\mathbf{Q}^*\mathbf{Q}d_{i-1},\end{aligned}$$

since the involved operators are linear. Therefore, the BB step sizes are rewritten as

$$\tau_i^{BB1} = \frac{\|\mathbf{Q}d_{i-1}\|^2}{\|\mathbf{Q}^*\mathbf{Q}d_{i-1}\|^2} \quad \text{and} \quad \tau_i^{BB2} = \frac{\|d_{i-1}\|^2}{\|\mathbf{Q}d_{i-1}\|^2},$$

i.e.,

$$\tau_i^{BB1} = \tau_{i-1}^{MG} \quad \text{and} \quad \tau_i^{BB2} = \tau_{i-1}^{SD}.$$

The idea is to use additional information of the previous iteration to compute the step size for the current iteration. Once again with the Cauchy-Schwarz inequality we obtain  $\tau_i^{BB1} \leq \tau_i^{BB2}$ . Generally, while the SD and MG method decrease monotonically, the BB step size choices are non-monotone as the error behaves non-monotonously, i.e.,  $\|\Phi - \Phi_{i+1}\| \leq \|\Phi - \Phi_i\|$  for the true solution  $\Phi$  is not fulfilled for every iteration  $i$ . Nevertheless, the BB method converges to a solution of (5.9) as found in [170].

The *Cauchy-Barzilai-Borwein* (CBB) step size is based on the idea to use the SD and BB step size alternating. The method, which was introduced in 2003 and is also called *alternate step size* (AS) *gradient method*, aims at reducing the zigzag-effect of the Cauchy method [45], and therefore leads to a faster convergence. The promising alternative to the BB method reads as

$$\tau_i^{CBB} = \tau_i^{AS} = \begin{cases} \tau_i^{SD}, & \text{for } i \text{ odd,} \\ \tau_i^{BB2}, & \text{for } i \text{ even.} \end{cases}$$

Due to  $\tau_i^{BB2} = \tau_{i-1}^{SD}$ , we use the same step size twice in two consecutive iterations. Furthermore, an alternate version of the MG method called *alternate minimization* (AM) *gradient method* was proposed in [46] having an SD iteration for every second step. Generally, the SD method becomes faster when one non-monotone (e.g., BB) step is made even after several SD steps [230]. In addition, a variety of step size choices have been introduced using combinations or shortened step size versions of the above mentioned options.

To reduce the computational effort of the algorithms a fixed step size can be used. Step sizes which are tuned heuristically depend mainly on the size of the telescope and the resolution of the pyramid wavefront sensor as well as its modulation amplitude. The steepest descent algorithm for the least-squares functional (5.9) reduces to the standard Landweber iteration for a fixed step size  $\tau_i = \beta$ .

### 5.2.3 Landweber approach

For Landweber iteration [127], the normal equation (5.8) is transformed into the equivalent fixed point equation

$$\Phi = \Phi + \mathbf{Q}^*(s - \mathbf{Q}\Phi).$$

In order to ensure convergence by  $\|\mathbf{Q}\| \leq 1$  we introduce a relaxation parameter  $0 < \beta \leq \|\mathbf{Q}\|^{-2}$  and iterate by

$$\Phi_i = \Phi_{i-1} + \beta\mathbf{Q}^*(s - \mathbf{Q}\Phi_{i-1}), \quad i \in \mathbb{N}.$$

Then,  $(\Phi_i)$  converges to a least-squares solution of (5.6)-(5.7) for  $s \in \mathcal{D}(\mathbf{Q}^\dagger)$  [58].

The Landweber iteration modified for wavefront reconstruction based on pyramid sensor measurements is described by Algorithm 5.3).

---

**Algorithm 5.3** linear Landweber Iteration for Pyramid Sensors (LIPS)

---

choose  $\Phi_0$ , set relaxation parameter  $\beta$

**for**  $i = 1, \dots, K$  **do**

$$\Phi_i = \Phi_{i-1} + \beta \mathbf{Q}^* (s - \mathbf{Q}\Phi_{i-1})$$

**endfor**

$$\Phi^{rec} = (\Phi_{x,K} + \Phi_{y,K}) / 2$$


---

Besides the above discussed methods for pyramid sensors and the Singular Value Type Reconstructor introduced in Chapter 4, there already exist several algorithms providing two reconstructions, one from data  $s_x$  and one from data  $s_y$  [191, 196]. Let us now introduced a different approach which combines the reconstructions already during the iteration steps.

### 5.2.4 Kaczmarz methods for wavefront reconstruction from pyramid sensor data

For the reconstruction of the incoming wavefront, the pyramid sensor provides two data sets  $s_x$  and  $s_y$ . This structure gives rise to the question of why use both data sets for wavefront reconstruction at all. However, there are several facts that support the usage of both measurement sets. On the one hand, we expect better reconstruction quality in case we utilize more information. This argument is additionally strengthened by the presence of noise in the sensor measuring process. Moreover, it was already stated in [212] that only the combination of both pyramid data sets is completely meaningful. Deeper investigations of the underlying operators in  $x$ - and  $y$ -direction show that they have different null spaces, i.e., depending on the underlying model of the reconstructors there exist modes that cannot be reconstructed. For instance, pyramid and roof wavefront sensors are not able to detect a constant added to the incoming phase  $\Phi$ . This undetectable constant, called piston mode (mode of order 0), has no influence on the measurements  $s$ .

While the null space of the operators representing the pyramid sensor model consists only of the global piston mode, which anyway does not influence the imaging quality, the null spaces of the roof sensor operators in  $x$ - and  $y$ -direction contain more and different modes.

In order to characterize effects that are invisible in sensor data, we discuss selected wavefront modes (of order 0 and 1) which are elements of the null space of the roof wavefront sensor operators, i.e., phase elements that deliver measurements equal to

zero. For the following investigations, we will consider the mathematical forward model of the linearized roof sensor  $\mathbf{R}^{lin}$  and analyze the null spaces of the corresponding operators described by

$$\mathcal{N}(\mathbf{R}^{lin}) := \{\Phi \in \mathcal{H}^{11/6}(\mathbb{R}^2) \mid \mathbf{R}^{lin}\Phi = 0\}.$$

We study the response of the linearized roof sensor to a global piston mode shown in Figure 5.1 left. Hence, we define

$$\Phi_{piston}(x, y) = c \cdot \mathcal{X}_\Omega(x, y),$$

where  $c \in \mathbb{R}$  is a constant. Furthermore, we analyze how the sensor responds to modes of order 1 called tip & tilt modes (see Figure 5.1 middle and right) represented by

$$\Phi_{tip/tilt}(x, y) = (ax + by) \cdot \mathcal{X}_\Omega(x, y)$$

for  $a, b \in \mathbb{R}$ .

**Proposition 5.1.** *Constant functions  $c \cdot \mathcal{X}_\Omega$  with  $c \in \mathbb{R}$  are elements of the null space of the linearized roof sensor operators  $\mathbf{R}^{\{n,c,l\},lin} = [\mathbf{R}_x^{\{n,c,l\},lin}, \mathbf{R}_y^{\{n,c,l\},lin}]$  with  $\mathbf{R}_x^{\{n,c,l\},lin}$  defined in (5.2) and  $\mathbf{R}_y^{\{n,c,l\},lin}$  accordingly. Tip signals ( $cx \cdot \mathcal{X}_\Omega(x, y)$ ) are in the null space of  $\mathbf{R}_y^{\{n,c,l\},lin}$  and tilt signals ( $cy \cdot \mathcal{X}_\Omega(x, y)$ ) are in the null space of  $\mathbf{R}_x^{\{n,c,l\},lin}$ .*

*Proof.* Global piston modes  $c \cdot \mathcal{X}_\Omega$  are in the null space of the roof sensor operator because of

$$\begin{aligned} (\mathbf{R}_x^{\{n,c,l\},lin} \Phi_{piston})(x, y) &= \mathcal{X}_\Omega(x, y) \frac{1}{\pi} \int_{\Omega_y} \frac{[\Phi_{piston}(x', y) - \Phi_{piston}(x, y)] k^{\{n,c,l\}}(x' - x)}{x' - x} dx' \\ &= \mathcal{X}_\Omega(x, y) \frac{1}{\pi} \int_{\Omega_y} \frac{[c - c] k^{\{n,c,l\}}(x' - x)}{x' - x} dx' = 0 \end{aligned}$$

and  $\mathbf{R}_y^{\{n,c,l\},lin}(x, y)$  respectively.

For exact investigations of tip & tilt modes, we split  $\Phi_{tip/tilt}(x, y)$  into

$$\Phi_{tip}(x, y) = ax \cdot \mathcal{X}_\Omega(x, y) \quad \text{and} \quad \Phi_{tilt}(x, y) = by \cdot \mathcal{X}_\Omega(x, y).$$

Then, we consider

$$\begin{aligned} (\mathbf{R}_x^{\{n,c,l\},lin} \Phi_{tip})(x, y) &= \mathcal{X}_\Omega(x, y) \frac{1}{\pi} \int_{\Omega_y} \frac{[\Phi_{tip}(x', y) - \Phi_{tip}(x, y)] k^{\{n,c,l\}}(x' - x)}{x' - x} dx' \\ &= \mathcal{X}_\Omega(x, y) \frac{1}{\pi} \int_{\Omega_y} \frac{[a(x' - x)] k^{\{n,c,l\}}(x' - x)}{x' - x} dx' \\ &= \mathcal{X}_\Omega(x, y) \frac{1}{\pi} \int_{\Omega_y} a \cdot k^{\{n,c,l\}}(x' - x) dx' \end{aligned}$$

and

$$\begin{aligned} \left(\mathbf{R}_y^{\{n,c,l\},lin}\Phi_{tip}\right)(x,y) &= \mathcal{X}_\Omega(x,y)\frac{1}{\pi}\int_{\Omega_x}\frac{[\Phi_{tip}(x,y')-\Phi_{tip}(x,y)]k^{\{n,c,l\}}(y'-y)}{y'-y}dy' \\ &= 0 \end{aligned}$$

as well as

$$\begin{aligned} \left(\mathbf{R}_x^{\{n,c,l\},lin}\Phi_{tilt}\right)(x,y) &= \mathcal{X}_\Omega(x,y)\frac{1}{\pi}\int_{\Omega_y}\frac{[\Phi_{tilt}(x',y)-\Phi_{tilt}(x,y)]k^{\{n,c,l\}}(x'-x)}{x'-x}dx' \\ &= 0 \end{aligned}$$

and

$$\begin{aligned} \left(\mathbf{R}_y^{\{n,c,l\},lin}\Phi_{tilt}\right)(x,y) &= \mathcal{X}_\Omega(x,y)\frac{1}{\pi}\int_{\Omega_x}\frac{[\Phi_{tilt}(x,y')-\Phi_{tilt}(x,y)]k^{\{n,c,l\}}(y'-y)}{y'-y}dy' \\ &= \mathcal{X}_\Omega(x,y)\frac{1}{\pi}\int_{\Omega_x}\frac{[b(y'-y)]k^{\{n,c,l\}}(y'-y)}{y'-y}dy' \\ &= \mathcal{X}_\Omega(x,y)\frac{1}{\pi}\int_{\Omega_x}b\cdot k^{\{n,c,l\}}(y'-y)dy'. \end{aligned}$$

Altogether, we obtain that tip is in the null space of  $\mathbf{R}_y^{\{n,c,l\},lin}$  and tilt in the null space of  $\mathbf{R}_x^{\{n,c,l\},lin}$ .  $\square$

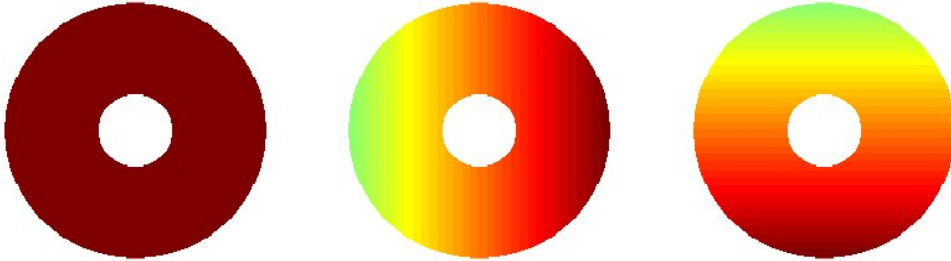


Figure 5.1: The figures indicate piston, tip and tilt mode (from left to right), source [109].

If we further simplify the roof sensor model by excluding the second term in (5.2) and consider the operators  $\mathbf{L}^{\{n,c,l\}}$  defined in (5.4), we note that these operators are injective, i.e.,  $\mathcal{N}(\mathbf{L}^{\{n,c,l\}}) = \{0\}$ . This assertion follows from the injectivity of the finite Hilbert transform shown in [57].

Note that the results of Proposition 5.1 are directly transferred to the non-linear roof sensor operators  $\mathbf{R}^{\{n,c,l\}}$  introduced in Definition 3.4. As soon as we consider functions

including various powers of  $x$  or  $y$  in  $\Phi_{tip/tilt}$ , the corresponding measurements in  $x$ - or  $y$ -direction are equal to zero as well. The fact that the roof sensor operators  $\mathbf{R}_x^{\{n,c,l\},lin}$  and  $\mathbf{R}_y^{\{n,c,l\},lin}$  have different null spaces intensifies the requirement of an appropriate combination of the two data sets  $s_x$  and  $s_y$  for reconstruction methods which are based on the roof sensor model.

One idea to appropriately combine both measurements is to reconstruct independently in both directions and average the reconstructions at the end as already considered for the CGNE, SD, and linear LIPS above. However, it is not guaranteed that the final (averaged) solution  $\Phi^{rec}$  fulfills both equations (5.6)-(5.7). Another possibility is to consider  $[\mathbf{Q}_x, \mathbf{Q}_y]$  as one single operator and a third one is to use a Kaczmarz strategy [116, 143] which is computationally cheaper and for which it is guaranteed that the equations (5.6)-(5.7) are fulfilled for the final solution. Kaczmarz methods in general have been developed for solving linear systems of equations. We have decided to implement Kaczmarz strategies for the pyramid sensor in combination with two of the above discussed algorithms.

### Landweber-Kaczmarz approach

In practice, the Landweber algorithm is used because it is simple and each iteration is cheap. Though, the process usually requires a high number of iterations. Anyway, we do not experience slow convergence for reconstruction from pyramid data due to a close similarity between adjoint and inverse operators as investigated in [107] for the non-modulated sensor, i.e., for the finite Hilbert transform operator. When using proper basis functions for the representation of the incoming wavefront  $\Phi$  and the measurements  $s = [s_x, s_y]$  (as later introduced in (5.13)), the involved operators can be precomputed offline. These facts make Landweber iteration coupled with a Kaczmarz strategy interesting for wavefront reconstruction from pyramid sensor data. A general convergence analysis of the linear Landweber-Kaczmarz method can be found in [126].

In the linear setting, the Landweber-Kaczmarz method for wavefront reconstruction from pyramid wavefront sensor measurements is introduced in Algorithm 5.4. Now, the two data sets are used alternating and measurements or reconstructions are combined already during two successive Landweber iteration steps.

### Steepest descent-Kaczmarz approach

The idea of modified steepest descent algorithms coupled with a Kaczmarz strategy is comparable to the method described in [33] for non-linear problems. As in the previous method, we cyclically consider each measurement equation (5.6) and (5.7).

Hence, for

$$J_x(\Phi) := \|\mathbf{Q}_x \Phi - s\|_{\mathcal{L}_2}^2, \quad J_y(\Phi) := \|\mathbf{Q}_y \Phi - s\|_{\mathcal{L}_2}^2,$$

---

**Algorithm 5.4** linear Kaczmarz-Landweber Iteration for Pyramid Sensors (KLIPS)

---

choose  $\Phi_0$ , set relaxation parameters  $\beta_1, \beta_2$   
**for**  $i = 1, \dots, K$  **do**  
 $\Phi_{i,0} = \Phi_{i-1}$   
 $\Phi_{i,1} = \Phi_{i,0} + \beta_1 \mathbf{Q}_x^* (s_x - \mathbf{Q}_x \Phi_{i,0})$   
 $\Phi_{i,2} = \Phi_{i,1} + \beta_2 \mathbf{Q}_y^* (s_y - \mathbf{Q}_y \Phi_{i,1})$   
 $\Phi_i = \Phi_{i,2}$   
**endfor**  
 $\Phi^{rec} = \Phi_K$

---

we modify Algorithm 5.2 and obtain the Steepest Descent-Kaczmarz (SD-K) method for wavefront reconstruction using pyramid sensors (Algorithm 5.5).

During an observation the reconstructions have to be repeated up to every 0.3 milliseconds. Assuming that the incoming wavefront do not change much from one time step to the next and, in particular, tip & tilt do not change significantly, another idea (implemented in Algorithm 5.6) would be to reconstruct in  $x$ -direction for even time steps  $t$  and in  $y$ -direction for the proximate odd time steps  $t + 1$ . The big advantage of Algorithm 5.6 consists in the reduction of the computational demand by more than 50% compared to the normal SD approach.

The post loop step of Algorithm 5.1 - 5.3, i.e., the averaging of the two reconstructions is not necessary for Algorithm 5.4 - 5.6 since we only obtain one reconstruction  $\Phi_K$ . Please note that for the Kaczmarz-type methods it is merely necessary to choose one

---

**Algorithm 5.5** Steepest Descent-Kaczmarz for pyramid sensors

---

choose  $\Phi_0$   
**for**  $i = 1, \dots, K$  **do**  
 $\Phi_{i-1,0} = \Phi_{i-1}$   
 $d_{i-1,1} = -J'_x(\Phi_{i-1,0})$   
 $\tau_{i-1,1} = \min_{t \in [0, \infty)} J_x(\Phi_{i-1,0} + td_{i-1,1})$   
 $\Phi_{i-1,1} = \Phi_{i-1,0} + \tau_{i-1,1} d_{i-1,1}$   
 $d_{i-1,2} = -J'_y(\Phi_{i-1,1})$   
 $\tau_{i-1,2} = \min_{t \in [0, \infty)} J_y(\Phi_{i-1,1} + td_{i-1,2})$   
 $\Phi_{i-1,2} = \Phi_{i-1,1} + \tau_{i-1,2} d_{i-1,2}$   
 $\Phi_i = \Phi_{i-1,2}$   
**endfor**  
 $\Phi^{rec} = \Phi_K$

---

initial guess  $\Phi_0$  instead of two as required for Algorithm 5.1 - 5.3.

---

**Algorithm 5.6** modified Steepest Descent-Kaczmarz for pyramid sensors

---

**if** ( $t \bmod 2 = 0$ ) **do**  
 apply Algorithm 5.2 in  $x$ -direction only  
**else if**  
 apply Algorithm 5.2 in  $y$ -direction only  
**endif**

---

### Details on the numerical implementation

To specify the representation of the incoming phase  $\Phi$  and the measurements  $s$  we denote the number of subapertures by  $n$ . There are various possible representations of the phase and the measurements, e.g., Zernike polynomials or bilinear spline functions. We choose a representation that guarantees maximum computational efficiency, and thus assume that the incoming phase and the measurements are a linear combination of characteristic functions of the subapertures, i.e.,

$$\Phi(x, y) = \sum_{i=1}^n \phi_i \mathcal{X}_{\Omega_i^y}(x), \quad s_x(x, y) = \sum_{i=1}^n s_{x,i} \mathcal{X}_{\Omega_i^y}(x), \quad (5.13)$$

where  $(\phi_i)_{1 \leq i \leq n}$ ,  $(s_{x,i})_{1 \leq i \leq n}$  denote basis coefficients and  $\Omega_i^y = [x_{i-1}^y, x_i^y]$  the  $i$ -th subaperture of a row for fixed  $y$ . As the wavefront sensor provides two measurements (one in  $x$ - and one in  $y$ -direction), for every single subaperture, the suggestion of representing the measurements via piecewise constant functions describing the subaperture grid is reasonable. The involved operators are then calculated as, e.g.,

$$\begin{aligned} (\mathbf{Q}_x \Phi)(x, y) &= -\mathcal{X}_{\Omega}(x, y) \frac{1}{2\pi} \int_{\Omega_y} \frac{[\Phi(x', y) - \Phi(x, y)] k^{\{n, c, l\}}(x' - x)}{x' - x} dx' \\ &= -\mathcal{X}_{\Omega}(x, y) \frac{1}{2\pi} \int_{\Omega_y} \frac{\left[ \sum_{i=1}^n \phi_i \mathcal{X}_{\Omega_i^y}(x') - \sum_{i=1}^n \phi_i \mathcal{X}_{\Omega_i^y}(x) \right] k^{\{n, c, l\}}(x' - x)}{x' - x} dx' \\ &= -\mathcal{X}_{\Omega}(x, y) \frac{1}{2\pi} p.v. \left[ \int_{\Omega_y} \frac{\sum_{i=1}^n \phi_i \mathcal{X}_{\Omega_i^y}(x') k^{\{n, c, l\}}(x' - x)}{x' - x} dx' \right. \\ &\quad \left. - \int_{\Omega_y} \frac{\sum_{i=1}^n \phi_i \mathcal{X}_{\Omega_i^y}(x) k^{\{n, c, l\}}(x' - x)}{x' - x} dx' \right] \end{aligned}$$

$$\begin{aligned}
 &= -\mathcal{X}_\Omega(x, y) \frac{1}{2\pi} \sum_{i=1}^n \phi_i \\
 &\quad p.v. \underbrace{\left[ \int_{x_{i-1}^y}^{x_i^y} \frac{k^{\{n,c,l\}}(x' - x)}{x' - x} dx' - \mathcal{X}_{\Omega_i^y}(x) \int_{\Omega_y} \frac{k^{\{n,c,l\}}(x' - x)}{x' - x} dx' \right]}_{=: \alpha_i^{\{n,c,l\}}(x, y)} \\
 &= -\mathcal{X}_\Omega(x, y) \frac{1}{2\pi} \sum_{i=1}^n \phi_i \alpha_i^{\{n,c,l\}}(x, y).
 \end{aligned}$$

The functions  $\alpha_i^{\{n,c,l\}}(x, y)$  are computed offline and do not influence the computational speed of the proposed methods. The implementation of all involved operators is performed analogously when choosing the basis representation (5.13).

### 5.3 Numerical results

We test the quality of the reconstruction approaches by continuously correcting the incoming wavefront in closed loop AO. In this setting, the wavefront sensor measures the incoming phase after passing the deformable mirror, i.e., the sensor sees the difference between the incoming wavefront and the correction induced by the mirror. For numerical simulations, we use the end-to-end simulation tool Octopus developed by ESO [129, 130]. We test the performance of the proposed methods for an ELT-sized telescope system. In particular, we consider the METIS instrument on the 39 m sized ELT for non-modulated and modulated pyramid wavefront sensors. The system runs at a frequency of 1 kHz for the non-modulated sensor and at a frequency of 500 Hz for the modulated sensor. The mirror geometry in the simulations corresponds to the M4 geometry planned for the ELT, telescope spiders are not taken into account. For the temporal control of the algorithms we use a simple integrator and optimize the gains with a resolution of 0.1.

The quality results of the algorithms are expressed in terms of long-exposure Strehl ratios at an observing wavelength of  $2.2 \mu m$  (K-band). Note that according to the specifications of the METIS instrument, K-band is not included in the science range. Instead, observations are performed in L-band (at  $\lambda_1 = 3.0 \mu m$ ,  $\lambda_2 = 3.7 \mu m$ ), in M-band (at  $\lambda = 4.7 \mu m$ ) and in N-band (at  $\lambda = 10.0 \mu m$ ). For analysis purposes, however, we find it useful to have the output at a shorter wavelength as well. As such, we use  $\lambda = 2.2 \mu m$  in the K-band where the imaging is performed.

In our numerical tests we evaluate the reconstruction quality in a range of photon flux levels between 50 and 10000 photons per subaperture per frame for median atmospheric conditions. The simulation parameters are summarized in Table 5.1. In order to speed up convergence to the closed loop, in the first 13 time steps we apply the CuReD reconstructor [179, 180], which corrects mainly for the low frequencies in the wavefront.

<b>Simulation parameters</b>	
telescope diameter	37 m
central obstruction	30%
science target	on-axis (SCAO)
WFS	PWFS
sensing band	K (2.2 $\mu\text{m}$ )
evaluation bands	K (2.2 $\mu\text{m}$ ) L (3.0, 3.7 $\mu\text{m}$ ) M (4.7 $\mu\text{m}$ ) N (10.0 $\mu\text{m}$ )
modulation	$[0, 4] \lambda/D$
controller	integrator
atmospheric model	von Karman
number of simulated layers	35
outer scale $L_0$	25 m
atmosphere	median
Fried radius $r_0$ at $\lambda = 500$ nm	0.157 m
number of subapertures	$74 \times 74$
number of active subapertures	[3912, 4128] out of 5476
frame rate	[1000, 500] Hz
DM delay	1
photon flux	[50, 100, 1000, 10000]
iterations per simulation	500

Table 5.1: Test case setting for numerical simulations using linear iterative reconstruction methods.

### 5.3.1 Optimal step size choice for SD iteration in the context of WF reconstruction from pyramid data

Before we compare the reconstruction quality of all proposed methods, we investigate the optimal step size choice for the steepest descent algorithm applied to WF reconstruction. For that analysis we consider the METIS instrument on the ELT having a pyramid sensor without modulation incorporated. The simulation parameters are identical to those listed in Table 5.1. As photon flux, we use 10000 photons per subaperture per frame. The reconstruction quality is evaluated after 500 time steps using 5 SD-iterations for each reconstruction in order to find the optimal choice of the step size. As listed in Table 5.2, best results are obtained for the SD iteration combined with the classical steepest descent step size. The reason for the small number of performed iterations is (amongst others) related to the roof sensor approximation

for modeling a pyramid sensor and discussed below in more detail.

step size choice	LE Strehl ratio
classical SD	0.8322
minimal gradient	0.8310
Barzilai-Borwein 1	0.8311
Barzilai-Borwein 2	0.8316
Cauchy-Barzilai-Borwein 1	0.8317

Table 5.2: SD-reconstruction (Algorithm 5.2) results for the non-modulated sensor in the K-band after 500 time steps using different step sizes.

### 5.3.2 Simulated closed loop performance

Let us analyze the closed loop performance of the developed algorithms and compare their reconstruction quality. Our reconstruction methods are all based on a simplification of the full pyramid sensor model. As a consequence, after some iteration steps, the reconstructions suffer from an approximation error and depart from the true solution of the full pyramid sensor model although the residuals

$$\left\| s - \frac{1}{2} \mathbf{R}^{lin} \Phi_i \right\| \quad (5.14)$$

with respect to the simplified model continue to scale down during the iterations. Due to the fact that the full non-linear pyramid sensor model  $\mathbf{P}$  consists of two terms  $\mathbf{P} = \mathbf{P}^{lin} + \mathbf{P}^{rest}$ , where the first term again is split into two terms  $\mathbf{P}^{lin} = \mathbf{R}^{lin} + \mathbf{S}^{lin}$  (see Section 3.2 - 3.4 for more details), a reduction of the roof sensor residual (5.14) can imply an error increase of  $\mathbf{S}^{lin} \Phi + \mathbf{P}^{rest} \Phi$  in the residual corresponding to the full pyramid sensor model

$$\left\| s - \frac{1}{2} \mathbf{P} \Phi_i \right\| = \left\| s - \frac{1}{2} \mathbf{R}^{lin} \Phi_i - \frac{1}{2} (\mathbf{S}^{lin} + \mathbf{P}^{rest}) \Phi_i \right\|.$$

Besides the approximation error, another error source, the data error, is present in the reconstruction process. It is inevitable to search for an adequate stopping criterion taking into account both the difference between the real pyramid operator  $\mathbf{P}$  providing the measurements  $s$  and the approximate operator  $\mathbf{R}^{lin}$ , which builds the foundation of the model-based reconstruction algorithms, as well as data errors. For choosing the regularization parameter in the generally non-linear problem of wavefront reconstruction from pyramid data, we discuss the usage of Morozov's discrepancy principle.

Assume that the pyramid sensor provides noisy data  $s^\delta$  fulfilling  $\left\| s - s^\delta \right\| < \delta$  for some noise level  $\delta > 0$ . The iteration is terminated with stopping index  $k_*(\delta, s^\delta)$  when for the first time the residual is below  $\tau\delta$  for some  $\tau > 1$ , i.e.,

$$\left\| s^\delta - \frac{1}{2} \mathbf{R}^{lin} \Phi_i^\delta \right\| > \tau\delta, \quad 0 \leq i < k_* \quad \text{and} \quad \left\| s^\delta - \frac{1}{2} \mathbf{R}^{lin} \Phi_{k_*}^\delta \right\| \leq \tau\delta.$$

The discrepancy principle combined with a criterion for controlling the approximation error can be transferred to the application of only a few CGNE- or SD-iterations resulting in a very low value for  $k_*$  as confirmed by a huge number of numerical simulations performed within this study. In particular, one iteration suffices to provide high reconstruction quality when using a warm restart of the system. That is, in the first time step, the initial guess is chosen as zero, i.e.,  $\Phi_{0,0} := 0$ , and at time step  $t > 0$  the initial value is set to the reconstructed phase of the previous step, i.e.,  $\Phi_{t,0} := \Phi_{t-1}^{rec}$ . By employing the reconstruction of the previous step as initial guess  $\Phi_0$  we significantly decrease the computational complexity since Algorithm 5.1 - 5.2 and 5.5 - 5.6 are scaled down to non-iterative gradient based methods by applying only one corresponding iteration step. The warm restart technique improves the convergence speed of the iterative solvers and additionally slightly increases the quality performance. The suitable number of iterations is also depending on the number of incident photons, since a high photon flux results in reduced data noise and vice versa.

In our applications a total number of  $K = 1$  iterations turned out to be optimal with respect to the reconstruction quality and the computational complexity of the methods. Except for the Landweber type approaches (Algorithm 5.3 - 5.4), we use more than one iteration, but already  $K = 5$  Landweber steps combined with an adapted choice of the relaxation parameter and the warm restart technique are sufficient to obtain satisfying reconstruction quality.

In case of one CGNE- or SD-iteration the two algorithms coincide when using the classical steepest descent step size (5.11). Additionally, the step sizes in the SD method discussed in the previous Section do not differ for one SD-iterate except for the classical SD step size and the MG step size. Hence, for the numerical simulations with results provided in Table 5.3 and Table 5.4 we used the minimal gradient step size (5.12) in the Algorithm 5.2 in order to have an additional comparison of step size choices as well. Since Algorithm 5.6 has a reduced computational complexity compared to Algorithm 5.5, we only consider the modified SD-Kaczmarz algorithm in our numerical tests. As above, one SD-Kaczmarz iteration suffices as well.

Numerical tests suggest that for METIS an interpolation to a finer grid than given by the subaperture spacing results in an increased reconstruction quality. In the XAO case the corresponding improvement was less significant. This may be related to the difference in subaperture sizes of both systems (21 cm in XAO versus 50 cm in METIS).

Corresponding results having a cold start ( $\Phi_0 = 0$ ) for every time step  $t$  can be found in Table 5.2 (giving the results for different step sizes) for Algorithm 5.2 utilizing a pyramid sensor without modulation while results using the warm restart technique for all presented algorithms are summarized in Table 5.3 for the non-modulated pyramid sensor and in Table 5.4 for the modulated pyramid sensor. Hence, the warm restart technique improves the reconstruction quality of the SD approach from an LE Strehl ratio of 0.8322 having a cold start to 0.8412 with the warm restart.

photon flux	CGNE	SD	lin. LIPS	lin. KLIPS	mod. SD-K
50	0.8374	0.8376	0.8332	0.8371	0.8331
100	0.8407	0.8409	0.8384	0.8415	0.8393
1000	0.8414	0.8413	0.8395	0.8420	0.8412
10000	0.8415	0.8412	0.8396	0.8419	0.8413

Table 5.3: Long-exposure Strehl ratios in the K-band for a pyramid sensor without modulation obtained with the presented linear algorithms after 500 closed loop simulation steps. Best results are obtained for the CGNE approach (Algorithm 5.1), the SD (Algorithm 5.2), and Landweber-Kaczmarz iteration (Algorithm 5.4).

In case of zero modulation, best reconstruction quality is obtained for the Landweber-Kaczmarz approach using the two measurement sets alternating and for the gradient based approaches (Algorithm 5.1 - 5.2) calculating two reconstructions and averaging at the end. For the sensor having modulation  $4 \lambda/D$ , surprisingly, the CGNE approach even outperforms the Landweber-Kaczmarz algorithm except for the simulations with 50 photons per subapertures per frame. However, the differences in the results are very small anyway. In addition to the K-band results shown in Table 5.3, we provide the long-exposure Strehl ratios in other science bands as defined by the instrument specifications. Table 5.5 shows the quality in the L-, M-, and N-bands in the high flux case (10000 ph/subaperture/frame) for the non-modulated sensor obtained with the Landweber-Kaczmarz algorithm.

photon flux	CGNE	SD	lin. LIPS	lin. KLIPS	mod. SD-K
50	0.8432	0.8434	0.8427	0.8439	0.8340
100	0.8524	0.8520	0.8517	0.8510	0.8454
1000	0.8597	0.8579	0.8590	0.8562	0.8570
10000	0.8604	0.8581	0.8595	0.8577	0.8580

Table 5.4: Long-exposure Strehl ratios in the K-band for a pyramid sensor with modulation  $4 \lambda/D$  obtained with the presented linear algorithms after 500 closed loop simulation steps. Here, the CGNE approach (Algorithm 5.1) provides the highest reconstruction quality in most of the cases.

The simulations for a modulated sensor whose results are presented in Table 5.4 were performed with a frame rate of 500 Hz. In order to have a direct comparison of the non-modulated and modulated sensor, we additionally run a simulation at a frame rate of 1 kHz (instead of 500 Hz) using a pyramid sensor with modulation  $4 \lambda/D$ . For the modulated sensor in the high flux case with the CGNE method we obtain the LE Strehl ratio of 0.8782 in the K-band after 500 time steps and for the non-modulated sensor the LE Strehl ratio of 0.8415. This result fits well our previous experiences

with other model-based reconstruction algorithms according to which the modulated sensor provides a higher quality compared to the non-modulated one.

All in all, the developed reconstruction algorithms deliver comparable quality and allow for robust and accurate wavefront reconstruction with low computational costs.

sensing wavelength	LE Strehl
2.2 $\mu\text{m}$	0.8419
3.0 $\mu\text{m}$	0.9107
3.7 $\mu\text{m}$	0.9401
4.7 $\mu\text{m}$	0.9623
10.0 $\mu\text{m}$	0.9915

Table 5.5: Long-exposure Strehl ratios in L-, M-, and N-bands obtained for the non-modulated pyramid sensor with the Landweber-Kaczmarz algorithm in the high flux case (10000 ph/subaperture/frame) after 500 closed loop simulation steps.

### 5.3.3 Comparison to interaction-matrix-based approaches

Let us now compare the reconstruction quality of the proposed methods to those nowadays primarily running on existing observing facilities, the interaction-matrix-based methods considered more precisely in Chapter 7 and Chapter 8 of the Thesis. Often, in practice and also in simulations, the non-modulated sensor being operated with an interaction-matrix-based approach, is reported to be unstable, see, e.g, [86, 132]. One can, for instance, apply some tricks, like using a “wrong” command matrix derived for the modulated sensor, or heavily fine-tune the regularization parameters to filter out the unstable modes in the correct interaction matrix (measured or computed for the sensor with modulation 0). This has to be performed on the fly and is a very time-consuming task.

There was a result published in [132] for the non-modulated sensor running in Octopus with a modal MVM (cf Section 8.2.4) at 1 kHz frame rate. The achieved quality in the K-band was reported to be 0.62 for the high flux case with 10000 photons/subaperture/frame. For comparison, the pyramid sensor with modulation  $4 \lambda/D$  was reported to provide in the same environment the LE Strehl ratio of around 0.80. As reported in [102], another variant of MVM, the zonal minimum variance reconstructor (cf Section 8.2.4) in the YAO simulation tool [172], which is a zonal regularized approach, achieves an LE Strehl of 0.89 in case of the modulated pyramid sensor (with modulation 4) and high photon flux.

Comparing the performances of the described algorithms, we can draw the following conclusions. For the pyramid sensor without modulation, our reconstruction algorithms, that use the forward model of the sensor, allow not only to close the loop

	operation	# of flops
loop	$\mathbf{Q}_x \Phi_x$	$2n^3 - n^2$
	$s_x - \mathbf{Q}_x \Phi_x$	$n^2$
	$\mathbf{Q}_x^* (s_x - \mathbf{Q}_x \Phi_x)$	$2n^3 - n^2$
	$\beta \mathbf{Q}_x^* (s_x - \mathbf{Q}_x \Phi_x)$	$n^2$
	$\Phi_x + \beta \mathbf{Q}_x^* (s_x - \mathbf{Q}_x \Phi_x)$	$n^2$
post loop step	$\Phi = \frac{1}{2} (\Phi_x + \Phi_y)$	$2n^2$

Table 5.6: The number of floating point operations to be performed online in the linear LIPS and KLIPS.

easily, but also to achieve a stable correction over time with a quality significantly higher compared to, e.g., the modal MVM estimate in [132]. In case of the pyramid sensor with the optimal amount of modulation, our algorithms achieve a reconstruction quality which is slightly below the best (known) result obtained with the zonal MMSE variant of MVM.

## 5.4 Computational complexity

We define the computational complexity of the algorithm as a number of required floating point operations (flops). Let  $n$  denote the number of subapertures in one direction, then  $N = n^2$  indicates approximately the number of unknowns to be found.

### 5.4.1 Complexity of linear LIPS and KLIPS

We only consider the complexity of the operations that have to be performed online and exclude the pre-calculations needed in the application of the operators  $\mathbf{Q}$  and  $\mathbf{Q}^*$  from our considerations. The number of floating point operations for every step in the Landweber iteration approach for wavefront reconstruction using pyramid sensors (Algorithm 5.3 - 5.4) is provided in Table 5.6. The post loop step of the linear LIPS consists of finding the average between the two resulting reconstructions, which requires one summation and one division by a scalar. Altogether, this step is summed up to  $2n^2$  operations.

Because we perform the mentioned operations in  $x$ - and in  $y$ -direction, i.e., twice, for  $K$  iterations we obtain the complexity

$$C_{lin.KLIPS}(n; K) = (8n^3 + 2n^2) \cdot K$$

for the linear Landweber-Kaczmarz approach (Algorithm 5.4) and

$$C_{lin.LIPS}(n; K) = (8n^3 + 2n^2) \cdot K + 2n^2$$

	operation	# of flops
loop	$J'(\Phi_x)$	$4n^3 - n^2$
	evaluation of $\tau_{SD}$	$2n^3 + 3n^2 + 1$
	$\Phi_x - \tau J'(\Phi_x)$	$2n^2$
post loop step	$\Phi = \frac{1}{2}(\Phi_x + \Phi_y)$	$2n^2$

Table 5.7: The number of floating point operations in the Steepest Descent and Steepest Descent-Kaczmarz for pyramid sensors.

for the application of the Landweber iteration (Algorithm 5.3) having the additional step of averaging.

#### 5.4.2 Complexity of SD and SD-Kaczmarz for pyramid sensors

We again only consider the operations performed online. The complexity of one steepest descent iteration (Algorithm 5.2, Algorithm 5.5 and Algorithm 5.6) is indicated in Table 5.7. In case of the classical steepest descent iteration (Algorithm 5.2) a subsequent averaging has to be performed, which costs additionally  $2n^2$  flops. Therefore, the number of floating point operations for the steepest descent-Kaczmarz approach applied to pyramid sensors (Algorithm 5.5) is given by

$$C_{SD-K}(n; K) = (12n^3 + 8n^2 + 2) \cdot K,$$

for the modified Algorithm 5.6 by

$$C_{mod.SD-K}(n; K) = (6n^3 + 4n^2 + 1) \cdot K,$$

and for the steepest descent approach (Algorithm 5.2) by

$$C_{SD}(n; K) = (12n^3 + 8n^2 + 2) \cdot K + 2n^2,$$

where  $K$  indicates the number of steepest descent steps.

#### 5.4.3 Complexity of CGNE for pyramid sensors

The CGNE method consists of three steps:

1. a pre-computation and initialization step which have to be done for both  $x$ - and  $y$ -direction once,
2. the CG-loop for  $K$  iterations performed twice in  $x$ - and  $y$ -direction,
3. a post loop step in which we average the two obtained reconstructions.

	operation	# of flops
init	computation of $d_{x,0}$	$2n^3$
	computation of $s_{x,0}$	$2n^3 - n^2$
	initialization of $p_{x,1}$	$n^2$
loop	computation of $q_x$	$2n^3 - n^2$
	computation of $\alpha$	$4n^2 + 1$
	computation of $\Phi_x$	$2n^2$
	computation of $d_x$	$2n^2$
	computation of $s_x$	$2n^3 - n^2$
	computation of $\beta$	$2n^2 + 1$
	computation of $p_x$	$2n^2$
post loop step	$\Phi = \frac{1}{2} (\Phi_x + \Phi_y)$	$2n^2$

Table 5.8: The number of floating point operations in the CGNE algorithm for pyramid sensors.

The number of floating point operation in the CGNE algorithm for pyramid sensors for operations which are not pre-computed offline is indicated in Table 5.8. Summing up the specified operations for both  $s_x$  and  $s_y$  data, we see that altogether the initialization step consists of  $8n^3$  flops, the loop of  $(8n^3 + 20n^2 + 4) \cdot K$  and the post loop step of  $2n^2$  operations. Hence, the CGNE complexity for pyramid sensors sums up as

$$C_{CGNE}(n; K) = (8n^3 + 20n^2 + 4) \cdot K + 8n^3 + 2n^2.$$

However, since the CG method is known to require the fewest number of iterations,  $K$  usually is smaller compared to, e.g., the Landweber iteration.

#### 5.4.4 Comparison to MVM

The complexity of standard MVM methods scales as  $\mathcal{O}(N^2) = \mathcal{O}(n^4)$  in our notations. In these studies, we calculate the reconstructions (mirror actuator commands) at the corners of the subapertures (cf Fried geometry), and thus need to consider approximately  $n' = n + 1$  phase values. For, e.g.,  $n = 200$  subapertures, the complexity of MVM is estimated as

$$C_{MVM}(200) = 201^4 \approx 16 \cdot 10^8 = 1600 \cdot 10^6.$$

The computational load of the developed methods are estimated in Table 5.9. Here, we assume that the mirror actuators are equidistantly spaced on a squared shape although this is not employed in practice since not all actuators are actively controlled. However, for a theoretical comparison of complexities such assumptions are still relevant. Note that in principle  $C_{CGNE}(n; 1) = C_{SD}(n; 1)$  because the CGNE algorithm can already

approach	complexity	flops	METIS	XAO	XAO in %
MVM	$\mathcal{O}(N^2)$	$C_{MVM}(n)$	$30 \cdot 10^6$	$1600 \cdot 10^6$	100 %
CGNE	$\mathcal{O}(N^{3/2})$	$C_{CGNE}(n; 1)$	$6,9 \cdot 10^6$	$130,9 \cdot 10^6$	8 %
SD	$\mathcal{O}(N^{3/2})$	$C_{SD}(n; 1)$	$5,1 \cdot 10^6$	$97,9 \cdot 10^6$	6 %
SD-K	$\mathcal{O}(N^{3/2})$	$C_{SD-K}(n; 1)$	$5,1 \cdot 10^6$	$97,8 \cdot 10^6$	6 %
modified SD-K	$\mathcal{O}(N^{3/2})$	$C_{mod.SD-K}(n; 1)$	$2,6 \cdot 10^6$	$48,9 \cdot 10^6$	3 %
lin. LIPS	$\mathcal{O}(N^{3/2})$	$C_{lin.LIPS}(n; 5)$	$16,9 \cdot 10^6$	$325,3 \cdot 10^6$	20 %
lin. KLIPS	$\mathcal{O}(N^{3/2})$	$C_{lin.KLIPS}(n; 5)$	$16,3 \cdot 10^6$	$325,2 \cdot 10^6$	20 %

Table 5.9: The computational complexities of the linear iterative algorithms compared to the implementation of an MVM method. Estimates of the number of floating point operations necessary for the METIS instrument having a pyramid wavefront sensor with  $74 \times 74$  and for an XAO system with  $200 \times 200$  subapertures are provided. The last column demonstrates the computational effort of the presented algorithms as percentage of the MVM effort for the XAO system.

be terminated after the calculation of  $\Phi_1$ . However, we consider one full CGNE step in the Table.

As a remark, we mention that in our comparison we have omitted the additional computational effort required in the presented model-based algorithms for the computation of deformable mirror commands from the reconstructed wavefront shape. This step can be represented as a bilinear interpolation from the  $n \times n$  grid of subapertures to the  $(n + 1) \times (n + 1)$  grid of DM actuators, which requires  $4(n + 1)^2$  floating point operations to be performed. Also, we would like to mention that the time-saving features of MVM approaches like parallelizability and pipelineability are valid for our algorithms as well.

The developed algorithms allow to significantly reduce the numerical effort of the wavefront reconstruction step in an AO loop compared to the computational load related to the solvers based on matrix-vector multiplication. This is illustrated especially well for the XAO system having a huge number of active actuators. The computational effort of MVM-based wavefront estimators is extremely demanding in this case. In contrast, the usage of analytically developed wavefront reconstructors allows to heavily reduce the numerical effort of the AO loop. For instance as shown in Table 5.9, the modified steepest descent algorithm reduces the computational load of the wavefront reconstruction step in the XAO loop to approximately 3% of the MVM effort while still providing high reconstruction quality.

## 5.5 Summary on linear iterative methods

This Chapter has been dedicated to the application of well-known iterative algorithms for solving the Inverse Problem of wavefront reconstruction from pyramid wavefront sensor data in the field of astronomical Adaptive Optics. From the performed end-to-end numerical simulations we can draw the conclusion that all studied algorithms

deliver very similar reconstruction quality. However, it is preferable to apply the Kaczmarz versions of the algorithms or the CGNE approach, since they provide a slightly better reconstruction quality, though, the difference in the achieved quality between all the methods is minor. The best quality is obtained with the CGNE approach (Algorithm 5.1) and with the Landweber-Kaczmarz iteration (Algorithm 5.4), which at the same time is part of the slowest among the algorithms under comparison. If one decides to go for speed at the cost of a negligible quality loss, one should choose the modified steepest descent-Kaczmarz version combined with the classical step size choice (Algorithm 5.6).

As shown by numerical results presented in this study, the proposed algorithms, which are partially iterative methods, allow to keep the numerical effort of the wavefront reconstruction step in an AO loop low compared to the computational load of solvers based on matrix-vector multiplication. This has an especially big impact for the considered XAO system having a huge number of active actuators. For instance, the modified steepest descent algorithm reduces the computational load of the wavefront reconstruction step in the XAO loop to approximately 3% of the MVM effort while still providing high reconstruction quality.

Even when using simplifications of the pyramid sensor model, all proposed algorithms provide stable reconstruction and (almost) reach the quality of interaction-matrix-based approaches in which the full pyramid model is assumed. A big advantage of the proposed iterative methods is the possibility to investigate the full pyramid sensor model for future developments. Those adaptations may lead to high quality improvements as additionally real life features such as telescope spiders or the low wind effect can easier be incorporated in the approaches presented in this Chapter than for other wavefront reconstructors as, e.g., the P-CuReD introduced in Chapter 7.

Finally, we would like to mention that investigations of the behavior of iterative algorithms in the presence of wide support structures of the secondary mirror segmenting the telescope pupil into disjoint parts as well as further quality evaluations to meet specifications of the METIS instrument will be part of our further research. For instance, one idea is to apply the iterative methods within the Split Approach presented in Chapter 8 of the Thesis in order to overcome differential piston effects arising on segmented pupils.



## Chapter 6

# Non-linear wavefront reconstruction using Landweber and Landweber-Kaczmarz iteration

We introduce a new idea of non-linear wavefront reconstruction from pyramid wavefront sensor data by applying the non-linear Landweber method or the non-linear Landweber-Kaczmarz method as presented in [106]. Both iterative algorithms have already been studied in-depth by the mathematical community with multiple applications in the field of Inverse Problems.

The non-linear problem of wavefront reconstruction is briefly recalled in Section 6.1. We also review the mathematical models of the wavefront sensor used for the development of the non-linear algorithms. In Section 6.2 we adapt the Landweber and Landweber-Kaczmarz iteration to the problem of non-linear wavefront reconstruction using pyramid sensors and introduce two new methods for wavefront reconstruction, namely the *non-linear Landweber Iteration for Pyramid Sensors* (LIPS) and the *non-linear Kaczmarz-Landweber Iteration for Pyramid Sensors* (KLIPS). The evaluation of the Fréchet derivatives and the corresponding adjoints which are needed for the application of the algorithms is done in Section 6.3. In Section 6.4 we mention some details on the discretization of the problem and the computational complexity of the proposed methods. The performance of the reconstructors using closed loop end-to-end simulations is shown in Section 6.5.

From a mathematical perspective, the relation between the incoming, unknown wavefront and the measured pyramid wavefront sensor response is non-linear. Basically, the pyramid sensor signal can be modeled as the incoming wave convolved the PSF of the sensor (cf (3.12)). Due to the sinusoidal nature of the measurements, the model has a suitable linear approximation depending on the amplitude of the incoming wavefront (cf Section 3.4). As later summarized in Table 7.1, almost all available wavefront reconstruction algorithms for pyramid sensors are based on a linearization of the model. In closed loop AO, already corrected wavefronts are measured by the wavefront sensor.

Thus, the existence of small incident wavefronts allows to assume a linear response of the PWFS. However, for open loop data or larger wavefront errors, for instance induced by non common path aberrations, this assumption is not fulfilled. Non common path errors appear in AO systems when the wavefront sensor does not belong to the same light path as the science camera. Then, the AO system suffers from aberration differences between the wavefront sensor and the science camera. Additionally, optical elements may be incorporated in the non common path as, for example, in the case of Multi Conjugate AO systems. In these cases, the assumption of small residual wavefronts being measured by the wavefront sensor and so the linearity of the pyramid sensor may be violated. Whenever the pyramid sensor is operated around a non-zero setpoint, the reconstruction performance of linear methods may be affected. Non-linear wavefront reconstructors are considered as one possibility to handle the non-linearity effects of the pyramid sensor depending on the modulation amplitude of the sensor or introduced by influences such as NCPAs. Other ideas to mitigate the non-linearity induced sensitivity loss are measuring the non-linearity and taking it into account in the wavefront reconstruction process. This is done by multiplying the measurements with the retrieved non-linearity factor or so-called modal optical gain compensation methods in which, depending on the statistics of the phase, global system parameters and spatial frequencies, different gain values are applied to different basis modes describing the wavefronts [50, 123, 124, 217]. Note that these adapted reconstruction approaches are still linear. Furthermore, there exist wavefront estimation approaches based on Newton's method for non-linear optimization [78, 79, 125] or a phase retrieval algorithm [38]. Important in this context are also the non-linear models in [72, 73] describing the pyramid sensor in a generalized framework of Fourier optics.

## 6.1 Non-linear problem of wavefront reconstruction using pyramid sensors

For wavefront reconstruction from pyramid sensor data the aim is to solve the non-linear pyramid sensor operator equation

$$s = \mathbf{P}\Phi \tag{6.1}$$

already introduced in (3.2) for pyramid wavefront sensor measurements  $s = [s_x, s_y]$ , the non-linear pyramid sensor operator  $\mathbf{P} : \mathcal{D}(\mathbf{P}) \rightarrow \mathcal{L}_2(\mathbb{R}^2)$  with  $\mathcal{D}(\mathbf{P}) \subseteq \mathcal{H}^{11/6}(\mathbb{R}^2)$  and the unknown incoming wavefront  $\Phi \in \mathcal{H}^{11/6}(\mathbb{R}^2)$  [55, 60, 108, 147]. The norms in the Hilbert spaces are considered to be the norms in  $\mathcal{L}_2(\mathbb{R}^2)$  with

$$\|\cdot\|_{\mathcal{L}_2(\mathbb{R}^2)} = \|\cdot\|_{\mathcal{L}_2(\Omega)}$$

because of the compact support on the telescope aperture  $\Omega$  of the involved phases and sensor measurements (cf Section 3.2) and are generally denoted by  $\|\cdot\|$  throughout this Chapter.

Since the unperturbed data  $s$  are almost never available in practice, we consider noisy data  $s^\delta$  and assume

$$\|s^\delta - s\| < \delta$$

for some noise level  $\delta > 0$ .

We start by recalling the pyramid and roof sensor operators and derive the necessary theoretical principles for the application of the Landweber iteration. Due to the structure of the measurement equation later defined in (6.2),  $\mathbf{P}^{\{n,c\}} := [-\frac{1}{2}\mathbf{P}_x^{\{n,c\}}, \frac{1}{2}\mathbf{P}_y^{\{n,c\}}]$  denote the pyramid sensor operators. The corresponding roof sensor operators are denoted by  $\mathbf{R}^{\{n,c\}} := [-\frac{1}{2}\mathbf{R}_x^{\{n,c\}}, \frac{1}{2}\mathbf{R}_y^{\{n,c\}}]$ . Whenever we omit the superscripts  $\{n,c\}$  in this Chapter, then the theory is applicable to both non-modulated and circular modulated pyramid sensors as well as the linear modulated roof wavefront sensor which is not specifically reviewed. The domain  $\mathcal{D}(\mathbf{P})$  of the pyramid operator either denotes  $\mathcal{D}(\mathbf{P}_x)$  or  $\mathcal{D}(\mathbf{P}_y)$  respectively depending on the direction we are considering the problem (for Landweber iteration) or  $\mathcal{D}(\mathbf{P}_x) \cap \mathcal{D}(\mathbf{P}_y)$  if we consider the problem as a system of two equations (in case of Landweber-Kaczmarz iteration).

In what follows we use the analytical pyramid wavefront sensor transmission mask model derived in Section 3.2.1.

The pyramid wavefront sensor data in the non-linear transmission mask model are represented as (cf Definition 3.2 and Theorem 3.3)

$$\begin{aligned} s_x^{\{n,c\}}(x, y) &= -\frac{1}{2} \left( \mathbf{P}_x^{\{n,c\}} \Phi \right) (x, y), \\ s_y^{\{n,c\}}(x, y) &= \frac{1}{2} \left( \mathbf{P}_y^{\{n,c\}} \Phi \right) (x, y), \end{aligned} \quad (6.2)$$

where the operators  $\mathbf{P}_x^{\{n,c\}} : \mathcal{H}^{11/6}(\mathbb{R}^2) \rightarrow \mathcal{L}_2(\mathbb{R}^2)$  in  $x$ -direction are given by

$$\begin{aligned} \left( \mathbf{P}_x^{\{n,c\}} \Phi \right) (x, y) &:= \mathcal{X}_{\Omega}(x, y) \frac{1}{\pi} \int_{\Omega_y} \frac{\sin[\Phi(x', y) - \Phi(x, y)] \cdot k^{\{n,c\}}(x' - x)}{x' - x} dx' \\ &+ \mathcal{X}_{\Omega_y}(x) \frac{1}{\pi^3} p.v. \int_{\Omega_y} \int_{\Omega_x} \int_{\Omega_x} \frac{\sin[\Phi(x', y') - \Phi(x, y'')] \cdot l^{\{n,c\}}(x' - x, y' - y)}{(x' - x)(y' - y)(y'' - y)} dy'' dy' dx' \end{aligned}$$

and the operators  $\mathbf{P}_y^{\{n,c\}} : \mathcal{H}^{11/6}(\mathbb{R}^2) \rightarrow \mathcal{L}_2(\mathbb{R}^2)$  in  $y$ -direction are given by

$$\begin{aligned} \left( \mathbf{P}_y^{\{n,c\}} \Phi \right) (x, y) &:= \mathcal{X}_{\Omega}(x, y) \frac{1}{\pi} \int_{\Omega_x} \frac{\sin[\Phi(x, y') - \Phi(x, y)] \cdot k^{\{n,c\}}(y' - y)}{y' - y} dy' \\ &+ \mathcal{X}_{\Omega_x}(y) \frac{1}{\pi^3} p.v. \int_{\Omega_y} \int_{\Omega_x} \int_{\Omega_y} \frac{\sin[\Phi(x', y') - \Phi(x'', y)] \cdot l^{\{n,c\}}(x'' - x', y' - y)}{(x' - x)(y' - y)(x'' - x)} dx'' dy' dx'. \end{aligned}$$

The functions  $k^{\{n,c\}}$  are defined by  $k^n(x) := 1$ ,  $k^c(x) := J_0(\alpha_\lambda x)$ , and the functions  $l^{\{n,c\}}$  by  $l^n(x, y) := 1$  and

$$l^c(x, y) := \frac{1}{T} \int_{-T/2}^{T/2} \cos[\alpha_\lambda x \sin(2\pi t/T)] \cos[\alpha_\lambda y \cos(2\pi t/T)] dt.$$

The function  $J_0$  denotes the zero-order Bessel function of the first kind, i.e.,

$$J_0(x) = \frac{1}{\pi} \int_0^\pi \cos(x \sin t) dt = \frac{1}{\pi} \int_0^\pi \cos(x \cos t) dt.$$

The modulation parameter  $\alpha_\lambda$  is defined in (3.7).

The roof sensor operators consist of the first term of the pyramid sensor operators and are used as a simplification of the full pyramid sensor model in the following.

The forward models of the non-modulated and modulated roof WFS in the transmission mask approach are represented by (cf Definition 3.4 and Theorem 3.5)

$$\begin{aligned} s_x^{\{n,c\}}(x, y) &= -\frac{1}{2} \left( \mathbf{R}_x^{\{n,c\}} \Phi \right) (x, y), \\ s_y^{\{n,c\}}(x, y) &= \frac{1}{2} \left( \mathbf{R}_y^{\{n,c\}} \Phi \right) (x, y) \end{aligned}$$

with operators  $\mathbf{R}_x^{\{n,c\}} : \mathcal{H}^{11/6}(\mathbb{R}^2) \rightarrow \mathcal{L}_2(\mathbb{R}^2)$ ,  $\mathbf{R}_y^{\{n,c\}} : \mathcal{H}^{11/6}(\mathbb{R}^2) \rightarrow \mathcal{L}_2(\mathbb{R}^2)$  defined by

$$\begin{aligned} \left( \mathbf{R}_x^{\{n,c\}} \Phi \right) (x, y) &:= \mathcal{X}_\Omega(x, y) \frac{1}{\pi} \int_{\Omega_y} \frac{\sin[\Phi(x', y) - \Phi(x, y)] \cdot k^{\{n,c\}}(x' - x)}{x' - x} dx', \\ \left( \mathbf{R}_y^{\{n,c\}} \Phi \right) (x, y) &:= \mathcal{X}_\Omega(x, y) \frac{1}{\pi} \int_{\Omega_x} \frac{\sin[\Phi(x, y') - \Phi(x, y)] \cdot k^{\{n,c\}}(y' - y)}{y' - y} dy'. \end{aligned}$$

The operators  $\mathbf{P}_x^{\{n,c\}}$  and  $\mathbf{P}_y^{\{n,c\}}$  as well as  $\mathbf{R}_x^{\{n,c\}}$  and  $\mathbf{R}_y^{\{n,c\}}$  are constructed in the same way. Please note that due to the similar structure of the operators, results for one direction are immediately transferred to the second direction.

## 6.2 Non-linear Landweber iteration for solving the wavefront reconstruction problem

Many existing wavefront reconstruction approaches assume a linear relation between the unknown wavefront or mirror actuator commands and the given pyramid wavefront sensor measurements. Such reconstruction methods for pyramid sensors are, for instance, several variations of interaction-matrix-based approaches summarized in [110], Fourier based methods [162, 194, 196], the fast P-CuReD algorithm [179, 198], or the methods introduced in Chapter 4 - 5. In Chapter 5 we already applied Landweber iteration for wavefront reconstruction from pyramid sensor data but based on the linearization of the model. Those results will serve as comparison to a potential improvement using non-linear methods as discussed in one of the subsequent Sections. Additionally, for the linear LIPS and KLIPS, we reconstructed by only using the one-term assumption of the roof sensor model, i.e., we excluded the second summands

in (3.27) and considered variations of the finite Hilbert transform operators defined in (3.28) in our numerical implementations. In the current approaches, we use the full roof sensor model (3.27), and hence may achieve additional gains in reconstruction performance.

In this Chapter, we propose two non-linear reconstruction algorithms for pyramid sensor measurements. As non-linear reconstruction procedure, we use either Landweber or Landweber-Kaczmarz iteration. We first review the general scheme of the Landweber algorithm originally proposed in the 1950s by Louis Landweber [127] for linear problems and emphasize that the theory for solving non-linear, ill-posed problems using Landweber iteration considered in this Chapter is mainly referred to [97, 117].

The Landweber method is an iterative technique for minimizing the residual of the quadratic functional

$$\| \mathbf{P}\Phi - s \|^2$$

and is an appealing alternative to Tikhonov regularization. The idea of Landweber iteration follows from the fixed point equation  $\Phi_{k+1} = F(\Phi_k)$  with fixed point operator

$$\mathbf{F}(\Phi) := \Phi + \mathbf{P}'(\Phi)^*(s - \mathbf{P}(\Phi))$$

assuming that the pyramid sensor operator is differentiable. The iterative procedure is described by

$$\Phi_{k+1}^\delta = \Phi_k^\delta + \mathbf{P}'(\Phi_k^\delta)^*(s^\delta - \mathbf{P}(\Phi_k^\delta)) \quad k = 0, 1, 2, \dots \quad (6.3)$$

with perturbed data  $s^\delta$  fulfilling  $\|s - s^\delta\| < \delta$  and adjoint  $\mathbf{P}'(\cdot)^*$  of the locally uniformly bounded Fréchet derivative  $\mathbf{P}'(\cdot)$ . Even if  $s^\delta$  does not belong to the range of  $\mathbf{P}$ , the Landweber iteration (6.3) is stable for a fixed number of iterations. The number of iterations acts as regularization in case of noisy data  $s^\delta$ .

Since the pyramid sensor decouples the two directions, we will consider  $x$ - and  $y$ -direction as independent Landweber iterations and are interested in a reconstruction  $[\Phi_x, \Phi_y]$  for every direction. More precisely, we apply Landweber iteration to the data set  $s_x$  and obtain a reconstruction of the wavefront denoted by  $\Phi_x$ , and we apply Landweber iteration independently to the data set  $s_y$  and obtain a second reconstruction  $\Phi_y$ . The final reconstruction  $\Phi$  is then calculated as the average of both directions,  $\Phi = \frac{1}{2}(\Phi_x + \Phi_y)$ . Due to the symmetry of the problem, both directions can be handled analogously, and hence are not examined individually here.

The iteration starts with initial guess  $\Phi_0$  which may include a priori knowledge of the exact solution  $\Phi_*$ . We always set  $\Phi_0^\delta = \Phi_0$ . In AO loops, reconstructions are needed for a number of subsequent time steps and the reconstruction of the previous time step usually is a good choice for the initial guess of the current time step. Hence, for subsequent time steps, we consider a warm restart technique meaning that as initial

guess at time step  $t + 1$ , denoted by  $\Phi_{0,t+1}$ , we choose the final reconstruction  $\Phi_{rec,t}$  of the last time step  $t$ , i.e.,  $\Phi_{0,t+1} = \Phi_{rec,t}$ .

For regularization, we use the discrepancy principle in case of noisy data: For an appropriate choice of  $\tau > 0$  the iteration is stopped after  $k_* = k_*(\delta, s^\delta)$  iteration steps fulfilling

$$\left\| s^\delta - \mathbf{P}(\Phi_k^\delta) \right\| > \tau\delta, \quad 0 \leq k < k_* \quad \text{and} \quad \left\| s^\delta - \mathbf{P}(\Phi_{k_*}^\delta) \right\| \leq \tau\delta. \quad (6.4)$$

For non-linear Inverse Problems, iteration procedures as, e.g., (6.3) will in general not converge globally to a solution of the non-linear operator equation (6.1). The convergence theory is based on the assumption that the fixed point operator  $\mathbf{F}$  is a nonexpansive operator, i.e.,

$$\left\| \mathbf{F}(\Phi) - \mathbf{F}(\tilde{\Phi}) \right\| \leq \left\| \Phi - \tilde{\Phi} \right\|, \quad \Phi, \tilde{\Phi} \in \mathcal{D}(\mathbf{F}).$$

Iterative methods for approximating fixed points of nonexpansive operators have been considered, for instance, in [8, 10, 27, 94]. As in many applications, it is difficult to verify analytically whether the fixed point operator  $\mathbf{F}$  is nonexpansive for the pyramid sensor. For that reason, the nonexpansivity of the fixed point operator is often replaced by properties that guarantee at least the local convergence of the iteration method and are easier to check. To obtain local convergence we assume the pyramid sensor operator equation (6.1) to be scaled according to

$$\left\| \mathbf{P}'(\Phi) \right\| \leq 1, \quad \Phi \in \mathcal{B}_{2\rho}(\Phi_0) \subset \mathcal{D}(\mathbf{P}) \quad (6.5)$$

for a ball  $\mathcal{B}_{2\rho}(\Phi_0)$  of radius  $2\rho$  around the initial guess  $\Phi_0$ .

The second condition needed to ensure local convergence in  $\mathcal{B}_\rho(\Phi_0)$  to a solution of (6.1) (provided that the equation is solvable in  $\mathcal{B}_\rho(\Phi_0)$ ) reads as

$$\left\| \mathbf{P}(\Phi) - \mathbf{P}(\tilde{\Phi}) - \mathbf{P}'(\Phi)(\Phi - \tilde{\Phi}) \right\| \leq \eta \left\| \mathbf{P}(\Phi) - \mathbf{P}(\tilde{\Phi}) \right\| \quad (6.6)$$

for  $\eta < \frac{1}{2}$ ,  $\Phi, \tilde{\Phi} \in \mathcal{B}_{2\rho}(\Phi_0) \subset \mathcal{D}(\mathbf{P})$ . Both conditions guarantee that the Landweber iteration is well-defined since all iterates  $\Phi_k^\delta, 0 \leq k \leq k_*$  remain elements of  $\mathcal{D}(\mathbf{P})$  if we employ the discrepancy principle.

Under the above mentioned conditions (6.5)-(6.6) and the discrepancy principle (6.4) we obtain the following convergence results.

**Theorem 6.1** ([117], Theorem 2.4 & Theorem 2.6). *If we assume that (6.1) is solvable in  $\mathcal{B}_\rho(\Phi_0)$  and that the conditions (6.5)-(6.6) hold, the non-linear Landweber iteration converges to a solution of  $\mathbf{P}\Phi = s$  in case of exact data  $s$ .*

*If  $k_*(\delta, s^\delta)$  defines a stopping index according to the discrepancy principle (6.4) for*

$$\tau > 2 \frac{1 + \eta}{1 - 2\eta} > 2 \quad (6.7)$$

with  $\eta$  as in (6.6), the Landweber iterates  $x_{k_*}^\delta$  converge to a solution of the Inverse Problem (6.1).

If  $\mathcal{N}(\mathbf{P}'(\Phi^\dagger)) \subset \mathcal{N}(\mathbf{P}'(\Phi))$  for all  $\Phi \in \mathcal{B}_\rho(\Phi^\dagger)$ , we obtain convergence of  $\Phi_k$  and, respectively, of  $\Phi_{k_*}^\delta$  to the  $\Phi_0$ -minimum-norm solution  $\Phi^\dagger$  as  $k \rightarrow \infty$  and  $\delta \rightarrow 0$ .

In order to ensure condition (6.5) we introduce a relaxation parameter  $\omega$ , which is chosen such that

$$\omega \left\| \mathbf{P}'(\Phi^\dagger) \right\|^2 \leq 1, \quad (6.8)$$

and consider the iteration scheme

$$\Phi_{k+1}^\delta = \Phi_k^\delta + \omega \mathbf{P}'(\Phi_k^\delta)^* (s^\delta - \mathbf{P}(\Phi_k^\delta)) \quad k = 0, 1, 2, \dots \quad (6.9)$$

as a modification of (6.3). Note that from Eq. (6.8) it follows that the relaxation parameter  $\omega$  is depending on the modulation amplitude of the pyramid wavefront sensor. On the one hand one can choose  $\omega$  small enough such that condition (6.8) is always fulfilled, on the other hand such a choice will lead to a slow convergence. Hence, the greatest possible value of  $\omega$  is preferable in order to obtain best convergence results.

## 6.2.1 Non-linear Landweber algorithm applied to pyramid sensors

For Algorithm 6.1, named non-linear Landweber Iteration for Pyramid Sensors, we apply non-linear Landweber iteration in  $x$ -direction and a second one independently in  $y$ -direction (combined with a warm restart of the system). Thus, we obtain two reconstructions  $\Phi = [\Phi_x, \Phi_y]$  of the incoming phase and average them at the end. As we observed in numerical simulations, the reconstruction quality exhibits most improvements in the first few Landweber iterations and little in subsequent iterations, we fix the number of iterations  $K$  in advance instead of using the discrepancy principle (6.4) in order to reduce the computational load of the method.

---

### Algorithm 6.1 non-linear Landweber Iteration for Pyramid Sensors

---

choose initial guess  $\Phi_{K,0}$ , set relaxation parameter  $\omega$

**for**  $t = 1, \dots, T$  **do**

$$\Phi_{0,t} = \Phi_{K,t-1}$$

**for**  $i = 1, \dots, K$  **do**

$$\Phi_{i,t} = \Phi_{i-1,t} + \omega \mathbf{P}'(\Phi_{i-1,t})^* (s_t - \mathbf{P}(\Phi_{i-1,t}))$$

**endfor**

**endfor**

$$\Phi_{K,T} = (\Phi_{x,K,T} + \Phi_{y,K,T}) / 2$$


---

### 6.2.2 Non-linear Landweber-Kaczmarz algorithm applied to pyramid sensors

The structure of the operator equation (6.2), consisting of two equations (one in  $x$ - and one in  $y$ -direction), allows to consider Kaczmarz strategies for wavefront reconstruction from pyramid sensor data. Advantages of Kaczmarz loops for wavefront reconstruction have already been analyzed in Section 5.2.4. In contrast to the two reconstructions  $[\Phi_x, \Phi_y]$ , one for each direction, we now only obtain one reconstruction for both directions, again denoted by  $\Phi$ .

The principal idea of Kaczmarz's method [11, 137, 138, 140, 144] can be used in combination with any iterative procedure. In image reconstruction, the method, which is also known as algebraic reconstruction technique (ART), was used in [100] for the first time.

The non-linear Kaczmarz-Landweber Iteration for Pyramid Sensors (Algorithm 6.2) applies a Kaczmarz method in combination with non-linear Landweber iteration (and the warm restart technique) to the problem of wavefront reconstruction from pyramid sensor data.

---

#### Algorithm 6.2 non-linear Kaczmarz-Landweber Iteration for Pyramid Sensors

---

choose initial guess  $\Phi_{K,0}$ , set relaxation parameter  $\omega_x, \omega_y$

**for**  $t = 1, \dots, T$  **do**

$\Phi_{0,t} = \Phi_{K,t-1}$

**for**  $i = 1, \dots, K$  **do**

$\Phi_{i,t,1} = \Phi_{i-1,t} + \omega_x \mathbf{P}'_x (\Phi_{i-1,t})^* (s_{x,t} - \mathbf{P}_x (\Phi_{i-1,t}))$

$\Phi_{i,t,2} = \Phi_{i,t,1} + \omega_y \mathbf{P}'_y (\Phi_{i,t,1})^* (s_{y,t} - \mathbf{P}_y (\Phi_{i,t,1}))$

$\Phi_{i,t} = \Phi_{i,t,2}$

**endfor**

**endfor**

---

Instead of averaging the reconstructions in the last step as in the previously described Landweber Iteration for Pyramid Sensors, we now apply the Landweber iteration steps cyclically. For convergence and stability proofs of this method [33, 126], one basically has to enforce the same conditions on every involved operator as for Landweber iteration. Since for the LIPS we have already considered the two directions as completely independent Landweber iterations, no further conditions necessary for the convergence and stability of the KLIPS have to be shown. As for the LIPS, an appealing alternative to the discrepancy principle in AO loops for pyramid sensors is to fix the number of iterates in advance in order to avoid time-consuming computations which do not deliver high quality improvements. In case we want to use the discrepancy principle

we modify (6.9) by

$$\Phi_{k+1}^\delta = \Phi_k^\delta + \sigma_{j,k} \omega_j \mathbf{P}'_j \left( \Phi_k^\delta \right)^* \left( s_j^\delta - \mathbf{P}_j \left( \Phi_k^\delta \right) \right) \quad k = 0, 1, 2, \dots$$

and use

$$\sigma_{j,k} := \begin{cases} 1, & \text{if } \tau\delta < \left\| s_j^\delta - \mathbf{P}_j \left( \Phi_k^\delta \right) \right\|, \\ 0, & \text{else,} \end{cases}$$

for  $j = x, y$  indicating the direction,  $k$  denoting the current iteration step and  $\tau$  chosen according to (6.7). The iteration procedure is stopped in case of a stagnation over one full cycle of iterations.

Note that both given algorithms have the warm restart technique incorporated but can also be used without a warm restart.

### 6.3 Fréchet derivatives and corresponding adjoint operators of the roof sensor model

For the application of the algorithms LIPS and KLIPS proposed above, we need to calculate the Fréchet derivatives and the corresponding adjoint operators. At this point, we can either use the full pyramid sensor model or the roof sensor as a simplification. Here, we consider the latter, i.e., we plug in the operators  $\mathbf{R}^{\{n,c\}}$  introduced in (3.17)-(3.18) instead of the operator  $\mathbf{P}$  in (6.3) for the reconstruction, but still use the full pyramid wavefront sensor data  $s$ .

For the derivation of the adjoint operators we utilize the inner product in  $\mathcal{L}_2(\mathbb{R}^2)$ .

**Proposition 6.2.** *The Fréchet derivatives  $\left( \mathbf{R}^{\{n,c\}} \right)'(\Phi) \in \mathcal{L}(\mathcal{H}^{11/6}, \mathcal{L}_2)$  of the roof sensor operators  $\mathbf{R}^{\{n,c\}}$  at  $\Phi \in \mathcal{D}(\mathbf{R}^{\{n,c\}})$  are given by*

$$\left( \left( \mathbf{R}_x^{\{n,c\}} \right)'(\Phi) \psi \right)(x, y) = \chi_\Omega(x, y) \frac{1}{\pi} \int_{\Omega_y} \frac{\cos[\Phi(x', y) - \Phi(x, y)] \cdot k^{\{n,c\}}(x' - x) [\psi(x', y) - \psi(x, y)]}{x' - x} dx'$$

and

$$\left( \left( \mathbf{R}_y^{\{n,c\}} \right)'(\Phi) \psi \right)(x, y) = \chi_\Omega(x, y) \frac{1}{\pi} \int_{\Omega_x} \frac{\cos[\Phi(x, y') - \Phi(x, y)] \cdot k^{\{n,c\}}(y' - y) [\psi(x, y') - \psi(x, y)]}{y' - y} dy'.$$

*Proof.* The Fréchet derivatives of the roof sensor operators were already introduced in Theorem 3.10 and Theorem 3.11.  $\square$

The calculation of the adjoint operators depends on the underlying Hilbert spaces and the accordant inner product. As we consider linear and continuous Fréchet derivatives  $\left( \mathbf{R}_x^{\{n,c\}} \right)'(\Phi) : \mathcal{H}^{11/6} \rightarrow \mathcal{L}_2$ , the corresponding adjoints map from  $\mathcal{L}_2$  into  $\mathcal{H}^{11/6}$ . In

order to calculate the adjoints of the operators defined from  $\mathcal{H}^{11/6}$  into  $\mathcal{L}_2$ , we consider the embedding operator introduced in (3.30) as

$$i_s : \mathcal{H}^{11/6} \rightarrow \mathcal{L}_2$$

and derive the corresponding adjoint operators  $\left( \left( \mathbf{R}_x^{\{n,c\}} \right)' (\Phi) \right)^* : \mathcal{L}_2 \rightarrow \mathcal{H}^{11/6}$  at  $\Phi$  according to [169] by

$$\left( \left( \mathbf{R}_x^{\{n,c\}} \right)' (\Phi) \right)^* = i_s^* \left( \left( \tilde{\mathbf{R}}_x^{\{n,c\}} \right)' (\Phi) \right)^*$$

for  $\left( \left( \tilde{\mathbf{R}}_x^{\{n,c\}} \right)' (\Phi) \right)^* : \mathcal{L}_2 \rightarrow \mathcal{L}_2$ . Hence, it is sufficient to derive the adjoint operators  $\left( \left( \tilde{\mathbf{R}}_x^{\{n,c\}} \right)' (\Phi) \right)^*$  with respect to the inner product in  $\mathcal{L}_2(\mathbb{R}^2)$ . For simplicity of notation, we use  $\left( \left( \mathbf{R}_x^{\{n,c\}} \right)' (\Phi) \right)^*$  for  $\left( \left( \tilde{\mathbf{R}}_x^{\{n,c\}} \right)' (\Phi) \right)^*$  in the following. Details on the implementation of the above considerations can be found in [169].

**Proposition 6.3.** *The adjoint operators  $\left( \left( \mathbf{R}_x^{\{n,c\}} \right)' (\Phi) \right)^* : \mathcal{L}_2(\mathbb{R}^2) \rightarrow \mathcal{L}_2(\mathbb{R}^2)$  of the roof sensor's Fréchet derivatives at  $\Phi$  are represented by*

$$\left( \left( \mathbf{R}_x^{\{n,c\}} \right)' (\Phi) \right)^* \psi(x, y) = -\mathcal{X}_\Omega(x, y) \frac{1}{\pi} \int_{\Omega_y} \frac{\cos[\Phi(x', y) - \Phi(x, y)] \cdot k^{\{n,c\}}(x' - x) [\psi(x', y) + \psi(x, y)]}{x' - x} dx' \quad (6.10)$$

and

$$\left( \left( \mathbf{R}_y^{\{n,c\}} \right)' (\Phi) \right)^* \psi(x, y) = -\mathcal{X}_\Omega(x, y) \frac{1}{\pi} \int_{\Omega_x} \frac{\cos[\Phi(x, y') - \Phi(x, y)] \cdot k^{\{n,c\}}(y' - y) [\psi(x, y') + \psi(x, y)]}{y' - y} dy'. \quad (6.11)$$

*Proof.* Since the proof for the operator in  $y$ -direction is analogous to  $x$ -direction, we only perform the calculation for  $\left( \left( \mathbf{R}_x^{\{n,c\}} \right)' (\Phi) \right)^*$ . For the evaluation of the adjoints, we divide the Fréchet derivatives into two parts

$$\left( \mathbf{R}_x^{\{n,c\}} \right)' (\Phi) = \left( \mathbf{T}_1^{\{n,c\}}(\Phi) \right) - \left( \mathbf{T}_2^{\{n,c\}}(\Phi) \right)$$

with

$$\begin{aligned} \left( \mathbf{T}_1^{\{n,c\}}(\Phi) \right) \psi(x, y) &:= \mathcal{X}_\Omega(x, y) \frac{1}{\pi} \int_{\Omega_y} \frac{\cos[\Phi(x', y) - \Phi(x, y)] \cdot k^{\{n,c\}}(x' - x) \psi(x', y)}{x' - x} dx', \\ \left( \mathbf{T}_2^{\{n,c\}}(\Phi) \right) \psi(x, y) &:= \mathcal{X}_\Omega(x, y) \frac{1}{\pi} \int_{\Omega_y} \frac{\cos[\Phi(x', y) - \Phi(x, y)] \cdot k^{\{n,c\}}(x' - x) \psi(x, y)}{x' - x} dx'. \end{aligned}$$

For any  $\psi, \varphi \in \mathcal{L}_2(\mathbb{R}^2)$  we consider

$$\begin{aligned}
 \left\langle \left( \mathbf{T}_1^{\{n,c\}}(\Phi) \right) \psi, \varphi \right\rangle_{\mathcal{L}_2(\mathbb{R}^2)} &= \int_{\mathbb{R}} \int_{\mathbb{R}} \mathcal{X}_{\Omega}(x, y) \left[ \frac{1}{\pi} \int_{\Omega_y} \frac{\cos[\Phi(x', y) - \Phi(x, y)] \cdot k^{\{n,c\}}(x' - x) \psi(x', y)}{x' - x} dx' \right] \\
 &\quad \cdot \varphi(x, y) dy dx \\
 &= \int_{\Omega_y} \int_{\Omega_x} \psi(x', y) \frac{1}{\pi} \int_{\Omega_y} \frac{\cos[\Phi(x', y) - \Phi(x, y)] \cdot k^{\{n,c\}}(x' - x) \varphi(x, y)}{x' - x} dx dy dx' \\
 &= \int_{\Omega_y} \int_{\Omega_x} \psi(x, y) \frac{1}{\pi} \int_{\Omega_y} \frac{\cos[\Phi(x, y) - \Phi(x', y)] \cdot k^{\{n,c\}}(x - x') \varphi(x', y)}{x - x'} dx' dy dx \\
 &= - \int_{\mathbb{R}} \int_{\mathbb{R}} \psi(x, y) \\
 &\quad \cdot \mathcal{X}_{\Omega}(x, y) \left[ \frac{1}{\pi} \int_{\Omega_y} \frac{\cos[\Phi(x', y) - \Phi(x, y)] \cdot k^{\{n,c\}}(x' - x) \varphi(x', y)}{x' - x} dx' \right] dy dx \\
 &= \left\langle \psi, \left( \mathbf{T}_1^{\{n,c\}}(\Phi) \right)^* \varphi \right\rangle_{\mathcal{L}_2(\mathbb{R}^2)}
 \end{aligned}$$

with

$$\left( \left( \mathbf{T}_1^{\{n,c\}}(\Phi) \right)^* \varphi \right) (x, y) = -\mathcal{X}_{\Omega}(x, y) \frac{1}{\pi} \int_{\Omega_y} \frac{\cos[\Phi(x', y) - \Phi(x, y)] \cdot k^{\{n,c\}}(x' - x) \varphi(x', y)}{x' - x} dx'$$

using the fact that  $k^{\{n,c\}}$  and cosine are even functions. The adjoints of the second part are derived by

$$\begin{aligned}
 \left\langle \left( \mathbf{T}_2^{\{n,c\}}(\Phi) \right) \psi, \varphi \right\rangle_{\mathcal{L}_2(\mathbb{R}^2)} &= \int_{\mathbb{R}} \int_{\mathbb{R}} \mathcal{X}_{\Omega}(x, y) \left[ \frac{1}{\pi} \int_{\Omega_y} \frac{\cos[\Phi(x', y) - \Phi(x, y)] \cdot k^{\{n,c\}}(x' - x) \psi(x, y)}{x' - x} dx' \right] \\
 &\quad \cdot \varphi(x, y) dy dx \\
 &= \int_{\mathbb{R}} \int_{\mathbb{R}} \psi(x, y) \\
 &\quad \cdot \mathcal{X}_{\Omega}(x, y) \left[ \frac{1}{\pi} \int_{\Omega_y} \frac{\cos[\Phi(x', y) - \Phi(x, y)] \cdot k^{\{n,c\}}(x' - x) \varphi(x, y)}{x' - x} dx' \right] dy dx \\
 &= \left\langle \psi, \left( \mathbf{T}_2^{\{n,c\}}(\Phi) \right)^* \varphi \right\rangle_{\mathcal{L}_2(\mathbb{R}^2)},
 \end{aligned}$$

which results in

$$\left( \left( \mathbf{T}_2^{\{n,c\}}(\Phi) \right)^* \varphi \right) (x, y) = \mathcal{X}_{\Omega}(x, y) \frac{1}{\pi} \int_{\Omega_y} \frac{\cos[\Phi(x', y) - \Phi(x, y)] \cdot k^{\{n,c\}}(x' - x) \varphi(x, y)}{x' - x} dx'.$$

Hence, the adjoints of the roof sensor Fréchet derivatives are given by

$$\begin{aligned} \left( \left( \mathbf{R}_x^{\{n,c\}} \right)' (\Phi) \right)^* \psi(x, y) &= \left( \left( \mathbf{T}_1^{\{n,c\}}(\Phi) \right)^* \psi \right)(x, y) - \left( \left( \mathbf{T}_2^{\{n,c\}}(\Phi) \right)^* \psi \right)(x, y) \\ &= -\mathcal{X}_\Omega(x, y) \frac{1}{\pi} \int_{\Omega_y} \frac{\cos[\Phi(x', y) - \Phi(x, y)] \cdot k^{\{n,c\}}(x' - x) [\psi(x', y) + \psi(x, y)]}{x' - x} dx'. \end{aligned}$$

□

## 6.4 Numerical implementation and complexity

In this Section, we summarize some numerical aspects as well as the computational complexities of the proposed methods. First, we choose an adequate representation of the incoming wavefront and the measurements for an  $n \times n$  pyramid sensor. We assume the two dimensional wavefront to be given as linear combination of characteristic functions  $\mathcal{X}_{\Omega_{ij}}(x, y)$  of the subapertures  $(\Omega_{ij})_{i,j=1}^n$ . For the annular telescope aperture  $\Omega = \Omega_y \times \Omega_x$ , the disjoint areas  $\Omega_{ij}$  are chosen such that

$$\Omega = \bigcup_{i,j=1}^n \Omega_{ij} \quad \text{and} \quad \Omega_{ij} \cap \Omega_{ml} = \emptyset \quad \text{for } i \neq m \wedge j \neq l \quad (6.12)$$

as well as

$$\Omega_L = \bigcup_{i=1}^n \Omega_{iL},$$

i.e., the term  $\Omega_L$  indicates the row of the symmetric telescope pupil  $\Omega$  located at  $y$ -position  $L$ . In order to describe an annular telescope aperture instead of a squared one, we assign all areas  $\Omega_{ij}$  being located outside the annular aperture to the empty set in (6.12) just for simplicity of notation. In reality, we have different numbers of subapertures in every row and column of the aperture. For the numerical implementation, we only consider those subapertures being located on the aperture to save computation time. The incoming wavefront is represented by

$$\Phi(x, y) = \sum_{i,j=1}^n \Phi_{ij} \mathcal{X}_{\Omega_{ij}}(x, y) \quad (6.13)$$

with coefficients  $\Phi_{ij} \in \mathbb{R}, 1 \leq i, j \leq n$ .

The pyramid sensor delivers data on every subaperture – more precisely, one measurement in  $x$ -direction and one measurement in  $y$ -direction for every subaperture. For these we choose the same representation as for the incoming phase, i.e.,

$$s(x, y) = \sum_{i,j=1}^n s_{ij} \mathcal{X}_{\Omega_{ij}}(x, y), \quad (6.14)$$

where  $s_{ij} \in \mathbb{R}, 1 \leq i, j \leq n$  denotes the coefficients for the measurements  $s = s_x$  or  $s = s_y$  respectively. The points  $(x_M, y_L)$  where data are assumed to be given can, for

instance, be chosen as the middle points of every subaperture of the symmetric pupil, i.e.,

$$x_M = \frac{-D-d}{2} + M \cdot d, \quad y_L = \frac{-D-d}{2} + L \cdot d \quad \text{for } M, L = 1, \dots, n.$$

Here,  $d = D/n$  again denotes the subaperture size for a primary mirror diameter  $D$ .

**Proposition 6.4.** *Using the representation (6.13) for the incoming phase  $\Phi$  and the direction  $\psi$ , the evaluation of the operators  $\mathbf{R}^{\{n,c\}}$  and  $\left(\left(\mathbf{R}^{\{n,c\}}\right)'(\Phi)\right)^*$  defined according to (3.17)-(3.18) and (6.10)-(6.11) in the middle point  $(x_M, y_L)$  of the subaperture  $\Omega_{ML} \subset \Omega$  for  $1 \leq M, L \leq n$  can be represented by*

$$\left(\mathbf{R}_x^{\{n,c\}}\Phi\right)_{M,L} = \frac{1}{\pi} \sum_{\substack{i=1 \\ i \neq M}}^n \sin[\Phi_{iL} - \Phi_{ML}] \alpha_{iL}^{\{n,c\}}(x_M)$$

and

$$\left(\left(\left(\mathbf{R}_x^{\{n,c\}}\right)'(\Phi)\right)^* \psi\right)_{ML} = -\frac{1}{\pi} \sum_{i=1}^n \cos[\Phi_{iL} - \Phi_{ML}] [\psi_{iL} + \psi_{ML}] \alpha_{iL}^{\{n,c\}}(x_M)$$

with

$$\alpha_{iL}^{\{n,c\}}(x_M) := \begin{cases} \int_{\Omega_{iL}} \frac{k^{\{n,c\}}(x' - x_M)}{x' - x_M} dx', & \text{for } i \neq M, \\ p.v. \int_{\Omega_{ML}} \frac{k^{\{n,c\}}(x' - x_M)}{x' - x_M} dx', & \text{for } i = M. \end{cases} \quad (6.15)$$

*Proof.* Utilizing the representation (6.13) we obtain

$$\begin{aligned} \left(\mathbf{R}_x^{\{n,c\}}\Phi\right)(x, y) &= \mathcal{X}_\Omega(x, y) \frac{1}{\pi} \int_{\Omega_y} \frac{\sin[\Phi(x', y) - \Phi(x, y)] \cdot k^{\{n,c\}}(x' - x)}{x' - x} dx' \\ &= \mathcal{X}_\Omega(x, y) \frac{1}{\pi} \int_{\Omega_y} \frac{\sin\left[\sum_{i,j=1}^n \Phi_{ij} \mathcal{X}_{\Omega_{ij}}(x', y) - \sum_{i,j=1}^n \Phi_{ij} \mathcal{X}_{\Omega_{ij}}(x, y)\right] \cdot k^{\{n,c\}}(x' - x)}{x' - x} dx' \\ &= \mathcal{X}_\Omega(x, y) \frac{1}{\pi} \int_{\Omega_y} \frac{\sin\left[\sum_{i,j=1}^n \Phi_{ij} \mathcal{X}_{\Omega_{ij}}(x', y) - \Phi_{ij} \mathcal{X}_{\Omega_{ij}}(x, y)\right] \cdot k^{\{n,c\}}(x' - x)}{x' - x} dx'. \end{aligned}$$

The application of the non-linear roof sensor operator being evaluated at a point  $(x_M, y_L) \in \Omega_{ML} \subset \Omega$  is represented by

$$\begin{aligned} \left(\mathbf{R}_x^{\{n,c\}}\Phi\right)(x_M, y_L) &= \mathcal{X}_\Omega(x_M, y_L) \frac{1}{\pi} \int_{\Omega_L} \frac{\sin\left[\sum_{i,j=1}^n \Phi_{ij} \mathcal{X}_{\Omega_{ij}}(x', y_L) - \Phi_{ij} \mathcal{X}_{\Omega_{ij}}(x_M, y_L)\right] \cdot k^{\{n,c\}}(x' - x_M)}{x' - x_M} dx' \\ &= \frac{1}{\pi} \int_{\Omega_L} \frac{\sin\left[\sum_{i=1}^n \Phi_{iL} \mathcal{X}_{\Omega_{iL}}(x') - \Phi_{ML}\right] \cdot k^{\{n,c\}}(x' - x_M)}{x' - x_M} dx' \end{aligned}$$

for  $M, L \in \mathbb{N}, 1 \leq M, L \leq n$ . As the subapertures are disjoint, these considerations result in

$$\begin{aligned}
\left(\mathbf{R}_x^{\{n,c\}}\Phi\right)_{M,L} &= \frac{1}{\pi} \int_{\Omega_L} \frac{\sin\left[\sum_{i=1}^n \Phi_{iL} \mathcal{X}_{\Omega_{iL}}(x') - \Phi_{ML}\right] \cdot k^{\{n,c\}}(x' - x_M)}{x' - x_M} dx' \\
&= \frac{1}{\pi} \int_{\Omega_{1L}} \frac{\sin\left[\sum_{i=1}^n \Phi_{iL} \mathcal{X}_{\Omega_{iL}}(x') - \Phi_{ML}\right] \cdot k^{\{n,c\}}(x' - x_M)}{x' - x_M} dx' \\
&\quad + \frac{1}{\pi} \int_{\Omega_{2L}} \frac{\sin\left[\sum_{i=1}^n \Phi_{iL} \mathcal{X}_{\Omega_{iL}}(x') - \Phi_{ML}\right] \cdot k^{\{n,c\}}(x' - x_M)}{x' - x_M} dx' + \dots \\
&\quad + \frac{1}{\pi} \int_{\Omega_{nL}} \frac{\sin\left[\sum_{i=1}^n \Phi_{iL} \mathcal{X}_{\Omega_{iL}}(x') - \Phi_{ML}\right] \cdot k^{\{n,c\}}(x' - x_M)}{x' - x_M} dx' \\
&= \frac{1}{\pi} \int_{\Omega_{1L}} \frac{\sin[\Phi_{1L} - \Phi_{ML}] \cdot k^{\{n,c\}}(x' - x_M)}{x' - x_M} dx' \\
&\quad + \frac{1}{\pi} \int_{\Omega_{2L}} \frac{\sin[\Phi_{2L} - \Phi_{ML}] \cdot k^{\{n,c\}}(x' - x_M)}{x' - x_M} dx' + \dots \\
&\quad + \frac{1}{\pi} \int_{\Omega_{nL}} \frac{\sin[\Phi_{nL} - \Phi_{ML}] \cdot k^{\{n,c\}}(x' - x_M)}{x' - x_M} dx' \\
&= \frac{1}{\pi} \sum_{\substack{i=1 \\ i \neq M}}^n \sin[\Phi_{iL} - \Phi_{ML}] \int_{\Omega_{iL}} \frac{k^{\{n,c\}}(x' - x_M)}{x' - x_M} dx' \\
&= \frac{1}{\pi} \sum_{\substack{i=1 \\ i \neq M}}^n \sin[\Phi_{iL} - \Phi_{ML}] \alpha_{iL}^{\{n,c\}}(x_M).
\end{aligned}$$

Analogously, for the adjoints of the Fréchet derivatives using the representation in (6.13) for both  $\Phi$  and  $\Psi$ , we obtain

$$\begin{aligned}
\left(\left(\mathbf{R}_x^{\{n,c\}}\right)'(\Phi)\right)^* \psi(x_M, y_L) &= -\mathcal{X}_{\Omega}(x_M, y_L) \frac{1}{\pi} \int_{\Omega_L} \frac{\cos[\Phi(x', y_L) - \Phi(x_M, y_L)] \cdot k^{\{n,c\}}(x' - x_M)}{x' - x_M} \\
&\quad \cdot [\psi(x', y_L) + \psi(x_M, y_L)] dx' \\
&= -\frac{1}{\pi} \int_{\Omega_L} \frac{\cos\left[\sum_{i,j=1}^n \Phi_{ij} \mathcal{X}_{\Omega_{ij}}(x', y_L) - \Phi_{ij} \mathcal{X}_{\Omega_{ij}}(x_M, y_L)\right]}{x' - x_M} \\
&\quad \cdot k^{\{n,c\}}(x' - x_M) \left[ \sum_{k,l=1}^n \psi_{kl} \mathcal{X}_{\Omega_{kl}}(x', y_L) + \psi_{kl} \mathcal{X}_{\Omega_{kl}}(x_M, y_L) \right] dx'
\end{aligned}$$

$$\begin{aligned}
 &= -\frac{1}{\pi} \int_{\Omega_L} \frac{\cos \left[ \sum_{i=1}^n \Phi_{iL} \mathcal{X}_{\Omega_{iL}}(x') - \Phi_{ML} \right] \cdot k^{\{n,c\}}(x' - x_M)}{x' - x_M} \\
 &\quad \cdot \left[ \sum_{k=1}^n \psi_{kL} \mathcal{X}_{\Omega_{kL}}(x') + \psi_{ML} \right] dx'.
 \end{aligned}$$

For disjoint subapertures  $\Omega_{ij}$  this results in

$$\begin{aligned}
 \left( \left( \left( \mathbf{R}_x^{\{n,c\}} \right)' (\Phi) \right)^* \psi \right)_{ML} &= -\frac{1}{\pi} \int_{\Omega_L} \frac{\cos \left[ \sum_{i=1}^n \Phi_{iL} \mathcal{X}_{\Omega_{iL}}(x') - \Phi_{ML} \right] \cdot k^{\{n,c\}}(x' - x_M)}{x' - x_M} \\
 &\quad \cdot \left[ \sum_{k=1}^n \psi_{kL} \mathcal{X}_{\Omega_{kL}}(x') + \psi_{ML} \right] dx' \\
 &= -\frac{1}{\pi} \sum_{i=1}^n \cos [\Phi_{iL} - \Phi_{ML}] [\psi_{iL} + \psi_{ML}] \text{ p.v.} \int_{\Omega_{iL}} \frac{k^{\{n,c\}}(x' - x_M)}{x' - x_M} dx' \\
 &= -\frac{1}{\pi} \sum_{i=1}^n \cos [\Phi_{iL} - \Phi_{ML}] [\psi_{iL} + \psi_{ML}] \alpha_{iL}^{\{n,c\}}(x_M)
 \end{aligned}$$

with functions  $\alpha_{iL}^{\{n,c\}}$  defined in (6.15). □

We precompute the functions  $\alpha_{iL}^{\{n,c\}}$  offline which significantly reduces the computational load of the algorithms. Please note that the principal value meaning only has to be used when computing the function values  $\alpha_{ML}^{\{n,c\}}(x_M)$ .

### 6.4.1 Computational complexity

For the evaluation of the numerical effort of the non-linear Landweber and Landweber-Kaczmarz iteration for pyramid sensors we only consider the complexity of the operations that have to be performed online. We exclude the pre-calculations  $\alpha^{\{n,c\}}$  in (6.15) needed for the application of the operators  $\mathbf{P}$  and  $(\mathbf{P}')^*$  from our considerations. As before,  $n$  indicates the number of subapertures in one direction. The number of active subapertures  $N \sim n^2$  denotes the number of unknowns to be found. Please note that the proposed algorithms provide the reconstructed wavefront. An additional step of transforming the reconstructed wavefront into mirror actuator commands must be applied at the end (cf Section 8.2.1 - 8.2.2). The effort of this projection step is not considered in the following.

An overview of the number of floating point operations for both algorithms is provided in Table 6.1. The post loop step necessary in case of the LIPS consists of finding the average of the two resulting reconstructions.

Since for both algorithms we perform the mentioned operations twice (in  $x$ - and in  $y$ -direction), for  $K$  iterations we end up with

$$C_{nonlin.LIPS}(n; K) = (8n^3 + 10n^2) \cdot K + 2n^2 \quad \text{flops}$$

	operation	# of flops
loop	$\mathbf{P}_x \Phi_x$	$2n^3$
	$s_x - \mathbf{P}_x \Phi_x$	$n^2$
	$\mathbf{P}'_x (\Phi_x)^* (s_x - \mathbf{P}_x \Phi_x)$	$2n^3 + 2n^2$
	$\omega \mathbf{P}'_x (\Phi_x)^* (s_x - \mathbf{P}_x \Phi_x)$	$n^2$
	$\Phi_x + \omega \mathbf{P}'_x (\Phi_x)^* (s_x - \mathbf{P}_x \Phi_x)$	$n^2$
post loop step	$\Phi = \frac{1}{2} (\Phi_x + \Phi_y)$	$2n^2$

Table 6.1: The number of floating point operations to be performed online in the non-linear Landweber and Landweber-Kaczmarz method. The post loop step is only necessary for the LIPS and omitted for the KLIPS.

for the application of the Landweber iteration (Algorithm 6.1) having the additional step of averaging and

$$C_{nonlin.KLIPS}(n; K) = (8n^3 + 10n^2) \cdot K \quad \text{flops}$$

for the non-linear Landweber-Kaczmarz approach (Algorithm 6.2). Thus, both algorithms have a computational effort of  $\mathcal{O}(N^{3/2})$ .

## 6.5 End-to-end simulation results

To analyze the performance quality of the proposed non-linear algorithms we simulate an instance of the ELT. We evaluate the reconstruction quality in a closed loop setting and compare the results with those of selected linear wavefront reconstruction algorithms. The presented results correspond to the same METIS-like case as in Chapter 5 for reasons of a direct comparison of the non-linear methods to linear LIPS and KLIPS. The simulation parameters are chosen such that they match those in Table 5.1.

Numerical tests are performed for a range of photon fluxes between 50 and 10000 photons per subapertures per frame. We tuned the relaxation parameter  $\omega$  in (6.9) adapted to the atmospheric parameters and the modulation amplitude of the pyramid sensor with a resolution of 0.1 and fixed it for all variations of photon fluxes. A simple integrator is used for the temporal control of the system. The gain is optimized manually and for the non-modulated sensor the same for all test cases, which underlines the stability of the algorithms with respect to parameter tuning. For the modulated sensor, the gain was adjusted in the simulations with 50 and 100 ph/subap/frame. We found that it is advantageous to have a frequency dependent loop gain correcting with main emphasis on low-order modes at the beginning of a closed loop simulation.

The number of Landweber or Landweber-Kaczmarz iterations is limited to 5. This allows for a reduction of the computational load at the expense of losing the rather minor quality improvements delivered by further iterations. For varying atmospheric

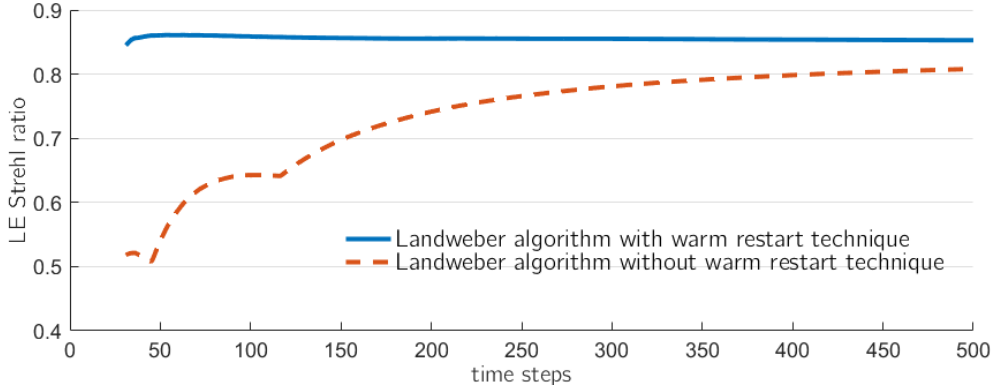


Figure 6.1: Warm restart effect for the non-modulated sensor, source [106]. Without using the warm restart technique (dotted line) the reconstructor suffers from slower convergence compared to the method with a warm restart (solid line). The results correspond to the non-linear LIPS approach for 10000 ph/subap/frame.

photon flux	non-lin. LIPS	non-lin. KLIPS	lin. LIPS	lin. KLIPS
50	0.8520	0.8517	0.8332	0.8371
100	0.8534	0.8534	0.8384	0.8415
1000	0.8530	0.8531	0.8395	0.8420
10000	0.8529	0.8530	0.8396	0.8419

Table 6.2: Long-exposure Strehl ratios in the K-band for a pyramid sensor without modulation obtained with the non-linear Landweber method (Algorithm 6.1) and the non-linear Landweber-Kaczmarz iteration (Algorithm 6.2) after 500 closed loop simulation steps. The simulation results listed for the linear LIPS (Algorithm 5.3) and the linear KLIPS (Algorithm 5.4) correspond to the LE Strehl ratios presented in Chapter 5.

parameters a different preselection of  $K$  may be adequate. As already discussed, we employ the warm restart technique. The initial guess for the first time step is chosen as zero. Then, for time steps  $t > 0$  the initial value is assigned the reconstruction of the last step. Omitting the warm restart but performing the same number of iterations per time step, we observe that the convergence is severely hampered as shown in Figure 6.1 for the non-modulated sensor. However, the warm restart technique was not effective for the modulated sensor. Since the non-linear algorithms do not seem to be best suited for wavefront reconstruction using a modulated pyramid sensor (accurately studied in Section 6.5.1), we attribute this impact to a higher error propagation by allowing errors of the last reconstruction being present in the current reconstruction through the warm restart technique.

photon flux	non-lin. LIPS	non-lin. KLIPS	lin. LIPS	lin. KLIPS
50	0.8155	0.8145	0.8427	0.8439
100	0.8253	0.8201	0.8517	0.8510
1000	0.8333	0.8248	0.8590	0.8562
10000	0.8342	0.8260	0.8595	0.8577

Table 6.3: Long-exposure Strehl ratios in the K-band for a pyramid sensor with modulation  $4 \lambda/D$  obtained with the non-linear Landweber iteration (Algorithm 6.1) and the non-linear Landweber-Kaczmarz iteration (Algorithm 6.2) after 500 closed loop simulation steps. The corresponding results from Chapter 5 obtained with the linear LIPS (Algorithm 5.3) and the linear KLIPS (Algorithm 5.4) are listed as well.

Since we observe a gain in performance by choosing a finer discretization, we divide every subaperture additionally into 3 pixel areas. Thus, on cost of computation time, the quality is increased by about 0.0337 in terms of the LE Strehl ratio after 500 time steps for the KLIPS in the high flux case, i.e., from 0.8193 to 0.8530 for the pyramid sensor without modulation. Additionally, we experience a faster convergence to higher Strehl ratios in case of a finer discretization.

As summarized in the first two columns of Table 6.2 for the non-modulated sensor and of Table 6.3 for the modulated sensor, both proposed algorithms provide stable wavefront reconstruction with comparable results among each other in terms of LE Strehl ratios.

In contrast to the results obtained with the linear iterative methods presented in Chapter 5, we obtain higher reconstruction quality with the non-modulated sensor compared to the modulated sensor in case we are using the proposed non-linear wavefront reconstruction methods. This may come from a higher sensitivity of the non-modulated sensor. Additionally, we experienced that for the modulated PWFS the non-linear algorithms are more sensitive with respect to loop gain and step size choices.

### 6.5.1 Comparison to the linear versions of the algorithms

The sensor without modulation suffers from higher non-linearity effects compared to a sensor having an adequate modulation. In contrast, the expense of the improved linearity range of the modulated sensor is reduced sensitivity of the device [38, 72, 73, 166, 212]. This property of the sensor gives us another reason why we are highly interested in an extension of the regime in which the non-modulated pyramid sensor effectually operates.

A comparison of the reconstruction quality using non-linear LIPS and non-linear KLIPS and their linear versions is given in Figure 6.2 as well as Table 6.2 for the non-modulated sensor. For this sensor type, we obtain higher reconstruction quality with the non-linear processes. Additionally, the Kaczmarz-type methods outperform

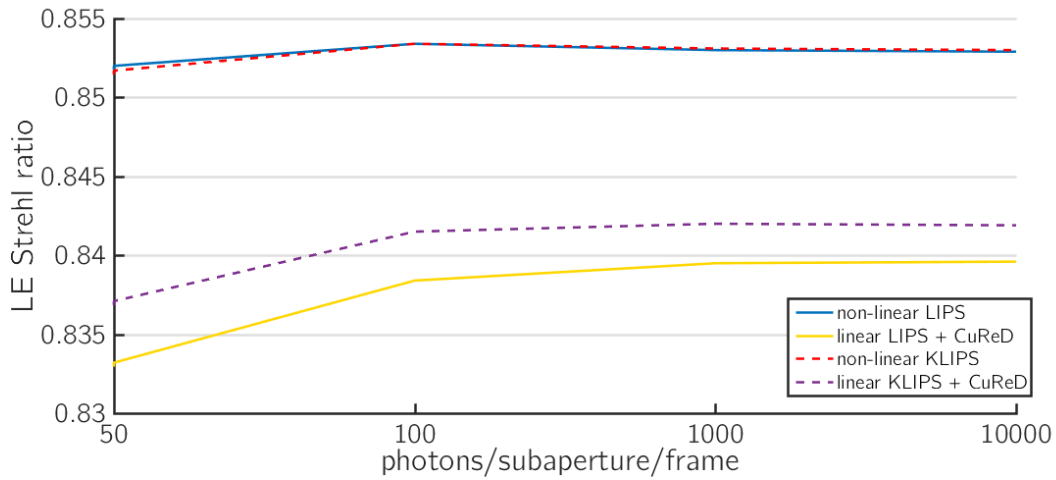


Figure 6.2: Comparison of non-linear and linear methods for the non-modulated sensor, source [106]. The non-linear algorithms outperform the linear approaches. While for the non-linear implementations there is almost no difference between the Landweber (solid lines) and the Landweber-Kaczmarz method (dashed lines), the Kaczmarz version of the linear reconstructors gives a higher improvement in quality.

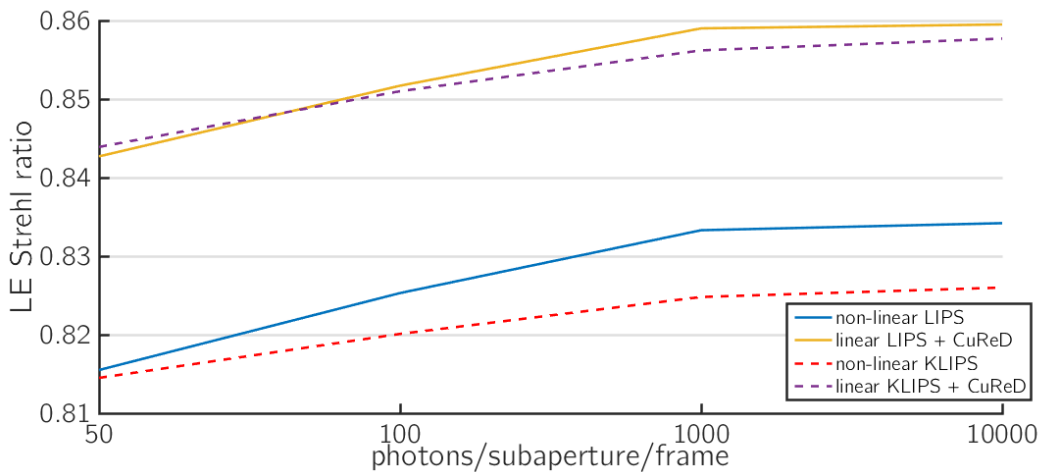


Figure 6.3: Comparison of non-linear and linear methods for the modulated sensor, source [106]. The linear algorithms clearly outmatch the non-linear processes. In the majority of cases the Landweber algorithms (solid lines) outperform the Landweber-Kaczmarz approaches (dashed lines).

the standalone Landweber iterations in most of the cases. These conclusions cannot be directly transferred to the modulated sensor. The results for the modulated sensor in Figure 6.3 as well as Table 6.3 indicate that the linear algorithms outmatch

the non-linear approaches. This may be due to the fact that modulation increases the linearity of the pyramid sensor, and therefore linear algorithms are better suited. Usually, non-linear algorithms for solving Inverse Problems are more error-prone than linear methods. Due to, e.g., numerical errors, the less non-linear an underlying relation is, the better linear algorithms perform. Please note that in the linear algorithms, the CuReD [179, 229] was applied for the first time steps of the AO loop in order to correct mainly for low frequencies.

We infer that an application of non-linear reconstruction methods can notably improve the image quality when using a non-modulated pyramid sensor. For the modulated sensor, we recommend employing linear reconstruction algorithms at least as long as it is guaranteed that the residual phases being sensed by the wavefront sensor are small, e.g., in closed loop AO without significant non-common path errors of the system.

XAO simulations for a non-modulated pyramid sensor on the EPICS instruments with simulation parameters later summarized in Table 7.3 and results presented in Table 6.4 for a variety of photon fluxes confirm the above assertions.

photon flux	CGNE	lin. KLIPS	non-lin. KLIPS
10	0.6268	0.7453	–
50	0.9011	0.8965	0.9002
100	0.9037	0.9005	0.9056
1000	0.9048	0.9002	0.9099
10000	0.9049	0.9006	0.9101

Table 6.4: LE Strehl ratios for the EPICS instrument with a non-modulated PWFS. Results are listed for those iterative reconstruction algorithms providing the most accurate wavefront estimates, namely the CGNE approach, the linear KLIPS and the non-linear KLIPS.

Concerning the computational complexity, the numerical effort of the proposed algorithms is comparable to the complexity of their linear versions being  $\mathcal{O}(N^{3/2})$  as derived in Chapter 5. Nevertheless, the amount of possible precomputations is larger in case of the linear versions of the algorithms which leads to a preference for linear methods with respect to the computational costs of online calculations.

## 6.6 Summary on non-linear LIPS and KLIPS

In this Chapter, we have established two methods, namely non-linear Landweber and Landweber-Kaczmarz iteration for accurate and stable non-linear wavefront reconstruction using pyramid sensors. The theoretical background was accompanied by

a first numerical evaluation of the reconstruction quality. Especially for the non-modulated sensor, the two algorithms provided outstanding performance, with the Landweber iteration being outmatched by its Kaczmarz version. Although the Landweber method is known to converge slowly, we experienced accelerated convergence for AO closed loop simulations using only a small amount of Landweber or Landweber-Kaczmarz iterations per time step. For the sensor having no modulation applied, the warm restart technique additionally speed up the convergence. The low number of necessary iterations positively impacts the computational load of the algorithms whose complexity is given by  $\mathcal{O}(N^{3/2})$ .

According to the results obtained when using linear and non-linear reconstruction methods in end-to-end simulations, we propose choosing the way of reconstruction, i.e., linear or non-linear, dependent on the modulation of the pyramid sensor. For the modulated sensor, we recorded higher reconstruction quality for linear reconstructors while for the non-modulated sensor we experienced better correction for the non-linear versions. However, note that this conclusion was drawn from a limited number of closed loop simulations without critical effects perturbing the linearity of the sensor such as NCPAs.

The assumption of small residual wavefronts being measured by the wavefront sensor and on account of this the linearity of the pyramid sensor may be violated by non common path errors of the system. Thus, the ability of existing linear and non-linear reconstruction strategies to deliver high-quality wavefront corrections even under the impact of large NCPAs is of great interest. We plan to come back to this topic including a detailed investigation of the reconstruction performance for the proposed non-linear algorithms LIPS and KLIPS in the presence of realistic NCPAs in the future. Generally, the influence of the magnitude of the incoming phase distortions on the reconstruction quality needs to be analyzed for both linear and non-linear reconstruction methods.

Obstruction effects induced by wide telescope spiders were omitted in the simulations. The non-linear LIPS and KLIPS both offer the possibility to be combined with Direct Segment Piston Reconstructors according to the so called Split Approach described in Chapter 8. Nevertheless, the stability of the algorithms for segmented pupils needs to be examined in detail.

Proper choices for the basis representations in (6.13)-(6.14), e.g., using wavelets, may significantly improve the reconstruction quality and will be analyzed in future work. However, the representation using the characteristic functions of the subapertures as basis functions allows for offline precomputations, an advantage which may not exist for different choices of basis representations.

Both wavefront reconstruction methods presented in this Chapter are based on the roof wavefront sensor forward model while data are obtained from pyramid sensors. The derivation of the Fréchet derivatives and their adjoint operators for the full pyramid sensor model are planned. Since the latter more precisely describes the pyramid wavefront sensor, we may gain in reconstruction performance.

At present, there already exist several methods that allow for accurate wavefront re-

construction such as MVM based approaches or the P-CuReD algorithm [198] with LE Strehl ratios around 0.89 as summarized in Table 7.4 of the following Chapter. Nevertheless, we want to emphasize the importance of the development of new algorithms since the high reconstruction performance with the linear methods is obtained in undisturbed closed loop AO systems. As recently as extensive studies on the behavior of the linear and non-linear algorithms in the presence of realistic ELT effects such as NCPAs, telescope spiders or the low wind effect have been performed, further conclusions on preferences can be drawn. Due to the non-linearity of the pyramid sensor, degradation of the image quality may appear for reconstructors which are based on the linearity assumption. Furthermore, the LIPS and KLIPS can easier be adapted to more precise pyramid sensor models or segmented telescope pupils as, for instance, the P-CuReD algorithm. The non-linear algorithms are in an early stage of development and improvements for future investigations are expected.

## Chapter 7

# Overview on wavefront reconstruction methods for pyramid sensors

This Chapter contains an extensive overview on wavefront reconstruction methods using pyramid wavefront sensor data. The overview was originally given in [111] as a joint work with Iuliia Shatokhina, Andreas Obereder, and Ronny Ramlau. The Chapter is divided into two parts. First, in Section 7.1 we give short descriptions of the main ideas of existing wavefront reconstruction methods for pyramid wavefront sensors which have not already been introduced in Chapter 4 - 6. Then, we compare existing and new wavefront reconstruction approaches by giving a well-arranged overview on the underlying models, quality results, their computational complexities, and whether they are applicable to sensors with and/or without modulation in Section 7.2.

Generally, we distinguish between interaction-matrix-based and model-based wavefront reconstruction algorithms. Standard approaches using the interaction matrix of the system allow to invert the most exact Fourier optics based model of the PWFS. Model-based methods often work with simplifications of the full pyramid sensor starting from a transmission mask model (cf Section 3.2.1) instead of the phase mask model (cf Section 3.2.2). The transmission mask approach does not take interference effects between the 4 intensity patterns on the detector into account. This assumption is valid if the 4 subbeams leaving the pyramidal prism reach the detector quadrants far from each other. Often, the pyramid model is further simplified by using the roof sensor approximation, i.e., excluding the cross terms in the pyramid operators. The roof sensor operators can be linearized, and then the linear model can be further simplified resulting in one-term operators (cf Section 3.4). For the non-modulated sensor, such a one-term representation coincides with the finite Hilbert transform of the incoming phase. For sensors having modulation, one has to adapt the Hilbert transform by the function indicating modulation. Although the simplifications leading to the one-term approximation are rather significant, numerical validation shows that several reconstruction methods based on that idea still perform very accurate wavefront estimation

by, at the same time, having a significantly reduced computational complexity.

Another distinguishing criterion of wavefront reconstruction algorithms is the non-linearity or linearity. The pyramid wavefront sensor is known to be a non-linear sensor with an almost linear response in closed loop AO when the residual wavefronts are small [28, 212]. The most common way to overcome non-linearity is to increase the linearity regime of the pyramid sensor by applying modulation at the cost of reduced sensitivity [38, 73, 212]. However, in some instruments currently under construction for ELT-sized telescopes, the pyramid sensor is going to be installed in a cryogenic environment. Physical modulation of the prism generates heat, and thus has a negative influence on cryogenic applications. The non-modulated sensor is also the fallback option in case modulating fails due to any technical reasons. Not only due to the enhanced sensitivity of the PWFS, but also because of these impacts becoming more prominent with increasing telescope sizes, the interest in the non-modulated sensor is increasing. Especially for the pyramid sensor without modulation, non-linear wavefront reconstruction algorithms are expected to yield high quality improvements.

While most of the algorithms are applicable with the same computational load to the PWFS both with and without modulation, several of them are not. For instance, the algorithms which are based on the inversion of the Hilbert transform are usually only applicable to the non-modulated sensor data. Some other algorithms have an increased computational demand for the modulated pyramid sensor or do not converge for a specific modulation scenario.

The reconstruction approaches we are considering in the following split into interaction-matrix-based approaches, Fourier domain methods, Hilbert transform based algorithms, as well as iterative methods and are listed below:

- Interaction-matrix-based reconstructors [12, 14, 55, 105, 129, 130, 142, 204]
  - deterministic setting: least-squares pseudo-inverse
  - deterministic setting: regularized least-squares pseudo-inverse
  - Bayesian setting: maximum a posterior (MAP) reconstructor
  - Bayesian setting: minimum mean-square estimator (MMSE)
- Fourier domain methods
  - Preprocessed Cumulative Reconstructor with Domain decomposition (P-CuReD) [198]
  - Fourier Transform Reconstructor (FTR) [162]
  - Convolution with the Linearized Inverse Filter (CLIF) [194, 196]
  - Pyramid Fourier Transform Reconstructor (PFTR) [194, 196]

- Hilbert transform methods
  - Hilbert Transform Reconstructor (HTR) [155, 197, 227]
  - Two Component Reconstructor (TCR) [228]
  - Finite Hilbert Transform Reconstructor (FHTR) [191]
- non-linear iterative methods
  - phase retrieval algorithm [38]
  - Jacobian reconstruction (JR) method [125]
  - quasi-Newton method for optimization [78, 79]

New algorithms which were already presented in Chapter 4 - 6 are:

- Hilbert transform methods
  - Singular Value Type Reconstructor (SVTR) [107]
- linear iterative methods
  - Conjugate Gradient for the Normal Equation (CGNE) for pyramid sensors [108, 109]
  - Steepest Descent (SD) for pyramid sensors [108, 109]
  - Steepest Descent-Kaczmarz (SD-K) for pyramid sensors [108, 109]
  - linear Landweber Iteration for Pyramid Sensors (LIPS) [108, 109]
  - linear Kaczmarz-Landweber It. for Pyramid Sensors (KLIPS) [108, 109]
- non-linear iterative methods
  - non-linear Landweber Iteration for Pyramid Sensors (LIPS) [106]
  - non-linear Kaczmarz-Landweber It. for Pyramid Sensors (KLIPS) [106]

Let us now briefly explain the core characteristics of those algorithms for wavefront reconstruction from pyramid sensor data which were not introduced in Chapter 4 - 6. A precise analysis of the proposed methods can be found in the mentioned references. Note that in the following we use the notations  $\mathbf{P} = \left[-\frac{1}{2}\mathbf{P}_x, \frac{1}{2}\mathbf{P}_y\right]$ ,  $\mathbf{R} = \left[-\frac{1}{2}\mathbf{R}_x, \frac{1}{2}\mathbf{R}_y\right]$ ,  $\mathbf{T} = \left[-\frac{1}{2}\mathbf{T}_x, \frac{1}{2}\mathbf{T}_y\right]$ ,  $\mathbf{H} = \left[-\frac{1}{2}\mathbf{H}_x, \frac{1}{2}\mathbf{H}_y\right]$  and  $s = [s_x, s_y]$  in order to be consistent with the various approximations of equation (3.8) utilizing the operators defined in Chapter 3.

## 7.1 Wavefront reconstruction: current state of the art

Since the pyramid sensor was introduced in the 1990s [164], a considerable amount of wavefront reconstruction attempts was found. First, the interaction-matrix-based MVM approaches, already established for other sensor types, were applied to pyramid sensor data [12, 14, 55, 105, 129, 130, 142, 204]. Later, Fourier transform methods existing for SH sensors were adapted to the application with a PWFS [162] and first experiments with non-linear algorithms were reported [38, 125]. Additionally, the development of fast model-based linear reconstructors [19, 107, 108, 109, 125, 155, 191, 194, 196, 197, 198, 227, 228] and again non-linear reconstructors [78, 79, 106] followed.

### 7.1.1 Interaction-matrix-based reconstructors

*Interaction-matrix-based methods* are the standard on existing telescope facilities. Several variants are often summarized as matrix-vector multiplication (MVM) approaches. An overview on these methods can be found in Chapter 8. The algorithms are generally applicable to pyramid sensors with and without modulation. Inverting the interaction matrix scales as  $\mathcal{O}(n_a^3)$  [55] and the MVM step as  $\mathcal{O}(n_a^2)$  with the number  $n_a$  of active actuators. The computational complexity is rather demanding, which makes MVM methods hardly feasible for large scale AO systems having, e.g., approximately 30000 actuators to control in real-time.

The idea of these methods is based on the simple matrix-relation between discrete sensor data  $\tilde{s}$  and the sought-after mirror actuator commands  $\tilde{a}$  (which are related to the unknown incoming wavefront  $\Phi$ ) given by

$$\tilde{s} = M\tilde{a}.$$

Thus, any procedure for finding the generalized inverse  $M^\dagger$  of the interaction matrix  $M$  (e.g., least-squares pseudo-inverse, regularized least-squares pseudo inverse, or inversion using a truncated singular value decomposition) can be seen as an interaction-matrix-based wavefront reconstruction approach.

### 7.1.2 Fourier domain methods: P-CuReD

The *Preprocessed Cumulative Reconstructor with Domain decomposition* (P-CuReD) [198] is a two step approach consisting of a data preprocessing part and the application of the CuReD [147, 179, 180, 229], originally developed for Shack-Hartmann sensors. The idea is applicable to pyramid sensors with and without modulation. The main argument for using the P-CuReD as wavefront reconstruction method for pyramid sensors is the low computational load of the algorithm by simultaneously providing exceptional quality performance. With a linear complexity, the algorithm

is (to our knowledge) the fastest reconstruction method available for pyramid sensors and gives quality results which are comparable to or even better than those obtained by interaction-matrix-based approaches.

The first step, the data preprocessing, is based on an analytical Fourier domain (FD) relation between linearized pyramid sensor data and Shack-Hartmann sensor data. Approximating the pyramid sensor by the simpler roof sensor model or, more precisely, the one-term assumption (3.28), this FD relation to SH measurements is given by

$$\mathcal{F}\{s_{sh}\}(\xi) = \mathcal{F}\{s_{pyr}\}(\xi) \cdot g_{sh/pyr}(\xi).$$

The measurements  $s_{sh}$  or  $s_{pyr}$  describe Shack-Hartmann or pyramid sensor data respectively and  $g_{sh/pyr}$  the SH-to-pyramid transmission filter. For the spatial frequency  $\xi$  we consider the interval  $[-\xi_{cut}, \xi_{cut}]$  with cut-off frequency  $\xi_{cut} = 1/(2d)$  for the subaperture size  $d$ . Since for the roof sensor the measurements are decoupled for  $x$ - and  $y$ -direction all these considerations can be made in 1d. The SH-to-pyramid transmission filter  $g_{sh/pyr}$  is formulated as

$$g_{sh/pyr}(\xi) := \frac{\mathcal{F}\{s_{sh}\}(\xi)}{\mathcal{F}\{s_{pyr}\}(\xi)} = \frac{g_{sh}(\xi)}{g_{pyr}(\xi)},$$

where  $g_{sh}$ ,  $g_{pyr}$  describe the SH or pyramid filter functions. As derived in [198, 212], for the non-modulated sensor the transmission filter is represented by

$$g_{sh/pyr}^n(\xi) = 2\pi d\xi \operatorname{sgn}(\xi) \quad \forall \xi \in [-\xi_{cut}, \xi_{cut}],$$

for the circularly modulated sensor by

$$g_{sh/pyr}^c(\xi) = \begin{cases} 2\pi d\xi \operatorname{sgn}(\xi), & |\xi| > \xi_{mod}, \\ \frac{\pi^2 d\xi}{\arcsin(\xi/\xi_{mod})}, & |\xi| \leq \xi_{mod}, \end{cases}$$

and for the linearly modulated sensor by

$$g_{sh/pyr}^l(\xi) = \begin{cases} 2\pi d\xi \operatorname{sgn}(\xi), & |\xi| > \xi_{mod}, \\ 2\pi d\xi_{mod}, & |\xi| \leq \xi_{mod}. \end{cases}$$

For a modulation amplitude  $\alpha$  and sensing wavelength  $\lambda$  (see (3.7)), the parameter  $\xi_{mod} = \alpha/\lambda$  indicates the frequency at which the transition between the two regimes of the pyramid sensor (slope versus phase mode) appears (cf Figure 3.2). Converting the transmission filters into space domain kernels by the application of the inverse Fourier transform, i.e.,

$$p_{sh/pyr}(x) = \mathcal{F}^{-1}\{g_{sh/pyr}\}(x)$$

and choosing a suited discretization approach we end up with a representation of the kernels having only few nonzero values. Thus, the data preprocessing, which is

approximated as a row- and column-wise convolution of the measurements with the corresponding kernel, is computationally cheap.

After the pyramid sensor measurements are transformed into SH-like data, the CuReD algorithm is applied to the modified pyramid signal. Besides detailed studies based on numerous closed loop end-to-end simulations, tests on sky proved a high-quality and high-speed performance of the CuReD for SH sensors [15, 16].

Putting the two steps together we obtain an accurate wavefront reconstruction method with a complexity of  $\mathcal{O}(n_a)$ . An additional advantage of the P-CuReD is the ease of usage compared to other approaches since no optimization of intrinsic regularization parameters is needed during the reconstruction process, e.g., if atmospheric conditions change. AO simulation tools users outside our group performed Octopus end-to-end simulations and compared the performances of a modal MVM with the P-CuReD for XAO settings, e.g., in [36, 41]. In [41] the MVM and P-CuReD algorithm give almost the same reconstruction quality with only very slight discrepancies. Moreover, it was shown that the P-CuReD has a faster convergence to high Strehl ratios than the tested MVM approach.

Please note that the P-CuReD algorithm can also be implemented as an MVM since both steps of the algorithm are linear. Nevertheless, for an implementation of this approach as MVM its main advantage, the linear complexity, gets lost.

In principle, the data preprocessing step can be applied in combination with any other reconstructor for Shack-Hartmann wavefront sensor. For instance, the AAO team reports first attempts in [149] to combine data preprocessing with the *Finite Element-Wavelet Hybrid Algorithm* (FEWHA) [168, 225, 226]. For atmospheric tomography, FEWHA calculates the Bayesian maximum a posterior estimate using a preconditioned conjugate gradient method that is coupled with a multi-scale strategy. The algorithm originally utilizes Shack-Hartmann data for the computation of turbulent layers and performs a projection step afterwards. For the discretization of the turbulent layers the method uses a finite element and a wavelet basis simultaneously.

In case of segmented pupils the P-CuReD algorithm combined with a *Direct Segment Piston Reconstructor* (DSPR) [110, 149] shows excellent performance without almost no loss in quality compared to simulations without telescope spiders realized for the METIS instrument on the ELT. This scheme named *Split Approach* is investigated in Chapter 8 in more detail.

### 7.1.3 Fourier domain methods: FTR

Similarly to the P-CuReD algorithm, the *Fourier Transform Reconstructor* (FTR) [162] applies an approach originally developed for SH sensors [161]. In contrast to the P-CuReD, the authors in [162] did not perform any adaption of the method to the pyramid sensor. Instead, the method is underpinned by the assumption of a large

amount of modulation being applied to the PWFS, which makes its response function linear and the sensor itself similar to the SH sensor. The method suggests to relate the pyramid sensor signal to the gradients of the incoming wavefronts. This connection results from the pyramid sensor model derived within the geometrical optics framework valid for large modulation amplitudes. In order to guarantee spatial periodicity, the pyramid sensor signal is appropriately extended outside the pupil mask. To the resulting and afterwards Fourier transformed data an inverse filter relevant for SH sensors is applied. The final DM commands are obtained by taking the inverse Fourier transform.

The FTR offers a possibility for wavefront reconstruction using pyramid sensors with a rather large amount of modulation and has a computational complexity of  $\mathcal{O}(n_a \log n_a)$  if the Fast Fourier Transform (FFT) is used. Since a close correlation between SH and pyramid data is only present for a large amount of modulation, the assumption of pyramid measurements being represented as the gradients of the incoming wavefronts is violated for small or no modulation applied to the PWFS. In case of arbitrary modulation amplitudes, this can be reformulated as follows: The similarity of the PWFS and the SH sensor is only provided for a certain part of the spatial frequencies and the FTR is outperformed by other methods. In [162] it is reported that for small modulations, e.g.,  $1 \lambda/D$  in an 8 m telescope simulation with a sensor having  $40 \times 40$  subapertures, the application of the method is without success. This may affect large-scale AO on Extremely Large Telescope systems stronger due to the reciprocal dependency of the telescope diameter on the modulation amplitude of the pyramid sensor.

Just recently, there were laboratory demonstrations of Fourier reconstruction published in [19] that is directly based on the pyramid sensor's Fourier model as the two Fourier domain methods presented below.

#### 7.1.4 Fourier domain methods: CLIF & PFTR

The *Convolution with the Linearized Inverse Filter* (CLIF) and the *Pyramid Fourier Transform Reconstructor* (PFTR) [194, 196] work with the correlation between the spectra of the discrete sensor data and the incoming wavefront. The PFTR is similar to the FTR but with Fourier domain filter functions being adapted to the pyramid sensor instead of SH filters. The CLIF is the spatial domain representation of the PFTR. CLIF and PFTR are applicable to the pyramid sensor with and without modulation and, as the P-CuReD algorithm, based on the linearized one-term approximation (3.28) of the pyramid sensor. The common idea of both algorithms is the application of the inverse Fourier domain filter functions. While for the CLIF method this is performed in the spatial domain resulting in a complexity of  $\mathcal{O}(n_a^{3/2})$ , for the PFTR the same inversion procedure is carried out in the Fourier domain, and therefore scales as  $\mathcal{O}(n_a \log n_a)$  together with the FFT.

Please note that in the following  $\tilde{s}$  indicates discrete pyramid sensor data and  $\tilde{\xi}$  discrete

frequencies. According to the descriptions in [196, 212], in a discrete setting the spectrum  $\mathcal{F}\{\tilde{s}\}$  of pyramid measurements  $\tilde{s}$  evaluated at the frequency  $\tilde{\xi}$  is a point-wise product of the wavefront spectrum  $\mathcal{F}\{\Phi\}$  with a filter  $g$ , i.e.,

$$\mathcal{F}\{\tilde{s}\}(\tilde{\xi}) = \mathcal{F}\{\Phi\}(\tilde{\xi}) \cdot g(\tilde{\xi}).$$

The discrete filter is given by

$$g(\tilde{\xi}) = g_{pyr}(\tilde{\xi}) \cdot \text{sinc}(d\tilde{\xi})$$

for the pyramid filter functions

$$g_{pyr}^n(\xi) = i \text{sgn}(\xi) \quad \forall \xi \in [-\xi_{cut}, \xi_{cut}]$$

in case of the non-modulated sensor,

$$g_{pyr}^c(\xi) = \begin{cases} i \text{sgn}(\xi), & |\xi| > \xi_{mod}, \\ \frac{2i}{\pi} \arcsin(\xi/\xi_{mod}), & |\xi| \leq \xi_{mod} \end{cases} \quad (7.1)$$

for the circularly modulated sensor, and

$$g_{pyr}^l(\xi) = \begin{cases} i \text{sgn}(\xi), & |\xi| > \xi_{mod}, \\ i\xi/\xi_{mod}, & |\xi| \leq \xi_{mod} \end{cases} \quad (7.2)$$

for the linearly modulated sensor.

Therefore, in the PFTR, the wavefront is reconstructed in the Fourier domain by the multiplication with the inverse filter

$$\mathcal{F}\{\Phi\}(\tilde{\xi}) = \mathcal{F}\{\tilde{s}\}(\tilde{\xi}) \cdot g^{-1}(\tilde{\xi})$$

and a subsequent inverse Fourier transform, or in the CLIF in the spatial domain by the convolution with the kernel

$$\Phi(\tilde{x}) = \left( \tilde{s} * \mathcal{F}^{-1}\{g^{-1}\} \right)(\tilde{x}).$$

Since for the roof wavefront sensor approximation data in  $x$ -direction are independent from  $y$ -direction and vice versa, the considered convolutions and Fourier transforms are in 1d. Data in both directions are handled separately and both obtained reconstructions are averaged afterwards.

The Fourier domain filters  $g^{\{n,c,l\}}$  for different modulation scenarios with modulations 0 and  $12\lambda/D$  are illustrated in Figure 7.1.

Several numerical simulations carried out in closed loop end-to-end simulations in a wide range of atmospheric conditions and photon fluxes showed that the CLIF and PFTR persuade especially for their high reconstruction quality in low flux cases. While results in high flux are slightly under those obtained with the P-CuReD or MVM, CLIF/PFTR outperforms the tested MVM approach for fainter stars in [196].

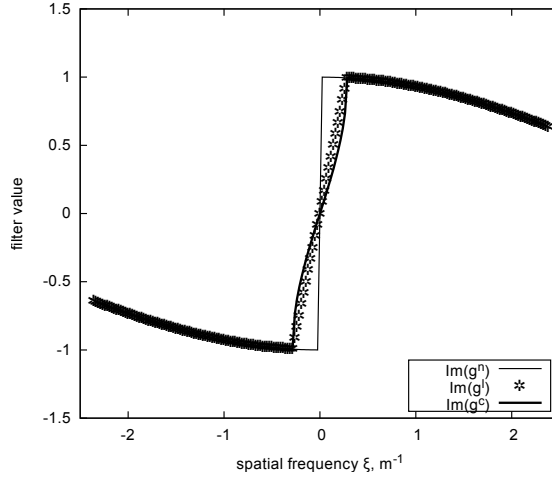


Figure 7.1: Fourier domain filters  $g^{\{n,c,l\}}$ , source [111].

### 7.1.5 Hilbert transform methods: HTR

The *Hilbert Transform Reconstructor* (HTR) arranges the transition from Fourier domain methods to reconstructors based on the inversion of the Hilbert transform  $\mathbf{H}$  according to the operators  $\mathbf{H}_x$  and  $\mathbf{H}_y$  in (3.21) given by

$$(\mathbf{H}_x \Phi)(x, y) := \frac{1}{\pi} p.v. \int_{\mathbb{R}} \frac{\Phi(x', y)}{x' - x} dx'.$$

These methods, generally, are only applicable to a pyramid sensor without modulation. If we assume an infinite telescope size in the definition of the operator  $\mathbf{L}^n$  in (3.28), the non-modulated pyramid sensor measurements can be approximated by the Hilbert transform operator applied to the incoming phase written as

$$s = \mathbf{H}\Phi.$$

Thus, any attempts of inverting the Hilbert transform  $\mathbf{H}$  can be utilized for reconstructing the wavefront  $\Phi$  from non-modulated pyramid sensor data  $s$ .

The inverse of the Hilbert transform is given by its negative, i.e.,  $\mathbf{H}^{-1} = -\mathbf{H}$ . The inversion itself is based on the simple Fourier domain representation of the Hilbert transform given by

$$\mathcal{F}\{\mathbf{H}\Phi\}(\xi) = -i \operatorname{sgn}(\xi) \mathcal{F}\{\Phi\}(\xi).$$

In the HTR algorithm, the inversion of the Hilbert transform is performed in the Fourier domain as a multiplication of the phase spectrum  $\mathcal{F}\{\Phi\}(\xi)$  with the corresponding filter function  $i \operatorname{sgn}(\xi)$ . The reconstructed phase spectrum is afterwards converted to the spatial domain by the application of a one dimensional inverse Fourier transform. Using the FFT algorithm, the mentioned reconstruction method has a computational complexity that scales as  $\mathcal{O}(n_a \log n_a)$ .

The idea was first proposed in [155]. Later, an adaption of the algorithm named the Hilbert Transform with Mean Restoration (HTMR) was found by the Austrian Adaptive Optics team [197, 227]. It was recognized that when using the HTR algorithm the mean values of each row for reconstructions in  $x$ -direction and of each column for reconstructions in  $y$ -direction are zero, and therefore the continuity of the wavefronts gets lost. The idea in the HTMR algorithm is to restore the mean values.

Compared to interaction-matrix-based results in closed loop simulations for an XAO setting on the ELT, these approaches give worse quality. One reason may be that the aperture mask has a strong influence on the sensor data. Hence, the assumption of an infinite telescope size possibly violates the reconstruction performance for annular telescope pupils.

### 7.1.6 Hilbert transform methods: TCR

Approximating the pyramid sensor by a linearized roof sensor (or, more precisely, the one-term assumption (3.28) of it) and considering the modulated filter functions (7.1)-(7.2) one sees that the spectrum of the sensor data consists of two different components, the high frequency part which is constant and given by  $i \operatorname{sgn}(\xi)$  and the low frequency part (almost) linear in  $\xi$ . While the high spatial frequencies of the wavefront are represented in the pyramid sensor data through the Hilbert transform, the low frequency component is represented in the same way as for the SH sensor, i.e., the signals are essentially the gradients of the incoming phases.

The idea of the *Two Component Reconstructor* (TCR) [228] is to consider these two parts separately. For that reason, the sensor data  $s$  are split into a high frequency component  $s_{high}$  and a low frequency component  $s_{low}$  with respect to the threshold frequency  $\xi_{mod} = \alpha/\lambda$ . The high frequency part is reconstructed using the HTMR algorithm and the low frequencies are estimated by application of the CuRe [179, 229], a predecessor of the CuReD [180] for SH sensors. Both reconstructions are then summed up to one final solution by using two different gains, which are individually adapted to both regimes.

The TCR was only applied to modulated pyramid sensor measurements and has a computational complexity of  $\mathcal{O}(n_a \log n_a)$ . After tests for an 8 m telescope having  $40 \times 40$  subapertures carried out in Octopus, the development of the algorithm was not continued and the AAO team concentrated on other more promising approaches as, for instance, the P-CuReD.

### 7.1.7 Hilbert transform methods: FHTR

Another wavefront reconstruction method for non-modulated pyramid sensors is the *Finite Hilbert Transform Reconstructor* (FHTR) [191]. As for the Hilbert transform reconstructors described above, the FHTR is based on a theoretical analysis of the

pyramid sensor transmission mask forward model. After a linearization, which is justified in closed loop AO [28, 212], the pyramid operator is approximated by the finite Hilbert transform  $\mathbf{T}_x : \mathcal{L}_2(\Omega) \rightarrow \mathcal{L}_2(\Omega)$  which is given by

$$(\mathbf{T}_x \Phi)(x, y) := \frac{1}{\pi} p.v. \int_{\Omega_y} \frac{\Phi(x', y)}{x' - x} dx'$$

for a line  $\Omega_y$  of the aperture  $\Omega$  (cf  $\mathbf{L}^n$  in (3.28)). In contrast to the HTR and HTMR, the algorithm now takes finite telescope apertures into account.

As before, the measurements in  $x$ - and  $y$ -directions are decoupled. Both directions are considered as independent, the reconstruction is performed in 1d, and then the two reconstructions are averaged.

In the FHTR approach, the wavefronts are reconstructed by applying the inverse  $\mathbf{T}_x^{-1}$  of the finite Hilbert transform operator  $\mathbf{T}_x$  to the data. One can either utilize the linearized pyramid sensor model (3.29)

$$s_x(x, y) = -\frac{1}{2} [(\mathbf{T}_x \Phi)(x, y) - \Phi(x, y) (\mathbf{T}_x 1)(x, y)],$$

where 1 represents the constant function being equal to 1, and reconstruct iteratively by

$$\Phi_{k+1}(x, y) = -\mathbf{T}_x^{-1}(2s_x - \Phi_k \cdot (\mathbf{T}_x 1))(x, y)$$

or simplify the pyramid sensor measurements further by

$$s_x(x, y) = -\frac{1}{2} (\mathbf{T}_x \Phi)(x, y) \tag{7.3}$$

and reconstruct just by

$$\Phi(x, y) = -2 (\mathbf{T}_x^{-1} s_x)(x, y).$$

In contrast to the classical Hilbert transform  $\mathbf{H}$  with inverse  $\mathbf{H}^{-1} = -\mathbf{H}$ , the inversion of the finite Hilbert transform is not straightforward. However, the inversion of the finite Hilbert transform is nowadays a well-studied problem with many different implementations of the formulas depending on the boundedness of the involved functions on the boundaries of the considered area of interest, e.g., those found in [103, 160, 205].

For the FHTR, the telescope aperture is mapped onto the interval  $[-1, 1]^2$  and the algorithm uses the inverse introduced in [160] as

$$(\mathbf{T}_x^{-1} s_x)(x, y) = -\frac{1}{\pi} \int_{-1}^1 \sqrt{\frac{1-x^2}{1-x'^2}} \frac{s_x(x', y)}{x' - x} dx'$$

for the operator in  $x$ -direction and a fixed  $y \in [-1, 1]$  which gives a problem in 1d. The application of the operator  $\mathbf{T}_y^{-1}$  to the data  $s_y$  is performed separately and in a similar way.

With the computational complexity of  $\mathcal{O}(n_a^{3/2})$ , the algorithm takes an intermediate position among the reviewed methods with respect to speed. Numerical closed loop AO simulations in Octopus showed that the reconstruction performance of the FHTR is rather limited compared to P-CuReD results.

### 7.1.8 Non-linear iterative methods: phase retrieval algorithm

Phase retrieval algorithms in their general form are iterative Fourier domain methods for finding the unknown phase, which satisfies a set of constraints for a measured amplitude, from a given complex signal. In [38], phase retrieval is performed in the context of AO and aims at reconstructing the incoming wavefront  $\Phi$  from intensity measurements provided by a flat pyramid-like sensor type. The authors adapted two well-known algorithms, namely the Gerchberg-Saxton [88] and the error-reduction method [77], to be used in conjunction with a lenslet array placed at the focal plane which constitutes such a sensor. In the paper, the Gerchberg-Saxton algorithm outperforms the error-reduction approach. The twin-image ambiguity problem represented with a lenslet array in the pupil plane, in contrary to SH sensors, can be avoided. The phase retrieval is performed in three Fourier planes and any confusion between an object and its complex conjugate can be removed because of the subdivision at the focal plane. The authors proposed two different choices for the starting value of the algorithm, either a zero phase or the reconstruction obtained from a linear interaction-matrix-based approach. The second idea obviously brings higher reconstruction performance. This means that an additive MVM step is executed which supplementary increases the computational load of approximately 200 expensive phase retrieval iterates.

As reported in [38], in simulations on a circular pupil the phase retrieval approaches yield better reconstruction quality than an interaction-matrix-based MAP reconstructor at the cost of the computational complexity highly outnumbering even that of the MVM. The latter constitutes the major drawback of these algorithms making them unfeasible for large AO systems on ELTs.

### 7.1.9 Non-linear iterative methods: JR method

A non-linear wavefront reconstruction algorithm named *Jacobian Reconstruction* (JR) method based on the transmission mask model of the non-modulated pyramid sensor has been presented in [125]. The idea is related to an iterative approach utilizing the analytical model of the sensor and Newton's method for reconstruction.

If only one Newton iteration is applied, the procedure is linear having a computational complexity comparable to that of conventional MVM algorithms given by  $\mathcal{O}(n_a^2)$ . In the non-linear approach, one has to apply more Newton iterations which dramatically increases the amount of computations. The Jacobian matrices need to be recomputed at each step. The computational requirements of the Jacobian matrix calculations

increase to the fourth power of the Jacobian resolution size, where the Jacobian resolution is at least as big as the size of the wavefront sensor measurement grid in one direction. This results in 50 – 1000 times slower reconstruction times depending on the incorporated solver methods compared to, e.g., the linear approach.

The pyramid sensor model used for deriving this wavefront reconstruction method as well as the numerical simulations do not take interference effects between the four images on the detector into account. Simulation results are obtained for an 8 m telescope having a non-modulated pyramid sensor with  $40 \times 40$  subapertures. It is reported in [125] that in a closed loop simulation the conventional MVM using Karhunen-Loève modes gives comparable results or is slightly outperformed by the JR method with 1 iteration, i.e, its linear version, and that the gain in performance when using additional Jacobi iterations was negligible. While correctly calibrated linear interaction-matrix-based algorithms are powerful strategies for reconstructions if a sensor is fully or almost linear, the JR method was experienced to be most useful at the non-linear regime of the pyramid sensor. In high turbulence, the AO performance of a conventional calibrated MVM method is improved by using a synthetic Jacobian-based reconstruction matrix. According to [125], the JR method mainly reduces the residual energy at low spatial frequencies which is of particular importance for exoplanet detection. Additionally, it was found that the roof sensor is more linear than the pyramid, i.e., most of the non-linearity properties are present in the cross terms of the pyramid sensor model.

Note that this approach describes a non-linear strategy for wavefront reconstruction. Nevertheless, as mentioned in [125], most of the Strehl ratio improvement was achieved by applying only one Newton iteration which again results in a linear reconstructor. Enhancements when using more iterations are negligible.

### 7.1.10 Non-linear iterative methods: quasi-Newton method

A non-linear iterative reconstructor for pyramid sensors that utilizes the pyramidal phase mask model including interference effects is presented in [78, 79]. The wavefront is estimated by solving an unconstrained non-linear minimization problem using Newton’s method as in the previously summarized JR method.

In contrary to the common definition using the intensity difference scheme, the pyramid operator is defined in [78] as the electromagnetic field in the detector plane. Although performing wavefront reconstruction from PWFS data, which are related in a non-linear way to the incoming phase, the idea is based on the fact that the pyramid operator is indeed non-linear with respect to the incoming phase  $\Phi$  but linear with respect to the electric field

$$\Psi = \Omega \cdot e^{-i\Phi},$$

where  $\Omega$  describes the real-valued amplitude.

Newton’s method in its general form requires the Jacobian and the Hessian of the cost function. The Hessian is inverted iteratively by solving a system of equations

using CG. A possible avoidance of this computational expensive steps is found by a variety of quasi-Newton methods which only need the gradient of the cost function. The quasi-Newton algorithm used in this approach is the Broyden-Fletcher-Goldfarb-Shannon (BFGS) method. As initial guess, the solution of the linear least-squares approach is used. This means that the quality improvement relies on two successive wavefront reconstruction processes at the price of computational complexity, as in the phase retrieval iterative method. However, the algorithm applied to pyramid sensors is efficient in the sense that most computationally demanding calculations can be computed offline. The attempt in [78] examines the pyramid sensor without modulation and it is mentioned that for a modulated sensor the computational expense of calculating the intensity and its derivatives will increase.

Simulations were carried out for a non-modulated pyramid sensor using a setting with parameters similar to the SCEXAO/Subaru on a circular aperture. It was assumed that a first-stage AO system has already removed many of the low order aberrations, i.e., there are wavefronts simulated which already correspond to a given Strehl ratio such as 0.3.

The author compared linear least-squares with the initial guess chosen as a flat wavefront and non-linear least-squares with the solution of the linear problem as starting point for the iteration. No straight conclusion can be drawn regarding which approach – linear or non-linear – provides a better reconstruction quality. Both methods have shown their advantages in different simulations depending on the photon flux, the signal-to-noise ratio, and the height of the Strehl ratio already obtained with the first-stage AO system if the non-linear method is used.

Throughout the Thesis we will name this reconstruction algorithm which is presented in [78] the quasi-Newton method for pyramid sensors.

## 7.2 Model, speed, and quality performance comparisons

In order to give a clear overview on the aforesaid algorithms for wavefront reconstruction in astronomical AO using pyramid wavefront sensors, we present the Tables 7.1 - 7.2 and 7.4, where selected properties for all methods are listed. More precisely, we consider the distinguishing criteria already mentioned at the beginning of this Chapter. The characteristics we recall are the pyramidal glass prism mask models on which the reconstruction methods are based, i.e., phase or transmission mask, whether the algorithms are linear or non-linear, and if the attempts are based on the full pyramid sensor model, the roof sensor or the one-term assumption. Additionally, we once more bring up the adaptability of the reconstruction processes to non- and modulated sensor data as well as the computational complexity of all approaches and the achievable reconstruction quality of selected algorithms.

Algorithm	Pyramidal mask		Linearity		Sensor			Modulation	
	phase	transm.	non-lin.	lin.	pyr.	roof	one-term	yes	no
Interaction-matrix-based	✓			✓	✓			✓	✓
P-CuReD		✓		✓			✓	✓	✓
FTR				✓			✓	✓	
CLIF		✓		✓			✓	✓	✓
PFTR		✓		✓			✓	✓	✓
HTR		✓		✓			✓		✓
TCR		✓		✓			✓	✓	
FHTR		✓		✓		✓	✓		✓
SVTR		✓		✓			✓		✓
CGNE		✓		✓	(✓)	(✓)	✓	✓	✓
SD		✓		✓	(✓)	(✓)	✓	✓	✓
SD-K		✓		✓	(✓)	(✓)	✓	✓	✓
linear LIPS		✓		✓	(✓)	(✓)	✓	✓	✓
linear KLIPS		✓		✓	(✓)	(✓)	✓	✓	✓
phase retrieval		✓	✓		✓				✓
JR method		✓	✓	✓	✓	✓			✓
quasi-Newton method	✓		✓		✓			(✓)	✓
non-linear LIPS		✓	✓		(✓)	✓		✓	✓
non-linear KLIPS		✓	✓		(✓)	✓		✓	✓

Table 7.1: Overview on existing wavefront reconstruction methods for the PWFS with respect to underlying pyramid sensor models. The check marks in brackets indicate that an according extension has already been considered in theory but has not been implemented yet.

To analyze the performance quality of the algorithms for the pyramid sensor we simulate the ELT currently under construction in Chile. Simulations are carried out for the METIS [24] and the EPICS [120] instrument in a closed loop setting. The reconstruction quality is quantified in terms of the LE Strehl ratio. The observing wavelength for the results presented in the following corresponds to  $\lambda_{science} = 2.2 \mu\text{m}$  (K-band). Table 7.3 provides an overview of the simulation parameters.

For a SCAO simulation we consider a METIS-like case [24] of the ELT having a primary mirror diameter of 39 meters of which only the inner 37 meters are used for the instrument. The edges of the real 39 m primary mirror are cropped such that it remains a circular pupil with roughly 30% of the primary mirror being obstructed by the secondary mirror. Six telescope spiders being 50 cm thick are taken into account in 2 of the simulations. The end-to-end simulation software generates a von Karman realization of median atmospheric conditions having 35 frozen layers at heights between 30 m and 26.5 km. The Fried parameter is equal to  $r_0 = 15.7 \text{ cm}$  at  $\lambda = 500 \text{ nm}$  and the outer scale is  $L_0 = 25 \text{ m}$ . The simulated screens are resolved with 0.05 m per pixel which results in  $740 \times 740$  pixels on the aperture for a 37 m telescope. Sensing is performed in the K-band at a wavelength of  $\lambda = 2.2 \mu\text{m}$ . The data in Octopus are simulated using the built-in model of a  $74 \times 74$  pyramid wavefront sensor without modulation and with modulation  $4 \lambda/D$ , i.e., the subaperture size is 0.5 m. The pyramid sensor measurements are read out 500 times per second for the modulated sensor or

Algorithm	Modulation		Complexity
	no	yes	
Interaction-matrix-based [12, 14, 55, 105, 129, 130, 142, 204]	+	+	$\mathcal{O}(n_a^2)$
P-CuReD [198]	+	+	$\mathcal{O}(n_a)$
FTR [162]	-	+	$\mathcal{O}(n_a \log n_a)$
CLIF [196]	+	+	$\mathcal{O}(n_a^{3/2})$
PFTR [196]	+	+	$\mathcal{O}(n_a \log n_a)$
HTR [155, 227]	+	-	$\mathcal{O}(n_a \log n_a)$
TCR [228]	-	+	$\mathcal{O}(n_a \log n_a)$
FHTR [191]	+	-	$\mathcal{O}(n_a^{3/2})$
SVTR [107]	+	-	$\mathcal{O}(n_a^{3/2})$
CGNE [109]	+	+	$\mathcal{O}(n_a^{3/2})$
SD [109]	+	+	$\mathcal{O}(n_a^{3/2})$
SD-K [109]	+	+	$\mathcal{O}(n_a^{3/2})$
linear LIPS [109]	+	+	$\mathcal{O}(n_a^{3/2})$
linear KLIPS [109]	+	+	$\mathcal{O}(n_a^{3/2})$
phase retrieval [38]	+	-	$\geq \mathcal{O}(n_a^2)$
JR method [125]	+	-	$\geq \mathcal{O}(n_a^2)$
quasi-Newton method [78]	+	-	$\geq \mathcal{O}(n_a^2)$
non-linear LIPS [106]	+	+	$\mathcal{O}(n_a^{3/2})$
non-linear KLIPS [106]	+	+	$\mathcal{O}(n_a^{3/2})$

Table 7.2: Overview on existing wavefront reconstruction methods for the PWFS showing the computational complexity and the modulation scenarios they were already implemented for.

1000 times per second for the non-modulated sensor. The deformable mirror geometry corresponds to the M4 geometry that is planned for the ELT (see Figure 2.11). In Octopus, a total number  $n_a = 5190$  of mirror actuators is controlled.

For the XAO case we simulate a variant of the EPICS instrument [120] on the originally planned 42 m ELT. The simulation parameters of the closed loop setting are summarized in Table 7.3. We have a central obstruction of 28% and do not take telescope spiders into account. The phase screens are generated according to the von Karman statistics for 9 atmospheric layers at heights between 47 m and 18 km. The seeing conditions are median, the Fried parameter is equal to  $r_0 = 12.9$  cm at  $\lambda = 500$  nm and the outer scale corresponds to  $L_0 = 25$  m. The resolution of the incoming screens is given by  $2000 \times 2000$  pixels on the pupil. Sensing is performed in the visible at  $\lambda = 0.7 \mu\text{m}$ . The data is provided by a non- and modulated  $200 \times 200$  pyramid wavefront sensor having a subapertures size of 0.21 m. The pyramid sensor measurements are read out 3330 times per second. For XAO, we control a total number of  $n_a = 29618$  mirror actuators of the deformable mirror positioned according to the Fried geometry.

SIMULATION PARAMETERS	METIS-like simulation	EPICS-like simulation
telescope diameter	37 m	42 m
central obstruction	30%	28%
science target	on-axis (SCAO)	on-axis (XAO)
WFS	PWFS	PWFS
sensing band $\lambda$	K (2.2 $\mu\text{m}$ )	R (0.7 $\mu\text{m}$ )
evaluation band $\lambda_{\text{science}}$	K (2.2 $\mu\text{m}$ )	K (2.2 $\mu\text{m}$ )
modulation	[0, 4]	[0, 4]
controller	integrator	integrator
atmospheric model	von Karman	von Karman
number of simulated layers	35	9
outer scale $L_0$	25 m	25 m
atmosphere	median	median
Fried radius $r_0$ at $\lambda = 500$ nm	0.157 m	0.129 m
number of subapertures	$74 \times 74$	$200 \times 200$
number of active subapertures	[3874, 3912, 4128] out of 5476	28796 out of 40000
linear size of simulation grid	740 pixels	2000 pixels
DM geometry	ELT M4 model	Fried
telescope spiders	yes/no	no
DM delay	1	1
frame rate	[1000, 500] Hz	3300 Hz
photon flux	[600, 10000] ph/subap/frame	50 ph/subap/frame
detector read-out noise	1 electron/pixel	2.8 electron/pixel
background flux	0.000321 photons/pixel/frame	0 photons/pixel/frame
simulation time	0.5 – 2 s ([500, 1000] iterations)	$\sim 0.15$ s (500 iterations)

Table 7.3: Overview of simulation parameters for the currently scheduled METIS and an EPICS-like instrument.

The numerical results in Table 7.4 indicate that the optimal choice of the wavefront reconstructor heavily depends on physical parameters related to the telescope facility and the sensor device such as subaperture size or the modulation amplitude of the pyramid sensor and on atmospheric parameters. Definitely, the most advanced reconstruction approaches for telescope systems having non-segmented pupils are interaction-matrix-based methods. These methods are nowadays running in AO systems of ground-based observing facilities having mirror sizes up to about 10 m, and therefore are those algorithms for which users have the most practical experience. MVM approaches usually have the most exact pyramid sensor model as a foundation since the calibration often is performed in realistic environments. Unfortunately, these methods have a major drawback – their high computational complexity. While the computational load is expected to be manageable at the time of future ELT launches for comparably small AO systems such as in SCAO, achieving the speed required for large scale AO systems is doubtful. As an alternative, we suggest fast, model-based wavefront reconstruction algorithms. As such, the P-CuReD is outstanding for its quality results, its speed, and its ease of usage in all performed test cases. For the non-modulated sensor, the non-linear LIPS and KLIPS give promising quality results. In particular in the XAO simulation and for the modulated sensor, the performance of the linear CGNE approach must be emphasized. Above all, the algorithms which were presented in

Algorithm	Quality in end-to-end simulations (Octopus)					
	(LE Strehl ratios in the K-band)					
	SCAO mod 0	SCAO mod 4	SCAO mod 0	SCAO mod 4	XAO mod 0	XAO mod 4
Modulation ( $\lambda/D$ )						
Photon flux (ph/pix/it)	10000	10000	10000	600	50	50
Frame rate (kHz)	1	0.5	1	0.5	3	3
Mirror geometry	M4	M4	M4	M4	Fried	Fried
Telescope spiders	$\times$	$\times$	$\checkmark$	$\checkmark$	$\times$	$\times$
Interaction matrix inversion: modal	$\approx 0.62$ [132]	0.888		0.859 [110]		0.96
Interaction matrix inversion: zonal		<b>0.89</b>	<b>0.890</b>	<b>0.894</b> [110]		
Preprocessed CuReD (P-CuReD)	<b>0.871</b>	0.887	0.865	0.878 [110]	<b>0.916</b>	<b>0.961</b>
Conv. with Lin. Inverse Filter (CLIF)					0.88	0.94
Pyramid FTR (PFTR)					0.88	0.94
Finite Hilbert Transform Rec. (FHTR)	0.779	NA		NA	0.853	NA
Singular Value Type Rec. (SVTR)	0.740	NA		NA	0.884	NA
Conj. Gradient for Normal Eq. (CGNE)	0.842 [109]	0.860 [109]			0.901	
Steepest Descent (SD)	0.841 [109]	0.858 [109]				
Steepest Descent-Kaczmarz (SD-K)	0.841 [109]	0.858 [109]				
linear Landweber iteration (LIPS)	0.840 [109]	0.860 [109]				
linear Kaczmarz-Landweber It. (KLIPS)	0.842 [109]	0.858 [109]			0.897	
non-linear LIPS	0.853 [106]	0.834 [106]				
non-linear KLIPS	0.853 [106]	0.826 [106]			0.903	

Table 7.4: Reconstruction quality of selected reconstruction algorithms for the METIS (SCAO) and EPICS (XAO) instrument of the ELT using pyramid sensors with or without modulation. We took telescope spiders into account for 2 simulations. The P-CuReD results for segmented pupils were obtained within the Split Approach (cf Chapter 8). The fields are left empty if no simulations were performed and “NA” means that the method is not applicable to this setting.

Chapter 4 - 6 in more depth, were experienced to provide accurate, robust and stable wavefront reconstruction for the pyramid wavefront sensor without modulation.

The mentioned approaches were, in particular, tested on non-segmented pupils for a pyramid wavefront sensor acting in its linear regime, e.g., in closed loop AO. One reason for starting to investigate non-linear approaches for wavefront reconstruction using pyramid sensor data was the presence of large non common path aberrations (NCPAs) on ELTs which affect the nonlinearity issue of the pyramid sensor. For large NCPAs, the linearity of the pyramid sensor may be violated and a usage of a non-linear reconstructor can become of great benefit. However, the results of non-linear LIPS and KLIPS are rather preliminary. Detailed studies in the future shall bring a better understanding of the nonlinearity effects of the sensor and, based on that, improvements of the methods themselves (cf Chapter 6).

Moreover, METIS simulations demonstrated that variants of zonal interaction-matrix-based MVM approaches and the P-CuReD coupled with a Direct Segment Piston Reconstructor provide (almost) differential piston-free wavefront estimates for fragmented telescope pupils, a phenomenon that has an especially big impact on ELT-sized telescopes with details studied in the next Chapter.

## Chapter 8

# Accurate wavefront reconstruction in the presence of telescope spiders

The new generation of Extremely Large Telescopes with mirror diameters up to 40 meters has thick secondary mirror support structures also known as spiders which cause difficulties in the wavefront reconstruction process. These spiders create areas where the information of the phase is disconnected on the wavefront sensor detector leading to pupil fragmentation and a loss of data on selected subapertures. The effects on wavefront reconstruction are differential pistons between segmented areas leading to extremely poor wavefront reconstruction. The resulting errors make the majority of existing control algorithms unfeasible for telescope systems having spiders incorporated. A solution, named the Split Approach, is presented, which suggests to separate reconstruction of segment piston modes from the rest of the wavefront. Further, two methods are introduced for the direct reconstruction of the segment pistons. Due to the separate handling of the piston offsets on the segments, the Split Approach makes any of the existing phase reconstruction algorithms developed for non-segmented pupils suitable for wavefront control in the presence of telescope spiders.

The content of this Chapter relies on a joint work with Iuliia Shatokhina, Andreas Obereder, and Ronny Ramlau presented in [110, 149].

### 8.1 Differential piston effects induced by telescope spiders

The pupils on the ELT-generation telescopes are inevitably segmented and partially shaded by thick support structures as shown in Figure 8.1. Due to small subapertures, the spiders lead to a fragmentation of the pupil into several disjoint segments and cover partially or even completely up to several subapertures. If a wavefront sensor provides only local information about the wavefront, as the Shack-Hartmann does, some gradient information is lost in case the sensor data is segmented into disconnected domains. An exact reconstruction of low-order modes is impossible. Differential pistons between

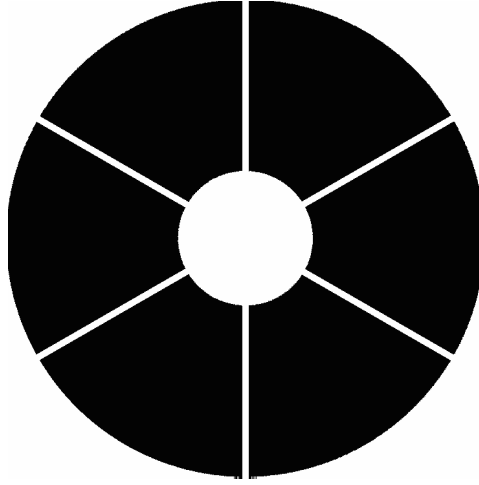


Figure 8.1: ELT pupil mask with spiders, source [110, 149]. The ELT will consist of a 39.3-meter-diameter primary mirror and a 4.2-meter-diameter secondary mirror which will be supported by 6 spiders each being 50 cm thick.

the segments are not seen by the sensor and can therefore not be controlled [21]. Hence, it is necessary to choose a wavefront sensor that can provide wavefront information which is spread globally across the whole pupil. As such, the pyramid wavefront sensor [164] is planned to be part of many instruments currently under development for ELT-sized telescopes.

Numerous end-to-end simulations performed with various reconstruction algorithms (summarized in Sections 8.2.5 and 8.3.2), however, have shown that even using the global-type wavefront sensor does not automatically lead to correct reconstructions of segmented pistons with an arbitrary reconstruction algorithm designed for non-segmented annular apertures. Many of the known methods fail, meaning that the residuals contain randomly appearing uncontrolled piston modes on the segments also known as island effect. The consequence is a significantly reduced correction quality in terms of Strehl ratio, PSF, and contrast. In addition to pupil segmentation, another challenge that wavefront reconstruction algorithms for the ELTs have to tackle with is the high number of correcting elements that need to be controlled in real-time.

Having these two points in mind, in Section 8.2 and Section 8.3 we give an overview of the available algorithms and their readiness / ability to operate both fast and stable with high quality on ELTs. The reconstructors we will be dealing with are using different forward models of the pyramid wavefront sensor or its approximations, a fact that turns out to be crucial under pupil fragmentation. The analysis is performed in the context of the METIS instrument [24] on the ELT containing a SCAO system with  $74 \times 74$  WFS subapertures. The geometry of the planned ELT M4 deformable mirror

is taken into account. The thickness of the 6 secondary mirror support structures is 50 cm and coincides with the subaperture size.

On the one hand, as shown in Section 8.2.5, the current status of the performed simulations tells that among all possible variants of the interaction-matrix-based MVM methods at least one, the minimum variance reconstructor using a zonal interaction matrix and Laplacian regularization, is able to provide a stable control of the segmented low-order modes. However, the well-known drawback of any MVM method is the related computational load. Though for the considered SCAO system the real-time application of matrix-vector multiplication is still doable, it is hardly feasible in case of the planned XAO system having tens of thousands correcting elements to control.

On the other hand, as presented in Chapter 4 - 7 and briefly reviewed in Section 8.3, there exists a variety of interaction-matrix-free, model-based wavefront reconstructors developed for pyramid wavefront sensors in the recent decade, all of them being significantly faster than MVM approaches. For instance, the fastest method available, the P-CuReD [191, 195, 198], has only a linear complexity  $O(n_a)$ , while any MVM is of complexity  $O(Nn_a)$  with  $N$  denoting the number of active subapertures and  $n_a$  the number of active actuators. However, since those methods were developed such that they are intrinsically using the approximate forward models of the sensor not including segmented pupils, these methods fail when being applied straightforward to segmented sensor data. In Section 8.3.2 we additionally mention several attempts for wavefront reconstruction on segmented pupils that unfortunately do not yield the expected performance. Therefore, in the presence of spiders, model-based wavefront reconstruction algorithms need to be adapted in order to handle the differential pistons between the pupil segments.

As a solution allowing for both high-quality and high-speed wavefront control we suggest in Section 8.4 a hybrid scheme. This approach combines the advantage of the interaction-matrix-based methods of being able to handle pupil segmentation and the advantage of the model-based reconstructors of being incredibly fast. The solution, named the *Split Approach*, treats the reconstruction of segmented pistons separately from the higher-order modes (or frequencies). Here, the piston-free wavefront reconstruction on segments is provided by some fast model-based algorithm, e.g., the P-CuReD, as described in Section 8.4.1. In parallel, the segment pistons are reconstructed from the same sensor data with an interaction-matrix-based MVM approach. Since for the direct segment piston reconstruction we are only interested in the modes of order zero, the computational load can be significantly reduced.

In Section 8.4.2 we demonstrate two possibilities towards the formulation of the direct piston reconstruction for segmented pupils. The first one employs the usual setting of the full zonal interaction matrix using a set of dedicated basis functions representing the wavefront. This big matrix is then inverted via standard techniques of regularization and the resulting intermediate control matrix is afterwards reduced to a new, small sized, control matrix relating the sensor data with the vector of segment pistons having only as many entries as pupil segments. Though still requiring the computationally expensive setting up and inversion of a dense matrix, which can be performed

off-line, the online calculations have linear complexity  $O(n_a)$  and are very cheap. In the second approach for direct segment piston reconstruction, the initial interaction matrix is formulated in the basis of segment pistons and is therefore very small from the start. Resulting in the same number of computations to be performed online, this approach is, in addition, free from the time-consuming (offline) operations involved in the first approach.

In combination with the P-CuReD, both direct segment piston reconstruction methods have an overall computational effort which scales linearly. In Section 8.5 we illustrate the performance of the Split Approach employing the two proposed methods for direct piston reconstruction for segmented pupils with end-to-end closed loop simulation results.

Let us denote the model of the pyramid sensor by an operator  $\mathbf{P} : \mathcal{H}^{11/6}(\mathbb{R}^2) \rightarrow \mathbb{R}^{2N}$ , which maps real-valued  $\mathcal{H}^{11/6}$ -functions (wavefronts, residual phases) to a vector of discrete measurements of length  $2N$ . The measurement process is given by

$$\vec{s} = \mathbf{P}\Phi + \vec{\eta}, \quad (8.1)$$

where  $\Phi$  describes the incoming phase,  $\vec{s} = \begin{pmatrix} \vec{s}_x \\ \vec{s}_y \end{pmatrix}$  pyramid sensor measurements, and  $\vec{\eta}$  the noise in the data. The Inverse Problem is to reconstruct the wavefront  $\Phi$  from given noisy sensor data  $\vec{s}$ . Throughout this Chapter, we assume the pyramid sensor to operate in closed loop AO, i.e., to be linear.

Due to the global response, the PWFS is able to sense the differential pistons, which has been successfully demonstrated in the laboratory [66, 70], supported by numerical simulations, and validated on sky under seeing-limited conditions [71]. The ability of the PWFS to sense the differential pistons of a segmented mirror and correct for it with an inversion based on the singular value decomposition of the measured interaction matrix was first demonstrated in numerical simulations in [62]. Among all in [201] tested WFS types, the PWFS takes the most sensitive measurements of the differential pistons on the segments. Apart from that, compared to the Shack-Hartmann WFS the PWFS provides an increased sensitivity which leads to higher limiting guide star magnitudes and higher sky coverage [64].

The interaction-matrix-based MVM methods are intentionally described in Section 8.2 with a much higher level of detail compared to the model-based algorithms in Section 8.3. As it was already done in more detail for the model-based reconstructors, which turned out to struggle under the circumstances of pupil fragmentation, in Chapter 4 - 7, we now aim at detailed descriptions of existing MVM-based methods. The focus of this Chapter is to study, compare, and understand the behavior of different algorithms under pupil fragmentation. As a result of these efforts, the current Chapter serves partially as a review of the currently available MVM-based wavefront reconstruction algorithms for pyramid wavefront sensors and, in particular, of the present status in the performance those reach on the ELT-era instruments under design.

The connection between incoming wavefronts  $\Phi$ , residual wavefronts  $\Phi_{res}$  and the mirror shape  $\varphi$  in an AO system is given by

$$\Phi_{res} = \Phi + \varphi.$$

Since for ideal compensation the residual wavefront  $\Phi_{res}$  should be equal to zero, the optimal choice for the DM shape is

$$\varphi = -\Phi.$$

For the control of deformable mirrors one needs to know either the mirror actuator commands or the shape of the incoming wavefront provided as the solution of the Inverse Problem (8.1) for  $\Phi$ .

## 8.2 Interaction-matrix-based reconstructors

In this Section, we analyze the applicability and performance of the so called interaction-matrix-based MVM methods for PWFS data and fragmented pupils. These methods involve a registration (or computation) of a WF-to-WFS interaction matrix, its inversion and a subsequent multiplication of the obtained control matrix with a vector of sensor data. In the literature there have been many variants of interaction-matrix-based MVM approaches presented: statistical estimation or solution in a least-squares sense; zonal or modal control approaches (i.e., the degrees of freedom are actuators or modes). The presented overview aims to summarize and compare the performance of existing interaction-matrix-based MVM methods in case of PWFS data fragmented by spiders. In Section 8.2.1 the generation of a WF-to-WFS interaction matrix is described, and the option of coupling or decoupling this step with the DM is explained in Section 8.2.2. In Section 8.2.3 the simplest least-squares approach and its regularized inversion are specified, while Section 8.2.4 deals with more sophisticated statistical approaches. Finally, the quality and speed performance of the interaction-matrix-based MVM algorithms are summarized in Section 8.2.5.

### 8.2.1 Generating the interaction matrix

We introduce  $(h_i)$  as a set of arbitrary basis functions to represent the wavefront,  $(h_i^m)$  as a set of modal/global basis functions, and  $(IF)$  denotes the DM influence functions (cf Section 2.4.4). In order to create the interaction matrix of the system, we need to relate the incoming wavefront with the output (measurements) of the PWFS. We represent the incoming wavefront  $\Phi$  using a set of basis functions  $(h_i)$ . Thus,  $\Phi$  can be approximated by

$$\Phi(x, y) = \sum_{j=1}^{n_c} c_j h_j(x, y), \quad (8.2)$$

where  $n_c$  indicates the number of used basis functions.

The interaction matrix  $\mathbf{M} \in \mathbb{R}^{2N \times n_c}$  is then given by

$$\mathbf{M} = \begin{pmatrix} \vec{s}_1 & \vec{s}_2 & \cdots & \vec{s}_{n_c} \end{pmatrix}, \quad (8.3)$$

i.e., the measurements

$$\vec{s}_i = \begin{pmatrix} \vec{s}_x(h_i) \\ \vec{s}_y(h_i) \end{pmatrix} = \mathbf{P}(h_i) \quad \text{for } i = 1, 2, \dots, n_c \quad (8.4)$$

corresponding to the basis function  $h_i$  build the  $i$ -th column of the interaction matrix. The obtained measurements in  $x$ - and  $y$ -direction are arranged in vectors  $\vec{s}_i \in \mathbb{R}^{2N}$ . The sensor equation, as already mentioned, reads as

$$\vec{s} = \mathbf{P}\Phi + \vec{\eta}$$

To reconstruct the incoming (residual) wavefront  $\Phi$  the matrix  $\mathbf{M}$  has to be “inverted” and applied to the measurements. This step is represented by

$$\vec{c} = \mathbf{M}^\dagger \vec{s}$$

with  $\vec{c} = (c_i)_{i=1, \dots, n_c}$ .

After the reconstruction step, one has to derive the corresponding actuator commands  $\vec{a} = (a_i)_{i=1, \dots, n_a}$  from the reconstruction  $\Phi$ , i.e., solve

$$\Phi(x, y) = \sum_{j=1}^{n_c} c_j h_j(x, y) = \sum_{j=1}^{n_a} a_j IF_j(x, y). \quad (8.5)$$

If the chosen basis  $h_i$  coincides with the influence functions of the deformable mirror, the vectors  $\vec{c}$  and  $\vec{a}$  are the same.

### 8.2.2 Working with DM influence functions

Often, the interaction matrix inversion is coupled with the DM in the sense that for the generation of an interaction matrix one creates a certain (zonal or modal) shape with the DM, which is then sensed by the wavefront sensor. In this approach one is restricted to wavefront shapes which can be represented by the DM, i.e., are a linear combination of the DM influence functions

$$\Phi(x, y) = \sum_{j=1}^{n_a} a_j IF_j(x, y) \quad (8.6)$$

or of DM modes

$$\Phi(x, y) = \sum_{j=1}^{n_c} c_j h_j^m(x, y) \quad (8.7)$$

and

$$h_j^m(x, y) = \sum_{l=1}^{n_a} m_l^j IF_l(x, y)$$

with actuator commands  $(m_l^j)$ . This results in

$$\Phi(x, y) = \sum_{j=1}^{n_c} c_j h_j^m(x, y) = \sum_{j=1}^{n_c} c_j \sum_{l=1}^{n_a} m_l^j IF_l(x, y).$$

Combining (8.1) with (8.6) or (8.7) produces a DM-to-WFS interaction matrix, which relates the sensor measurements  $\vec{s}$  directly with the command vectors,

$$\vec{s} = \mathbf{P}\Phi + \vec{\eta} = \mathbf{P} \left( \sum_{j=1}^{n_c} a_j IF_j \right) + \vec{\eta} = \sum_{j=1}^{n_c} a_j \mathbf{P} (IF_j) + \vec{\eta} =: \mathbf{M}^{IF} \vec{a} + \vec{\eta},$$

or

$$\vec{s} = \mathbf{P}\Phi + \vec{\eta} = \mathbf{P} \left( \sum_{j=1}^{n_c} c_j h_j^m \right) + \vec{\eta} = \sum_{j=1}^{n_c} c_j \mathbf{P} (h_j^m) + \vec{\eta} =: \mathbf{M}^m \vec{c} + \vec{\eta},$$

assuming a linear response of the pyramid sensor. In, e.g., the approaches presented in Chapter 4 - 6 or the P-CuReD, which are more general, the steps of wavefront reconstruction and projection to the DM are decoupled. One is not limited to using only the DM influence functions or modes. The wavefront is reconstructed on an arbitrary grid and afterwards either projected on the telescope specific DM or evaluated at the actuator positions.

### 8.2.3 Deterministic setting

Let us start with considering the inversion of the interaction matrix in a deterministic setting.

#### Least-squares pseudo-inverse

The least-squares problem

$$\vec{c} = \arg \min_{\vec{c}} \|\mathbf{M}\vec{c} - \vec{s}\|_2^2$$

of finding the best wavefront fit  $\vec{c}_{LS}$  to the given WFS data vector  $\vec{s}$  is uniquely solved by the least-squares minimum norm solution given as the Moore-Penrose generalized inverse

$$\mathbf{M}^\dagger = (\mathbf{M}^T \mathbf{M})^{-1} \mathbf{M}^T.$$

Such a *pseudo-inversion of the interaction matrix* is considered to be the simplest reconstruction algorithm possible. Historically, least-squares with zonal representation was the first approach applied to the wavefront reconstruction problem involving the Shack-Hartmann wavefront sensor [81]. For wavefront reconstruction using pyramid wavefront sensor measurements, the least-squares approach allows to reach high correction accuracy without regularization, at least if the number of degrees of freedom is not very high. With the pyramid wavefront sensor, the least-squares reconstructor has provided reasonable results on small scale systems having up to  $30 \times 30$  subapertures within an 8 m telescope diameter as it was demonstrated in [67] with modal DM control using Karhunen-Loève (KL) polynomials.

### Regularized least-squares pseudo-inverse

For large-scale AO systems or more sophisticated configurations like MCAO the corresponding system matrices have large condition numbers and are difficult to invert. In this case the conventional least-squares reconstructor performance is not satisfactory, and a special treatment is required in the form of a regularization or filtering of unstable modes.

Sensor noise is modeled as a random process obeying zero-mean Gaussian statistics,  $\eta \sim \mathcal{N}(0, C_\eta = \sigma^2 I)$ ,  $C_\eta \in \mathbb{R}^{2N \times 2N}$ , where  $\sigma^2$  denotes the sensor noise variance. The *noise-covariance-weighted least-squares* (also known as minimum norm maximum likelihood [14]) reconstructor, which minimizes

$$\vec{c} = \arg \min_{\vec{c}} \|\mathbf{M}\vec{c} - \vec{s}\|_{C_\eta^{-1}}^2,$$

allows one to take the stochastic measurement uncertainties into account. The solution is given by

$$\mathbf{M}_\eta^\dagger = (\mathbf{M}^T C_\eta^{-1} \mathbf{M})^{-1} \mathbf{M}^T C_\eta^{-1}.$$

The pseudo-inverse can be computed using the eigendecomposition of  $\mathbf{M}^T C_\eta^{-1} \mathbf{M}$  or the singular value decomposition of  $C_\eta^{-1/2} \mathbf{M}$ . In practice such decompositions are related with expensive computations and small computation errors in eigen- or singular values lead to instabilities in the reconstruction due to noise amplification. As a regularization method, in the truncated SVD (TSVD) one filters out the modes corresponding to singular values smaller than a given parameter  $\alpha > 0$ .

Alternatively, a similar effect is achieved by **Tikhonov regularization**, well-known in the field of Inverse Problems [218]. For solving the Inverse Problem (8.1) we consider the least-squares problem

$$\vec{c} = \arg \min_{\vec{c}} \left\{ \|\mathbf{M}\vec{c} - \vec{s}\|_2^2 + \alpha \|\vec{c}\|_2^2 \right\}.$$

Then, the regularized pseudo-inverse is derived by

$$\mathbf{M}_\alpha^\dagger = (\mathbf{M}^T \mathbf{M} + \alpha \mathbf{I})^{-1} \mathbf{M}^T \quad (8.8)$$

with a Tikhonov regularization term consisting of a regularization parameter  $\alpha > 0$  and the identity matrix  $\mathbf{I}$ .

For (relatively) small scale systems having up to  $30 \times 30$  subapertures on an 8 m telescope, high correction quality has been achieved with both an SVD-regularized zonal [63] and modal least-squares reconstructor using Zernike polynomials [65] or KL polynomials [68, 69, 158].

Due to noise propagation, the least-squares wavefront reconstruction algorithm performs poorly for large-scale or laser guide star based AO applications [55, 105]. Hence, there has been a tendency observed in the AO community to prefer the regularized variants of interaction-matrix-based MVM methods taking atmospheric statistics into account.

### 8.2.4 Bayesian setting

With  $\sigma^2$  denoting the sensor noise variance, wavefront shapes and sensor noise are independent random processes obeying zero-mean Gaussian statistics,  $\Phi \sim N(0, C_\Phi)$ ,  $\eta \sim N(0, C_\eta = \sigma^2 I)$ ,  $C_\Phi \in \mathbb{R}^{n_c \times n_c}$ ,  $C_\eta \in \mathbb{R}^{2N \times 2N}$  within a stochastic context. Such a point of view allows one to use in the reconstruction the prior knowledge of the atmosphere and measurement noise statistics, expressed with the corresponding covariance matrices  $C_\phi$  and  $C_\eta$ , in order to regularize or stabilize the solution.

Two Bayesian statistical approaches, both using a prior probability density assumed on the phase, have been applied to the problem of wavefront reconstruction from sensor data — *minimum variance estimation* and *maximum a posterior (MAP) estimation*. The minimum variance (or minimum mean-square error (MMSE)) estimator minimizes the variance of the phase estimation error. The maximum a posterior (MAP) estimator identifies the most likely value of  $\Phi$  given the observed data  $\vec{s}$  and prior knowledge on the distribution of  $\Phi$ . As wavefront reconstruction deals with zero-mean Gaussian signal and perturbation, the minimum variance reconstructor providing the minimal MSE coincides with the MAP reconstructor [14, 204].

In the Bayesian setting, the measurement vector  $\vec{s}$  is a function of the atmospheric turbulence profile. The sensor equation (8.1) using the representation of the wavefront (8.2) formulated in terms of arbitrary coefficients  $c_i \in \mathbb{R}$ , in the stochastic setting is formulated in terms of wavefront coefficients  $\phi_i \in \mathbb{R}$  as

$$\vec{s} = \mathbf{P}\Phi + \vec{\eta} = \mathbf{P} \sum_{i=1}^{n_c} \phi_i h_i + \vec{\eta} = \sum_i^{n_c} \phi_i \mathbf{P} h_i + \vec{\eta} = \sum_i^{n_c} \phi_i \vec{s}_i + \vec{\eta} = \mathbf{M}\vec{\Phi} + \vec{\eta}$$

The aim in this setting is to compensate the turbulence-induced wavefront error. The minimum variance / MAP reconstructor minimizes the penalized noise-weighted least-squares functional

$$\vec{\Phi} = \arg \min_{\vec{\Phi}} \left\{ \left\| \mathbf{M}\vec{\Phi} - \vec{s} \right\|_{C_\eta^{-1}}^2 + \mu_0 \left\| \vec{\Phi} \right\|_{C_\Phi^{-1}}^2 \right\}, \quad (8.9)$$

which can be seen as an estimator regularized with a Tikhonov term  $\mu_0 \left\| \vec{\Phi} \right\|_{C_\Phi^{-1}}^2$ . The weighting parameter  $\mu_0$  allows one to balance between fitting to the data and the prior statistics. The corresponding regularized normal equation is

$$(\mathbf{M}^T C_\eta^{-1} \mathbf{M} + \mu_0 C_\Phi^{-1}) \vec{\Phi} = \mathbf{M}^T C_\eta^{-1} \vec{s}$$

and the MAP reconstruction is given by

$$\vec{\Phi} = \mathbf{M}_{MAP}^\dagger \vec{s}$$

with control matrix  $\mathbf{M}_{MAP}^\dagger$

$$\mathbf{M}_{MAP}^\dagger = (\mathbf{M}^T C_\eta^{-1} \mathbf{M} + \mu_0 C_\Phi^{-1})^{-1} \mathbf{M}^T C_\eta^{-1}.$$

Note that besides the pseudo-inverse, there exist several other methods based on the above normal equation for solving the Inverse Problem. The inverse of the phase covariance  $C_{\Phi}^{-1}$  must be chosen such that it is physically realistic. Typically, because of singularities (or ill-conditioning) in the turbulence spectra, it is inevitable to assume some discrete approximation on  $C_{\Phi}^{-1}$  and an additional regularization, which results in some loss of accuracy but yields stability [55].

With the MAP / minimum variance estimators two kinds of errors are related: the approximation error that tells how well the reconstructor approximates the inverse of the sensing operator  $\mathbf{P}$ , and the noise propagation error related to sensor noise. The sources of the model error are the chosen basis representation of the wavefront and the accuracy of the a priori statistical knowledge of the atmosphere.

A statistical estimation method necessarily needs regularization parameter tuning for an accurate wavefront reconstruction. The numerical simulations indicate that the MAP / minimum variance reconstructor with an optimized parameter  $\mu_0$  performs better (is more stable) than the (noise-weighted) least squares solution [37, 142].

In the following, we briefly focus on the implementation details of two variants of Bayesian reconstructors that proved to be efficient in astronomical AO.

### MAP reconstructor with modal control of the DM

The modal MAP wavefront reconstructor, as described in [36, 128, 142], uses a modal control of the DM allowed by the construction of the interaction matrix  $\mathbf{M}^m$  utilizing the first  $n_c$  atmospheric Karhunen-Loève (KL) polynomials  $(K_i^{dm})_{1 \leq i \leq n_c}$  defined on the telescope pupil  $\Omega$ . The number of considered modes  $n_c$  is typically chosen smaller or equal to the number of actuators in the DM. The command vector  $\vec{m}^i \in \mathbb{R}^{n_a}$  is defined such that the DM shape produced by this command is the closest to the  $i$ -th mode  $K_i^{dm}$ . This is done by minimizing [178]

$$\vec{m}^i = \arg \min_{\vec{m}} \left\{ \int_{\Omega} \left( K_i^{dm}(x, y) - \sum_{l=1}^{n_a} m_l IF_l(x, y) \right)^2 d(x, y) : \vec{m} \in \mathbb{R}^{n_a} \right\},$$

where the coordinates  $(x, y)$  describe a point in the pupil plane and  $IF_l$  describes the influence function of the  $l$ -th actuator. Afterwards, a KL polynomial-based interaction matrix  $\mathbf{M}^m$  is constructed by applying to all DM actuators the pre-defined  $\vec{m}^i$  commands.

In this method,  $C_{\Phi}$  in (8.9) is the von Karman wavefront covariance matrix restricted to the modal space of the DM. The parameter  $\mu_0$ , which scales as the inverse of the square of the signal-to-noise ratio, allows to weight the sensor noise and atmospheric priors in a flexible way.

This reconstructor is, e.g., implemented in Octopus [129, 130, 142].

**Zonal minimum variance estimator with regularized sparse approximation of  $C_\Phi$**

Another variant of MVM that provides high-quality reconstruction is the zonal minimum variance estimator using a regularized sparse discrete approximation of  $C_\Phi^{-1}$ , as suggested in [55], by

$$C_\Phi^{-1} = \frac{1}{c_0} \mathbf{L}^2, \tag{8.10}$$

where  $\mathbf{L}$  denotes a discrete Laplacian matrix approximating the Laplacian operator. The constant  $c_0$  is physically interpreted as the strength of the turbulence and additionally normalizes the approximation of  $C_\Phi$  in order to fit the von Karman turbulence spectrum [12, 55].

Using this covariance approximation corresponds to regularization by the  $l_2$ -norm of the Laplacian, i.e., to solving the penalized least-squares functional

$$\arg \min_{\vec{\Phi}} \left\{ \left\| \mathbf{M}\vec{\Phi} - \vec{s} \right\|_{C_\Phi^{-1}}^2 + \frac{\mu_0}{c_0} \left\| \mathbf{L}\vec{\Phi} \right\|_2^2 \right\}$$

with regularization term  $\frac{\mu_0}{c_0} \left\| \mathbf{L}\vec{\Phi} \right\|_2^2$  that removes waffle mode and other high frequency errors in the phase estimates [12].

This reconstructor using DM influence functions as basis functions is incorporated in YAO, an open-source AO simulation tool written in yorick [171]. For the current study we have also implemented it in Octopus. In the numerical implementation, stabilization with respect to the wavefront sensor noise is performed by filtering out the columns in the registered interaction matrix corresponding to basis functions whose WFS response was smaller than a certain predefined value (e.g., expressed in a percentage of the maximum registered response). This parameter can be tuned in order to optimize the performance of the reconstructor for different flux settings or spider thickness. Note that in the numerical simulations, the parameter  $c_0$  is heuristically tuned as well for various atmosphere strengths and guide star fluxes.

**8.2.5 Performance of interaction-matrix-based MVM in presence of spiders**

**Quality**

Earlier it was already shown in the context of EPICS, the XAO instrument on the ELT, that interaction-matrix-based MVM reconstructors for pyramid wavefront sensors are indeed able to solve the pupil fragmentation problem in case of 4 thick spiders [122]. It was reported in the paper that both the zonal and modal reconstructors provide the same quality in the presence of 4 spiders. Apart from that, two important points were underlined: the light behind spiders needs to be used in the reconstruction; and the amount of modulation should not be too large, otherwise the sensor loses its sensitivity to low-order modes.

Now, we report on the performance we obtained with two variants of Bayesian reconstructors described above in the presence of spiders. Recall that we consider the METIS instrument on the ELT here.

The zonal minimum variance reconstructor that we implemented in Octopus gives an LE Strehl ratio of about 0.894 for simulations with the ELT spiders and the real ELT M4 geometry.

In the corresponding Octopus simulation without spiders, the modal MAP reconstructor achieves the same LE Strehl ratio of 0.89. However, in contrary to the zonal approach, its performance in the presence of spiders is not as good. After running multiple tests over a set of tuning (regularization) parameters, the best LE Strehl ratio that we were able to achieve is 0.859. In the residual screens we always observed uncompensated random segmented pistons. Note that in order to obtain the more or less reasonable results, one has to set the illumination parameter close to 0.45 and use data from the subapertures partially covered by the spiders. If one does not use this information, the reconstruction is worse as also investigated in [59].

YAO simulation results obtained for the METIS case with the zonal minimum variance reconstructor are summarized in [102]. To give an idea to the reader, we mention here the YAO results obtained for a median atmosphere, on-axis correction and high photon flux. In this setting the LE Strehl ratio of 0.89 is obtained both without and with spiders. Hence, this reconstructor handles the spiders well.

Please note that the modal MAP result from Octopus and the zonal reconstructor results from YAO were obtained using a regular Fried geometry instead of the real ELT M4 geometry.

## Speed

Interaction matrix inversion is related to a high computational load. Assuming that an interaction-matrix-based MVM algorithm is implemented using conventional matrix inversions and matrix-vector multiplications, the computation of the control matrix scales as  $O(n_a^3)$  and its application as  $O(Nn_a)$  [55]. Clearly, the computational complexity becomes a significant limitation of these approaches if the values of  $n_a$  are of order 10000 as currently under consideration for XAO systems on ELTs.

## 8.3 Advanced model-based reconstructors

In Chapter 4 - 7 we have already given an overview on several novel algorithms that have been developed based on the mathematical analysis of the forward models of the PWFS. The main feature of these algorithms is a low computational complexity resulting in an adequate handling of wavefront reconstruction on AO systems in real-time and still guaranteeing high-quality and robustness of the methods.

Algorithm	Modulation			Complexity
	no	small	large	
interaction-matrix-based MVM	+	+	+	$O(n_a^2)$
FHTR, SVTR	+	-	-	$O(n_a^{3/2})$
iterative methods	+	+	+	$O(n_a^{3/2})$
CLIF	+	+	+	$O(n_a^{3/2})$
PFTR	+	+	+	$O(n_a \log n_a)$
P-CuReD	+	+	+	$O(n_a)$

Table 8.1: Comparison of some currently existing algorithms for wavefront reconstruction from pyramid sensor data in terms of their flexibility and computational complexity.

### 8.3.1 Quality and speed performance of model-based reconstructors without spiders

Table 8.1 provides a comparison of some wavefront reconstruction algorithms for pyramid sensors in terms of their computational complexities. From the Table one can see that all recently developed model-based reconstruction algorithms require much fewer computations to be performed than any MVM approach. Especially remarkable is the P-CuReD method which has a linear complexity. For a detailed comparison of the methods with respect to the reconstruction quality we refer to the corresponding publications and Chapter 4 - 7. As a brief summary, we mention that in closed loop simulations all the model-based methods achieve good quality depending on the atmosphere used in test cases. The fastest method available, the P-CuReD, reaches the highest quality results in a variety of tested conditions. Additionally, the high reconstruction quality obtained with the model-based reconstructors for the non-modulated sensor is notable.

Another point we would like to stress here is that the model-based reconstructors are free from the time-consuming precomputation of matrices and fine tuning of the regularization parameters associated with MVM approaches. Since there are no intrinsic regularization parameters necessary to consider during the reconstruction process, no optimization is needed if atmospheric conditions change. This is a great advantage of the model-based reconstruction algorithms, as confirmed by the AO simulation tools users outside our group. For instance, in [36, 41] the authors performed end-to-end simulations and compared the performances of the modal MAP reconstructor implemented in Octopus with the P-CuReD method for XAO settings. Apart from that, the CuReD method, which was originally developed for the Shack-Hartmann sensor [179, 180] and also constitutes a part of the P-CuReD method for pyramid sensor, has been successfully tested on-sky [15]. In the named cases, the authors underlined the ease of usage of those algorithms compared to other approaches.

### 8.3.2 Adapting advanced reconstructors to segmented pupils

Let us describe our first approaches to overcome the difficulties caused by pupil fragmentation or spider effects when the width of the spiders is no longer negligible compared to the size of the subapertures. Numerical investigations were performed for the ELT having a primary mirror divided into 6 segments as shown in Figure 8.1. As reconstruction method we use the P-CuReD algorithm. Almost as important as the width of the spiders is their placement. If the spiders are parallel to the  $x$ - and  $y$ -axis, some basic attempts described in the following succeed, while for arbitrarily located spiders we examine poor wavefront reconstruction suffering from differential piston influences. Although one can theoretically investigate support structures of secondary mirrors situated parallel to the axes, this assumption will not be fulfilled in reality due to unpreventable misalignment. Please note that the following attempts for wavefront reconstruction in the presence of telescope spiders were only investigated with application of the P-CuReD algorithm. Different reconstruction algorithms may behave differently.

One idea is to make the illumination factor necessary for the usage of subapertures for wavefront reconstruction very low, i.e., utilizing (almost) all available subapertures for reconstruction, also those being less illuminated. This method combined with the reconstruction algorithm P-CuReD does not lead to success since the light suffers from obstruction effects especially at the boundaries of the pupil segments. The wavefront reconstruction is adversely influenced on the whole pupil by differential piston effects. However, an appropriate choice of the illumination factor is crucial as, e.g., investigated in [59].

Another approach to overcome the effects of pupil segmentation is data interpolation or interpolation of the reconstructed phase under the spiders. Instead of using defective measurements under the spiders provided by the pyramid sensor we generate data or reconstructions artificially in these areas. For that purpose we considered bilinear and spline interpolation. Unfortunately, these approaches do not eliminate differential piston effects.

A more sophisticated attempt incorporates the pyramid sensor model in the measurement continuation process by applying iterative measurement extension methods as, e.g., the approach presented in [20] or the idea already introduced in Section 4.3.1 which was originally developed for wavefront reconstruction on annular, non-segmented telescope pupils. The basic concept is to generate artificial but pyramid related data under the spiders by application of the finite Hilbert transform which is a simplification of the Fourier optics based pyramid sensor model. Thus, the provided data correspond better to pyramid measurements as it is the case for a general interpolation procedure described above. However, the simulation results are quite similar to the approach using bilinear or spline interpolation, differential piston effects are developing within time and make the reconstruction poor.

An additional experiment is to replace the obstructed data by zeros, i.e., it is assumed that the wavefront is planar in the areas obstructed under the spiders. Note that zero padding is successfully used for the central obstruction induced by a secondary mirror for some of the reconstructors mentioned in this Thesis, e.g., the SVTR. In contrast to obstruction induced by spiders, a central obstruction does not cause segmented mirrors and hence does not induce differential pistons. Several numerical simulations show that the results of this approach differ significantly for different spider locations. In particular, if one considers 4 paraxial spiders (as those first investigated for Shack-Hartmann sensors in [21]), the zero padding approach gives satisfying reconstruction quality with the pyramid sensor. Considering the 6 ELT spiders, the approach again suffers from differential piston development as shown in Figure 8.2.

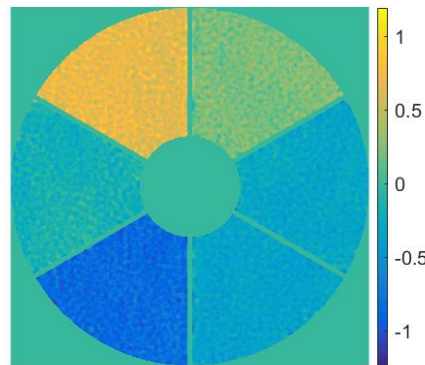


Figure 8.2: Residual screen in radians (evaluated in the K-band) for the “padding with zeros under the spiders” approach, source [110, 149]. Attempts like measurement continuation, interpolation of data or the reconstructed phase as well as reconstruction using the light under the support structures deliver similar poor results.

Approaches like jump minimization between the segments by boundary integral coupling do bring quality improvements but not as high as we have hoped for. For Shack-Hartmann sensors, this method will precisely be described in an upcoming paper of our group. Actuator coupling/slaving of those actuators that are situated at the boundary of spiders is a hot topic for pyramid sensors on ELTs, especially for wavefront sensing at shorter wavelengths than the K-band (cf, e.g., [187, 188, 189]).

Altogether, the above described methods do not satisfactorily handle the impact of 1 or 2 subaperture thick spiders on the wavefront correction performance. However, after trying all the described methods, a new way for successfully eliminating spider obstruction effects was found. The idea is to reconstruct the segmented piston modes separately from other frequencies in the wavefront. Within these attempts, which we recap as Split Approach, one can still use the fast interaction-matrix-free wavefront

reconstruction algorithms presented in Chapter 4 - 7 and at the same time obtain stable wavefront correction in the presence of spiders.

In the next Section, we introduce the basic concept of the Split Approach and two different algorithms tested for direct segment piston reconstruction. Due to the high-end performance of the P-CuReD, both in terms of quality and speed, we choose this method as one of the components in the Split Approach aimed at segment-piston-free reconstruction of the wavefront for segmented pupils.

## 8.4 Split Approach

We introduce robust algorithms that allow to compute optimal mirror configurations from signals containing telescope spider obstruction by dividing the wavefront reconstruction into two parts:

1. Piston-free wavefront reconstruction on each segment: This wavefront reconstruction method handles all modes seen by the PWFS except modes of order zero (piston modes) on each segment.
2. Direct segment piston reconstruction: Here, we focus on modes of order zero on each segment solely.

The reason why we suggest to split piston reconstruction from the full phase reconstruction is twofold. On the one hand, we want to make stable wavefront reconstruction in the presence of spiders feasible with the fast model-based algorithms presented in Chapter 4 - 7. Those algorithms were developed using the forward model of the sensor for annular apertures that do not include segmented pupils and spider effects. Straightforward attempts as described in Section 8.3.2 of applying these algorithms to sensor data “spoiled ” by spider obstruction failed so far. On the other hand, it was recognized that the interaction-matrix-based approaches, as described in Section 8.2, are able to correct for differential pistons, but are very time-consuming. The related computational effort may be affordable for the METIS system, but hardly feasible for XAO systems. Therefore, our goal was to combine the P-CuReD (or any other fast model-based wavefront reconstruction method) and the advantages of interaction-matrix-based reconstruction to obtain a fast and robust reconstruction approach for segmented pupils having less computational complexity than an MVM.

We recall that  $\mathbf{P}$  describes the pyramid sensor operator,  $\Phi$  the incoming phase, and  $\vec{s}$  pyramid sensor measurements. Usually, all wavefront modes (frequencies) that are seen by the pyramid wavefront sensor and afterwards corrected, are treated within the same wavefront reconstruction process. In the Split Approach, we separate the incoming wavefront  $\Phi$  into the parts

$$\Phi = \sum_{i=1}^k \Phi_i + p_i,$$

where  $\Phi_i$  indicates the piston-free wavefront reconstruction on segment  $\Omega_i$ . The corresponding reconstruction procedure denoted by  $\tilde{\mathbf{P}}^\dagger$  is given by any of the existing model-based algorithms which provide high-quality reconstruction on each segment. The term  $p_i$  describes the corresponding piston information on every segment for  $i = 1, 2, \dots, k$  calculated independently using direct segment piston reconstruction methods that will be described in Section 8.4.2 and are in the following denoted by  $\mathbf{\Pi}$ .

Hence, we separate the whole wavefront reconstruction into two parts

$$\Phi = \Phi_{pistonfree} + \Phi_{piston} = \tilde{\mathbf{P}}^\dagger \vec{s} + \mathbf{\Pi} \vec{s},$$

which is feasible in closed loop AO for an almost linear pyramid sensor response [28, 212].

### 8.4.1 Piston-free wavefront reconstruction on segments

Let us first focus on piston-free wavefront reconstruction on segments. For the estimation of the wavefront  $\Phi_{pistonfree}$  we can use any of the existing fast model-based wavefront reconstruction algorithms described in Chapter 4 - 7. These methods have shown exceptional wavefront correction quality on non-segmented pupils, i.e., on the annular telescope aperture in the following denoted by  $\Omega$ . The spiders divide the aperture into segments meaning that for  $k$  spiders we obtain  $k$  disjoint segments indicated by  $\Omega_i, i = 1, 2, \dots, k$  (for instance the 6 spiders of the ELT shown in Figure 8.1). For segmented pupils, the wavefront reconstruction method  $\tilde{\mathbf{P}}^\dagger$  – in addition to standard wavefront reconstruction requirements – fulfills two conditions:

1. The method is implemented on segments  $\Omega_i, i = 1, 2, \dots, k$  instead of the full mask  $\Omega$ .
2. The reconstruction  $\Phi_i$  on every segment  $\Omega_i, i = 1, 2, \dots, k$  needs to be piston-free.

Note that the second condition does not constitute a restriction since one can always compute the local piston information of a full segment from the reconstructed wavefront and subtract it afterwards. Condition 1 may possibly be attenuated to an algorithm being implemented on the full aperture but dividing the reconstruction into segments thereafter. In this case also the elimination of zero order modes on the segments can be performed separately from the reconstruction process. However, we clearly want to point out that we did not investigate this idea in detail. Until now, we only used a piston-free reconstruction method implemented on the segments. An analysis of these considerations will be part of a subsequent study.

For the segment-piston-free wavefront reconstruction we use the P-CuReD [191, 195, 198] applied to each segment. With linear computational complexity, this algorithm is the fastest method available for wavefront reconstruction from pyramid sensor data, and at the same it provides a reconstruction quality close to the theoretical limits.

### 8.4.2 Direct segment piston reconstruction

Now we introduce two methods for direct segment piston reconstruction denoted by  $\mathbf{\Pi}$  providing the piston information  $(p_i)_{i=1,2,\dots,k}$  on the disjoint segments divided by  $k$  spiders. All of them follow the idea of an interaction-matrix-based reconstruction using MVM. In contrast to the conventional approach, we now do not focus on the reconstruction of the complete wavefront, but only on the reconstruction of piston modes on segments. The first method uses a zonal interaction matrix containing the sensor response to every single zonal basis function. The second one is rather modal with a very small number of modes used as basis. Namely, we use a segment basis consisting of  $k$  modes, where each mode depicts a piston on a given segment.

#### Direct Segment Piston Reconstructor (DSPR) I: Single-Poke-Approach

We start with wavefront reconstruction using a full zonal interaction matrix as already described in Section 8.2 and transform this algorithms to the reconstruction of segment pistons solely.

For the so called Single-Poke-Approach, we measure the response of the pyramid sensor for every basis function. More precisely, we use the full interaction matrix  $\mathbf{M}$  of the system as described in (8.3)-(8.4) computed for a set of zonal basis functions. The amplitude corresponding to the mentioned basis functions has to be small to ensure a linear response of the pyramid sensor. The control matrix  $\mathbf{M}_\alpha^\dagger \in \mathbb{R}^{n_c \times 2N}$  is created as in (8.8) using Tikhonov regularization with the exception that we use a better suited Tikhonov matrix instead of the identity matrix. In order to guarantee a stable direct segment piston reconstruction, an optimal choice of the regularization parameter and, as already mentioned, of the Tikhonov matrix was experienced to be crucial. A good choice of the latter turned out to be the squared Laplacian, as described in (8.10). Since we are only interested in the reconstruction of segment pistons and omit the reconstruction of other modes, the dimension of the problem is drastically reduced. Assume we have the complete wavefront  $\vec{\Phi} = \mathbf{M}_\alpha^\dagger \vec{s}$  reconstructed. Extraction of the segment piston information  $\vec{p} = (p_i)_{1 \leq i \leq k}$  from the known wavefront  $\vec{\Phi}$  is obtained by averaging the phase values within each segment. This step is modeled as a multiplication of  $\vec{\Phi} \in \mathbb{R}^{n_c}$  with a matrix  $\mathbf{Q} \in \mathbb{R}^{k \times n_c}$ , where the  $i$ -th row of  $\mathbf{Q}$  contains a vector representation of the segment  $\Omega_i$  divided by the number of active subapertures on the segment  $\Omega_i$  (for the averaging). The application of the matrix  $\mathbf{Q}$  leads to

$$\vec{p} = \mathbf{Q}\vec{\Phi} = \mathbf{Q}\mathbf{M}_\alpha^\dagger \vec{s} =: \mathbf{\Pi}_1 \vec{s} \quad (8.11)$$

with a dense but small matrix  $\mathbf{\Pi}_1 \in \mathbb{R}^{k \times 2N}$ . This means that the piston information on the segments is reconstructed from the given sensor data with a linear computational complexity. Hence, we reduce the computationally expensive full interaction matrix approach with complexity  $O(Nn_a)$  to a cheap direct segment piston reconstruction method. For a usage of the P-CuReD within the Split Approach the partition of

wavefront reconstruction into separate piston and higher-order frequencies reconstruction only slightly decreases the speed of the reconstruction method, which is still faster as the full interaction matrix approach. Of course, the interaction matrix of the system still needs to be set up for the application of this direct segment piston reconstruction method but these calculations are done offline.

Intermediate reconstructions of an Octopus simulation using the Split Approach with the P-CuReD and the first Direct Segment Piston Reconstructor for wavefront reconstruction are shown in Figure 8.3.

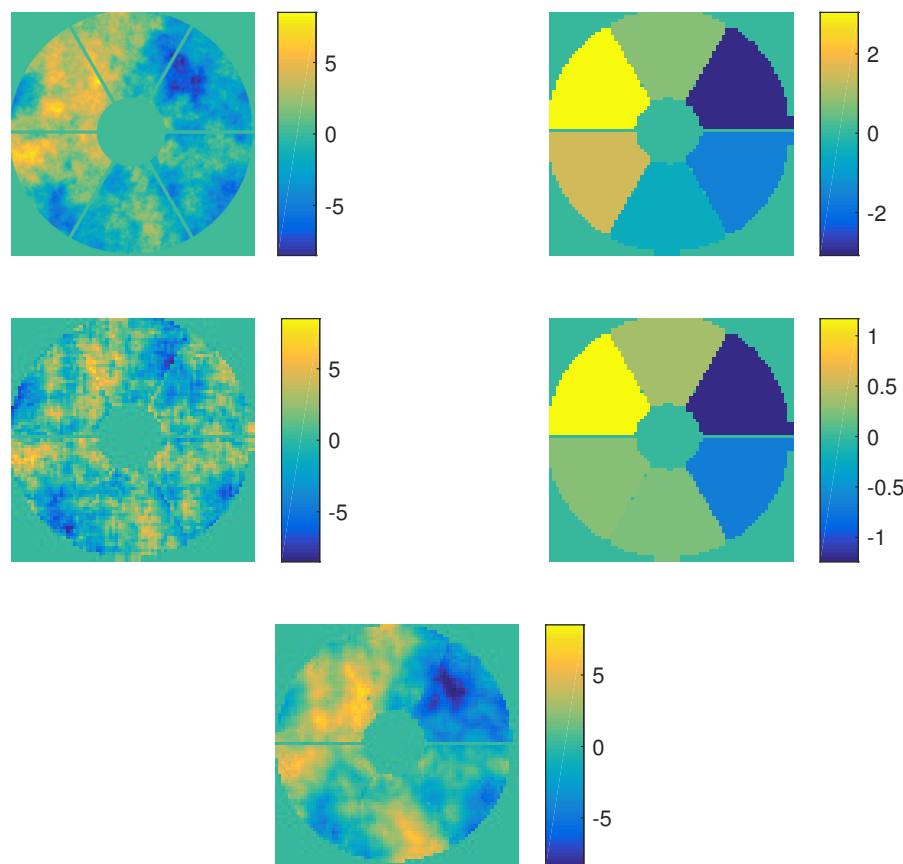


Figure 8.3: Illustration of wavefront reconstruction with the Split Approach at the third time step in an AO loop performed in Octopus, source [110, 149]. The first line shows an incoming screen given in radians (K-band) and the corresponding pistons on the 6 segments. The second line shows the segment-piston-free wavefront reconstruction using the P-CuReD on segments and the DSPR I. In the last line we see the combination of both, i.e., the whole wavefront reconstruction. The algorithm gives reasonable reconstructions of the piston-free wavefront as well as the segment pistons. The simulation parameter correspond to the ones specified in Section 8.5.1.

**Direct Segment Piston Reconstructor (DSPR) II: Segment-Poke-Approach**

Inspired by the simple relation (8.11) connecting segment piston values  $\vec{p}$  with the sensor data  $\vec{s}$  through a small-size matrix  $\mathbf{\Pi}_1$ , we want to formulate another direct segment piston reconstruction approach which will allow us to skip the computationally expensive and time-consuming step of setting up the full interaction matrix of the system. Rewriting (8.11) as

$$\vec{s} = \mathbf{\Pi}_1^\dagger \vec{p}$$

we see that, formally, it is possible to define a new, small interaction matrix of the system in the basis consisting of only a few segment pistons  $p_i, i = 1, \dots, k$ .

We again consider arbitrary located secondary mirror support structures consisting of  $k$  spiders, i.e., dividing the aperture into  $k$  disjoint segments  $\Omega_i, i = 1, 2, \dots, k$ . The effects of a piston offset with amplitude  $c$  on a single segment are described by

$$\vec{s}_i = \mathbf{P}(c \cdot \mathcal{X}_{\Omega_i}(x, y)) \quad \text{for } i = 1, 2, \dots, k$$

with

$$\mathcal{X}_{\Omega_i}(x, y) := \begin{cases} 1, & \text{for } (x, y) \in \Omega_i, \\ 0, & \text{else} \end{cases}$$

denoting the characteristic functions of the telescope aperture segments  $\Omega_i$ . Again we assume that the pyramid sensor fulfills the linearity assumption if  $c$  is chosen small enough.

Using the data vectors  $\vec{s}_i \in \mathbb{R}^{2N}$ ,  $\vec{s}_i = \begin{pmatrix} \vec{s}_x^i \\ \vec{s}_y^i \end{pmatrix}$  for every segment  $\Omega_i, i = 1, 2, \dots, k$  we obtain a piston interaction matrix  $\mathbf{M}^P \in \mathbb{R}^{2N \times k}$  consisting of

$$\mathbf{M}^P = \begin{pmatrix} \vec{s}_1 & \vec{s}_2 & \dots & \vec{s}_k \end{pmatrix}.$$

The pyramid response to a segment poke is shown in Figure 8.4. While in the previous method a very time-consuming precomputation of the full interaction matrix is required, the matrix necessary for this approach only has dimension  $2N \times k$ , and hence its computation is much cheaper. Therefore, setting up the matrix containing the WFS response to segment piston modes can be recomputed fast for changing seeing conditions and readily performed online.

Now, the piston reconstruction on every segment is described as minimization of

$$\min_{\vec{p}} \|\mathbf{M}^P \vec{p} - \vec{s}\|_2^2 + \alpha \|\mathbf{\Gamma} \vec{p}\|_2^2$$

for a suitable chosen Tikhonov matrix  $\mathbf{\Gamma}$  and regularization parameter  $\alpha > 0$ . Solving the equation in a least squares sense leads to the normal equation

$$\mathbf{M}^{P^T} \mathbf{M}^P \vec{p} + \alpha \mathbf{\Gamma}^T \mathbf{\Gamma} \vec{p} = \mathbf{M}^{P^T} \vec{s},$$

where the right hand side represents a projection of the measurements containing all modes seen by the pyramid sensor  $\vec{s}$  to data  $\mathbf{M}^{p^T} \vec{s}$  including piston information only. Using Tikhonov regularization we obtain the piston control matrix  $\mathbf{\Pi}_2 \in \mathbb{R}^{k \times 2N}$  for the direct piston reconstruction on segments. The segment piston  $\vec{p} \in \mathbb{R}^k$  are then obtained by

$$\vec{p} = \mathbf{\Pi}_2 \vec{s}.$$

### 8.4.3 Fast and robust wavefront reconstruction under pupil segmentation using the Split Approach

The general scheme of the Split Approach for wavefront reconstruction using one of the above introduced direct segment piston reconstruction methods is described by the following algorithm:

---

**Algorithm 8.1** Split Approach

---

choose segment-piston-free wavefront reconstruction method  $\tilde{\mathbf{P}}^\dagger$   
 choose direct segment piston reconstruction method  $\mathbf{\Pi}$   
**for** all time steps **do**  
     get measurements  $\vec{s}$   
     **for** segments  $i = 1, 2, \dots, k$  **do**  
          $\vec{\Phi}_i = \tilde{\mathbf{P}}^\dagger(\vec{s})$   
         subtract global piston for every  $\vec{\Phi}_i$  if necessary  
     **endfor**  
      $\vec{p} = \mathbf{\Pi} \vec{s}$   
      $\vec{\Phi} = \sum_{i=1}^k \vec{\Phi}_i + \vec{p}$   
**endfor**

---

The segment piston control matrices  $\mathbf{\Pi}_i, i = 1, 2$  are dense but only of dimension  $k \times 2N$  which leads to an optimization of the proposed approaches with respect to computational complexity. The expensive steps can be precomputed offline, thus, the algorithms scale linearly. This is a clear advantage to the computationally expensive wavefront reconstruction using full interaction-matrix-based MVM approaches as indicated in Figure 8.5. For a moderately large-scale SCAO system such as METIS, the gain in the computational efficiency provided by the Split Approach is of order  $10^4$ . For an extremely large-scale SCAO system as the planned XAO system the corresponding gain is of order  $10^5$ .

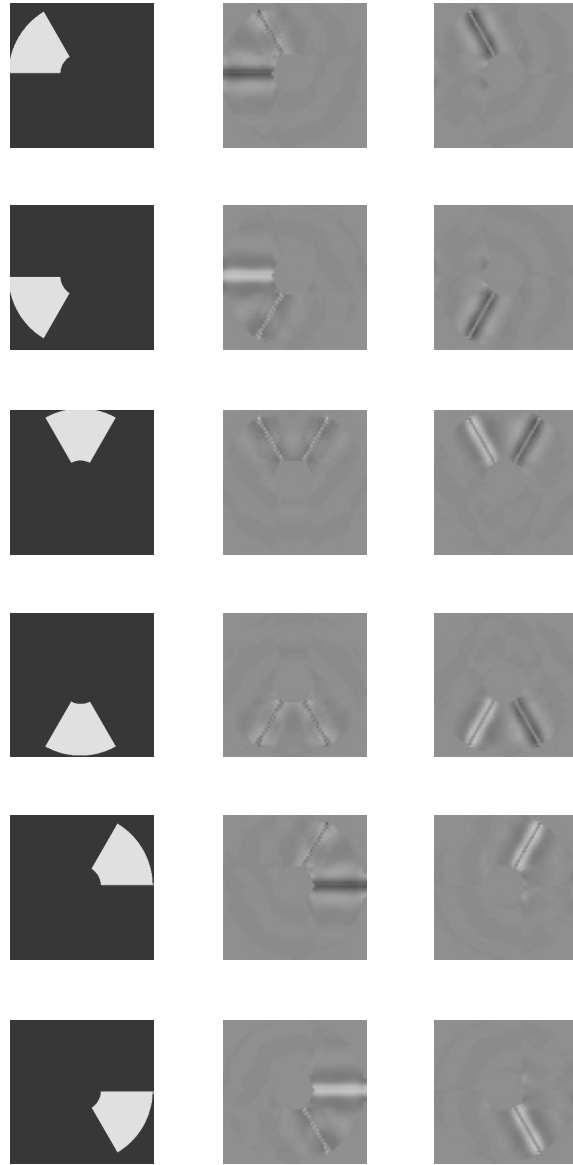


Figure 8.4: Measurements of piston modes, source [110, 149]. Pyramid sensor measurements for a single segment piston mode of height  $5 \cdot 10^{-8}$  m are indicated. The first column shows the segment piston, the second and third column illustrate the corresponding sensor measurements in  $x$ - and  $y$ -direction. The measurements are shown in the range  $[-1.5 \cdot 10^{-8}, 1.5 \cdot 10^{-8}]$  m.

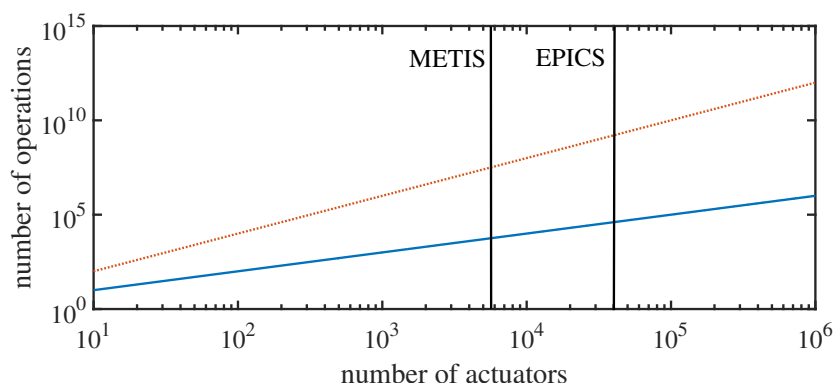


Figure 8.5: Logarithmic plot of the approximate complexities of MVM methods using the full control matrix (dotted line) and of the Split Approach using any of the described methods for direct segment piston reconstruction applying the small-size control matrices (solid line), source [110, 149].

## 8.5 Numerical validation

For a numerical analysis of the introduced methods, we use the simulation tool Octopus [129, 130] provided by the European Southern Observatory.

### 8.5.1 Simulation environment and parameters

As in Chapter 7 we study the mid-infrared ELT imager and spectrograph METIS having a Single Conjugate Adaptive Optics system incorporated. As sensing device, we simulate a pyramid wavefront sensor having  $74 \times 74$  subapertures corresponding to a subaperture size of 0.5 m. The simulation grid size is selected as  $740 \times 740$  pixels on the aperture resulting in a resolution of 0.05 m per pixel for a 37 m telescope. Only if a subaperture is illuminated on more than 45 % of the subaperture surface, the corresponding measurements are used. This means that for the direct segment piston reconstruction methods sensor data under the two paraxial telescope spiders are entirely used while the measurements under the four remaining spiders are only partially utilized. For the piston-free wavefront reconstruction on segments performed by the P-CuReD we only use data on subapertures which are illuminated more than 75 %. We will provide more details on the illumination factor, which is decisive for the success of the Split Approach, in the next Section. We consider two different photon fluxes of 600 and 100 incident photons per subaperture per frame. A key element of every AO system is the deformable mirror. It provides fast steering capabilities to compensate for wavefront aberrations caused by atmospheric turbulence and telescope perturbations in real-time and hence allows to optimize the telescope performance. The actuator positions of the M4 deformable mirror used in the performed simulations correspond to the real ELT M4 geometry currently implemented in Octopus and have already been shown in Figure 2.11. We use the M4 influence functions internally

incorporated in Octopus. Altogether, we have 3874 active subapertures and 5190 active actuators in use. All test case parameters are summarized in Table 8.2.

### 8.5.2 Numerical results

A numerical performance analysis and a comparison of the approaches in terms of the reconstruction quality for the above described simulation environment are provided in Table 8.3 - 8.5 and Figure 8.6. The three tables present the long-exposure Strehl ratios evaluated at three different wavelengths  $\lambda = 2.2 \mu\text{m}$ ,  $\lambda = 3.7 \mu\text{m}$ , and  $\lambda = 10.0 \mu\text{m}$  correspondingly. In each of the three tables the test cases cover two photon fluxes of 600 and 100 photons/subaperture/frame and three zenith angles of  $0^\circ$ ,  $30^\circ$ , and  $60^\circ$ . Each Table demonstrates the results obtained with the P-CuReD for a spider-free simulation as benchmark and the spider effected results obtained within the Split Approach using each of the DSPR.

From the Tables we see that, compared to the case without spiders, some small loss in quality is present when pupil segmentation due to spiders is taken into account and solved with the Split Approach. Moreover, one can see that the loss increases slowly for larger zenith angles and that the DSPR I provides slightly higher Strehl ratios compared to the DSPR II. Figure 8.6 showing the corresponding short-exposure Strehl ratios over the simulation time demonstrates that the DSPR I is indeed more stable compared to the DSPR II. More precisely, the performance of the two methods is not identical because phase averaging over the segments and matrix inversion are interchanged in the DSPR II compared to the DSPR I. As confirmed in Figure 8.7 showing the residual pistons on each segment for the DSPR I, the reconstructions obtained with the Split Approach are free from large differential piston effects.

Based on the provided reconstruction quality and stability features, the conclusion is that the DSPR I method is preferable. However, one should keep in mind that in case the atmospheric or observational conditions change, registration and inversion of a new interaction matrix will be required. This process is very time-consuming and may lead to a loss of precious operational time on the telescope. On the contrary, in the DSPR II method, the underlying interaction matrix is much smaller. Therefore significantly less operations are needed for its registration and inversion. Since the DSPR II method provides acceptable reconstruction quality as well, it can be used at least as a substitute of the DSPR I method when the latter requires some updates to be performed.

Table 8.4 - 8.5 contain the ESO goals and ESO requirements. Note that both are defined as performance evaluations over at least 15 minutes of telescope operations under nominal conditions. These include wind induced vibrations which we have not yet taken into account in our simulations. Therefore, we cannot straightforwardly compare our results, that evaluate only 2 seconds of operation, with the ESO goals and requirements, but we can still see that there is a big safety gap allowed for vibrations reducing the quality.

<b>Simulation parameters</b>	
telescope diameter	37 m
central obstruction	30%
pupil mask	ELT pupil with 50 cm wide spiders
pupil segments	6
science target	on-axis (SCAO)
WFS	PWFS
sensing band	K (2.2 $\mu\text{m}$ )
evaluation bands	K (2.2 $\mu\text{m}$ ) L (3.7 $\mu\text{m}$ ) N (10.0 $\mu\text{m}$ )
modulation	4 $\lambda/D$
controller	integrator
atmospheric model	von Karman
number of simulated layers	35
outer scale $L_0$	25 m
atmosphere	median
Fried radius $r_0$ at $\lambda = 500$ nm	0.157 m
coherence time $\tau_0$ at $\lambda = 500$ nm	5.35 ms
number of subapertures	74 $\times$ 74
minimum subaperture illumination	45%
number of active subapertures	3874 out of 5476
linear size of simulation grid	740 pixels
DM geometry	ELT M4 model
DM delay	1
number of active actuators	5190
detector read-out noise	1 electron/pixel
background flux	0.431 photons/pixel/frame, or 4.19 ADU/m <sup>2</sup> /ms/arcsec <sup>2</sup>
frame rate	500 Hz
photon flux or guide star brightness	[100, 600] photons/subaperture/frame or [10, 8] mag
zenith angle	[0°, 30°, 60°]
simulation time	2 s (1000 iterations)

Table 8.2: Simulation parameters used in the tests on the segmented ELT pupil.

Moreover, in each of the Tables we show the roughly estimated theoretical limit of the achievable long-exposure Strehl ratio. These rough estimates are obtained using the assumption that in high flux the reachable quality is limited from above by the two main error sources, the fitting and the temporal delay error. Following the approach of [142], we evaluate the fitting error by

$$\sigma_{fitting}^2 = 0.287(d_a/r_0)^{5/3},$$

where  $d_a$  denotes the average actuator's distance and  $r_0$  the Fried radius, and the delay error by

$$\sigma_{delay}^2 = 0.962(\tau/\tau_0)^{5/3},$$

where  $\tau$  is the delay, and  $\tau_0$  the coherence time of the atmospheric turbulence.

Furthermore, we want to remark that the results presented in the Tables were obtained with the same loop gains for different guide star magnitudes and zenith angles which clearly underlines the stability of the algorithms. The quality results of several numerical simulations can even be slightly improved by applying a loop gain being optimized with respect to the special parameter choices of the individual test cases. Except the DSPR II was rather sensitive to the choice of the loop gain for a zenith angle of  $60^\circ$ .

photon flux	zenith angle	no spiders	DSPR I	DSPR II	theoretical limit
600	$0^\circ$	0.8851	0.8775	0.8654	0.8882
	$30^\circ$	0.8690	0.8597	0.8462	
	$60^\circ$	0.7799	0.7660	0.7412	
100	$0^\circ$	0.8741	0.8650	0.8523	
	$30^\circ$	0.8578	0.8473	0.8327	
	$60^\circ$	0.7712	0.7551	0.7307	

Table 8.3: Long-exposure Strehl ratios in the K-band ( $2.2 \mu\text{m}$ ) after 1000 closed loop simulation steps. As reconstruction method, we use the P-CuReD. We compare the results for a benchmark simulation without spiders using the P-CuReD only and employing the Split Approach combined with the proposed Direct Segment Piston Reconstructors in the presence of telescope spiders.

## 8.6 Details on the realization

We will focus on a few numerical implementation details of the Split Approach, namely the incorporated pyramid sensor model, illumination factor, loop gain, and phase ambiguity.

flux	zenith angle	no spiders	DSPR I	DSPR II	ESO goal	ESO requirement	theoretical limit
600	0°	0.9577	0.9547	0.9500			0.9605
	30°	0.9515	0.9478	0.9425			
	60°	0.9157	0.9095	0.8990		0.57	
100	0°	0.9535	0.9499	0.9449			
	30°	0.9472	0.9429	0.9371	0.80	0.60	
	60°	0.9121	0.9052	0.8944			

Table 8.4: LE Strehl ratios in the L-band ( $3.7 \mu\text{m}$ ) after 1000 closed loop simulation steps using the P-CuReD in all simulations.

flux	zenith angle	no spiders	DSPR I	DSPR II	ESO goal	ESO requirement	theoretical limit
600	0°	0.9941	0.9937	0.9930			0.9946
	30°	0.9932	0.9927	0.9919			
	60°	0.9880	0.9871	0.9855		0.60	
100	0°	0.9935	0.9930	0.9923			
	30°	0.9926	0.9920	0.9911	0.95	0.93	
	60°	0.9875	0.9864	0.9848			

Table 8.5: LE Strehl ratios in the N-band ( $10 \mu\text{m}$ ) after 1000 closed loop simulation steps using the P-CuReD in all simulations.

For the proposed direct segment piston reconstruction methods the non-linear pyramid wavefront sensor model including interference effects can be taken into account for the calculation of the piston control matrices  $\Pi_i$ ,  $i = 1, 2$  (cf Section 3.2.2).

Numerical simulations show that wavefront estimation under pupil fragmentation is extremely sensitive to the illumination factor determining which subapertures are active, and further used for wavefront reconstruction. As already discussed, we perform the segment-piston-free reconstruction on disjoint segments, hence we only use subapertures which are illuminated at least 75%. In contrast, for the Direct Segment Piston Reconstructor usage of measurements on less illuminated subapertures is crucial. When using an illumination factor of 75% we are not able to eliminate the differential pistons in the reconstructed phases. If we utilize partially illuminated subapertures corresponding to an illumination factor of 45%, the direct segment piston reconstruction methods correct the piston offsets. Please note that once we obtained reasonable results using an illumination factor of 45%, we did not further tune the parameter extensively.

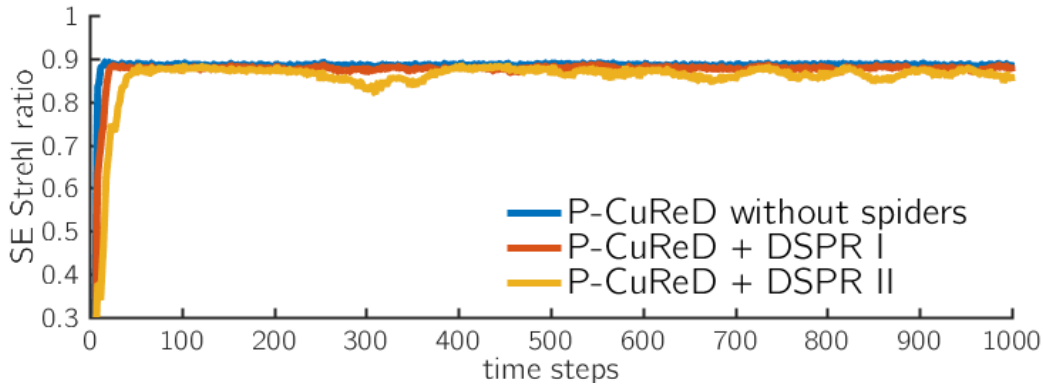


Figure 8.6: Robustness of the DSPR I and the instabilities of the DSPR II method illustrated by the corresponding short-exposure Strehl ratios in the K-band for 1000 time steps of test case 1 (600 photons/subaperture/frame and zenith angle  $0^\circ$ ), source [110, 149].

The loop gains for the two parts of the Split Approach have to be considered separately. We identify an optimal loop gain for the segment-piston-free wavefront reconstruction using the P-CuReD and another one for the direct segment piston reconstruction, which is, generally, about half of the P-CuReD loop gain. Concerning the sensitivity with respect to varying loop gains, the two DSPR approaches behave somewhat differently. While the DSPR I method displays stronger resistance to varying loop gains, the performance of the DSPR II method is more sensitive to changes of the loop gain, especially for zenith angles of  $60^\circ$ . Compared to smaller zenith angles, a slightly larger loop gain was found to be optimal for large zenith angles, i.e., it is necessary to give more weight on the correction of low-order modes for larger zenith angles.

There are different possibilities to efficiently close the AO loop. At the beginning of a closed loop simulation, it is crucial to avoid phase ambiguity caused by the sinusoidal part of the pyramid data, meaning that piston offsets of size  $2\pi$  radians in the phase cannot be distinguished by the pyramid sensor but heavily influence the image quality [156]. Due to the non-linearity of the PWFS (“optical gain”) and the need to correct low frequencies fast, we use a higher integrator control loop gain for the DSPR in the first iterations. This results in a stronger emphasis on the correction of low-order modes and provides an adequate control of piston offsets for data corresponding to larger phases.

The last step of the algorithm contains the projection of the reconstructed wavefront on the DM. One can therefore either solve equation (8.5) or evaluate  $\Phi$  at the actuator positions. We did choose the second approach. To be able to control also actuators outside the reconstruction area we smoothly extend the reconstruction  $\Phi$  to a larger domain covering all used DM actuator positions.

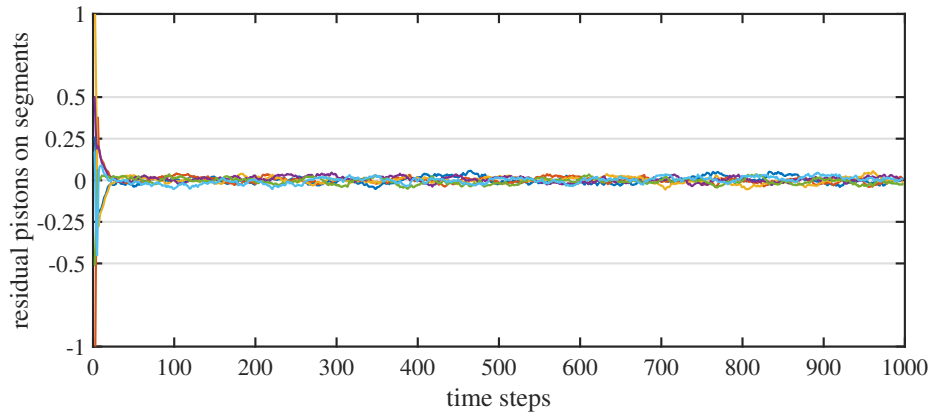


Figure 8.7: Residual pistons in radians (K-band) on the disjoint segments for the Split Approach using the DSPR I, source [110, 149]. The photon flux corresponds to 100 photons/subaperture/frame using a zenith angle of  $30^\circ$ . There is almost no residual piston development. Additionally, the reconstructions do not suffer from the phase ambiguity of the pyramid sensor since the piston offsets between the segments are very much smaller than  $2\pi$  radians. The global piston is subtracted from each of the segment pistons for better visibility.

## 8.7 Summary on wavefront reconstruction in the presence of spiders

The first part of the Chapter contained a brief overview on the ability of existing algorithms to reconstruct wavefronts from pyramid wavefront sensor data in the presence of support structures for the secondary mirror, the so called spiders. It is known that a partial or complete shading of subapertures, depending on the thickness of the spiders, leads to difficulties in controlling piston modes on disjoint pupil segments. We have shown that on the one hand, at least some variants of the interaction-matrix-based MVM approaches are able to handle spider obstruction effects successfully, though they are known to be computationally demanding. On the other hand, there exist several fast interaction-matrix-free model-based algorithms, which provide high-quality reconstruction in case of annular apertures without spiders. Unfortunately, they run into problems when dealing with sensor data (partially) shaded by spiders. In end-to-end simulations we observe in this case random uncontrolled segment pistons in the residuals. For the high-contrast large-scale AO systems in design, a combination of the advantages of both reconstructor types, i.e., the ability to reconstruct wavefronts with high precision and speed in the presence of spiders, is highly desirable.

In the second part of the Chapter we presented a solution, the so called Split Approach, which combines the advantages of the interaction-matrix-based and -free methods and provides a high-quality wavefront reconstruction in the presence of spiders with little computational demand. The solution is based on the idea to split the reconstruction of pistons on the pupil segments from the reconstruction of higher-order modes. For

the latter part, one can use any of the available fast model-based algorithms reviewed in Chapter 4 - 7. Especially beneficial here is the P-CuReD which has the smallest computational load and also provides the best reconstruction quality when no support structures shade the pupil.

For segment piston reconstruction we presented two approaches. One of them requires the registration and inversion of a full interaction matrix. However, the control matrix is afterwards projected to the space of segment pistons only, hence reduced in size. Another one uses a small size interaction matrix instead which is registered in the basis of segment pistons. The resulting control matrices are in both methods of small size and the direct segment piston reconstruction step has a linear complexity. Combined with the P-CuReD used for reconstruction of higher-order modes, the number of computations required for the complete wavefront reconstruction scales linearly with the number of controlled actuators. This represents a big advantage of the Split Approach compared to the usual interaction-matrix-based MVM, whose complexity scales quadratically with the number of actuators. While MVM approaches may still be computationally doable for relatively large-scale systems like METIS having a  $74 \times 74$  pyramid sensor in 2026, they are hardly feasible for extremely large systems like XAO having  $200 \times 200$  subapertures and a corresponding number of actuators to be controlled in real-time. The presented Split Approach causes, in contrast, no difficulties for the real-time implementation even on the largest AO systems of ELT-sized telescopes.

Moreover, the Split Approach makes existing model-based phase reconstruction algorithms developed for non-segmented pupils suitable for wavefront control in the presence of telescope spiders. Alternatively, another idea to overcome the effects of pupil fragmentation with the model-based algorithms consists in an appropriate adjustment of the underlying forward models. A corresponding extension of the algorithms will be necessary and may allow for a stable control of segmented piston offsets without using interaction-matrix-based attempts. The question whether such an extension is possible and for which methods it is applicable needs further investigations.

The analysis of the Split Approach was done in the context of the instrument METIS for sensing in the K-band. Further investigations on Direct Segment Piston Reconstructors using pyramid sensors in different sensing wavelengths are of high interest for several instruments in development for ELTs and planned future work. Although the theory of the Split Approach is nonspecific to the instrument and therefore applicable to any AO system, the wavefront reconstruction may possibly suffer from phase ambiguity or other wavelength dependent effects of the pyramid sensor.

Once again we would like to stress out that our aim in the current study was to push the fastest available reconstruction method for PWFS, the P-CuReD, towards high-quality performance for fragmented ELT pupils. The numerical results indeed point out that the goal was reached with the Split Approach at least for sensing in the K-band.

## Chapter 9

# Conclusions and Outlook

In this Thesis, we have presented and analyzed a well-defined mathematical model of the pyramid wavefront sensor, several linear and non-linear wavefront reconstruction algorithms for pyramid sensors and an approach for accurate wavefront reconstruction on segmented pupils of ELTs.

First, we considered the mathematical background of pyramid wavefront sensors, which are widely used in Adaptive Optics systems for astronomy, microscopy, or ophthalmology. We derived the mathematical model of the non- and modulated pyramid sensor, of the physically simpler roof wavefront sensors as well as their various approximations in a distributional sense. The interference effects and the phase shift introduced by the pyramidal prism were considered in the derivation of the forward models but partially neglected in the development of wavefront reconstruction algorithms. In our analysis, we allowed the sensors to be utilized in both the modulated and non-modulated fashion. Due to the closed loop operation assumption, we could linearize the initially non-linear forward operators. We further calculated Fourier transforms, singular value decompositions, Fréchet derivatives, or adjoint operators which build the foundation for the application of several mathematical approaches from the field of Inverse Problems.

The theoretical analysis of the operators representing pyramid sensor forward models was aimed at a subsequent development of fast and stable algorithms for wavefront reconstruction. Several Chapters of the Thesis were devoted to the application of mathematical methods to the problem of wavefront reconstruction from pyramid wavefront sensor data. Among those, we introduced the following reconstructors:

- the Hilbert transform method:
  - Singular Value Type Reconstructor,
- linear iterative methods:
  - Conjugate Gradient for the Normal Eq. (CGNE) for pyramid sensors,

- Steepest Descent (SD) for pyramid sensors,
- Steepest Descent-Kaczmarz (SD-K) for pyramid sensors,
- linear Landweber Iteration for Pyramid Sensors (LIPS),
- linear Kaczmarz-Landweber Iteration for Pyramid Sensors (KLIPS),
- non-linear iterative methods:
  - non-linear Landweber Iteration for Pyramid Sensors (LIPS),
  - non-linear Kaczmarz-Landweber Iteration for Pyramid Sensors (KLIPS).

Additionally, we have given an extensive overview on existing wavefront reconstruction algorithms for the pyramid sensor. We presented interaction-matrix-based approaches, Fourier domain methods, iterative algorithms, and methods based on the inversion of the Hilbert transform. The main emphasis was put onto the various underlying models of the reconstruction algorithms. We distinguished between phase mask and transmission mask pyramid sensor models, between full pyramid sensor models or roof sensor simplifications, as well as linear approximations. The theoretical investigations were completed with detailed comparisons of computational complexities of all reviewed methods and numerical results for selected algorithms.

From the performed numerical end-to-end simulations we can draw the conclusion that it strongly depends on physical parameters of the telescope and wavefront sensor (sub-aperture size, modulation amplitude, sensing wavelength, non common path aberrations, etc.) and on atmospheric parameters which reconstruction method is preferable. However, all algorithms that were introduced in this Thesis deliver satisfying reconstruction quality. Moreover, the proposed algorithms, which are partially iterative methods, allow to keep the numerical effort of the wavefront reconstruction step in an AO loop low compared to the computational load of solvers based on matrix-vector multiplication which has an especially big impact for XAO systems having a huge number of active actuators to be controlled. All of them meet the requested demands with respect to computational complexity. The increased amount of currently available approaches for wavefront reconstruction from pyramid sensor data allows users of AO systems on any ground-based telescope facility to choose from several high-quality and high-speed algorithms which method best complies with their requirements.

Finally, we investigated the ability of existing algorithms to reconstruct wavefronts from pyramid wavefront sensor data in the presence of wide support structures for secondary mirrors. Depending on the thickness of the spiders, pupil fragmentation leads to difficulties in controlling piston modes on disjoint pupil segments. We have experienced that at least some variants of the interaction-matrix-based MVM approaches are able to handle spider obstruction effects successfully, though they are known to be computationally demanding. In order to overcome randomly appearing differential piston effects when using fast model-based reconstructors, we developed the so called Split Approach, which combines the advantages of the interaction-matrix-based and

matrix-free methods. The algorithm is based on the idea to split the reconstruction of pistons on the pupil segments from the reconstruction of higher-order modes. For the separated direct segment piston reconstruction, we presented two new approaches. For the reconstruction of the remaining modes, already existing reconstructors can be used. The main focus in this study was to push the fastest available reconstruction method for pyramid sensors, the P-CuReD, towards high-quality performance on segmented ELT pupils. The numerical results indeed pointed out that the goal was reached with the Split Approach at least for sensing in the K-band.

There exist several ideas for further developments of the presented algorithms:

- The implementations of all new methods presented in this Thesis and moreover of all other model-based reconstructors developed by the AAO team are based on the roof wavefront sensor approximation. Even when using this simplification of the pyramid sensor model, all proposed algorithms provide high-quality reconstruction comparable to approaches currently used on existing AO systems. Nevertheless, we suggest mathematical investigations of the full transmission and phase mask pyramid sensor model for future developments of reconstruction algorithms in order to improve the wavefront estimates even more.
- The idea of non-linear reconstruction algorithms for the pyramid sensor is still in development and we would like to continue our work on improving the quality performance of the non-linear algorithms accompanied by a detailed analysis of non-linearity effects of the pyramid sensor.
- The assumption of small residual wavefronts being measured by the wavefront sensor and, on account of this, the linearity of the pyramid sensor may be violated by, e.g., non common path errors of the system. Thus, the ability of existing linear and non-linear reconstruction strategies to deliver accurate wavefront corrections even under the impact of large NCPAs is of great interest. We plan to come back to this topic including a detailed investigation of the reconstruction performance of the proposed algorithms in the presence of realistic NCPAs. Generally, the influence of the magnitude of the incoming phase distortions on the reconstruction quality needs to be analyzed for both linear and non-linear reconstruction methods.
- The Split Approach makes existing model-based wavefront reconstruction algorithms developed for non-segmented pupils suitable for wavefront estimation in the presence of telescope spiders. An alternative idea to overcome the effects of pupil fragmentation with the model-based algorithms consists in an appropriate adjustment of the underlying forward models. A corresponding extension of the algorithms will be necessary and may allow for a stable control of segmented piston offsets without using interaction-matrix-based attempts. The question whether such an extension is possible and for which methods it is applicable needs further considerations.

- The analysis of the Split Approach was done in the context of the instrument METIS for sensing in the K-band. Further investigations on Direct Segment Piston Reconstructors using pyramid sensors in different sensing wavelengths are of high interest for several instruments in development for ELTs and planned future work. Although the theory of the Split Approach is nonspecific to the instrument and applicable to any AO system, the wavefront reconstruction may possibly suffer from phase ambiguity or other sensing wavelength dependent effects of the pyramid sensor.
- We would further like to continue our work on investigating the behavior of the new reconstruction algorithms in the presence of telescope spiders when using the Split Approach. So far, mainly the P-CuReD was utilized in combination with a Direct Segment Piston Reconstructor.
- For a more specified establishment of the presented algorithms, tests on optical benches and on-sky verifications are needed in order to imitate (more) realistic settings.

Until now, we have only investigated the pyramid sensor operating in a Single Conjugate AO system of a telescope. Extensions to different operating modes such as Multi Conjugate AO or applications in microscopy and ophthalmology are possible and dedicated to future work.

In conclusion, we believe that the presented reconstructors are promising tools for wavefront reconstruction on ground based telescope systems using pyramid wavefront sensors. The methods, in principle, can be applied on any telescope system without enhanced adaptations or heavy precomputations because they were developed independently from technical structures such as pupil or mirror sizes, mirror actuator positions or parameters as, e.g., the sensing wavelength of the sensor. Operators of the presented reconstruction algorithms benefit from the ease of usage since very few to no parameters have to be tuned in the approaches.

# Appendix A

## Mathematical preliminaries

### Lebesgue space

Let  $(X, \mathcal{A}, \mu)$  be a measure space,  $\mathbb{K} \in \{\mathbb{R}, \mathbb{C}\}$ , and  $1 \leq p < \infty$ . We consider the Lebesgue spaces with respect to  $\mu$  defined as

$$\mathcal{L}_p(X) := \left\{ f : X \rightarrow \mathbb{K}, f \text{ is measurable, } \int_X |f|^p d\mu < \infty \right\}$$

and

$$\mathcal{L}_\infty(X) := \{f : X \rightarrow \mathbb{K}, f \text{ is measurable, } |f| < \infty \mu - \text{almost everywhere on } X\}.$$

The  $p$ -seminorm  $\|\cdot\|_{\mathcal{L}_p(X)}$  on  $\mathcal{L}_p(X)$  is introduced as

$$\|f\|_{\mathcal{L}_p(X)} = \left( \int_X |f(x)|^p d\mu \right)^{1/p}$$

for  $1 < p < \infty$  and

$$\|f\|_{\mathcal{L}_\infty(X)} = \operatorname{ess\,sup}_{x \in X} |f(x)|.$$

The Lebesgue space  $\mathcal{L}_2(X)$  is a Hilbert space with inner product

$$\langle f, g \rangle = \int_X f(x) \overline{g(x)} d\mu.$$

### Fourier transform

We define the Fourier transform (FT) of an integrable function  $f \in \mathcal{L}_1(\mathbb{R}^n)$  by

$$\mathcal{F}\{f\}(\xi) := \frac{1}{(2\pi)^{n/2}} \int_{\mathbb{R}^n} f(x) e^{-ix \cdot \xi} dx,$$

where  $\cdot$  denotes the standard euclidian scalar product in  $\mathbb{R}^n$ . The corresponding inverse Fourier transform (IFT) is given by

$$\mathcal{F}^{-1}\{f\}(x) := \frac{1}{(2\pi)^{n/2}} \int_{\mathbb{R}^n} f(\xi) e^{ix \cdot \xi} d\xi.$$

## Convolution

The convolution  $f * g$  of two locally integrable functions  $f, g : \mathbb{R}^n \rightarrow \mathbb{C}$  is defined by

$$(f * g)(x) := \int_{\mathbb{R}^n} f(x') g(x - x') dx'.$$

Convolution theorem:

For  $f, g \in \mathcal{L}_1(\mathbb{R}^n)$  holds that

$$\mathcal{F}\{f * g\}(\xi) = (2\pi)^{n/2} \mathcal{F}\{f\}(\xi) \cdot \mathcal{F}\{g\}(\xi) \quad \forall \xi \in \mathbb{R}^n. \quad (\text{A.1})$$

## Distributions

The Schwartz space  $\mathcal{S}(\mathbb{R}^n)$  is the function space

$$\mathcal{S}(\mathbb{R}^n) := \left\{ \varphi \in \mathcal{C}^\infty(\mathbb{R}^n) : \|\varphi\|_{\alpha, \beta} < \infty \quad \forall \alpha, \beta \in \mathbb{N}_0^n \right\}$$

for the set of smooth functions  $\mathcal{C}^\infty(\mathbb{R}^n)$ , multi-indices  $\alpha, \beta$ , and

$$\|\varphi\|_{\alpha, \beta} := \sup_{x \in \mathbb{R}^n} |x^\beta \mathcal{D}^\alpha \varphi(x)|.$$

The space of tempered distributions  $\mathcal{S}'(\mathbb{R}^n)$  is the space of all continuous, linear functionals  $\varphi : \mathcal{S}(\mathbb{R}^n) \rightarrow \mathbb{C}$  (dual space of  $\mathcal{S}(\mathbb{R}^n)$ ).

## Sobolev space

The Sobolev space  $\mathcal{H}^s(\mathbb{R}^n)$  for all  $s \in \mathbb{R}$  is represented by

$$\mathcal{H}^s(\mathbb{R}^n) := \left\{ f \in \mathcal{S}'(\mathbb{R}^n) : \left(1 + |\xi|^2\right)^{s/2} \mathcal{F}\{f\}(\xi) \in \mathcal{L}_2(\mathbb{R}^n) \right\}.$$

## Generalized Minkowski's integral inequality

Suppose that  $\mathbf{T} : S_1 \times S_2 \rightarrow \mathbb{R}$  is measurable for the  $\sigma$ -finite measure spaces  $(S_1, \mu_1)$  and  $(S_2, \mu_2)$  and  $1 \leq p < \infty$ . Then, the generalized Minkowski's integral inequality is (cf, e.g., [98, Theorem 202],[200])

$$\left( \int_{S_2} \left| \int_{S_1} \mathbf{T}(x, y) \mu_1(dx) \right|^p \mu_2(dy) \right)^{1/p} \leq \int_{S_1} \left( \int_{S_2} |\mathbf{T}(x, y)|^p \mu_2(dy) \right)^{1/p} \mu_1(dx). \quad (\text{A.2})$$

# List of Figures

2.1	Fundamental idea of astronomical AO, source: [43]. Reflection of the light of a distorted wavefront on a mirror results in a corrected wavefront propagating to the science camera. . . . .	6
2.2	Size comparison of existing and planned telescope systems, source: [150]. The Very Large Telescope, Extremely Large Telescope (largest telescope planned), Keck Telescopes, Thirty Meter Telescope, Gran Telescopio Canarias (largest state of the art telescope), Subaru Telescope, South African Large Telescope, New Technology Telescope, Giant Magellan Telescope, and Large Synoptic Survey Telescope (from left to right). . . . .	7
2.3	Diffraction limited PSF of an 8 m and a 42 m telescope, source [191]. The PSF of the ELT better approximates a delta distribution. . . . .	10
2.4	Design of an AO system, source [107]. Adaptive Optics improves the performance of optical systems by deforming a mirror in order to reduce the effect of wavefront aberrations. . . . .	15
2.5	Sketch of cone effect introduced by an LGS, source [6]. . . . .	16
2.6	Spot elongation caused by an LGS, source [6]. . . . .	17
2.7	LGS tip-tilt indetermination, source [6]. Light emitted by a GS is refracted by a wedge of cold air. On the detectors of the telescope, the GS appears dislocated. However, the true location of the natural guide star is known, and therefore the tip-tilt indetermination is overcome. . . . .	17
2.8	Scheme of a Shack-Hartmann sensor, source [6]. Signals detected from undistorted and distorted wavefronts are shown as well as a signal captured on the sensor array which corresponds to a blurred image (from left to right). . . . .	18
2.9	Concept of a pyramid and roof wavefront sensor, source [164, 212]. . . . .	19
2.10	Different DM types, source [52]. . . . .	21
2.11	Actuator positions of the ELT M4 geometry implemented in the end-to-end simulation tool Octopus (cf Section 2.5.3), source [110, 149]. Additionally, the telescope spider positions, which are considered in Chapter 8, are shown. . . . .	21
2.12	Principle of SCAO, source [150]. . . . .	23

2.13	Schemes of fundamental AO operating modes, source [6]. The red/green stars indicate natural/laser guide stars, the magenta spirals stand for the astronomical object one wants to observe and the blue areas will be corrected by the AO system. . . . .	24
3.1	Optical setting of a PWFS, source [108]. . . . .	31
3.2	Fourier signal-to-noise ratio curves, source [212]. The dotted line represents the response to varying spatial frequencies (plotted on the x-axis) for a Shack-Hartmann sensor and the solid line for a pyramid sensor. One can clearly identify both regimes of the pyramid sensor with the threshold $\alpha/\lambda$ . The system's cut-off frequency is denoted by $F_c$ and the subaperture size by $d$ . . . . .	33
3.3	Borders of the annular aperture mask for fixed $x$ and $y$ , source [108]. The domain $\Omega_x$ changes with $x$ and $\Omega_y$ with $y$ respectively. In some cases the intervals are split due to the central obstruction of the telescope. . . . .	34
4.1	Transformation of telescope aperture, source [107]. We transform the annular telescope aperture $\Omega$ onto the region $[-1, 1]^2$ . The blue line represents a chord $\bar{\Omega} = \Omega_y$ of the pupil for fixed $y$ . If the chord consists of two parts (dotted red line), we consider each part separately. . . . .	70
4.2	Wavefront reconstruction with the SVTR, source [107]. The incoming wavefront averaged over subapertures, the reconstructed wavefront as well as the residual wavefront are plotted for the reconstruction without measurement extension. The highest errors occur at the boundary of the telescope pupil mask. The RMSE is around $3.1527 \times 10^{-7}$ . . . . .	79
4.3	Scheme of the measurement continuation, [107]. For the iterative method with measurement extension we reconstruct on the whole square $[-1, 1] \times [-1, 1]$ . In the darkgray region the real measurements are known. Outside the annular shape (lightgray region) we calculate extended measurements using the finite Hilbert transform operator. . . . .	79
4.4	SVTR with iterative measurement extension, source [107]. The incoming wavefront averaged over subapertures, the reconstructed wavefront as well as the residual wavefront are plotted for the iterative reconstruction with measurement extension. Compared to Figure 4.2, we could improve the errors on the boundary. After 20 iteration steps, the RMSE is around $8.8045 \times 10^{-8}$ . . . . .	80
4.5	LE Strehl ratio in the K-band obtained with the singular value type reconstructor using the parameters from Table 4.2, source [107]. At the beginning, the continuation of measurements guarantees a faster convergence to higher Strehl ratios. After 1000 iterations the LE Strehl ratio is about 0.89 for both SVTR methods. . . . .	82
5.1	The figures indicate piston, tip and tilt mode (from left to right), source [109]. . . . .	93

6.1	Warm restart effect for the non-modulated sensor, source [106]. Without using the warm restart technique (dotted line) the reconstructor suffers from slower convergence compared to the method with a warm restart (solid line). The results correspond to the non-linear LIPS approach for 10000 ph/subap/frame. . . . .	125
6.2	Comparison of non-linear and linear methods for the non-modulated sensor, source [106]. The non-linear algorithms outperform the linear approaches. While for the non-linear implementations there is almost no difference between the Landweber (solid lines) and the Landweber-Kaczmarz method (dashed lines), the Kaczmarz version of the linear reconstructors gives a higher improvement in quality. . . . .	127
6.3	Comparison of non-linear and linear methods for the modulated sensor, source [106]. The linear algorithms clearly outmatch the non-linear processes. In the majority of cases the Landweber algorithms (solid lines) outperform the Landweber-Kaczmarz approaches (dashed lines). . . . .	127
7.1	Fourier domain filters $g^{\{n,c,l\}}$ , source [111]. . . . .	139
8.1	ELT pupil mask with spiders, source [110, 149]. The ELT will consist of a 39.3-meter-diameter primary mirror and a 4.2-meter-diameter secondary mirror which will be supported by 6 spiders each being 50 cm thick. . . . .	150
8.2	Residual screen in radians (evaluated in the K-band) for the “padding with zeros under the spiders” approach, source [110, 149]. Attempts like measurement continuation, interpolation of data or the reconstructed phase as well as reconstruction using the light under the support structures deliver similar poor results. . . . .	163
8.3	Illustration of wavefront reconstruction with the Split Approach at the third time step in an AO loop performed in Octopus, source [110, 149]. The first line shows an incoming screen given in radians (K-band) and the corresponding pistons on the 6 segments. The second line shows the segment-piston-free wavefront reconstruction using the P-CuReD on segments and the DSPR I. In the last line we see the combination of both, i.e., the whole wavefront reconstruction. The algorithm gives reasonable reconstructions of the piston-free wavefront as well as the segment pistons. The simulation parameter correspond to the ones specified in Section 8.5.1. . . . .	167
8.4	Measurements of piston modes, source [110, 149]. Pyramid sensor measurements for a single segment piston mode of height $5 \cdot 10^{-8}$ m are indicated. The first column shows the segment piston, the second and third column illustrate the corresponding sensor measurements in $x$ - and $y$ -direction. The measurements are shown in the range $[-1.5 \cdot 10^{-8}, 1.5 \cdot 10^{-8}]$ m. . . . .	170

- 
- 8.5 Logarithmic plot of the approximate complexities of MVM methods using the full control matrix (dotted line) and of the Split Approach using any of the described methods for direct segment piston reconstruction applying the small-size control matrices (solid line), source [110, 149]. . . . . 171
- 8.6 Robustness of the DSPR I and the instabilities of the DSPR II method illustrated by the corresponding short-exposure Strehl ratios in the K-band for 1000 time steps of test case 1 (600 photons/subaperture/frame and zenith angle  $0^\circ$ ), source [110, 149]. . . . . 176
- 8.7 Residual pistons in radians (K-band) on the disjoint segments for the Split Approach using the DSPR I, source [110, 149]. The photon flux corresponds to 100 photons/subaperture/frame using a zenith angle of  $30^\circ$ . There is almost no residual piston development. Additionally, the reconstructions do not suffer from the phase ambiguity of the pyramid sensor since the piston offsets between the segments are very much smaller than  $2\pi$  radians. The global piston is subtracted from each of the segment pistons for better visibility. . . . . 177

## List of Algorithms

5.1	CGNE for pyramid sensors . . . . .	88
5.2	Steepest Descent for pyramid sensors . . . . .	88
5.3	linear Landweber Iteration for Pyramid Sensors (LIPS) . . . . .	91
5.4	linear Kaczmarz-Landweber Iteration for Pyramid Sensors (KLIPS) . . . . .	95
5.5	Steepest Descent-Kaczmarz for pyramid sensors . . . . .	95
5.6	modified Steepest Descent-Kaczmarz for pyramid sensors . . . . .	96
6.1	non-linear Landweber Iteration for Pyramid Sensors . . . . .	115
6.2	non-linear Kaczmarz-Landweber Iteration for Pyramid Sensors . . . . .	116
8.1	Split Approach . . . . .	169



# List of Tables

2.1	Parameters of the 9-layer atmosphere used in the EPICS simulations. The layer heights (in m) and approximate $c_n^2$ -profiles (in $\text{m}^{-2/3}$ ) of the ESO standard 9-layer atmosphere are listed. The corresponding Fried parameter is $r_0 = 12.9$ cm. . . . .	13
4.1	Parameters of ELT simulations for testing the SVTR. . . . .	77
4.2	Test case setting for Octopus simulations using the SVTR. . . . .	78
4.3	LE Strehl ratios obtained with the Finite Hilbert Transform Reconstructor and the Singular Value Type Reconstructor on an XAO system and a SCAO system. . . . .	82
5.1	Test case setting for numerical simulations using linear iterative reconstruction methods. . . . .	98
5.2	SD-reconstruction (Algorithm 5.2) results for the non-modulated sensor in the K-band after 500 time steps using different step sizes. . . . .	99
5.3	Long-exposure Strehl ratios in the K-band for a pyramid sensor without modulation obtained with the presented linear algorithms after 500 closed loop simulation steps. Best results are obtained for the CGNE approach (Algorithm 5.1), the SD (Algorithm 5.2), and Landweber-Kaczmarz iteration (Algorithm 5.4). . . . .	101
5.4	Long-exposure Strehl ratios in the K-band for a pyramid sensor with modulation $4 \lambda/D$ obtained with the presented linear algorithms after 500 closed loop simulation steps. Here, the CGNE approach (Algorithm 5.1) provides the highest reconstruction quality in most of the cases. . . . .	101
5.5	Long-exposure Strehl ratios in L-, M-, and N-bands obtained for the non-modulated pyramid sensor with the Landweber-Kaczmarz algorithm in the high flux case (10000 ph/subaperture/frame) after 500 closed loop simulation steps. . . . .	102
5.6	The number of floating point operations to be performed online in the linear LIPS and KLIPS. . . . .	103
5.7	The number of floating point operations in the Steepest Descent and Steepest Descent-Kaczmarz for pyramid sensors. . . . .	104

5.8	The number of floating point operations in the CGNE algorithm for pyramid sensors. . . . .	105
5.9	The computational complexities of the linear iterative algorithms compared to the implementation of an MVM method. Estimates of the number of floating point operations necessary for the METIS instrument having a pyramid wavefront sensor with $74 \times 74$ and for an XAO system with $200 \times 200$ subapertures are provided. The last column demonstrates the computational effort of the presented algorithms as percentage of the MVM effort for the XAO system. . . . .	106
6.1	The number of floating point operations to be performed online in the non-linear Landweber and Landweber-Kaczmarz method. The post loop step is only necessary for the LIPS and omitted for the KLIPS. . .	124
6.2	Long-exposure Strehl ratios in the K-band for a pyramid sensor without modulation obtained with the non-linear Landweber method (Algorithm 6.1) and the non-linear Landweber-Kaczmarz iteration (Algorithm 6.2) after 500 closed loop simulation steps. The simulation results listed for the linear LIPS (Algorithm 5.3) and the linear KLIPS (Algorithm 5.4) correspond to the LE Strehl ratios presented in Chapter 5. .	125
6.3	Long-exposure Strehl ratios in the K-band for a pyramid sensor with modulation $4 \lambda/D$ obtained with the non-linear Landweber iteration (Algorithm 6.1) and the non-linear Landweber-Kaczmarz iteration (Algorithm 6.2) after 500 closed loop simulation steps. The corresponding results from Chapter 5 obtained with the linear LIPS (Algorithm 5.3) and the linear KLIPS (Algorithm 5.4) are listed as well. . . . .	126
6.4	LE Strehl ratios for the EPICS instrument with a non-modulated PWFS. Results are listed for those iterative reconstruction algorithms providing the most accurate wavefront estimates, namely the CGNE approach, the linear KLIPS and the non-linear KLIPS. . . . .	128
7.1	Overview on existing wavefront reconstruction methods for the PWFS with respect to underlying pyramid sensor models. The check marks in brackets indicate that an according extension has already been considered in theory but has not been implemented yet. . . . .	145
7.2	Overview on existing wavefront reconstruction methods for the PWFS showing the computational complexity and the modulation scenarios they were already implemented for. . . . .	146
7.3	Overview of simulation parameters for the currently scheduled METIS and an EPICS-like instrument. . . . .	147

---

7.4	Reconstruction quality of selected reconstruction algorithms for the METIS (SCAO) and EPICS (XAO) instrument of the ELT using pyramid sensors with or without modulation. We took telescope spiders into account for 2 simulations. The P-CuReD results for segmented pupils were obtained within the Split Approach (cf Chapter 8). The fields are left empty if no simulations were performed and “NA“ means that the method is not applicable to this setting. . . . .	148
8.1	Comparison of some currently existing algorithms for wavefront reconstruction from pyramid sensor data in terms of their flexibility and computational complexity. . . . .	161
8.2	Simulation parameters used in the tests on the segmented ELT pupil. .	173
8.3	Long-exposure Strehl ratios in the K-band ( $2.2 \mu\text{m}$ ) after 1000 closed loop simulation steps. As reconstruction method, we use the P-CuReD. We compare the results for a benchmark simulation without spiders using the P-CuReD only and employing the Split Approach combined with the proposed Direct Segment Piston Reconstructors in the presence of telescope spiders. . . . .	174
8.4	LE Strehl ratios in the L-band ( $3.7 \mu\text{m}$ ) after 1000 closed loop simulation steps using the P-CuReD in all simulations. . . . .	175
8.5	LE Strehl ratios in the N-band ( $10 \mu\text{m}$ ) after 1000 closed loop simulation steps using the P-CuReD in all simulations. . . . .	175



## References

- [1] R. A. Adams. *Sobolev Spaces*. Pure and Applied Mathematics. Academic Press New York San Francisco London, 1975.
- [2] V. Akondi, S. Castillo, and B. Vohnsen. “Digital pyramid wavefront sensor with tunable modulation”. In: *Opt. Express* 21.15 (July 2013), pp. 18261–18272.
- [3] V. Akondi, S. Castillo, and B. Vohnsen. “Multi-faceted digital pyramid wavefront sensor”. In: *Optics Communications* 323 (2014), pp. 77–86.
- [4] C. Arcidiacono. “Beam divergence and vertex angle measurements for refractive pyramids”. In: *Optics Communications* 252.4 (2005), pp. 239–246.
- [5] F. Assemat, E. Gendron, and F. D. Hammer. “The FALCON concept: multi-object adaptive optics and atmospheric tomography for integral field spectroscopy – principles and performance on an 8-m telescope”. In: *Mon. Not. R. Astron. Soc* 376 (2007), pp. 287–312.
- [6] G. Auzinger. “New Reconstruction Approaches in Adaptive Optics for Extremely Large Telescopes”. PhD thesis. Johannes Kepler University Linz, 2017.
- [7] G. Auzinger, M. Le Louarn, A. Obereder, and D. Saxenhuber. “Effects of reconstruction layer profiles on atmospheric tomography in E-ELT AO systems”. In: *Adaptive Optics for Extremely Large Telescopes 4–Conference Proceedings*. Vol. 1. 1. 2015.
- [8] A. B. Bakushinsky and A. Goncharsky. *Iterative Methods for the Solution of Incorrect Problems*. Radon Series on Computational and Applied Mathematics. Nauka, Moscow, 1989.
- [9] A. B. Bakushinsky, M. M. Kokurin, and M. Y. Kokurin. *Regularization Algorithms for Ill-Posed Problems*. Inverse and Ill-Posed Problems Series 61. Berlin, Boston: De Gruyter, 2018.
- [10] A. B. Bakushinsky and M. Y. Kokurin. “Iterative Methods for Approximate Solution of Inverse Problems”. In: *Mathematics and Its Applications* 577 (2004).
- [11] R. E. Bank and D. J. Rose. “Analysis of a Multilevel Iterative Method for Nonlinear Finite Element Equations”. In: *Mathematics of Computation* 39.160 (1982), pp. 453–465.

- [12] J. M. Bardsley. “Wavefront reconstruction methods for Adaptive Optics systems on ground-based telescopes”. In: *SIAM Journal on Matrix Analysis and Applications* 30 (2008), pp. 67–83.
- [13] J. Barzilai and J. Borwein. “Two-point step size gradient methods”. In: *IMA Journal of Numerical Analysis* 8 (1988), pp. 141–148.
- [14] C. Béchet, M. Tallon, and É. Thiébaud. “Comparison of minimum-norm maximum likelihood and maximum a posteriori wavefront reconstructions for large adaptive optics systems”. In: *J. Opt. Soc. Am. A* 26.3 (Mar. 2009), pp. 497–508.
- [15] U. Bitenc, A. Basden, N. A. Bharmal, T. Morris, N. Dipper, E. Gendron, F. Vidal, D. Gratadour, G. Rousset, and R. Myers. “On-sky tests of the CuReD and HWR fast wavefront reconstruction algorithms with CANARY”. In: *Monthly Notices of the Royal Astronomical Society* 448.2 (2015), pp. 1199–1205.
- [16] U. Bitenc, M. Rosensteiner, N. Bharmal, A. Basden, T. Morris, A. Obereder, N. Dipper, E. Gendron, F. Vidal, G. Rousset, D. Gratadour, O. Martin, Z. Hubert, and R. Myers. “Tests of novel wavefront reconstructors on sky with CANARY”. In: *Proceedings of the Third AO4ELT Conference*. 2013.
- [17] C. Z. Bond, P. Wizinowich, M. Chun, D. Mawet, S. Lilley, S. Cetre, N. Jovanovic, J.-R. Delorme, E. Wetherell, S. Jacobson, C. Lockhart, E. Warmbier, J. K. Wallace, D. N. Hall, S. Goebel, O. Guyon, C. Plantet, G. Agapito, C. Giordano, S. Esposito, and B. Femenia-Castella. “Adaptive optics with an infrared Pyramid wavefront sensor”. In: *Proc. SPIE*. Vol. 10703. 2018, 10703 – 107031Z –11.
- [18] C. Z. Bond, K. El Hadi, J.-F. Sauvage, C. Correia, O. Fauvarque, D. Rabaud, M. Lamb, B. Neichel, and T. Fusco. “Experimental study of an optimised Pyramid wave-front sensor for Extremely Large Telescopes”. In: *Proc. SPIE 9909, Astronomical Telescopes and Instrumentation*. 2016, pp. 990964–990964–13.
- [19] C. Z. Bond, C. M. Correia, J.-F. Sauvage, K. El Hadi, B. Neichel, and T. Fusco. “Fourier wavefront reconstruction with a pyramid wavefront sensor”. In: *Proc. SPIE*. Vol. 10703. 2018, pp. 10703 –107034M –8.
- [20] C. Z. Bond, C. M. Correia, J.-F. Sauvage, B. Neichel, and T. Fusco. “Iterative wave-front reconstruction in the Fourier domain”. In: *Opt. Express* 25 (2017), pp. 11452–11465.
- [21] S. Bonnefond, M. Tallon, M. Le Louarn, and P.-Y. Madec. “Wavefront reconstruction with pupil fragmentation: study of a simple case”. In: *Proc. SPIE*. Vol. 9909. 2016, pp. 9909–9909–6.
- [22] H. Brakhage. “On ill-posed problems and the method of conjugate gradients”. In: *Inverse and Ill-Posed Problems*. Ed. by H. W. Engl and C.W. Groetsch. Academic Press, 1987, pp. 165 –175.

- [23] B. R. Brandl, M. Feldt, A. Glasse, M. Guedel, S. Heikamp, M. Kenworthy, R. Lenzen, M. R. Meyer, F. Molster, S. Paalvast, E. J. Pantin, S. P. Quanz, E. Schmalzl, R. Stuik, L. Venema, C. Waelkens, and the NOVA-Astron Instrumentation Group. *METIS: the Mid-infrared E-ELT Imager and Spectrograph*. <https://arxiv.org/pdf/1409.3087.pdf>.
- [24] B. R. Brandl, T. Agócs, G. Aitink-Kroes, T. Bertram, F. Bettonvil, R. van Boekel, O. Boulade, M. Feldt, A. Glasse, A. Glauser, M. Güdel, N. Hurtado, R. Jager, M. A. Kenworthy, M. Mach, J. Meisner, M. Meyer, E. Pantin, S. Quanz, H. M. Schmid, R. Stuik, A. Veninga, and C. Waelkens. “Status of the mid-infrared E-ELT imager and spectrograph METIS”. In: *Proc. SPIE* 9908 (2016), pp. 9908–9908–15.
- [25] H. Brezis and P. Mironescu. “Composition in fractional Sobolev spaces”. In: *Discrete & Continuous Dynamical Systems - A* 7(2) (2001), pp. 241–246.
- [26] H. Brezis and P. Mironescu. “Gagliardo-Nirenberg, composition and products in fractional Sobolev spaces”. In: *Journal of Evolution Equations* 1(4) (2001), pp. 387–404.
- [27] F. E Browder and W. V Petryshyn. “Construction of fixed points of nonlinear mappings in Hilbert space”. In: *Journal of Mathematical Analysis and Applications* 20.2 (1967), pp. 197–228.
- [28] A. Burvall, E. Daly, S. R. Chamot, and C. Dainty. “Linearity of the pyramid wavefront sensor”. In: *Optics Express* 14 (25) (2006), pp. 11925–11934.
- [29] P. L. Butzer and R. J. Nessel. *Fourier Analysis and Approximation*. Vol. 1. Birkhäuser Verlag Basel, 1971.
- [30] M. Carbillet, C. Vérinaud, B. Femenia, A. Riccardi, and L. Fini. “Modelling astronomical adaptive optics – I. The software package CAOS”. In: *Mon. Not. R. Astron. Soc.* 356 (2005), pp. 1263–1275.
- [31] A. Cauchy. “Méthode générale pour la résolution des systemes d’équations simultanées”. In: *Comp. Rend. Sci. Paris* 25 (1847), pp. 536–538.
- [32] M. Cayrel. “E-ELT optomechanics: overview”. In: *Proc. SPIE*. Vol. 8444. 2012, pp. 8444–18.
- [33] A. De Cezaro, M. Haltmeier, A. Leitao, and O. Scherzer. “On Steepest-Descent-Kaczmarz methods for regularizing systems of nonlinear ill-posed equations”. In: *Applied Mathematics and Computation* 202.2 (2008), pp. 596–607.
- [34] S. R. Chamot, C. Dainty, and S. Esposito. “Adaptive optics for ophthalmic applications using a pyramid wavefront sensor”. In: *Optics Express* 14.2 (2006), pp. 518–526.
- [35] L. Chen, J. Wang, K. Yao, X. Liu, X. Lin, L. Wang, and M. Wang. “Experimental Demonstration of Sequential Operation Approach for a Three-Sided Pyramid Wavefront Sensor”. In: *IEEE Photonics Journal* 8.4 (Aug. 2016), pp. 1–13.

- [36] R. Clare and M. Le Louarn. “Numerical simulations of an Extreme AO system for an ELT”. In: *Proc. AO4ELT2*. 2011, pp. 1100–1107.
- [37] R. M. Clare and R. G. Lane. “Comparison of wavefront sensing with the Shack-Hartmann and pyramid sensors”. In: *Proc. SPIE 5490, Advancements in Adaptive Optics*. 2004.
- [38] R. M. Clare and R. G. Lane. “Phase retrieval from subdivision of the focal plane with a lenslet array”. In: *Appl. Opt.* 43.20 (July 2004), pp. 4080–4087.
- [39] R. M. Clare and R. G. Lane. “Wavefront sensing from spatial filtering at the focal plane”. In: *Proc. SPIE 5169*. 2003, pp. 43–54.
- [40] R. M. Clare, M. Le Louarn, and C. B chet. “Optimal noise-weighted reconstruction with elongated Shack–Hartmann wavefront sensor images for laser tomography adaptive optics”. In: *Appl. Opt.* 49.31 (Nov. 2010), G27–G36.
- [41] R. M. Clare, B. E. Engler, S. Weddell, Iu. Shatokhina, A. Obereder, and M. Le Louarn. “Numerical evaluation of pyramid type sensors for extreme adaptive optics for the European Extremely Large Telescope”. In: *Proceedings of the Fifth AO4ELT Conference*. 2017.
- [42] Y. Cl net, T. Buey, G. Rousset, E. Gendron, S. Esposito, Z. Hubert, L. Busoni, M. Cohen, A. Riccardi, F. Chapron, M. Bonaglia, A. Sevin, P. Baudoz, P. Feautrier, G. Zins, D. Gratadour, F. Vidal, F. Chemla, F. Ferreira, N. Doucet, S. Durand, A. Carlotti, C. Perrot, L. Schreiber, M. Lombini, P. Ciliegi, E. Diolaiti, J. Schubert, and R. Davies. “Joint MICADO-MAORY SCAO mode: specifications, prototyping, simulations and preliminary design”. In: *Proc. SPIE 9909, Adaptive Optics Systems V*. 2016, 99090A–99090A–12.
- [43] W. Commons. *Deformable mirror correction*. 2011.
- [44] R. Conan and C. Correia. “Object-oriented Matlab adaptive optics toolbox”. In: *Proc. SPIE*. Vol. 9148. 2014, pp. 9148–9148–17.
- [45] Y.-H. Dai. “Alternate step gradient method”. In: *Optimization* 52.4-5 (2003), pp. 395–415.
- [46] Y.-H. Dai and Y.-X. Yuan. “Alternate minimization gradient method”. In: *IMA Journal of Numerical Analysis* 23(3) (2003), pp. 377–393.
- [47] E. M. Daly and C. Dainty. “Ophthalmic wavefront measurements using a versatile pyramid sensor”. In: *Appl. Opt.* 49.31 (Nov. 2010), G67–G77.
- [48] M. A. van Dam, R. Conan, A. H. Bouchez, and B. Espeland. “Design of a truth sensor for the GMT laser tomography adaptive optics system”. In: *Proc. SPIE 8447, Adaptive Optics Systems III*. 2012, p. 844717.
- [49] R. Davies, J. Alves, R. Ramlau, R. Wagner, V. Hutterer, J. Niebsch, et al. “The MICADO first light imager for the ELT: overview, operation, simulation”. In: *Proc. SPIE*. 2018, 10702 –107021S.

- [50] V. Deo, E. Gendron, G. Rousset, F. Vidal, and T. Buey. “A modal approach to optical gain compensation for the pyramid wavefront sensor”. In: *Proc. SPIE*. Vol. 10703. 2018, pp. 10703–1070320–18.
- [51] C. A. Diez. “A 3-sided Pyramid Wavefront Sensor Controlled by a Neural Network for Adaptive Optics to reach diffraction-limited Imaging of the Retina”. PhD thesis. 2006.
- [52] N. Doble, D. T. Miller, G. Yoon, and D. R. Williams. “Requirements for discrete actuator and segmented wavefront correctors for aberration compensation in two large populations of human eyes”. In: *Appl. Opt.* 46.20 (July 2007), pp. 4501–4514.
- [53] R. K. Tyson (ed.) *Adaptive Optics Engineering Handbook*. New York, Basel: Marcel Dekker Inc., 2000.
- [54] B. Ellerbroek and C. R. Vogel. “Simulations of closed-loop wavefront reconstruction for multiconjugate adaptive optics on giant telescopes”. In: *Proc. SPIE*. Vol. 5169. 2003, pp. 206–217.
- [55] B. L. Ellerbroek. “Efficient computation of minimum-variance wave-front reconstructors with sparse matrix techniques”. In: *JOSA A* 19.9 (2002), pp. 1803–1816.
- [56] B. L. Ellerbroek and C. R. Vogel. “Inverse problems in astronomical adaptive optics”. In: *Inverse Problems* 25.6 (2009), p. 063001.
- [57] H. W. Engl. *Integralgleichungen*. Springer Wien, 1997.
- [58] H. W. Engl, M. Hanke, and A. Neubauer. *Regularization of Inverse Problems*. Dordrecht, Boston, London: Kluwer Academic Publishers, 2000.
- [59] B. Engler, S. Weddell, M. Le Louarn, and R. Clare. “Effects of the telescope spider on extreme adaptive optics systems with pyramid wavefront sensors”. In: *Proc. SPIE*. Vol. 10703. 2018, 10703–107035F–13.
- [60] M. Eslitzbichler, C. Pechstein, and R. Ramlau. “An  $H^1$ -Kaczmarz reconstructor for atmospheric tomography”. In: *Journal of Inverse and Ill-Posed Problems* 21.3 (June 2013), pp. 431–450.
- [61] S. Esposito. “Introduction to Multi-Conjugate Adaptive Optics systems”. In: *Comptes Rendus Physique* 6.10 (2005). Multi-Conjugate Adaptive Optics for very large telescopes, pp. 1039–1048.
- [62] S. Esposito and N. Devaney. “Segmented telescopes co-phasing using Pyramid Sensor”. In: *Proc. Beyond Conventional Adaptive Optics*. 2001.
- [63] S. Esposito, O. Feeney, and A. Riccardi. “Laboratory test of a pyramid wavefront sensor”. In: *Proc. SPIE 4007, Adaptive Optical Systems Technology*. Ed. by P. L. Wizinowich. July 2000, pp. 416–422.

- [64] S. Esposito and A. Riccardi. “Pyramid Wavefront Sensor behavior in partial correction Adaptive Optic systems”. In: *Astronomy and Astrophysics* 369 (2001), pp. L9–L12.
- [65] S. Esposito, A. Riccardi, and O. Feeney. “Closed-loop performance of pyramid wavefront sensor”. In: *Proc. SPIE 4034, Laser Weapons Technology*. 2000, pp. 184–189.
- [66] S. Esposito, E. Pinna, A. Tozzi, P. Stefanini, and N. Devaney. “Cophasing of segmented mirrors using the pyramid sensor”. In: *Proc. SPIE 5169, Astronomical Adaptive Optics Systems and Applications*. 2003.
- [67] S. Esposito, A. Riccardi, F. Quirós-Pacheco, E. Pinna, A. Puglisi, M. Xompero, R. Briguglio, L. Busoni, L. Fini, P. Stefanini, G. Brusa, A. Tozzi, P. Ranfagni, F. Pieralli, J. C. Guerra, C. Arcidiacono, and P. Salinari. “Laboratory characterization and performance of the high-order adaptive optics system for the Large Binocular Telescope”. In: *Applied Optics* 49.31 (Nov. 2010), G174–G189.
- [68] S. Esposito, A. Riccardi, E. Pinna, A. Puglisi, F. Quirós-Pacheco, C. Arcidiacono, M. Xompero, R. Briguglio, G. Agapito, L. Busoni, L. Fini, J. Argomedo, A. Gherardi, G. Brusa, D. Miller, J. C. Guerra, P. Stefanini, and P. Salinari. “Large Binocular Telescope Adaptive Optics System: new achievements and perspectives in adaptive optics”. In: *Proc. SPIE 8179, SAR Image Analysis, Modeling, and Techniques XI*. 2011, pp. 814902–814902–10.
- [69] S. Esposito, A. Riccardi, L. Fini, E. Pinna, A. Puglisi, F. Quiros, M. Xompero, R. Briguglio, L. Busoni, P. Stefanini, C. Arcidiacono, G. Brusa, and D. Miller. “LBT AO on-sky results”. In: *Proceedings of the Second AO4ELT Conference*. Sept. 2011, p. 3.
- [70] S. Esposito, E. Pinna, A. Puglisi, A. Tozzi, and P. Stefanini. “Pyramid sensor for segmented mirror alignment”. In: *Opt. Lett.* 30.19 (Oct. 2005), pp. 2572–2574.
- [71] S. Esposito, E. Pinna, F. Quirós-Pacheco, A. T. Puglisi, L. Carbonaro, M. Bonaglia, V. Biliotti, R. Briguglio, G. Agapito, C. Arcidiacono, L. Busoni, M. Xompero, A. Riccardi, L. Fini, and A. Bouchez. “Wavefront sensor design for the GMT natural guide star AO system”. In: *Proc. SPIE 8447, Adaptive Optics Systems III*. 2012, pp. 84471L–84471L–10.
- [72] O. Fauvarque, B. Neichel, T. Fusco, J.-F. Sauvage, and O. Girault. “General formalism for Fourier-based wave front sensing”. In: *Optica* 3.12 (Dec. 2016), pp. 1440–1452.
- [73] O. Fauvarque, B. Neichel, T. Fusco, J.-F. Sauvage, and O. Girault. “General formalism for Fourier-based wave front sensing: application to the pyramid wave front sensors”. In: *Journal of Astronomical Telescopes Instruments and Systems (JATIS)*. Vol. 3. Proc SPIE 019001. Jan. 2017.

- [74] O. Fauvarque, B. Neichel, T. Fusco, and J.-F. Savage. “Variation around the Pyramid theme: optical recombination and optimal use of photons”. In: *Proceedings of the Fourth AO4ELT Conference*. 2015.
- [75] R. Fefferman. “Singular integrals on product domains”. In: *Bull. Amer. Math. Soc. (N.S.)* 4.2 (Mar. 1981), pp. 195–201.
- [76] M. Feldt, D. Peter, S. Hippler, T. Henning, J. Aceituno, and M. Goto. “PYRAMIR: first on-sky results from an infrared pyramid wavefront sensor”. In: *Proc. SPIE 6272, Advances in Adaptive Optics II*. 2006, p. 627218.
- [77] J. R. Fienup. “Reconstruction of an object from the modulus of its Fourier transform”. In: *Opt. Lett.* 3.1 (July 1978), pp. 27–29.
- [78] R. A. Frazin. “Efficient, nonlinear phase estimation with the nonmodulated pyramid wavefront sensor”. In: *J. Opt. Soc. Am. A* 35.4 (Apr. 2018), pp. 594–607.
- [79] R. A. Frazin and L. Jolissaint. “Nonlinear estimation with a pyramid wavefront sensor”. In: *Proc. SPIE*. Vol. 10703. 2018, pp. 10703 –1070354 –6.
- [80] D. L. Fried. “Anisoplanatism in adaptive optics”. In: *J. Opt. Soc. Am.* 72.1 (Jan. 1982), pp. 52–61.
- [81] D. L. Fried. “Least-square fitting a wave-front distortion estimate to an array of phase-difference measurements”. In: *J. Opt. Soc. Am.* 67.3 (Mar. 1977), pp. 370–375.
- [82] D. L. Fried. “Optical Resolution Through a Randomly Inhomogeneous Medium for Very Long and Very Short Exposures”. In: *J. Opt. Soc. Am.* 56.10 (Oct. 1966), pp. 1372–1379.
- [83] T. Fusco, N. Thatte, S. Meimon, M. Tecza, F. Clarke, and M. Swinbank. “Adaptive optics systems for HARMONI: a visible and near-infrared integral field spectrograph for the E-ELT”. In: *Proc. SPIE 7736, Adaptive Optics Systems II*. 2010, pp. 773633–773633–12.
- [84] T. Fusco, S. Meimon, Y. Clenet, M. Cohen, H. Schnetler, J. Paufique, V. Michau, J.-P. Amans, D. Gratadour, C. Petit, C. Robert, P. Jagourel, E. Gendron, G. Rousset, J.-M. Conan, and N. Hubin. “ATLAS: the E-ELT laser tomographic adaptive optics system”. In: *Proc. SPIE 7736, Adaptive Optics Systems II*. 2010, pp. 77360D–77360D–12.
- [85] T. Fusco, J.-M. Conan, G. Rousset, L.M. Mugnier, and V. Michau. “Optimal wave-front reconstruction strategies for multi conjugate adaptive optics”. In: *J. Opt. Soc. Am. A* 18.10 (2001), pp. 2527–2538.
- [86] A. Garcia-Rissmann and M. Le Louarn. “SCAO Simulation Results with a Pyramid Sensor on an ELT-like Telescope”. In: *1st AO4ELT Conference - Adaptive Optics for Extremely Large Telescopes proceedings*. 2010.

- [87] E. Gaviola. “On the Quantitative Use of the Foucault Knife-Edge Test”. In: *J. Opt. Soc. Am.* 26.4 (Apr. 1936), pp. 163–169.
- [88] R. W. Gerchberg and W. O. Saxton. “A practical algorithm for the determination of phase from image and diffraction plane pictures”. In: *Optik* 35.2 (1972), pp. 237–246.
- [89] A. Ghedina, M. Cecconi, R. Ragazzoni, J. Farinato, A. Baruffolo, G. Crimi, E. Diolaiti, S. Esposito, L. Fini, M. Ghigo, E. Marchetti, T. Niero, and A. Puglisi. “On-sky test of the pyramid wavefront sensor”. In: *Proc. SPIE 4839, Adaptive Optical System Technologies II*. 2003, pp. 869–877.
- [90] S. F. Gilyazov. “Iterative solution methods for inconsistent operator equations”. In: *Moscow Univ. Comput. Math. Cybernet* 3 (1977), pp. 78–84.
- [91] J. W. Goodman. *Introduction to Fourier Optics*. 3rd. Freeman, W.J. & Company New York, 2004.
- [92] O. Guyon. “Limits of Adaptive Optics for High-Contrast Imaging”. In: *The Astrophysical Journal* 629.1 (2005), p. 592.
- [93] K. El Hadi, M. Vignaux, and T. Fusco. “Development of a Pyramid Wave-front Sensor”. In: *Proceedings of the Third AO4ELT Conference*. 2013.
- [94] B. Halpern. “Fixed points of nonexpanding maps”. In: *Bull. Amer. Math. Soc.* 73.6 (1967), pp. 957–961.
- [95] G. Hamel. *Integralgleichungen: Einführung in Lehre und Gebrauch*. Springer-Verlag, 1949.
- [96] M. Hanke. “Conjugate Gradient Type Methods for Ill-Posed Problems”. In: *Longman Scientific & Technical, Harlow, Essex* (1995).
- [97] M. Hanke, A. Neubauer, and O. Scherzer. “A convergence analysis of the Landweber iteration for nonlinear ill-posed problems”. In: *Numerische Mathematik - NUMER MATH* 72 (Nov. 1995), pp. 21–37.
- [98] G. H. Hardy, J. E. Littlewood, and G. Pólya. *Inequalities*. Cambridge Mathematical Library. Cambridge University Press, 1988.
- [99] John W. Hardy. *Adaptive optics for astronomical telescopes*. Oxford University Press, 1998.
- [100] G. T. Herman. *Image Reconstruction from Projections: The Fundamentals of Computerized Tomography*. Academic Press, New York - London, 1980.
- [101] M. R. Hestenes and E. Stiefel. “Methods of Conjugate Gradients for Solving Linear Systems”. In: *Journal of Research of the National Bureau of Standards* 49.6 (1952), pp. 409–436.
- [102] S. Hippler, M. Feldt, T. Bertram, W. Brandner, F. Cantalloube, B. Carlomagno, O. Absil, A. Obereder, Iu. Shatokhina, and R. Stuik. *Single conjugate adaptive optics for the ELT instrument METIS*. submitted. 2017.

- [103] H. Hochstadt. *Integral Equations*. Wiley Classics Library. 2011.
- [104] C. Hofer. “Point spread function reconstruction for single conjugated adaptive optics systems”. MA thesis. Johannes Kepler University Linz, 2014.
- [105] R. H. Hudgin. “Wave-front reconstruction for compensated imaging”. In: *J. Opt. Soc. Am.* 67.3 (Mar. 1977), pp. 375–378.
- [106] V. Hutterer and R. Ramlau. “Non-linear wavefront reconstruction methods for pyramid sensors using Landweber and Landweber-Kaczmarz iteration”. In: *Applied Optics* (2018), to be published.
- [107] V. Hutterer and R. Ramlau. “Wavefront reconstruction from non-modulated pyramid wavefront sensor data using a singular value type expansion”. In: *Inverse Problems* 34.3 (2018), p. 035002.
- [108] V. Hutterer, R. Ramlau, and Iu. Shatokhina. *Real-time Adaptive Optics with pyramid wavefront sensors: A theoretical analysis of the pyramid sensor model*. submitted. 2018.
- [109] V. Hutterer, R. Ramlau, and Iu. Shatokhina. *Real-time Adaptive Optics with pyramid wavefront sensors: Accurate wavefront reconstruction using iterative methods*. submitted. 2018.
- [110] V. Hutterer, Iu. Shatokhina, A. Obereder, and R. Ramlau. *Advanced reconstruction methods for segmented ELT pupils using pyramid sensors*. submitted. 2018.
- [111] V. Hutterer, Iu. Shatokhina, A. Obereder, and R. Ramlau. “Wavefront reconstruction for ELT-sized telescopes with pyramid wavefront sensors”. In: *Proc. SPIE*. Vol. 10703. 2018, pp. 10703 –1070344 –18.
- [112] I. Iglesias. “Pyramid phase microscopy”. In: *Opt. Letters* 36.18 (2011), pp. 3636–3638.
- [113] I. Iglesias and F. Vargas-Martin. “Quantitative phase microscopy of transparent samples using a liquid crystal display”. In: *Journal of Biomedical Optics* 18.2 (2013), pp. 026015–1–5.
- [114] I. Iglesias, R. Ragazzoni, Y. Julien, and P. Artal. “Extended source pyramid wave-front sensor for the human eye”. In: *Optics Express* 10.9 (2002), pp. 419–428.
- [115] J. A. Johnson, R. Kupke, D. Gavel, and B. Bauman. “Pyramid wavefront sensing: theory and component technology development at LAO”. In: *Proc. SPIE*. Vol. 6272. 2006, 62724R–62724R–11.
- [116] S. Kaczmarz. “Angenäherte Auflösung von Systemen linearer Gleichungen”. In: *Bulletin International de l’Académie Polonaise des Sciences et des Lettres* 35 (1937), pp. 355–357.

- [117] B. Kaltenbacher, A. Neubauer, and O. Scherzer. *Iterative Regularization Methods for Nonlinear Ill-Posed Problems*. Radon Series on Computational and Applied Mathematics. De Gruyter, 2008.
- [118] W. J. Kammerer and M. Z. Nashed. “On the Convergence of the Conjugate Gradient Method for Singular Linear Operator Equations”. In: *SIAM Journal on Numerical Analysis* 9.1 (1972), pp. 165–181.
- [119] T. von Karman. “Mechanische Ähnlichkeit und Turbulenz”. In: *Göttinger Nachr. math. phys. Kl.* (1930), p. 30.
- [120] M. Kasper, J.-L. Beuzit, C. Vérinaud, et al. “EPICS: direct imaging of exoplanets with the E-ELT”. In: *Proc. SPIE*. Vol. 7735. 2010, pp. 7735–7735–9.
- [121] A. N. Kolmogorov. “The Local Structure of Turbulence in Incompressible Viscous Fluid for Very Large Reynolds Numbers”. In: *Dokl. Akad. Nauk SSSR* 30 (1941), pp. 299–303.
- [122] V. Korkiakoski and C. Vérinaud. “Extreme adaptive optics simulations for EPICS”. In: *Proceedings of the First AO4ELT Conference*. 2010, p. 03007.
- [123] V. Korkiakoski, C. Vérinaud, and M. Le Louarn. “Applying sensitivity compensation for pyramid wavefront sensor in different conditions”. In: *Proc. SPIE*. Vol. 7015. 2008, pp. 7015 –7015 –10.
- [124] V. Korkiakoski, C. Vérinaud, and M. Le Louarn. “Improving the performance of a pyramid wavefront sensor with modal sensitivity compensation”. In: *Applied Optics* 47.1 (Jan. 2008), pp. 79–87.
- [125] V. Korkiakoski, C. Vérinaud, M. Le Louarn, and R. Conan. “Comparison between a model-based and a conventional pyramid sensor reconstructor”. In: *Applied Optics* 46.24 (2007), pp. 6176–6184.
- [126] R. Kowar and O. Scherzer. “Convergence analysis of a Landweber-Kaczmarz method for solving nonlinear ill-posed problems”. In: *Journal of Ill-Posed and Inverse Problems* 23 (Jan. 2002), pp. 253–270.
- [127] L. Landweber. “An Iteration Formula for Fredholm Integral Equations of the First Kind”. In: *American Journal of Mathematics* 73.3 (1951), pp. 615–624.
- [128] N. F. Law and R. G. Lane. “Wavefront estimation at low light levels”. In: *Optics Communications* 126 (1996), pp. 19–24.
- [129] M. Le Louarn, C. Vérinaud, V. Korkiakoski, N. Hubin, and E. Marchetti. “Adaptive optics simulations for the European Extremely Large Telescope”. In: *SPIE Astronomical Telescopes+Instrumentation*. International Society for Optics and Photonics. 2006, pp. 627234–627234.
- [130] M. Le Louarn, C. Vérinaud, V. Korkiakoski, and E. Fedrigo. “Parallel simulation tools for AO on ELTs”. In: *Advancements in Adaptive Optics*. Proc. SPIE 5490. 2004, pp. 705–712.

- [131] J. LeDue, L. Jolissant, J.-P. Véran, and C. Bradley. “Calibration and testing with real turbulence of a pyramid sensor employing static modulation”. In: *Optics Express* 17.9 (2009), pp. 7186–7195.
- [132] M. Le Louarn, P.-Y. Madec, S. Oberti, J. Paufigue, M. Sarazin, S. Stroebele, and M. Esselborn. *Latest AO simulation results for the E-ELT*. Poster presented at AO4ELT5 Conference. 2017.
- [133] A.K. Louis. *Inverse und schlecht gestellte Probleme*. B.G: Teubner Stuttgart, 1989.
- [134] B. Macintosh, M. Troy, R. Doyon, J. Graham, K. Baker, B. Bauman, C. Marois, D. Palmer, D. Phillion, Lisa Poyneer, I. Crossfield, P. Dumont, B. M. Levine, M. Shao, G. Serabyn, C. Shelton, G. Vasisht, J. K. Wallace, J.-F. Lavigne, P. Valee, N. Rowlands, K. Tam, and D. Hackett. “Extreme adaptive optics for the Thirty Meter Telescope”. In: *Proc. SPIE 6272, Advances in Adaptive Optics II*. 2006, 62720N–62720N–15.
- [135] O. Martin, S. Turbide, F. Legacé, F. Lévesque, G. Anctil, F. Châteauneuf, D. Brousseau, W. Deschênes, and J.-P. Véran. “INO Pyramidal Wavefront Sensor Demonstrator: first closed-loop on-sky operation at Mont-Mégantic Telescope”. In: *Proceedings of the Fourth AO4ELT Conference*. 2015.
- [136] L.M. Martinez, N. Yaitskova, P. Dierickx, and K. Dohlen. “Mach-Zehnder wavefront sensor for phasing of segmented telescopes”. In: *Future Giant Telescopes. Proc. SPIE*. Vol. 4840. 2003, p. 564.
- [137] S. F. McCormick. “The Methods of Kaczmarz and Row Orthogonalization for Solving Linear Equations and Least Squares Problems in Hilbert Space”. In: *Indiana University Mathematics Journal* 26.6 (1977), pp. 1137–1150.
- [138] Steve F. McCormick. “An iterative procedure for the solution of constrained nonlinear equations with application to optimization problems”. In: *Numerische Mathematik* 23.5 (Oct. 1975), pp. 371–385.
- [139] T. S. McKechnie. *General theory of light propagation and imaging through the atmosphere*. Springer. 2016.
- [140] K.-H. Meyn. “Solution of the Undetermined Nonlinear Equations by Stationary Iteration Methods.” In: *Numerische Mathematik* 42 (1983), pp. 161–172.
- [141] E. Mieda, M. Rosensteiner, M. van Kooten, J.-P. Véran, O. Lardiere, and G. Herriot. “Testing the pyramid truth wavefront sensor for NFIRAOS in the lab”. In: *Proc. SPIE 9909, Adaptive Optics Systems V*. 2016, 99091J–99091J–10.
- [142] I. Montilla, C. Béchet, M. Le Louarn, M. Reyes, and M. Tallon. “Performance comparison of wavefront reconstruction and control algorithms for Extremely Large Telescopes”. In: *J. Opt. Soc. Am. A* 27.11 (Nov. 2010), A9–A18.
- [143] F. Natterer. *The Mathematics of Computerized Tomography*. Wiley, 1986.

- [144] F. Natterer and F. Wübbeling. *Mathematical Methods in Image Reconstruction*. Society for Industrial and Applied Mathematics, 2001.
- [145] M. N'Diaye, A. Vigan, K. Dohlen, J. F. Sauvage, et al. “Calibration of quasi-static aberrations in exoplanet direct-imaging instruments with a Zernike phase-mask sensor II. Concept validation with ZELDA on VLT/SPHERE”. In: *Astronomy and Astrophysics - A&A* 592.A79 (Aug. 2016).
- [146] B. Neichel, T. Fusco, J.-F. Sauvage, C. Correia, K. Dohlen, K. El-Hadi, L. Blanco, N. Schwartz, et al. “The adaptive optics modes for HARMONI: from Classical to Laser Assisted Tomographic AO”. In: *Proc. SPIE 9909, Adaptive Optics Systems V*. 2016, pp. 990909–990909–15.
- [147] A. Neubauer. “A new cumulative wavefront reconstructor for the Shack - Hartmann sensor”. In: *J. Inv. Ill-Posed Problems* 21 (2013), pp. 451–476.
- [148] A. Obereder, R. Ramlau, and E. Fedrigo. “Mathematical Algorithms and Software for ELT Adaptive Optics The Austrian In-kind Contributions for Adaptive Optics”. In: *The Messenger* 156 (May 2014), pp. 16–20.
- [149] A. Obereder, R. Raffetseder, Iu. Shatokhina, and V. Hutterer. “Dealing with spiders on ELTs: using a Pyramid WFS to overcome residual piston effects”. In: *Proc. SPIE*. Vol. 10703. 2018, pp. 10703 –107031D –19.
- [150] European Southern Observatory. URL: <http://www.eso.org>.
- [151] Thirty Meter Telescope International Observatory. URL: <https://www.tmt.org>.
- [152] Giant Magellan Telescope Organization. URL: <https://www.gmto.org>.
- [153] F. Pedichini, M. Stangalini, F. Ambrosino, A. Puglisi, E. Pinna, V. Bailey, L. Carbonaro, M. Centrone, J. Christou, S. Esposito, J. Farinato, F. Fiore, E. Giallongo, J. M. Hill, P. M. Hinz, and L. Sabatini. “High contrast imaging in the visible: first experimental results at the Large Binocular Telescope”. In: *The Astronomical Journal* 154.2 (2017), p. 74.
- [154] D. Peter, M. Feldt, T. Henning, S. Hippler, J. Aceituno, L. Montoya, J. Costa, and B. Dorner. “PYRAMIR: Exploring the On-Sky Performance of the World’s First Near-Infrared Pyramid Wavefront Sensor”. In: *Publications of the Astronomical Society of the Pacific* 122 (Jan. 2010), pp. 63–70.
- [155] D. W. Phillion and K. Baker. “Two-sided pyramid wavefront sensor in the direct phase mode”. In: *Proc. SPIE*. Vol. 6272. 2006, pp. 627228–627228–12.
- [156] E. Pinna, S. Esposito, A. Puglisi, F. Pieralli, R. Myers, L. Busoni, A. Tozzi, and P. Stefanini. “Phase ambiguity solution with the Pyramid Phasing Sensor”. In: *Proceedings of SPIE - The International Society for Optical Engineering*. Vol. 6267. July 2006.

- [157] E. Pinna, A. T. Puglisi, F. Quirós-Pacheco, L. Busoni, A. Tozzi, S. Esposito, E. Aller-Carpentier, and M. Kasper. “The pyramid wavefront sensor for the high order testbench (HOT)”. In: *Proc. SPIE 7015, Adaptive Optics Systems*. 2008, pp. 701559–1–701559–8.
- [158] E. Pinna, F. Pedichini, S. Esposito, M. Centrone, A. Puglisi, J. Farinato, L. Carbonaro, G. Agapito, et al. “XAO at LBT: current performances in the visible and upcoming upgrade”. In: *Proceedings of the Fourth AO4ELT Conference*. 2015.
- [159] Ben C. Platt and R. Shack. “History and Principles of Shack-Hartmann Wavefront Sensing”. In: *Journal of Refractive Surgery* 17.5 (2001).
- [160] A.D. Polyanin and A.V. Manzhirov. *Handbook of Integral Equations*. Taylor & Francis, 1998.
- [161] L. A. Poyneer, D. T. Gavel, and J. M. Brase. “Fast wave-front reconstruction in large adaptive optics systems with use of the Fourier transform”. In: *J. Opt. Soc. Am. A* 19.10 (Oct. 2002), pp. 2100–2111.
- [162] F. Quirós-Pacheco, C. Correia, and S. Esposito. “Fourier transform-wavefront reconstruction for the pyramid wavefront sensor”. In: *Proceedings of the First AO4ELT Conference*. 2010, p. 07005.
- [163] A. Quirrenbach. “The Effects of Atmospheric Turbulence on Astronomical Observations”. In: *Extrasolar Planets*. Saas-Fee Advanced Course 31. 2006, pp. 130–143.
- [164] R. Ragazzoni. “Pupil plane wavefront sensing with an oscillating prism”. In: *J. of Modern Optics* 43.2 (1996), pp. 289–293.
- [165] R. Ragazzoni, E. Diolaiti, and E. Vernet. “A pyramid wavefront sensor with no dynamic modulation”. In: *Optics Communications* 208 (2002), pp. 51–60.
- [166] R. Ragazzoni and J. Farinato. “Sensitivity of a pyramidal Wave Front sensor in closed loop Adaptive Optics”. In: *Astronomy and Astrophysics* 350 (1999), pp. L23–L26.
- [167] R. Ragazzoni, A. Baruffolo, J. Farinato, A. Ghedina, E. Marchetti, S. Esposito, L. Fini, P. Ranfagni, F. Bortoletto, M. D’Alessandro, M. Ghigo, and G. Crimi. “Final commissioning phase of the AdOpt@TNG module”. In: *Adaptive Optical Systems Technology*. Vol. 4007. Proc. SPIE. July 2000, pp. 57–62.
- [168] R. Ramlau, D. Saxenhuber, and M. Yudytskiy. “Iterative reconstruction methods in atmospheric tomography: FEWHA, Kaczmarz and Gradient-based algorithm”. In: *Proc. SPIE*. 2014, 91480Q–91480Q–15.
- [169] R. Ramlau and G. Teschke. “Regularization of Sobolev Embedding Operators and Applications Part I: Fourier and Wavelet based Methods”. In: *Sampling Theory in Signal and Image Processing* 3.2 (2004), pp. 175–196.

- [170] M. Rayden. “On the Barzilai and Borwein choice of steplength for the gradient method”. In: *IMA Journal of Numerical Analysis* 13.3 (1993), pp. 321–326.
- [171] F. Rigaut and M. van Dam. “ELT AO simulations on a laptop with YAO”. In: *Proc. AO4ELT3*. 2013.
- [172] F. Rigaut and M. Van Dam. “Simulating astronomical Adaptive Optics systems using yao”. In: *Proc. AO4ELT3*. 2013, p. 18.
- [173] L. C. Roberts, M. D. Perrin, F. Marchis, A. Sivaramakrishnan, R. B. Makidon, J. C. Christou, B. A. Macintosh, L. A. Poyneer, M. van Dam, and M. Troy. “Is that really your Strehl ratio”. In: *Proc. SPIE*. Vol. 5490. 2004, pp. 5490–5490–12.
- [174] F. Roddier. *Adaptive Optics in Astronomy*. Cambridge, U.K. ; New York : Cambridge University Press, 1999, p. 411.
- [175] F. Roddier. “Curvature sensing and compensation: a new concept in adaptive optics”. In: *Applied Optics* 27.7 (1988), pp. 1223–1225.
- [176] F. Roddier. *The Effects of Atmospheric Turbulence in Optical Astronomy*. North-Holland Publishing Company, 1981.
- [177] F. Roddier and C. Roddier. “Wavefront reconstruction using iterative Fourier transforms”. In: *Appl. Opt.* 30.11 (Apr. 1991), pp. 1325–1327.
- [178] M. C. Roggemann and B. Welsh. *Imaging through turbulence*. CRC Press laser and optical science and technology series. CRC Press, 1996.
- [179] M. Rosensteiner. “Cumulative Reconstructor: fast wavefront reconstruction algorithm for Extremely Large Telescopes”. In: *J. Opt. Soc. Am. A* 28.10 (Oct. 2011), pp. 2132–2138.
- [180] M. Rosensteiner. “Wavefront reconstruction for extremely large telescopes via CuRe with domain decomposition”. In: *J. Opt. Soc. Am. A* 29.11 (Nov. 2012), pp. 2328–2336.
- [181] M. Rosensteiner and R. Ramlau. “Efficient iterative atmospheric tomography reconstruction from LGS and additional tip/tilt measurements”. In: *Proc. SPIE 8447, Adaptive Optics Systems III*. 2012, 84475S–84475S–6.
- [182] M. Rosensteiner and R. Ramlau. “The Kaczmarz algorithm for multi-conjugate adaptive optics with laser guide stars”. In: *J. Opt. Soc. Am. A* 30.8 (2013), pp. 1680–1686.
- [183] M. Sarazin, M. Le Louarn, J. Ascenso, G. Lombardi, and J. Navarrete. “Defining reference turbulence profiles for E-ELT AO performance simulations”. In: *Proceedings of the Third AO4ELT Conference*. Vol. 13383. 2013.
- [184] D. Saxenhuber. “Gradient-based reconstruction algorithms for atmospheric tomography in Adaptive Optics systems for Extremely Large Telescopes”. PhD thesis. Johannes Kepler University Linz, 2016.

- [185] D. Saxenhuber and R. Ramlau. “A Gradient-based method for atmospheric tomography”. In: *Inverse Problems and Imaging* 10.3 (2016), pp. 781–805.
- [186] D. Saxenhuber, G. Auzinger, M. Le Louarn, and T. Helin. “Comparison of methods for the reduction of reconstructed layers in atmospheric tomography”. In: *Appl. Opt.* 56.10 (Apr. 2017), pp. 2621–2629.
- [187] N. Schwartz, J.-F. Sauvage, C. Correia, B. Neichel, T. Fusco, F. Quiros-Pacheco, K. Dohlen, K. El Hadi, G. Agapito, N. Thatte, and F. Clarke. “Analysis and mitigation of pupil discontinuities on adaptive optics performance”. In: *Proc. SPIE*. Vol. 10703. 2018, pp. 10703 –1070322 –12.
- [188] N. Schwartz, J.-F. Sauvage, C. Correia, C. Petit, F. Quiros-Pacheco, T. Fusco, K. Dohlen, K. El Hadi, N. Thatte, F. Clarke, J. Paufique, and J. Vernet. “Sensing and control of segmented mirrors with a pyramid wavefront sensor in the presence of spiders”. In: *Proceedings AO4ELT5*. 2017.
- [189] N. Schwartz et al. *Update on the mitigation of the island effect for the ELT*. <https://www.dur.ac.uk/resources/cfai/workshop2018/schwartzFriday.pdf>. Talk presented at the AO Workshop Week, Durham, 2018.
- [190] Ronald Shack. “Production and use of a lenticular Hartmann screen”. In: *J. Opt. Soc. Am.* 61.656 (1971).
- [191] Iu. Shatokhina. “Fast wavefront reconstruction algorithms for extreme adaptive optics”. PhD thesis. Johannes Kepler University Linz, 2014.
- [192] Iu. Shatokhina. *Simulation of the modulated pyramid and roof wavefront sensors*. Tech. rep. E-TRE-AAO-528-0011 Issue 1. Austrian In-Kind Contribution - AO, 2011.
- [193] Iu. Shatokhina. *Simulation of the non-modulated pyramid wavefront sensor*. Tech. rep. E-TRE-AAO-528-0007 Issue 1. Austrian In-Kind Contribution - AO, 2011.
- [194] Iu. Shatokhina, V. Hutterer, and R. Ramlau. “Two novel algorithms for wavefront reconstruction from pyramid sensor data: Convolution with Linearized Inverse Filter and Pyramid Fourier Transform Reconstructor”. In: *Proceedings AO4ELT5*. 2017.
- [195] Iu. Shatokhina, A. Obereder, and R. Ramlau. “Fast algorithm for wavefront reconstruction in XAO/SCAO with pyramid wavefront sensor”. In: *Proc. SPIE* 9148, Adaptive Optics Systems IV. 2014, 91480P–1–15.
- [196] Iu. Shatokhina and R. Ramlau. “Convolution- and Fourier-transform-based reconstructors for pyramid wavefront sensor”. In: *Applied Optics* 56.22 (2017), pp. 6381–6390.
- [197] Iu. Shatokhina, M. Zhariy, and R. Ramlau. *Wavefront reconstruction for XAO*. Poster presented at the Second Conference on Adaptive Optics for Extremely Large Telescopes. Victoria, British Columbia, Canada, Sept. 2011.

- [198] Iu. Shatokhina, A. Obereder, M. Rosensteiner, and R. Ramlau. “Preprocessed cumulative reconstructor with domain decomposition: a fast wavefront reconstruction method for pyramid wavefront sensor”. In: *Applied Optics* 52.12 (2013), pp. 2640–2652.
- [199] S. L. Sobolew. *Einige Anwendungen der Funktionalanalysis auf Gleichungen der mathematischen Physik*. (Translation from Russian). Berlin: Akademie-Verlag, 1964.
- [200] E. M. Stein. *Singular Integrals and Differentiability Properties of Functions*. Princeton University Press N. J., 1970.
- [201] I. Surdej. “Co-phasing segmented mirrors: theory, laboratory experiments and measurements on sky”. PhD thesis. 2011.
- [202] M. Tallon, I. Tallon-Bosc, C. Béchet, and E. Thiébaud. “Shack-Hartmann wavefront reconstruction with elongated sodium laser guide stars: improvements with priors and noise correlations”. In: vol. 7015.1. Marseille, France: SPIE, 2008, 70151N.
- [203] G. I. Taylor. “The Spectrum of Turbulence”. In: *Proceedings of the Royal Society of London Series A, Mathematical and Physical Sciences*.164 (1938), pp. 476–490.
- [204] E. Thiébaud and M. Tallon. “Fast minimum variance wavefront reconstruction for extremely large telescopes”. In: *J. Opt. Soc. Am. A* 27 (2010), pp. 1046–1059.
- [205] F.G. Tricomi. *Integral Equations*. New York: Interscience, 1957.
- [206] H. Triebel. *Höhere Analysis*. Hochschulbücher für Mathematik, Band 76. Berlin: VEB Deutscher Verlag der Wissenschaften, 1972.
- [207] S. Turbide, M. Wang, J. Gauvin, O. Martin, M. Savard, P. Bourqui, J.-P. Véran, W. Deschênes, G. Anctil, and F. Chateaufneuf. “Development of a pyramidal wavefront sensor test-bench at INO”. In: *Proceedings of the Third AO4ELT Conference*. 2013.
- [208] G. A. Tyler. “Bandwidth considerations for tracking through turbulence”. In: *J. Opt. Soc. Am. A* 11.1 (Jan. 1994), pp. 358–367.
- [209] R. K. Tyson. *Introduction to Adaptive Optics*. SPIE Tutorial Texts in Optical Engineering Vol. TT41, 2000.
- [210] J.-P. Véran, F. Rigaut, H. Maître, and D. Rouan. “Estimation of the adaptive optics long exposure point spread function using control loop data”. In: *J. Opt. Soc. Am. A* 14.11 (Nov. 1997), pp. 3057–3069.
- [211] J.-P. Véran, S. Esposito, P. Spanò, G. Herriot, and D. Andersen. “Pyramid versus Shack-Hartmann: Trade Study Results for the NFIRAOS NGS WFS”. In: *Proceedings of the Fourth AO4ELT Conference*. 2015.

- [212] C. Vérinaud. “On the nature of the measurements provided by a pyramid wavefront sensor”. In: *Optics Communications* 233 (2004), pp. 27–38.
- [213] C. Vérinaud, M. Le Louarn, V. Korhikoski, and M. Carbillet. “Adaptive optics for high-contrast imaging: pyramid sensor versus spatially filtered Shack-Hartmann sensor”. In: *Mon. Not. R. Astron. Soc.: Letters* 357 (2005), pp. L26–L30.
- [214] C. Vérinaud, C. Arcidiacono, M. Carbillet, E. Diolaiti, R. Ragazzoni, E. Vernet-Viard, and S. Esposito. “Layer Oriented multi-conjugate adaptive optics systems: performance analysis by numerical simulations”. In: *Adaptive Optical System Technologies II*. Proc. SPIE 4839. 2003, pp. 524–535.
- [215] V. Viotto, D. Magrin, M. Bergomi, M. Dima, J. Farinato, L. Marafatto, and R. Ragazzoni. “A study of Pyramid WFS behaviour under imperfect illumination”. In: *Proceedings of the Third AO4ELT Conference*. 2013.
- [216] V. Viotto, R. Ragazzoni, M. Bergomi, D. Magrin, and J. Farinato. “Expected gain in the pyramid wavefront sensor with limited Strehl ratio”. In: *Astronomy and Astrophysics* 593 (Sept. 2016), A100–1–A100–6.
- [217] V. Viotto, M. Bergomi, M. Dima, J. Farinato, D. Greggio, D. Magrin, E. Portaluri, R. Ragazzoni, S. Esposito, and E. Pinna. “PWFSs on GMCAO: a different approach to the non-linearity issue”. In: *Proc. SPIE*. Vol. 9909. 2016, pp. 9909–9909–6.
- [218] C. R. Vogel and Q. Yang. “Multigrid algorithm for least-squares wavefront reconstruction”. In: *Applied Optics* 45.4 (2006), pp. 705–715.
- [219] B. Vohnsen, S. Castillo, and D. Rativa. “Wavefront sensing with an axicon”. In: *Opt. Lett.* 36.6 (Mar. 2011), pp. 846–848.
- [220] R. Wagner. “From Adaptive Optics systems to Point Spread Function Reconstruction and Blind Deconvolution for Extremely Large Telescopes”. PhD thesis. Johannes Kepler University Linz, 2017.
- [221] R. Wagner, C. Hofer, and R. Ramlau. “Point spread function reconstruction for Single-conjugate Adaptive Optics”. In: *Journal of Astronomical Telescopes, Instruments, and Systems* (2018), accepted.
- [222] J. Wang, F. Bai, Y. Ning, L. Huang, and Sh. Wang. “Comparison between non-modulation four-sided and two-sided pyramid wavefront sensor”. In: *Optics Express* 18.26 (Dec. 2010), pp. 27534–27549.
- [223] D. Werner. *Funktionalanalysis*. Springer-Lehrbuch. Springer Berlin Heidelberg, 2011.
- [224] K. Yao, J. Wang, X. Liu, H. Li, M. Wang, B. Cui, and S. Yu. “Pyramid wavefront sensor using a sequential operation method”. In: *Appl. Opt.* 54.13 (May 2015), pp. 3894–3901.

- 
- [225] M. Yudytskiy. “Wavelet methods in adaptive optics”. PhD thesis. Johannes Kepler University Linz, 2014.
- [226] M. Yudytskiy, T. Helin, and R. Ramlau. “Finite element-wavelet hybrid algorithm for atmospheric tomography”. In: *J. Opt. Soc. Am. A* 31.3 (Mar. 2014), pp. 550–560.
- [227] M. Zhariy. *Hilbert transform reconstructor for non-modulated PWS measurements*. Tech. rep. E-TRE-AAO-528-0013. Austrian In-Kind Contribution - AO, 2011.
- [228] M. Zhariy. *Two component reconstructor for modulated PWS measurements*. Tech. rep. E-TRE-AAO-528-0015. Austrian In-Kind Contribution - AO, 2011.
- [229] M. Zhariy, A. Neubauer, M. Rosensteiner, and R. Ramlau. “Cumulative Wavefront Reconstructor for the Shack-Hartman Sensor”. In: *Inverse Problems and Imaging* 5.4 (Nov. 2011), pp. 893–913.
- [230] B. Zhou, L. Gao, and Y.-H. Dai. “Gradient Methods with Adaptive Step-Sizes”. In: *Computational Optimization and Applications* 35.1 (2006), pp. 69–86.
- [231] W. Zou and J. P. Rolland. “Iterative zonal wave-front estimation algorithm for optical testing with general-shaped pupils”. In: *J. Opt. Soc. Am. A* 22.5 (May 2005), pp. 938–951.
- [232] W. Zou, X. Qi, G. Huang, and St. A. Burns. “Improving wavefront boundary condition for in vivo high resolution adaptive optics ophthalmic imaging”. In: *Biomed. Opt. Express* 2.12 (Dec. 2011), pp. 3309–3320.

# Eidesstattliche Erklärung

Ich erkläre an Eides statt, dass ich die vorliegende Dissertation selbstständig und ohne fremde Hilfe verfasst, andere als die angegebenen Quellen und Hilfsmittel nicht benutzt bzw. die wörtlich oder sinngemäß entnommenen Stellen als solche kenntlich gemacht habe. Die vorliegende Dissertation ist mit dem elektronisch übermittelten Textdokument identisch.

Linz, Oktober 2018

---

Victoria Hutterer



# Curriculum Vitae

---

## PERSONAL INFORMATION

Date of birth November 3<sup>rd</sup>, 1992, Gmunden, Austria  
Address Mühlenstraße 14, 4656 Kirchham, Austria  
Email victoria.hutterer@indmath.uni-linz.ac.at  
Phone +43 699 109 88 237

---

## EMPLOYMENT

01/17 – today **University Assistant**, Industrial Mathematics Institute,  
Johannes Kepler University, Linz, Austria  
09/16 – today **Trainer for Mathematics**, Wifi OÖ GmbH, Linz, Austria  
12/15 – 01/17 **Research Assistant**, Doctoral Program “Computational  
Mathematics”, Johannes Kepler University, Linz, Austria

---

## EDUCATION

12/15 – today Doctoral program, **Engineering Sciences, Industrial  
Mathematics**, Johannes Kepler University, Linz, Austria  
08/14 – 11/15 Master’s program, **Mathematics for Natural Sciences**, with  
distinction, *Master thesis: Orthogonale Projektionen auf  
Splineräume*, Johannes Kepler University, Linz, Austria  
10/11 – 07/14 Bachelor’s program, **Technical Mathematics**, *Bachelor Thesis:  
Monte Carlo Methoden und Varianzreduktionstechniken*,  
Johannes Kepler University, Linz, Austria  
09/03 – 06/11 **High School**, with distinction, Gymnasium des Schulvereins  
der Kreuzschwestern, Gmunden, Austria

---

## GRANTS

10/13 – 10/15 **Merit-based scholarships**, Johannes Kepler University, Linz,  
Austria

---

## PROGRAMMING SKILLS

- **Matlab**, working knowledge
- **C, C#, C++**, basic knowledge

---

## LANGUAGE SKILLS

- German, mother tongue
- English, fluent
- French, intermediate
- Spanish, elementary
- Latin

---

## PUBLICATIONS

- [1] Iu. Shatokhina, V. Hutterer, R. Ramlau, *Two novel algorithms for wavefront reconstruction from pyramid sensor data: Convolution with Linearized Inverse Filter and Pyramid Fourier Transform Reconstructor*, Conference Proceedings AO4ELT5, (2017)
- [2] V. Hutterer, R. Ramlau, *Wavefront Reconstruction from Non-modulated Pyramid Wavefront Sensor Data using a Singular Value Type Expansion*, Inverse Problems, 34, 035002 (2018)
- [3] V. Hutterer, Iu. Shatokhina, A. Obereder, R. Ramlau, *Wavefront reconstruction for ELT-sized telescopes with pyramid wavefront sensors*, Proc. SPIE 10703-44, (2018)
- [4] A. Obereder, S. Raffetseder, Iu. Shatokhina, V. Hutterer, *Dealing with Spiders on ELTs: using a Pyramid WFS to overcome residual piston effects*, Proc. SPIE 107031D, (2018)
- [5] R. Davies et al., *The MICADO first light imager for the ELT: overview, operation, simulation*, Proc. SPIE 107021S, (2018)
- [6] V. Hutterer, R. Ramlau, *Non-linear wavefront reconstruction methods for pyramid sensors using Landweber and Landweber-Kaczmarz iteration*, Applied Optics, to be published
- [7] V. Hutterer, Iu. Shatokhina, A. Obereder, R. Ramlau, *Advanced reconstruction methods for segmented ELT pupils using pyramid sensors*, submitted
- [8] V. Hutterer, R. Ramlau, Iu. Shatokhina, *Real-time Adaptive Optics with pyramid wavefront sensors: A theoretical analysis of the pyramid sensor model*, submitted
- [9] V. Hutterer, R. Ramlau, Iu. Shatokhina, *Real-time Adaptive Optics with pyramid wavefront sensors: Accurate wavefront reconstruction using iterative methods*, submitted

---

## CONFERENCES AND WORKSHOPS

- 09/18 **Doctoral Program “Computational Mathematics” Statusseminar**, Talk: *Analysis and mitigation of the island effect on segmented ELT pupils*, Strobl, Austria
- 09/18 **Member Meeting of the SFB “Tomography across the Scales”**, Talk: *Analysis of disconnectedness on Extremely Large Telescope pupils*, Altenmarkt, Austria
- 07/18 **First Internal Meeting of the SFB “Tomography across the Scales”**, Talk: *Wavefront reconstruction with pyramid sensors on segmented pupils*, Vienna, Austria
- 06/18 **SPIE Astronomical Telescopes and Instrumentation**, Poster: *Wavefront reconstruction for ELT-sized telescopes with pyramid wavefront sensors*, Austin, Texas
- 06/18 **SIAM Conference on Imaging Science**, Talk: *Accurate wavefront reconstruction for real-time AO with pyramid wavefront sensors*, Bologna, Italy

- 05/18 **L2 Kick-off meeting**, *Talk: Wavefront reconstruction using pyramid sensors on ELT-sized telescopes*, LAM Marseille, France
- 03/18 **AO Workshop**, *Talk: High-quality wavefront reconstruction for pyramid sensors using a non-linear approach*, Durham, Great Britain
- 03/18 **Inverse Problems in the Alps (Workshop)**, Obergurgl, Austria
- 03/18 **SFB Tomography across the Scales**, *Talk: Wavefront Reconstruction in Astronomical Adaptive Optics using Pyramid Sensors*, Obergurgl, Austria
- 02/18 **ESO Lunch Talk**, *Talk: Wavefront reconstruction with pyramid wavefront sensors and pupil fragmentation*, European Southern Observatory, Garching, Germany
- 02/18 **METIS SCAO Progress meeting**, *Max-Planck Institute for Astronomy, Heidelberg, Germany*
- 10/17 **SFB Tomography across the Scales**, *Poster: Wavefront Reconstruction in Astronomical AO for Pyramid Sensors*, Vienna, Austria
- 10/17 **Wavefront Sensing in the VLT/ELT era II (Workshop)**, *Talk: Direct piston reconstruction approaches to control segmented ELT-mirrors*, Padua, Italy
- 07/17 **Doctoral Program “Computational Mathematics” Workshop**, *Talk: New ideas of wavefront reconstruction in AO based on the inversion of the finite Hilbert transform*, Linz, Austria
- 06/17 **Adaptive Optics for Extremely Large Telescopes 5**, *Poster: Wavefront Reconstruction from Pyramid Sensor Measurements based on the Inversion of the Finite Hilbert Transform, Poster: Two novel algorithms for wavefront reconstruction from pyramid sensor data: Convolution with Linearized Inverse Filter and Pyramid Fourier Transform Reconstructor, Poster: Status of the SCAO design of METIS and end-to-end simulation performances*, Tenerife, Spain
- 05/17 **Applied Inverse Problems**, *Talk: Wavefront Reconstruction in AO from Pyramid Sensor Data*, Hangzhou, China
- 03/17 **100 Years of the Radon Transform**, *Poster: Wavefront Reconstruction in AO using a Singular Value Type Expansion*, Linz, Austria
- 03/17 **Riemann International School of Mathematics**, *Poster: Wavefront Reconstruction in AO using a Singular Value Type Expansion*, Varese, Italy
- 12/16 **IFIP WG 7.4 Inverse Problems and Imaging (Workshop)**, *Talk: Wavefront Reconstruction in AO using Pyramid Sensors*, Mühlheim, Germany
- 10/16 **Wavefront Sensing in the VLT/ELT era (Workshop)**, *Talk: The Inverse Problem of Wavefront Reconstruction from Pyramid Wavefront Sensor Data*, Marseille, France
- 09/16 **Doctoral Program “Computational Mathematics” Statusseminar**, *Talk: Inverse Problems in Astronomical Adaptive Optics*, Strobl, Austria

- 09/16 **Chemnitz Symposium on Inverse Problems**, *Talk: The Inverse Problem of Wavefront Reconstruction from Pyramid Sensor Data*, Chemnitz, Germany
- 06/16 **MICADO E-ELT Consortium Meeting**, Vienna, Austria
- 05/16 **A\* Meeting**, Linz, Austria
- 04/16 **METIS E-ELT Consortium Meeting**, Heidelberg, Germany
- 03/16 **Inverse Problems in the Alps (Workshop)**, Obergurgl, Austria
- 12/15 **2<sup>nd</sup> Symposium: From Ground to Space**, Vienna, Austria

---

### TEACHING

- 2017|2018 **Teaching Assistant**, *Mathematics 2 for Chemistry*, Johannes Kepler University, Linz, Austria
- 2016|2017|2018 **Teaching Assistant**, *Mathematics 1 for Chemistry*, Johannes Kepler University, Linz, Austria
- 2013|2014|2015 **Teaching Assistant**, Department of Knowledge-Based Mathematical Systems, Johannes Kepler University, Linz, Austria
- 2013|2014 **Teaching Assistant**, Institute of Financial Mathematics and Applied Number Theory, Johannes Kepler University, Linz, Austria

---

### PARTICIPATION AT SCHOOLS

- 07/16 - 08/16 **Summer School on Adaptive Optics**, University of California Santa Cruz, California, USA

---

### OTHER QUALIFICATIONS AND AWARDS

- 09/18 **Basic program course 17 for academic staff (Focus teaching and research)**, Johannes Kepler University, Linz, Austria
- 05/18 **Rhetoric Diploma**, Wifi Gmunden, Austria
- 10/17 **Trainer Diploma**, Wifi Linz, Austria
- 06/16 **Skilled Worker in Agriculture**, Altmünster, Austria
- 05/15 **FLA (Feuerwehrleistungsabzeichen) Gold**, Linz, Austria
- 2013 – 2015 **Chair of Student Representative for Technical Mathematics**, Austrian Student Union (ÖH), Johannes Kepler University, Linz, Austria
- 2012 – 2015 **Member of Study Commission Technical Mathematics**, Johannes Kepler University, Linz, Austria

---

### HOBBIES

- Volunteer Fire Company, Kirchham, Austria
- Skiing, SRC Union Kirchham, Austria
- Outdoor sports

*Do not worry about your difficulties in Mathematics.  
I can assure you mine are still greater.*  
(Albert Einstein)